DISSERTATION

ANALYSIS AND APPLICATION OF THE CASA IP1 X-BAND POLARIMETRIC RADAR NETWORK

Submitted by

Brenda Dolan

Department of Atmospheric Science

In partial fulfillment of the requirements

for the Degree of Doctor of Philosophy

Colorado State University

Fort Collins, Colorado

Spring 2009

COLORADO STATE UNIVERSITY

January 27, 2009

WE HEREBY RECOMMEND THAT THE DISSERTATION PREPARED UNDER OUR SUPERVISION BY BRENDA DOLAN ENTITLED ANALYSIS AND APPLICATION OF THE CASA IP1 X-BAND POLARIMETRIC RADAR NETWORK BE ACCEPTED AS FULFILLING IN PART REQUIREMENTS FOR THE DEGREE OF DOCTOR OF PHILOSOPHY.

Committee on Graduate Work

William Cotton

Steven A. Rutledge, Advisor

Department Head

ABSTRACT OF DISSERTATION

ANALYSIS AND APPLICATION OF THE CASA IP1 X-BAND POLARIMETRIC RADAR NETWORK

The Collaborative Adaptive Sensing of the Atmosphere's Integrated Project 1 (CASA IP1) network of four X-band, polarimetric, Doppler, adaptively scanning radars is investigated for studying storm microphysics and kinematics. The complications of non-Rayleigh scattering and attenuation at X-band are explored for impact on microphysical interpretation. The rapid and adaptive scanning strategy is evaluated for application of dual-Doppler techniques to retrieve the 3-D wind field, and general understanding of storm interactions. Several rain rate algorithms are invoked to estimate surface rainfall. A case study from 10 June 2007 illustrates the capabilities and limitations of using the IP1 network for studies of storm interactions, and lightning data are analyzed to relate these interactions to storm electrification. The nearby S-band, polarimetric KOUN radar is studied for comparison.

Scattering simulations using the T-matrix model are performed on seven hydrometeor types (excluding hail) to understand the non-Rayleigh effects at X-band compared with S-band. The simulations show the greatest non-linearities in Z_{dr} and K_{dp} of rain and graupel. Results of the simulations are used to develop a specific X-band fuzzy logic hydrometeor identification algorithm (HID) for diagnosing bulk regions of hydrometeors.

Attenuation and non-Rayleigh scattering are present in the IP1 data, but with mitigation techniques these have minimal impact on the analysis. The high temporal resolution is integral in resolving up- and downdrafts, as well as hydrometeor evolution, but the inconsistent and lack of upper-level coverage are significant limitations for quantitative analysis of kinematic and microphysical relationships.

Observations using IP1 data of a storm on 10 June 2007 show the development of the updraft, subsequent graupel echo volume evolution, and onset of lightning. Development of the downdraft is preceded by large volumes of graupel in the mid-levels. A second peak in intra-cloud lightning is observed to be associated with an increase in height of the upper positive charge, resulting from a kinematic intensification. Many of these trends are corroborated by KOUN. Rain rate estimation comparisons show that the X-band blended algorithm performs better compared with ground-based sensors than the simple Z-R relationship and employs polarimetric estimators more often than S-band blended methods.

Brenda Dolan
Department of Atmospheric Science
Colorado State University
Fort Collins, CO 80523
Spring 2009

ACKNOWLEDGMENTS

I would like to thank my advisor, Prof. Steven Rutledge, for his encouragement and advice over the years, and for providing interesting projects and opportunities. Thanks to my committee, Dr. William Cotton, Dr. Christian Kummerow, Dr. V. Chandrasekar, and Dr. Keith Brewster (OU) for their suggestions and direction. I also extend appreciation to Prof. Chandrasekar for his enthusiasm and assistance with the CASA IP1 project.

The members of the radar meteorology group, past and present, were integral in my accomplishments. Discussions with and suggestions by Dr. Robert Cifelli and Dr. Timothy Lang were invaluable. I would also like to thank Dr. Kyle Wiens, Dr. Sarah Tessendorf, Dr. Gustavo Pereira, and Dr. Steve Nesbitt, as well as Ms. Jillian L'Ecuyer, Ms. Margi Cech, Ms. Angela Rowe, Ms. Kristen George, and Ms. Amanda Anderson for their knowledge, input, support and friendship. I also extend a special thanks to Mr. Paul Hein, who was always ready to tackle any computer question or coding problem I threw at him.

I would also like to thank all of those in CASA for which this research would not be possible without their hard work and support of my research, especially Dr. David McLaughlin (UMASS), Dr. Jerry Brotzge (OU), and Ms. Brenda Philips (UMASS). Additionally, I would like to recognize all those who helped me obtain and work with the data necessary for this project: Dr. Yanting Wang (CSU), Dr. S. Lim (CSU), and other members of the CSU ECE department (Mr. Nitin Bharadwaj, Ms. Ledya Leon, Dr. Francesc Yunyent). Dr. Terry Schuur (NSSL) provided KOUN data, Dr. Don

MacGorman (NSSL) supplied the OK-LMA data, and Dr. Guifu Zhang (OU) furnished the 2D-VD data. Mesonet data were obtained from the Oklahoma Climatological Survey.

This work is supported primarily by the Engineering Research Centers Program of the National Science Foundation under NSF award 0313747, Colorado State University, and University of Massachusetts contract number UM04-002341.

This dissertation is dedicated to my husband Ryan. Thanks for all your support, understanding, advice, and encouragement over the years.

Brenda Dolan
Colorado State University
Spring 2009

Table of Contents

List of Figures

List of Tables

Chapter 1

Introduction

1.1 Collaborative Adaptive Sensing of the Atmosphere (CASA)

The NSF Engineering Research Center Collaborative Adaptive Sensing of the Atmosphere (CASA) was funded in 2003 as a collaborative effort between Colorado State University (CSU), the University of Oklahoma, the University of Massachusetts (lead institution), and the University of Puerto Rico-Mayaguez. The primary objective is to improve observations and forecasting of devastating weather such as flash floods, tornados, high winds, and hail by developing new paradigms for sensing the atmosphere. These near-surface events are often missed by the current S-band national radar observation network, NEXRAD, due to the Earth's curvature, radar beam refraction and separation between radars. Additionally, since NEXRAD is comprised of only 151 radars to blanket the entire United States, each radar must scan a large area, and as such cannot be used to pinpoint specific storms of interest. To cover each area, NEXRAD radars typically scan 14 elevation angles in a time period of 5 minutes. Finally, large gaps in radar coverage areas exist, particularly in the western United States where beam-blockage due to terrain is common. CASA has proposed a new observational model to address some of these shortcomings of the current nation-wide radar observation network.

The main objective of CASA is to "revolutionize the way we observe, understand, and predict hazardous weather by creating distributed collaborative adaptive sensing networks that sample the atmosphere where and when end user needs are greatest" (McLaughlin, 2001; http://www.casa.umass.edu, 2009). The new paradigm proposed by CASA is to make the allocation of resources (i.e., radar scan time) driven by the users who are interested in the information. In order to accomplish this, a network of radars that could decide where and when to scan autonomously was required. A Meteorological Command and Control (MC&C) was developed to run the radars. The MC&C decides which radars to use, the sector size, and the number of elevation angles based on the types of echoes in the network and a set of user-defined rules for scanning certain types of echoes (Zink et al., 2008). The rapid and adaptive scanning strategy can optimize the coverage for particular types of meteorological events and change in real-time to adaptively accommodate features as they evolve in the network. To solve the coverage problem and minimize curvature effects, CASA proposed dense networks of short-range radars that could sit on existing infrastructure.

Since most hazardous weather events occur near the surface of the Earth and are relatively localized (floods, tornados, hail, straight line winds, etc.), CASA first developed a network of low-looking, short-range radars that use the MC&C technology to quickly and adaptively scan hazardous weather. The CASA objectives necessitated the use of inexpensive, small, and low-power radars that could easily be installed on existing structures such as small buildings and cell phone towers. X-band was determined to be the most appropriate wavelength for this application. The first test bed, or Integrated Project 1 (IP1), was established in southwestern Oklahoma to improve detection and forecasting of tornados. IP1 consists of four X-band, polarimetric, Doppler radars with overlapping coverage (Fig. 1.1). The IP1 radars are situated to optimize low-level dual-Doppler coverage, making kinematic retrievals possible. The polarimetric capabilities of the radars also allow for inference of bulk hydrometeors, which can be used to study microphysical processes in the context of Doppler-derived flow fields. Thus, the IP1 radars have the potential to be used for scientific studies beyond forecasting and detection of tornados and low-level hazardous weather.

The possible future implementation of regional or national networks of adaptively and rapidly scanning X-band, polarimetric radars could have profound scientific research applications beyond improving Numerical Weather Prediction and forecast lead times. A broad radar network capable of retrieving microphysical and kinematic processes on short timescales (1-3 minutes) could provide insight into storm initiation, intensification, and evolution, as well as provide the basis for more detailed climatological studies. One of the main objectives of this dissertation is to take IP1 beyond the low-levels and assess the potential for studying overall storm microphysics and kinematics.

1.2 Previous X-band work

Historically, long wavelength radars (S-band, 10 cm) have been used for observations and study of storm microphysics and evolution due to the lack of significant attenuation and non-Rayleigh scattering, although early studies by Battan employed X-band (3.2 cm) to study hail and vertical velocities (Battan, 1964; Battan and Theiss, 1972; Battan and Theiss, 1973). Recently there has been renewed interest in utilizing shorter wavelengths, such as X-band, for studying storm morphology due to their compact and mobile nature (e.g. Bluestein et al., 2007a, b; Iwanami et al., 2001) and increased sensitivity of specific differential phase compared to S-band (e.g. Martner, et al., 2001; Matrosov et al., 2002; Anagnostou et al., 2004; Anagnostou et al., 2006; Matrosov et al., 2006). These types of studies are possible with improved methodologies for attenuation correction, such as that proposed by Testud et al. (2000), Gorgucci and Chandrasekar (2005), Park et al. (2005), Gorgucci et al. (2006), Liu et al. (2006), and Chandrasekar and Lim (2008).

The complicated non-Rayleigh effects at X-band have been studied by many authors (Bringi et al., 1990; Jameson, 1991; Jameson, 1992; Matrosov et al., 1999; Tian et al., 2002; Chandrasekar et al., 2002; Matrosov et al., 2002; Maki et al. 2005; Matrosov et al., 2005; Ryzhkov and Zrnic, 2005; Chandrasekar et al., 2006; Thurai et al., 2007). These studies found that X-band reflectivity is generally higher than S-band for drop diameters greater than 3 mm. Additionally, at diameters of 3 to 4 mm, X-band Z_{dr} values can be 0.5 dB larger than S-band. These modeling studies were also used to determine the possibilities for using X-band for quantitative precipitation estimation (QPE), based on the principle that the specific differential phase increases with decreasing wavelength, leading to larger phase shifts in areas of lighter rain compared to S-band (Matrosov et al., 2002).

Recently, studies have employed polarimetric X-band radars for observations of severe weather (Bluestein and Wakimoto, 2003; Bluestein et al., 2007b) and snow (Nissen et al., 2001), as well as for retrieval of rainfall and microphysical parameters (Ryzhkov et al., 1994; Anagnostou et al., 2004; Matrosov et al., 2006; Gorgucci et al., 2008). Bluestein et al. (2007a) illustrated the advantages of small, mobile polarimetric X-band systems for tornado observations in that they could get closer and therefore have better spatial resolution than fixed S-band radars. Nissen et al. (2001) used two X-band radar systems to estimate the three-dimensional wind field in Canadian snow storms using variational analysis methods. X-band is also being investigated for QPE (Matrosov et al., 2002; Anagnostou et al., 2006; Matrosov et al., 2006). Matrosov et al. (2002) noted no significant effects from backscatter phase shift in heavy rain, and additionally found the best agreement between rain gauge data and radar estimated rainfall using a combined polarimetric estimator employing both differential reflectivity (Z_{dr}) and specific differential phase (K_{dp}). Anagnostou et al. (2004) used a polarimetric X-band radar in Iowa to retrieve rainfall, and found that a multiparameter rainfall estimator using Z_{dr} and difference reflectivity (Z_{dp}) provided the optimal estimation. Comparisons between specific differential phase (K_{dp}) precipitation estimators showed the advantages of X-band in light rain (2.5-15 mm h^{-1}), where larger phase shifts translate to more reliable K_{dp} values and better estimates of rain rates than at S-band, where the same estimators are generally not available until 8-10 mm h^{-1} (Matrosov et al., 2006). Research has also focused on retrieving parameters of the drop-size distribution (DSD) from X-band observations, such as the intercept (N_w) and mean drop diameter (D_o; Anagnostou et al., 2006; Gorgucci et al., 2008).

Many of the studies at X-band described above would not have been possible without new advancements for attenuation mitigation. Several correction methods have been proposed: a simple differential phase-based correction (e.g. Bringi et al., 1990), a range profiling algorithm with a constraint on the differential phase (Φ_{dp}; Testud et al., 2000), so-called self-consistent correction methods (Park et al., 2005; Gorgucci et al., 2006; Liu et al., 2006), and network-based corrections (Chandrasekar and Lim, 2008). The self-consistency algorithms take advantage of relationships that must exist between radar measurements in a rain medium, which can then be used to estimate the specific and differential attenuation (Gorgucci et al., 2006). The network-based correction method proposed by Chandrasekar and Lim (2008) exploits the different viewing angles of radars in a network, which result in unique differential attenuation paths that can be used to reconstruct the reflectivity and differential reflectivity in a network of radars. However, all methods of attenuation correction are only effective when the signal to noise ratio of the attenuated signal remains above the noise floor. Complete attenuation of the signal is still a limitation of using X-band, particularly in intense convection and heavy rain. Nonetheless, these new methodologies for attenuation mitigation increase the range of situations in which X-band radars can provide observations.

1.3 Objectives

The CASA IP1 polarimetric radar network provides exciting opportunities for the possibility of studying kinematics and microphysics at short range with relatively high temporal resolution (3 minutes). However, the experimental design of the IP1 network means that new technologies, strategies and algorithms are being implemented, which need to be assessed for application to studies of overall storm interactions. The objectives for this dissertation are three-fold: first, to identify the advantages and limitations of an adaptive, polarimetric network of radars such as IP1 for the scientific study of storm kinematics and microphysics; second, to understand the applicability and shortcomings of using X-band for scientific study of storm interactions; and third, to utilize data from the IP1 network to characterize kinematic and microphysical interactions and their relation to storm electrification for an ordinary storm. These broad goals will be addressed through answering the more specific questions below.

What are the strengths and weaknesses of using adaptive scanning for retrieving the three-dimensional wind field and diagnosing bulk hydrometeor regions? The adaptive scanning (DCAS) proposed by CASA is crucial to meeting the overall CASA objective of having user-driven data sampling. This technique can result in rapid update times because areas of interest can be targeted, and specific dual-Doppler scanning techniques can be implemented. However, it can also result in lack of coverage needed for this application, and compromises between temporal resolution and coverage must be made. *How do these factors balance for dual-Doppler retrievals and understanding the overall storm evolution?*

What are the non-Rayleigh effects on X-band polarimetric observations of different hydrometeors? It is well understood that non-Rayleigh scattering applies to large rain drops and hail at X-band, but non-Rayleigh effects for other particle types such as snow, ice crystals, and graupel are less certain. *How do X-band measurements translate into a hydrometeor identification algorithm that can be applied to determine bulk storm microphysics?* One of the advantages of X-band over S-band is the increased differential phase shift that scales with frequency. This can translate into larger phase shifts in light rain situations, and could also improve differentiation of hydrometeor species such as vertical ice. Additionally, specific differential phase has been shown in modeling studies and observations to be even larger than what is predicted by simple wavelength scaling (Matrosov et al., 2006). *How much larger is K_{dp} at X-band than S-band, and how does this influence rainfall estimation and hydrometeor identification?*

How does the development of the updraft relate to graupel and lightning production? What influences development of the downdraft and precipitation processes? How is the kinematic intensity related to storm electrification and charge structure? What are the kinematic and microphysical relationships to lightning flash rates? Many studies have found correlations between lightning and updraft and downdraft dynamics, as well as the formation of graupel (e.g. Carey and Rutledge, 1998; Lang and Rutledge, 2002; Wiens et al., 2005). *Is IP1 able to see similar relationships despite the limitations from inconsistent coverage and X-band non-Rayleigh effects? Does IP1 provide additional insight into kinematic, microphysical and lightning relationships due to the increased (3 minute) temporal resolution? How do IP1 rainfall retrievals compare to S-band and ground-based sensor observations? Is IP1 data able to provide advantages in rainfall retrieval over longer-wavelength polarimetric retrievals?*

Some of these questions will be investigated through the use of scattering simulations to model different particle types to understand their scattering properties, while some will be answered through analysis of IP1 data collected on 10 June 2007. This case study was specifically chosen due to the availability of other observations for comparison (ie: S-band radar data, ground rainfall measurement stations, and lightning observations), as well as the lack of complete extinction of the signal due to significant attenuation, and minimal contamination from hail (to reduce complications from non-Rayleigh effects).

The dissertation is laid out as follows: Chapter 2 gives a detailed look at the data processing, algorithm development, model setup and simulation parameters, and quality control performed during this study. Chapter 3 investigates the theoretical scattering properties of different hydrometeor types that are then combined into a new X-band fuzzy logic hydrometeor identification algorithm (HID). Differences between X-band and S-band polarimetric observations are investigated, and the new HID algorithm is tested on 10 June 2007 data. Chapter 4 presents kinematic, microphysical and lightning observations from the 10 June 2007 case and makes inferences about relationships between the dynamics, microphysics and electrification as observed by both IP1 and KOUN. Chapter 5 examines retrieval of rainfall from IP1 in comparison with S-band. Chapter 6 will finalize conclusions found in this work, suggest modifications to IP1 that could improve future studies of storm interactions, and outline future work.

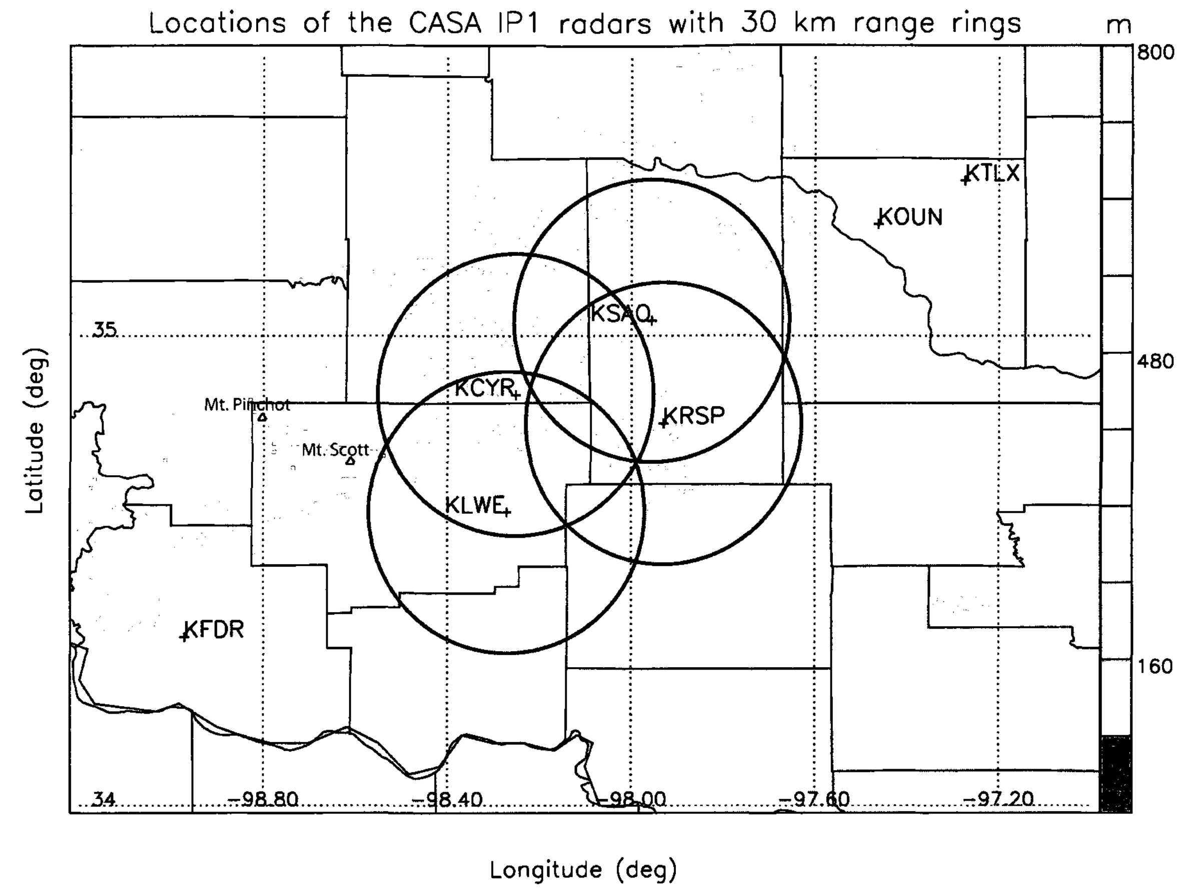

Fig. 1.1: The CASA IP1 X-band radar network in southwestern Oklahoma. The purple circles represent the 30 km range rings for each radar. The nearby S-band radars (KOUN, KTLX, KFDR) are also indicated. Color shading represents the terrain height in m.

Chapter 2

Data and Methods

2.1 IP1 Data

The CASA IP1 data used throughout these analyses were collected during the spring of 2007 in collaboration with the Department of Energy (DOE) Atmospheric Radiation Measurement (ARM) Cloud and Land Surface Integration Campaign (CLASIC; Miller et al., 2007). Participation in this campaign allowed for relaxation of the normal 3 km maximum height and 60 second volume scanning interval ("heartbeat") scanning strategy of the IP1 radars. The heartbeat was increased to three minutes in order to accommodate more elevation angles to reach the tops of storms, an important consideration for studies of storm microphysics and kinematics. This scanning strategy became known as the "CLASIC" scanning strategy. CLASIC was implemented nearly continuously between 10 June and 30 June 2007. This happened to be an active period for weather in the CASA IP1 testbed. Many different storms were captured during this period, including a low-pressure system, an MCS, multi-cellular storms and widespread convection.

The case chosen for analysis occurred on the very first day of CLASIC operations, 10 June 2007. This case was selected for numerous reasons, including the storm lifetime in the network, placement within the multi-Doppler coverage area, lack of severe weather (i.e. tornados or hail), lightning activity, and availability of supplemental data (such as the polarimetric NEXRAD prototype radar, KOUN, the National Lightning

Detection Network (NLDN), Oklahoma Lightning Mapping Array (OK-LMA), and the National Severe Storms Laboratory 2-dimensional video disdrometer, etc). The type of storm (multi-cellular) did not specifically factor into the case selection.

The IP1 radars transmit at a frequency of 9.41 GHz (wavelength of 3.2 cm). Alternating pulse repetition frequencies of 2.1 kHz and 1.6 kHz are used to increase the effective Nyquist velocity to 38 m s^{-1}, as well as help with second trip identification. During this project, the maximum range of the IP1 radars was 30 km due to range gate recording, although later during the CLASIC experiment the maximum range was increased to 40 km to improve coverage. The radars have a 3 dB beam width of 1.8°, and scan at 20° s^{-1}, resulting in oversampling in azimuth. Forty-seven sample pairs are generally used for each integration cycle, the peak power is 25 kW, and the radars sit on towers with average heights of 10 m. The radars have the ability to scan up to 32° in elevation; higher angles are not possible due to a hardware limitation. The average separation of the radars is on the order of 25 km. The sensitivity of the IP1 radars is 8.5 dBZ at a range of 30 km. A summary of IP1 characteristics can be found in Table 2.1, and the locations of the radars are listed in Table 2.2.

The most unique feature of the CASA IP1 radars is the Distributed Collaborative Adaptive Sensing (DCAS), which means that a Meteorological Command and Control (MC&C) steers the radars rather than a radar scientist (Zink et al., 2008). The MC&C makes real-time decisions based on a set of rules about how to scan echoes in the network and how to allocate radar resources. This means that the sector size, direction, number of elevation angles and radar used for scanning particular echoes may change during each heartbeat. In order to get a 'big picture' of what is in the network, a 360° sweep at 2° in elevation is performed during each volume scan cycle. Anywhere from 4 to 13 elevation sweeps can be included during each heartbeat (scanning decision interval). Although the original scanning strategy was developed for detection of tornados and estimation of surface rain rates, accommodations were made to collect volume data for kinematic and microphysical studies such as this one. This included extending the heartbeat from 60 to 180 seconds, and increasing the height and number of elevation angles in each volume scan. After 15 June 2007, the maximum range was also extended to 40 km for more coverage and larger dual-Doppler regions. And finally, during the spring of 2008, a new dual-Doppler scanning strategy was implemented in the MC&C to determine which radars to scan echoes based on the most useful dual-Doppler configuration (best viewing angle, closest, ability to top the echo; Wang et al., 2008). This new scanning strategy also includes the possibility for more elevation angles during a 60 second heartbeat.

Due to the experimental nature of the IP1 radars, the data went through extensive quality control and processing, and new algorithms had to be developed to specifically accommodate the IP1 network setup. Fig. 2.1 shows the processing methodology applied to the IP1 data. Each step will be discussed in detail below or in the following chapters.

2.1.1 Attenuation Correction

With the relatively short wavelength of the CASA IP1 radars, one of the main concerns is attenuation of the power-based variables. The polarimetric capabilities and network configuration of the IP1 radars afford the unique opportunity to correct for attenuation using two different methodologies. The first is to use specific differential phase shift, which is directly proportional to the specific attenuation (α_h) at a given range gate.

$$\alpha_h = aK_{dp}^{\ b} \tag{2.1}$$

For the IP1 data, the coefficients are computed by minimizing a self-consistent cost function using least squares (Park et al., 2005; Liu et al., 2006). This correction method is applied on a ray-by-ray basis, and can be applied to both reflectivity and differential reflectivity. However, the polarimetric-based method is unable to recover attenuation due to rain on the radome, it can be sensitive to the coefficients chosen for a and b, and performance can be poor in areas of wet ice, where the phase shift is small but significant attenuation still occurs. During the CLASIC experiment, this method was applied to the IP1 data in real-time to both Z_h and Z_{dr}. Z_{dr} values were corrected by applying the self-consistent method to Z_v and Z_h separately, then taking the ratio to get the differential reflectivity.

The second method of attenuation correction takes advantage of the different viewing angle of radars in a network configuration. This method is referred to as the network-based retrieval system (NRS; Chandrasekar and Lim, 2008). The principle behind the NRS method is that the path attenuation to a volume within the network is different for each radar, so by using the differential attenuation from each radar at a single point, the actual reflectivity of the volume can be reconstructed (Chandrasekar and Lim, 2008). Unlike the polarimetric method, this methodology is not sensitive to wet ice, but the limitation is that reflectivity can only be recovered where at least two radars are viewing the same volume.

The first course of action was to determine which method of attenuation correction was better for this particular case. Data from KOUN, as well as the two nearby WSR-88D radars KTLX and KFDR, were obtained for comparison. S-band data were gridded to 1 km in x, y and z, and IP1 data were gridded to 0.5 km in x, y, and z using the Cressman weighting scheme (Cressman, 1959). IP1 data were then merged using the greatest value from each radar at each grid point to form a single reflectivity field. Fig. 2.2 shows an example comparison of reflectivity at approximately 2341 UTC on 10 June 2007 for KTLX, KFDR, KOUN and IP1 at 2.5 km MSL. The decreased sensitivity of the IP1 radars is immediately noticeable around the edges when compared to the higher power, S-band radars. The small differences between the S-band radars can be attributed to storm evolution between sampling times (KTLX volume starting before KOUN and IP1, KFDR starting after), as well as lack of inter-radar calibration between the WSR-88D radars and KOUN. Differences between wavelengths are not significant at this low level, but noticeable differences between the polarimetric attenuation correction method and NRS do exist. At this level, KOUN hydrometeor identification using the CSU fuzzy logic HID described in Tessendorf et al. (2005) identifies only rain and drizzle (Fig. 2.2d).

Significant differences are obvious in the reflectivity comparison at 6.5 km MSL (Fig. 2.3). Although the generally smaller area of the IP1 echo is due to scanning strategy and radar sensitivity, the region of high reflectivities (40+ dBZ) are diminished compared to the other radars when the polarimetric-based attenuation correction is applied. Although some of the differences are due to the coverage by the IP1 radars, the diminished reflectivity in the main cores, particularly to the southwest, is likely due to attenuation. To ensure this was not an artifact of the gridding and/or merging process, several sensitivity studies (not shown) were conducted by changing the radius of influence (size and type—x, y, z or azimuth and elevation), type of weighting (Cressman, closest point), and grid spacing. The results showed that the IP1 reflectivity anomaly was not due to the gridding scheme. The NRS method increases the agreement between radars at this level and the echo area of >45 dBZ is enlarged (Fig. 2.3f). Scatter plots of IP1 reflectivity and the S-band radars at this same time illustrate the under-representation of higher reflectivities by the IP1 polarimetric attenuation corrected reflectivity (Fig. 2.4). This is particularly noticeable in the comparison with KTLX (Fig. 2.4c). Although some differences between the wavelengths is expected, non-Rayleigh effects usually result in larger reflectivities at X-band for > 35 dBZ. Differences could be attributed to calibration differences, but scatter between the S-band radars does not exhibit the same trend (not shown); above about 15 dBZ, the S-band radars have generally much higher reflectivity by up to 15 dBZ compared to IP1 (Fig. 2.4). The IP1 NRS reflectivity shows this bias to be smaller, and more points above 35 dBZ show greater IP1 reflectivites than S-band, which is more consistent with Mie theory.

The KOUN hydrometeor identification provides insight into why the polarimetric attenuation correction may not be reproducing the reflectivities in this instance. KOUN classifies a large area in the main reflectivity core as high-density graupel (HDG; Fig. 2.3d). As small, nearly spherical, ice particles fall though the melting layer, they develop a coating of water leading to high reflectivity but low K_{dp} values. KOUN HID also classifies a small amount of hail, both large and small, in the southwestern core. IP1 K_{dp} values at 2.5 and 6.5 km are shown in Fig. 2.5. In the high reflectivity cores at 6.5 km,

K_{dp} is relatively small (< 1 ° km^{-1}), while large K_{dp} values (> 4.5 ° km^{-1}) are observed in the reflectivity cores associated with rain in the lower levels (Fig. 2.5a).

The NRS correction improves the qualitative comparison of IP1 reflectivity with local S-band reflectivities (Figs. 2.2 and 2.3). Additionally, the scatter plots of NRS reflectivity show a bias towards X-band in the higher reflectivities, more in line with what is expected from Mie theory. This example is an illustration of why the NB method was chosen to correct the IP1 reflectivity data for this case, although the overall area of the echo is decreased, as can be seen in Figs. 2.2 and 2.3.

2.1.2 Quality Control

Unfortunately, differential reflectivity (Z_{dr}) were uncalibrated for CLASIC operations. Inter-radar biases were noted, particularly with high KRSP values and low KLWE values. Additionally, the NRS correction was not readily available for differential reflectivity, so the polarimetric correction was necessitated. Since Z_{dr} provides important information about the shape of particles within a volume for hydrometeor identification (HID), we wanted to preserve Z_{dr} if possible. Therefore, a method for estimating Z_{dr} bias was developed using data from the trailing stratiform region of an MCS that passed through the IP1 network on 20 June 2007 (Fig. 2.6). Uniform, low reflectivity (<25 dBZ) areas of trailing stratiform regions of MCSs are often associated with nearly spherical raindrops, resulting in very little differential power return. In addition, attenuation is small in such regions of light reflectivity. Thus, by comparing the Z_{dr} values from each radar under these circumstances and evaluating the departure from Z_{dr}=0, an estimate of the bias was possible.

Reflectivities remained below 40 dBZ from 1000-1100 UTC on 20 June 2007. Z_{dr} data between 1021 and 1059 UTC were thresholded on reflectivity less than 30 dBZ. The mean Z_{dr} for each radar was estimated at each time at points that were common among all four radars. Z_{dr} means were used to estimate the difference between each radar and zero. Table 2.3 shows the estimated Z_{dr} biases for each radar based on using this methodology. The corrections were small (< 1.0 dB), with KLWE having the largest correction factor.

The bias was assumed to be approximately the same over the 10-day period between 10 June 2007 and 20 June 2007, although the KRSP magnetron was replaced during this period. However, this was the best case for examining relatively small, uniform particles to estimate the Z_{dr} bias. Thus, the values in Table 2.3 were applied to Z_{dr} values during the 10 June case. A comparison of the polarimetric corrected Z_{dr} (not corrected for the bias) and polarimetric corrected, bias corrected Z_{dr} histograms at 2321 UTC 10 June 2007 is shown in Fig. 2.7. It is clear that this application of the estimated bias brought Z_{dr} values into better agreement. The mosaic of Z_{dr} is greatly improved (Fig. 2.8) with a much smoother overall field and fewer extreme (>4.5 dB) areas. Clearly this methodology improved the bias among radars, although the absolute calibration is not known, and this methodology relies on several assumptions (stable bias over 10 days, spherical particles, etc). As such, it was decided that Z_{dr} would be included in the HID, but the weighting in the fuzzy logic scoring process would be set low due to these uncertainties.

The specific differential phase was calculated in real-time using a finite impulse response filter and a least squares estimation fitting. This method produced a relatively smooth specific differential phase (K_{dp}) field (Fig. 2.5). The radial velocity (VE) was "unfolded" in real-time up to the effective Nyquist interval of 38 ms^{-1}. The radial velocities during this case rarely exceeded this threshold.

The correlation coefficient at zero lag (ρ_{hv}) was also noted to be uncharacteristically low. Fig. 2.9 shows a histogram of ρ_{hv} at 2321 UTC on 10 June 2007. There are very few points greater than 0.98, and an unusual number of points below 0.8 that were associated with meteorological echoes. This is particularly true of KCYR and KLWE, although KRSP and KSAO have a significant number of points below 0.9, which is generally the type of values that would be associated with hail, or a tornado debris cloud. In this case, mosaicing data from all 4 radars using the highest value improves the overall ρ_{hv}, with most values occurring over 0.9 and only a small number less between 0.8 and 0.9 (Fig. 2.9). ρ_{hv} provides information about mixtures and orientation of particles within a volume, and like Z_{dr}, it was determined that ρ_{hv} would be included in HID but with relatively low weight in the fuzzy logic. Low ρ_{hv} values will have the most impact on the quality control methodology used for this study. The relatively inexpensive magnetrons used for the CASA IP1 radars were determined to be partially responsible for the low values.

Data were also corrected for an angle reporting issue where the angle was reported at the end of each integration cycle instead of in the middle of the integration cycle. This resulted in a difference in echo location between counterclockwise and clockwise sweeps. Additionally, the angle reported was offset by one beamwidth. Thus it was necessary to increase the angle of each ray reported by 2.3° for CCW sweeps and decrease the angle for CW sweeps by the same amount.

As described by Ryzhkov and Zrnic (1998) the polarimetric variables can be used to discriminate meteorological echoes from non-meteorological echoes. Generally this is done using thresholds on the correlation coefficient, ρ_{hv}, and standard deviation of differential phase, sdev(ϕ_{dp}). This methodology works best when the thresholds are determined specifically for the radars being used, as well as for the particular case, since anomalously high sdev(ϕ_{dp}) can be associated with backscatter from hail, and low ρ_{hv} values can be found in meteorological echoes associated with tornado dust clouds and fine lines. Thus, setting the thresholds too strict may delete some data of interest, while too loose of a threshold will result in extraneous echoes. Another variable that can be used to remove non-meteorological echo is the normalized coherent power (NCP). NCP is the ratio of the magnitude of the first lag autocorrelation divided by the zero lag correlation (Keeler and Passarelli, 1990).

To determine the appropriate variables and thresholds for the IP1 radars, a sensitivity study was performed. The "raw" reflectivity data are shown in Fig. 2.10a. Thresholds ranging from 0.5 to 0.8 for ρ_{hv} were applied, as were sdev(ϕ_{dp}) from 15 to 30°. These values were chosen based on the values used for CHILL, which are sdev(ϕ_{dp}) of 18° and ρ_{hv} of 0.7. However, since the ρ_{hv} values were low in this case, lower values were selected. Additionally, the backscattering component of differential phase is increased at X-band compared to S-band, so higher deviations were allowed. Clearly, the most liberal threshold of $\rho_{hv} < 0.4$ and sdev(ϕ_{dp})> 30° was not enough to clear out some of the non-meteorological echo to the northwest of KCYR (Fig. 2.10b). However, the most stringent threshold of ρ_{hv} <0.8 and sdev(ϕ_{dp})> 15° clearly removed a significant portion of real echo (Fig. 2.10c). NCP thresholds between 0.5 and 0.9 were also applied to the data to determine if it was a better variable for cleaning up the data. However, a high threshold such as 0.7 removed some of the echoes of interest (Fig. 2.10d), but a low threshold of 0.5 was not enough to eliminate speckles (Fig. 2.10e). A low ρ_{hv} threshold of 0.5 and moderate sdev(ϕ_{dp}) of 25° was determined to be a good compromise between eliminating echo within the storm of interest but minimizing extraneous non-meteorological echo (Fig. 2.10f).

2.1.3 Data Processing

The IP1 data were gridded using the REORDER software package from the National Center for Atmospheric Research (NCAR) to a grid of 0.5 km in x, y and z dimensions using a Cressman weighting scheme (Cressman, 1959) with a radius of influence of 1°. Again a sensitivity study was performed to determine the best parameters for the gridding to find a balance between creating artificial data and smoothing the data too much (not shown). Several radii of influence were tested, as well as different interpolation schemes, such as closest point. All of the radars were gridded to a common point centered in the network (Table 2.2).

The question of how to best analyze four independent but networked radars is an important consideration, and has implications for application of the algorithms described herein. To preserve detail captured by each radar but yet avoid unnecessary processing of the data, one might be tempted to consider each radar individually, and average the final field of interest (such as rain rate or hydrometeor identification). However, this presents a problem in the case of hydrometeor identification which uses discrete numbers for each category, and as such cannot be easily averaged. Thus, we chose to mosaic the individual radar observations by taking the greatest value at each grid point. The greatest value mosaic was applied to Z_h, Z_{dr}, K_{dp} and ρ_{hv} before applying the HID and rain rate algorithms. One might ask if all of the variables can necessarily be mosaicked by taking the highest value, especially those that depend on radar viewing angle and provide information about orientation. First of all, the data have already been averaged through the gridding process, and data have been interpolated from the radar reference frame to the gridded reference frame. Secondly, since higher Z_{dr} and K_{dp} values are indicative of oblateness and water content respectively, one could argue that the highest value would come from the radar with the "best" viewing angle, i.e. the lowest elevation angle providing the greatest difference between the vertical and horizontal polarizations. The exception would be for vertical ice (VI), where negative values of K_{dp} become important. However, if vertically aligned ice crystals are present, all radars should observe a negative K_{dp} unless they are looking directly under the volume in which case K_{dp} would be near zero. The case for mosaicing ρ_{hv} is more difficult to argue. One could argue that the lowest values of ρ_{hv} are the most useful for indicating mixtures of particles or ice particles, but low values of ρ_{hv} are also associated with noise. Much as the case with VI, two radars looking at a volume of the same particles should return the same ρ_{hv} notwithstanding any differences in radar hardware. Finally, taking the highest value of any radar observation could lead to anomalies and discontinuities in the merged product. To minimize these occurrences, data were first quality controlled on an individual radar basis, and the Z_{dr} biases were applied. Perhaps future studies could look into taking a weighted average of all available radars based on the distance to the grid point to alleviate some of these discontinuities.

Fig. 2.11 shows an example CAPPI of the merged IP1 radar product for reflectivity, Z_{dr}, K_{dp} and ρ_{hv}. No obvious discontinuous boundaries are evident in the mosaic at this time. Vertical cross-sections are a bit more enlightening in terms of the contribution to each mosaicked variable from individual radars (Figs. 2.12-2.15). The difference in coverage area is immediately noticeable. In this particular cross-section, only three of the radars are covering the area of interest (KCYR, KRSP, and KSAO), and only two of the radars cover the same area above 3 km (KCYR and KRSP). Although some of the same features show up in the KCYR data, the reflectivity mosaic is dominated by the KRSP observations, and KLWE adds observations not seen by any other radar (Fig. 2.12). KCYR Z_{dr} values are <0 dB near the reflectivity core, while KRSP shows Z_{dr} values greater than 3.5 in the same region (Fig. 2.13). Again, the Z_{dr} mosaic is dominated by the KRSP data. In the case of K_{dp}, KRSP shows a tilted column of large K_{dp} values, with a smaller area south of the main core between 4-5 km (Fig. 2.14). This same enhanced region is the main K_{dp} feature in the KCYR data, but values are much larger than the KRSP values. The main K_{dp} core observed by KRSP is located at the surface at about 7 km north of the center of the network. KSAO, which only sees low-level K_{dp} values, shows a core at 10 km. In the mosaic, these features get blended together to make a wider column of high near-surface K_{dp}, which would impact surface rain rate calculations. Individual radar ρ_{hv} fields are significantly different, with KCYR and KLWE values remaining below 0.97 and KRSP and KSAO values much higher (Fig. 2.15). The mosaicked ρ_{hv} results in the most disjoint field. The same KOUN fields are provided for references in Fig. 2.16. It is clear that despite some assumptions and unrealistic boundaries, considering the combined information from all four radars provides a much more complete picture than any individual radar and makes the analysis much less complicated.

2.1.4 Algorithms

2.1.4.1 Dual-Doppler Analysis

Although the IP1 network seems well suited for dual-Doppler analysis, deriving the 3-D wind field from this dataset requires special consideration due to the adaptive scanning strategy and incomplete coverage. Most of the dual-Doppler area is covered by only two radars, although in some areas three radars are available, and in the center of the network, all four radars can be used for determination of the wind field. Coverage by three or more radars improves wind retrieval by reducing error variances (Ray et al., 1978).

Neglecting the Earth's curvature and beam refraction, the relationship between radial velocity (v_r) and the 3-D wind field is given by the following equation:

$$\hat{v}_r = \hat{u}\sin a\cos e + \hat{v}\cos a\cos e + (w \hat{+} v_t)\sin\alpha \tag{2.2}$$

where u, v and w are the east-west, north-south, and vertical components of the 3-D wind, the particle fallspeed is represented by v_t, a is the azimuth angle, and α is the elevation angle (Mohr and Miller, 1983; appendix F). There are four unknowns in Eqn. 2.2: u, v, w, and v_t. In the case of only two radars, assumptions about the particle fallspeed (v_t) can be made to reduce the problem to three unknowns. By employing the mass-continuity equation, two radars can be used to diagnose the vertical component of the wind field (w) from measured horizontal divergence. If three or more radars are available, then the solution becomes over-determined and the third radar can be used as a constraint on the unknown quantity $w+v_t$. This type of analysis was applied to the IP1 data. At points with three or more radars, the over-determined solution was used to determine u and v, and for points where only two radars were available, the two-radar solution was used. A study was performed to determine the impact of using three or more radars to derive u and v compared to just using two radars. There was very little difference between the two (Fig. 2.17), so for this study as many radial wind fields as are available at each point are used to synthesize the u and v winds. Once the u and v winds were determined, the convergence was calculated and the anelastic form of the continuity equation (assuming density is only a function of height) was used to derive the vertical wind field.

$$\int_{z_1}^{z_2} \frac{\partial(\rho w)}{\partial z} dz = -\int_{z_1}^{z_2} \rho\left(\frac{\partial u}{\partial x} + \frac{\partial v}{\partial y}\right) dz \tag{2.3}$$

Density (ρ) was assumed to be an exponential function of height (z).

$$\rho = \exp^{(-z*0.1)} \tag{2.4}$$

The integration can either proceed from the surface to echo top (upward integration, W_{up}) or from echo top to the surface (downward integration). O'Brien (1970) proposed a third integration method whereby the downward integration was used, but since the vertical velocity at the surface is required to be zero, the residual vertical motion at the surface after the integration was redistributed throughout the column in order to satisfy both top and bottom conditions. This is called the variational method (W_{var}).

Sampling the storm top is particularly important for estimating vertical motions, because boundary conditions at the top and bottom of the storm are needed for integration of the continuity equation (O'Brien, 1970; Nelson and Brown, 1987). If the radar does not scan to the top of the storms, applying an inaccurate boundary condition produces erroneous vertical winds. Generally an upward integration method is used in those cases (W_{up}). However, due to density stratification in the atmosphere, large errors can result from this type of integration. The preferred method of integration if both top and bottom boundary conditions are known is W_{var}, which is the technique most often adopted for dual-Doppler retrievals.

In the case of IP1, not all echoes were topped during each heartbeat, requiring an upward integration method. However, where the upper boundary condition is known, it would be best to use W_{var}. A decision tree was implemented to determine if the storm was "topped" or not on a column-by-column basis (Fig. 2.1). Due to the sensitivity of the IP1 radars, echoes were considered to be "topped" if the reflectivity at the highest grid point was < 20 dBZ, and if two or more radars had observations from the highest good grid point. If the aforementioned criterion were met, W_{var} was used and if not, then W_{up}

was chosen. This combination method of determining w will be referred to as W_{com}. For W_{var}, the upper boundary condition was defined as w=0 at one-half a grid point above the highest measured level of divergence. This methodology will obviously lead to discontinuities at some points in the vertical wind field, but will reduce the necessity to use upward integration when the top boundary is known.

To estimate the uncertainties that might be associated with using W_{up}, the difference between the vertical wind (w) determined from W_{up} and W_{var} in each "topped" column was calculated. Differences between the two will provide an estimate of the errors that result from using W_{up} instead of W_{var}, which is generally accepted as being more accurate than W_{up}. The mean vertical winds using W_{up} and W_{var} at three different times are shown in Fig. 2.18. As expected, using the upward integration method results in large uncertainties compared to the W_{var} analysis, with mean differences ranging from 0.8 to 5 ms^{-1}. Clearly significant differences between W_{up} and W_{var} magnitudes exist. However, the general trends in vertical motion with height are persevered between the two integration methods.

The upward and downward motion was separated and averaged to determine an uncertainty associated with the up- and downdrafts (Fig. 2.19). The upward motion uncertainties range from 0.1-1.0 ms^{-1}, while much larger uncertainties are associated with the downdrafts, ranging from 1.2-6.4 ms^{-1}. This is due to the amplification of the accumulated divergence as the integration proceeds from the surface to the top of the storm. One point to note is that general trends in the up and downdrafts are captured by both integration methods, despite differences in the magnitudes of w. By restricting the analysis to less than 8 km, the uncertainty in the downward and upward motion decreases, indicating that the two methods deviate the most significantly in the upper levels of the storm (as expected). This provides some basis for using the W_{up} method despite rather large errors in the actual magnitudes.

Several studies were performed to understand the robustness of the trends found in the IP1 kinematic analysis (detailed kinematic analysis can be found in Chapt. 4). Time-height plots of up- and downward echo areas (number of points meeting up- and downward motion thresholds multiplied by the area of a grid point, 0.5 km x 0.5 km) were constructed using the W_{com} method, as well as by restricting the analysis to only "topped" columns where the more trustworthy W_{var} method could be applied (Fig. 2.20). Although many fewer columns are used when only "topped" columns are considered, the general trends in up- and downdraft area are similar using the W_{com} and W_{var} methods. To this extent, it was determined that trend analysis of the dual-Doppler derived kinematics is physically realistic, although large uncertainties exist in the magnitude and caution must be used when interpreting data above about 6-8 km. Additionally, thresholds on the downward motion were set relatively low to remove influences of the anomalously strong upper level downward motion resulting from the upward integration method. This restriction left mostly the low-level downdrafts for analysis. A sensitivity study was also performed to determine if changing the up and down magnitude thresholds resulted in different trends. Increasing the upward threshold to >10 ms^{-1} reduced the overall area of updraft (Fig. 2.20e), but the peak vertical velocity was at the same time as the peaks using W_{var} (topped) >5 ms^{-1} and the W_{com} > 5 ms^{-1} methodology. Increasing the downdraft threshold to <-5 ms^{-1} resulted in the same general trend of a descending downdraft, and maximums occurred at the same time (Fig. 2.20f).

These studies provide the justification for the thresholds and methodology used for the dual-Doppler analysis. Although the upward integration method results in significant errors, the imposed scanning strategy dictated the use of W_{up} in greater than 50% of columns during the 10 June 2007 storm lifetime. These uncertainties translate into large errors in the actual speeds of the vertical motion, but general trends are preserved compared with the W_{var} method in columns where the vertical analysis could be trusted. Uncertainties in downward motion magnitudes were especially large, although generally uncertainties were much larger above 6-8 km. Thus, some caution must be exercised when interpreting the dual-Doppler derived 3-D wind field.

An example cross-section of a projection of the vertical winds is shown in Fig. 2.21. The main differences between W_{var}, W_{up}, and W_{com} are noted above 8 km, as was found in the mean analysis. Generally, all three methods of retrieving the vertical wind result in the same flow patterns; an exception being at x=8 km along the cross section above 8 km. W_{up} shows strong downward motion (Fig. 2.21c), while W_{var} indicates upward motion of nearly the same magnitude (Fig. 2.21d). Fig. 2.21f illustrates that these columns did not meet the "topped" criterion, and thus W_{com} uses W_{up}. Less than a quarter of the columns in this case were "topped", so the upward integration method was most often used (Fig. 2.21f). It should be noted that discontinuities between the transitions from using W_{up} to W_{var} are generally minor.

2.1.4.2 Hydrometeor Identification

A new X-band specific fuzzy logic hydrometeor identification algorithm (HID) built on scattering simulations of hydrometeors at X-band was developed for use with the

IP1 radars. The scattering simulation methodology is detailed in Sec. 2.3. The HID algorithm was applied to gridded, mosaicked IP1 data.

2.1.4.3 Rain estimation

The information contained in the polarimetric variables can be exploited to improve rainfall estimates over simple Z-R relationships by utilizing different rain rate equations based on the specific radar volume (Chandrasekar et al., 1993). For example, the phase-based specific differential phase (K_{dp}) is immune to drop size distribution assumptions, as well as contamination by ice, but is still sensitive to drop-shape assumptions and can be rather noisy. The differential reflectivity, Z_{dr}, provides information about shape and size, but is a power-based variable that can be sensitive to calibration errors and drop size distribution assumptions. By making decisions about the quality of variables and types of particles within a radar volume, the best method for calculating rain rate can be chosen. For example, if a significant amount of ice is suspected in a volume, the algorithm seeks to use K_{dp}, which is directly proportional to the liquid water in a volume (and immune to hail). This type of rain rate algorithm has been coined a "blended algorithm" (Cifelli et al., 2002).

A blended algorithm for the IP1 data was adapted from that described in Cifelli et al. (2002). Since Z_{dr} for this case was uncalibrated as described previously, the ice fraction was not calculated, and rain rate relationships employing Z_{dr} were not included. This reduces the blended algorithm decision tree to a two-algorithm choice: R-Z or R-K_{dp}. In accordance with larger differential phase and thus more sensitive K_{dp} at X-band, the threshold for good K_{dp} was lowered to $>0.1\ ^{o}km^{-1}$. In the case that K_{dp} did not meet this threshold, the results from the HID were used to determine if Z_h was contaminated by ice, and if the volume was identified as a liquid particle type (DZ or RN), then the NEXRAD Z-R relationship was used (Fulton et al., 1998):

$$Z=300R^{1.4} \tag{2.5}$$

An additional constraint of $Z_h < 53$ dBZ was imposed on reflectivity to ensure no ice contamination. The blended algorithm decision tree is illustrated in Fig. 2.1.

According to Bringi and Chandrasekar (2001), R-K_{dp} relationships can be scaled with frequency. Thus, to take advantage of the Oklahoma tuned R-K_{dp} relationship determined for S-band during the Joint Polarization Experiment (JPOLE; Ryzhkov et al., 2005), the scaled X-band R-K_{dp} relationship is:

$$R=17.38K_{dp}^{0.79} \tag{2.6}$$

The rain algorithm and application will be discussed further in Chap. 5.

2.2 Other platforms

2.2.1 KOUN

Data from the NOAA/National Severe Storms Laboratory (NSSL) KOUN S-band (11 cm) polarimetric radar were obtained for comparison with IP1 data. KOUN is located in Norman, OK about 75 km from the center of the IP1 network (Fig. 1.1). KOUN is a prototype polarimetric NEXRAD radar (Ryzhkov et al., 2005), and as such scans 360° full volumes with 13 elevation angles up to 19.5° approximately every 5 minutes. The half power beamwidth of KOUN is 1° (Ryzhkov et al., 2005). A summary of KOUN attributes can be found in Table 2.4. Due to the polarimetric capabilities, KOUN data were quality-controlled using ρ_{hv} and sdev(ϕ_{dp}). A sensitivity study was also performed to establish appropriate thresholds, which were determined to be 0.6 for ρ_{hv} and 18° for sdev(ϕ_{dp}). KOUN data were gridded using REORDER using Cressman weighting, a 1° radius of influence, and a grid spacing of 1 km in x, y and z.

Several versions of fuzzy logic were applied to the KOUN data, as will be detailed in Chapter 3. The 9-category CSU HID described in Tessendorf et al. (2005) was applied to verify the presence (or absence) of hail, which were specifically left out of the HID developed for X-band due to complications from Mie effects.

A "blended rainfall algorithm" similar to that applied to the IP1 data was used with the KOUN data. The S-band "blended algorithm" uses Z_h, Z_{dr}, K_{dp} and Z_{dp} (difference reflectivity) to determine the best rain rate relationship based on the quality of each variable as well as the ice fraction in a volume. An outline of the S-band blended algorithm is illustrated in Fig. 2.22. The ice fraction is calculated from Z_{dp} (which is related linearly to the observed horizontal reflectivity in rain). This relationship is called the rain line (Golestani et al., 1989). A rain line was derived for this case and was found to be:

$$Z_{dp}=1.02499Z_h - 5.57062 \tag{2.7}$$

The rain rate equations used in the blended algorithm were taken from JPOLE conducted in Oklahoma from 2002-03 with the KOUN radar, which extensively tuned and tested the rain rate relationships specifically for the Oklahoma environment and KOUN radar using comparisons with ground-based sensors (Ryzhkov et al., 2003; Ryzhkov et al., 2005). The KOUN R-K_{dp} relationship found during JPOLE was

$$R=45.3K_{dp}^{0.786} \tag{2.8}$$

where R is in mm h^{-1} and K_{dp} is in ° km^{-1}. The R-Z_h-Z_{dr} relationship is:

$$R=1.42x10^{-2}Z_h^{0.770}Z_{dr}^{-1.67} \tag{2.9}$$

And finally, a R-K_{dp}-Z_{dr} relationship of:

$$R=136\ K_{dp}^{0.968}Z_{dr}^{-2.86} \tag{2.10}$$

was used. (Z_{dr} in Eqns. 2.9 and 2.10 is in linear units, as is Z_h in Eqn. 2.7). The NWS Z-R relationship for mid-latitudes (Eqn. 2.5) was used for the Z-R relationship. The proposed decision tree outlined in Ryzhkov et al. (2005, Appendix A) was also applied to the KOUN data, hereafter termed the "KOUN NSSL" algorithm.

2.2.2 Lightning

The Oklahoma Lightning Mapping array (OK-LMA) consists of 11 VHF receiving stations situated in west-central Oklahoma. The OK-LMA detects VHF RF-emissions emitted from lightning (Thomas et al., 2004). Using time-of-arrival techniques, the location of the sources can be inferred. A description of the LMA instrumentation and application can be found in Rison et al. (1999) and Thomas et al. (2004). To decrease the number of erroneous sources, a threshold on χ^2 was set to 1 and the number of stations required for detecting a source was set at 7.

The charge structure of a storm can be inferred from LMA data if assumptions are made about the nature of breakdown in lightning strikes (Rust et al., 2005; Wiens et al., 2005). Models and observations of lightning discharge have shown it is a bidirectional process in which breakdown begins between two regions of opposite charge (Kasemir, 1960; Williams et al., 1985; Rison et al., 1999; Mansell et al., 2002). The discharge then propagates away from the initial origin with two leaders in opposite directions, one with negative charge (negative breakdown) and one with positive charge (positive breakdown). It is generally assumed that the negative breakdown advances through positive charge, and positive breakdown through negative charge. Rison et al. (1999) showed that in the VHF, negative breakdown is inherently noisier than positive breakdown, and as such, regions of positive charge have more VHF sources compared to regions of negative charge. Therefore by looking at individual lightning flashes captured by the LMA, the general nature of charge regions can be inferred by looking at the initial discharge height and subsequent breakdown profile.

Using these assumptions, analysis of three-dimensional LMA data can be used to determine bulk charge structure. An example of LMA data from a single intra-cloud (IC) lightning flash are shown in Fig. 2.23. As can be seen by the altitude histogram of sources, the largest number of sources were located around 13 km, likely associated with positive charge. The somewhat smaller peaks below 10 km are likely regions of negative charge, suggesting the presence of a normal polarity charge dipole (Williams, 1989; Williams, 2001; Wiens et al., 2005).

LMA sources can be grouped temporally and spatially into lightning flashes thereby providing an estimation of flash rate (Thomas et al., 2003), as well as 3-D reconstruction of the lightning channel. At least 10 VHF sources were required to be considered a flash, and flash rates were calculated for one, three and five minute time periods to correspond to NLDN flash rates, IP1 scan interval, and KOUN scan interval, respectively.

The National Lightning Detection Network (NLDN) is able to detect cloud-to-ground lightning flashes (Cummins et al., 1998), as well as the polarity of each stroke. Due to anomalous classification of some positive lightning, a threshold of 10 kA on the peak power was used to limit the NLDN positive flashes. Cummins et al. (1998) estimates the detection efficiency of the NLDN over southwestern Oklahoma at 80%. Location errors are on the order of 1-2 km. Cloud-to-ground flash rates were also calculated on one, three and five minute intervals to correspond to the LMA, IP1 and KOUN data.

2.2.3 Surface rainfall observations

Two surface-based rainfall observations were available for the storm studied. The NSSL 2-D video disdrometer (2D-VD) was deployed in Cement, OK for the duration of the CASA IP1 2007 spring experiment and CLASIC operations (Zhang et al., 2007). The reader is referred to Kruger and Krajewski (2002) for details of the 2D-VD measurement platform. Rain rates were calculated from the DSD data using the following relationship:

$$R = 3.6x10^{6} a N_0 \frac{\pi}{6} \frac{\Gamma(\mu + 4 + b)}{\Lambda^{(\mu+4+b)}} \tag{2.11}$$

where $3.6*10^6$ is a conversion factor, a and b come from a fallspeed relationship (here assumed to be 386.6 $m^{1/3}$ s^{-1} and 0.67, respectively), μ and N_0 come from the DSD, and Λ is related to D_0 through

$$D_0 = \frac{3.67}{\Lambda} \tag{2.12}$$

(Doviak and Zrnic, 1993), assuming the Beard and Chuang (1987) drop shape model. Here D_0 is in m, N_0 is m^{-4}, R is in mm h^{-1}.

Tipping buckets located at Chickasha (CHIC), Ninnekah (NINN), Apache (APAC) and Acme (ACME) as part of the Oklahoma Mesonet (McPherson et al., 2007) also provided surface-based rainfall estimates. The tipping bucket records five minute rainfall accumulations between 0 and 24 UTC, and has a resolution of 0.254 mm. The OK Mesonet tipping buckets have an accuracy of +/-5% between 0 and 50 mm h^{-1} (McPherson et al., 2007).

2.3 Scattering Simulations

In order to characterize the behavior of Mie scatterers at X-band (3.2 cm), the T-matrix scattering matrix model was used (Barber and Yeh, 1975; Vivekanandan et al., 1991). The T-matrix model takes microphysical inputs of specific particles and computes the backscattering cross-section at a particular incident wavelength. The T-matrix model inputs are particle axis ratio (a/b, where a is the minor axis and b the major axis), temperature (T), radar wavelength (λ), and particle bulk density (ρ). The backscattering cross-section is calculated for a variety of input diameters. Details of the T-matrix scattering model are described in Barber and Yeh (1975) and Vivekanandan et al. (1991). Once the scattering properties of a single particle are determined, the Mueller matrix model is used to calculate the radar moments for a distribution of particles in a specified volume. Details of the Mueller matrix can also be found in Vivekanandan et al. (1991). The inputs necessary for the Mueller matrix are canting angle distribution properties (assumed distribution type, mean angle, θ_m, and standard deviation, σ), particle size distribution properties (distribution type, slope, intercept), and radar elevation angle and volume. Mueller matrix calculates a variety of radar observables but this study focuses on the resulting reflectivity (Z_h), differential reflectivity (Z_{dr}), specific differential phase (K_{dp}), and correlation coefficient (ρ_{hv}).

Scattering simulations were run for seven different hydrometeor types: Drizzle/light rain (DZ), Rain (RN), Aggregates (AG), Ice Crystals (CR), Low-density graupel (LDG), High density graupel/precipitation ice (HDG), which includes both melting graupel and wet-growth small hail, and vertically aligned ice (VI). Due to the significant Mie effects and attenuation associated with large hail at X-band, we chose to focus on the aforementioned seven hydrometeor types. An "unclassified" (UC) category was included for the case in which the HID score for all types was zero. Simulations were also run at 11 cm for comparison and to maintain a reference point against expected ranges of variable values, such as those given for S-band in Straka et al. (2000; henceforth S00). Additionally, the Colorado State University Radar Meteorology Group hydrometeor identification algorithm, CSUHID (discussed in Tessendorf et al. 2005), was used as a baseline for comparison with the S-band scattering simulations. S00 and

CSUHID variable ranges are determined based on previous modeling studies, *in situ* observations, and personal experience with S-band polarimetric radar observations.

Numerous scattering simulations (over 19,000), intended to span possible physical conditions associated with each hydrometeor type, were carried out at S- and X-band (11 cm and 3.2 cm, respectively) by simulating a wide variety of microphysical conditions (including different temperatures, axis ratios, particle size distributions, and canting angle distributions). The resulting model output for S-band were compared with S00 and CSUHID to ensure the physical representativeness of the simulated conditions. The parameters used for each of the seven hydrometeor types are described below. Since differential measurements, such as Z_{dr} and K_{dp}, can depend on viewing angle, two different radar elevation angles were used; one at low elevation (1°) and one at high elevation (30°, corresponding to the approximate highest elevation angle scanned by the CASA IP1 radars). A Gaussian canting angle distribution was assumed, with a varying standard deviation, σ. Simulations were comprised of single hydrometeor types only; no mixtures of particle types were simulated. The maximum and minimum values resulting from the set of simulations for each hydrometeor type were then used as a basis for developing the membership beta functions for the X-band fuzzy logic identification scheme (detailed in Sec. 3.3). The specific hydrometeor input parameters outlined below for the T-matrix model are listed in Table 2.5, and the input parameters for the Mueller model are described in Table 2.6.

2.3.1 Rain (RN)

Although the microphysical characteristics of rain are probably the best understood of all hydrometeor types, questions still remain about drop-axis ratio relationships and size-distributions. A wide variety of drop shape models have been suggested to describe the shape of falling large raindrops (Pruppacher and Beard, 1970; Pruppacher and Pitter, 1971; Jameson, 1983, Goddard and Cherry, 1984; Beard and Chuang, 1987; Chuang and Beard, 1990; Brandes et al., 2002; and others). Six different axis ratio relationships were chosen for use in this study: Pruppacher and Pitter (1971; henceforth PP71), Goddard and Cherry (1984; henceforth GC84), Jameson (1983; henceforth J83), Beard and Chuang (1987; henceforth BC87), Chuang and Beard (1990; henceforth CB90) and Brandes et al. (2002; henceforth B02). Beard and Jameson (1983) and Hendry et al. (1976) described canting angle distributions of raindrops. Based on those findings, a truncated Gaussian distribution with a mean of 0° and σ of 1°, 4° and 10° were used. A normalized gamma distribution (henceforth NGAMMA; Ulbrich, 1983; Willis, 1984; Bringi and Chandrasekar, 2001) was used for the drop size-distribution,

$$N(D) = N_w f(\mu) \left(\frac{D}{D_0}\right) \exp\left[-(3.67+\mu)\frac{D}{D_0}\right] \tag{2.13}$$

where both N(D) and N_w have units of mm^{-1} mm^{-3} and

$$f(\mu) = \frac{6}{(3.67)^4}\frac{(3.67+\mu)^{\mu+4}}{\Gamma(\mu+4)} \tag{2.14}$$

Rain rates (R) calculated from the gamma distribution were used to limit the retrieval to $2.5<R<300$ mm h^{-1} (Chandrasekar et al., 2006).

2.3.2 *Drizzle/ Light Rain (DZ)*

Drizzle was modeled using a monodisperse population of droplets (MONO). Diameters between 0.3 mm and 0.55 mm were simulated at temperatures ranging from 0 °C to 20 °C. The very small size of the drops results in little deformation due to drag forces, so spherical axis ratios were used. The drizzle category is also intended to capture light rain, below the 2.5 mm h^{-1} rain rate threshold used in the rain simulations. For simulations of light rain, the Goddard and Cherry (1984) drop-axis ratio was assumed, and a simple Marshall-Palmer exponential particle-size distribution (EXPON) was used (MP; Marshall and Palmer, 1948):

$$N(D) = N_0 \exp(-\Lambda D) \tag{2.15}$$

where N_0 was assumed to be 80,000 m^{-3} cm^{-1} and Λ is related to the rain rate by

$$\Lambda = 4.1 R^{-0.21} \tag{2.16}$$

where Λ has units of mm^{-1}. Rain rates from 0.1 - 2.5 mm h^{-1} were simulated for light rain.

2.3.3 *Low Density Graupel (LDG)*

The bulk microphysical characteristics of graupel are less certain. For example, the bulk density of graupel reported in the literature ranges from 0.05 g cm^{-3} (Locatelli and Hobbs, 1974) up to $>$ 0.7 g cm^{-3} (List, 1958; Braham, 1963; Zikmunda and Vali, 1972; Heymsfield, 1978). For the low bulk density category, densities >0.25 g cm^{-3} and

≤ 0.55 g cm^{-3} were considered, which is consistent with the findings of a number of studies (Fletcher, 1962; Zikmunda and Vali, 1972; Locatelli and Hobbs, 1974; Pruppacher and Klett, 1997; Heymsfield et al., 2004). Additionally, there are a variety of shapes for graupel (conical, lump, hexagonal; Locatelli and Hobbs, 1974; Heymsfield, 1978). As noted by Aydin and Seliga (1984), axis ratios of graupel can be larger than unity. Axis ratios between 0.65 and 1.25 were used (Heymsfield, 1978; Pruppacher and Klett, 1997). Observations by Zikmunda and Vali (1972) showed that conical graupel particles could oscillate around the vertical with amplitudes up to 20°, though studies by List and Schemenauer (1971) showed that higher amplitude oscillations could occur with larger graupel sizes. A Gaussian canting angle distribution of graupel with a standard deviation of 10° and 20° was used in this study.

The size distribution of graupel particles is also difficult to characterize. Many studies have found graupel distributions can be modeled with exponential distributions (Eqn. 2.15; Pruppacher and Klett, 1997). Cheng and English (1983) derived an exponential relationship between the shape parameter and the slope intercept:

$$N_0 = A\Lambda^B \tag{2.17}$$

where A=115, B=3.63, N_0 (m^{-3} mm^{-1}) and Λ (mm^{-1}). This type of distribution will be called "GRAUP". D_0 was varied between 2 mm and 5 mm (Cheng and English, 1983; Xu, 1983), and the respective N_0 and Λ values were calculated. For smaller mean diameters of 1.5 mm to 2.5 mm, the exponential distribution was used with N_0 set to a constant 80,000 m^{-3} cm^{-1} (Xu, 1983). Eqn. 2.12 was assumed to describe the relationship between D_0 and Λ.

Low-density graupel is expected in relatively cold regions of storms, and thus the temperatures were set to -10 °C and -20 °C.

2.3.4 High Density Graupel/Precipitation Ice (HDG)

Graupel growing in regions of large supercooled water contents, melting graupel, and freezing of supercooled rain are all processes that promote graupel of greater bulk density compared to LDG; thus a high-density graupel/precipitation ice category was also included. As S00 note, graupel and small hail have similar characteristics, and as such it may be unrealistic to distinguish between them using radar observations. Thus, we have chosen to group these two hydrometeor types into one category. Many of the low-density graupel microphysical inputs were also used for HDG. However, HDG particles have higher densities by definition, ranging from 0.55 to 0.9 g cm^{-3} (including the effects of melting; Auer, 1971; Locatelli and Hobbs, 1974; Heymsfield, 1978). Since high density graupel could be associated with particles as they fall through the melting layer, temperatures were allowed to extend above freezing, up to 5 °C. Axis ratios used for high density graupel were 0.5 to 1.25. Canting angle standard deviations for HDG were set to 10° and 20°, similar to LDG. The Cheng and English (1983) exponential distribution (GRAUP) was used for HDG, and D_0 values ranged from 3 mm to 7.5 mm (Cheng and English, 1983; Xu, 1983).

2.3.5 *Ice Crystals (CR)*

One of the limitations of the T-matrix model is that it is unable to model complex and intricate shapes associated with ice crystals growing by vapor deposition. Rather, ice crystals are modeled as oblate spheroids, a reasonable approximation according to the findings of Matrosov et al. (1996). Ice crystals are generally small ($D < 1.5$ mm, Locatelli and Hobbs, 1974) with small axis ratios ranging from 0.1 to 0.3 due to preferential growth along one axis during vapor deposition (Zikmunda and Vali, 1972, Rottner and Vali, 1974). The density of ice crystals growing by vapor deposition tends to be near that of pure ice, so ice crystal densities between 0.4 and 0.9 g cm^{-3} were simulated (Heymsfield, 1972; Ono, 1970). Temperatures of -10 °C and -40 °C were used in the simulations.

Gunn and Marshall (1958) proposed a modified Marshall-Palmer relationship between number concentration and size for snow, which was later modified by Sekhon and Srivastava (1970). Sekhon and Srivastava (1970) related the snowfall rate to the exponential size distribution (Eqn. 2.15) via the relations:

$$D_0=0.14R^{0.45} \tag{2.18}$$

where D_0 is in cm and R is the water equivalent precipitation rate in mm^{-1} and N_0 (mm^{-1} m^{-3}) is given as:

$$N_0=2.5x10^3R^{-0.94} \tag{2.19}$$

In this case, D_0 is the equivalent melted diameter of the ice crystal. This modified Marshall-Palmer distribution for snow will be referred to as 'MPS'. For the purposes of this study, precipitation rates between 0.01 and 10 mm h^{-1} were included (Sekhon and Srivastava, 1970).

Canting angles of snowflakes can be significant (Zikmunda and Vali, 1972; Bringi and Chandrasekar, 2001; Matrosov et al., 2006). Canting angle σ of 15° and 30° were used.

2.3.6 Aggregates (AG)

Aggregates, which are made up of a conglomeration of smaller ice crystals, were assumed to be much larger than ice crystals, with diameters ranging from 1 to 12 mm (Locatelli and Hobbs, 1974). Since aggregates are formed as different ice crystals stick together in random orientations, they were assumed to be semi-spherical, with axis ratios from 0.2 to 0.9 (Barthazy and Shefold, 2003). Aggregates have much lower (and less certain) bulk densities than pristine ice crystals. Pruppacher and Klett (1997) report aggregate densities ranging from 0.05 to 0.5 g cm^{-3}, with the most probable densities being from 0.01 to 0.2 g cm^{-3}. Previous studies have suggested that the bulk density of particles varies with particle diameter. Brandes et al. (2006; hereafter BR06) suggest the following relationship between particle bulk density and particle diameter for rimed and unrimed snowflakes:

$$\rho=0.178*D^{-0.922} \tag{2.20}$$

where D is the diameter of the particle in mm and ρ is in g cm^{-3}.

A density-size relationship suggested by Hogan et al. (2000; hereafter H00) for irregular crystals and aggregates was also used:

$$\rho = 0.175 * D^{-0.66} \tag{2.21}$$

For aggregate simulations, both fixed (0.1-0.2 g cm^{-3}) and size-dependant relationships (BR06 and H00) for density were used.

The MPS particle size distribution was also used for aggregates, and the equivalent rain rates were assumed to be 0.5 to 10.0 mm h^{-1}. Canting angle standard deviations of 15° and 30° were used.

Numerous studies have found that aggregation occurs most prolifically near 0 °C, and decreases with decreasing temperature (Hobbs et al., 1974; Rogers, 1974; Willis and Heymsfield, 1989). A secondary maximum in aggregation has also been observed from around -10 °C to -17 °C, which is likely associated with the dendritic ice habit growth regime since dendrites are the most favorable ice crystal habit for aggregate formation (Hobbs et al., 1974; Rogers, 1974; Field, 1999). Magono (1954) noted that no aggregates were observed at temperatures colder than -10 °C, and Hobbs et al. (1974) found that for small particle concentrations, aggregates were unlikely to form below -15 °C. More recently, Field (1999) found evidence of aggregation down to -30 °C, though pristine ice crystals were dominant at temperatures below -15 °C. Studies by Willis and Heymsfield (1989) also found that some large aggregates could persist to +5 °C. For simulations of aggregates, temperatures of -15 °C and 5 °C were used.

2.3.7 Vertically aligned Ice (VI)

Vertically aligned ice crystals can be a useful category for diagnosing regions of possible strong electric fields. Under a strong vertical electric field, small ice crystals are acted on by Coulomb forces and align themselves with the electric field. This generally results in negative specific differential phase (K_{dp}) values (Carey and Rutledge, 1998; Ryzhkov and Zrnic, 1998; Ryzhkov et al., 1998; Straka et al., 2000). Calculations by Weinheimer and Few (1987) showed that electric fields typically occurring in thunderstorms were sufficient to align particles with major dimensions up to 1 mm, and that column crystals were much more likely to align in the field than plate-like crystals. To simulate the vertically oriented ice, the same microphysical characteristics of ice crystals were use, except the mean canting angle was set to 90° to simulate prolate crystals (see Table 2.6).

Table 2.1:Attributes of the CASA IP1 radars during the CLASIC experiment, June 2007.

Transmitter	Frequency	9.41 GHz
Antenna	Maximum Peak power	25 kW
	Maximum Average power	25 W
	PRF	1.6 and 2.4 kHz
	Sensitivity	8 dBZ at 30 km
	Pulse length	100 m, 200m
	Diameter	1.5 m
Scanning	Rotation rate	20°/sec
	Maximum 3 dB beamwidth	1.8°
	Volume repetition	3 minutes
	Elevation angles	1.0-32°

Table 2.2: Locations and tower heights (except in the case of KOUN, the radar altitude is given) of the IP1 and KOUN radars.

	Latitude	Longitude	Tower height (m)
KCYR	34.87	-98.25	15.24
KLWE	34.62	-98.27	6.10
KRSP	34.81	-97.93	6.10
KSAO	35.03	-97.56	19.81
KOUN	35.23	-97.46	381.3 (altitude)
Network center	34.83	-98.10	

Table 2.3: Estimated radar Z_{dr} biases for IP1 data in June 2007.

Radar	Z_{dr} bias (dB)
KCYR	-0.1847
KLWE	+0.6
KRSP	-0.236
KSAO	+0.101

Table 2.4: Attributes of the KOUN radar.

Transmitter	Frequency	2.7 GHz
Antenna	Peak power	760 kW
	Sensitivity	-11 dBZ at 30 km
		-3.5 dBZ at 75 km
	Diameter	8.5 m
Scanning	Rotation rate	24°/sec
	Maximum 3 dB beamwidth	0.93°
	Volume repetition	5 minutes

Table 2.5: Scattering simulation inputs for the T-matrix model for the seven modeled hydrometeor types.

HID	a/b	Temp (°C)	Density (g cm^{-3})	D_{min} (mm)	D_{max} (mm)	Δd
AG	0.2, 0.9	-15.0, 5.0	0.1,0.2,BR06,H00	1	12	0.1
CR	0.125,0.15,0.35	-40,-10	0.4,0.9	0.05	1.5	0.005
DZ	1.0,0.9999	0,5,10,20	_	0.1	10	0.05
DZ	1.0, 0.999, GC84	5, 20	_	0.35	0.55	0.01
HDG	0.5,0.65,0.75,0.9,1.1,1.25	-5.0,5.0	0.55,0.65,0.75,0.85,0.9	1	10	0.1
LDG	0.5,0.65,0.75,0.9,1.1,1.25	-20,-10	0.25,0.35,0.45,0.55	1	10	0.1
LDG	0.65,0.0,1.1,1.25	-10	0.25,0.35,0.45.055	1	10	0.1
RAIN	CB90,PP71,J83,BR02,GC84, BC87	3,10,20	_	0.5	10	0.05
VI	0.125,0.15,0.35	-40,-10	0.4,0.9	0.05	1.5	0.005

Table 2.6: Scattering simulation inputs for the Mueller matrix model.

HID	θ_m (°)	σ (°)	Distribution type	μ	RR (mm h^{-1})	D_0 (mm)	Elev. Angle(°)	N_0 (cm^{-1} m^{-3})	Total #
AG	0	15,30	MPS	_	0.5, 10.	_	1,30	_	128
CR	0	15,30	MPS	_	0.01,0.1,10	_	1,30	0.05, 0.055, 0.04,0.035	144
DZ	0	1	MONO	_	1	1	1,30	80000	256
DZ	0	0.1, 1.0, 4.0	MP	_	0.1,0.5,1.0,2.0, 2.5	_	1,30	80000	900
HDG	0	10,20	GRAUP	_	_	0.3,0.4,0.5,0.55, 0.65,0.7,0.75	1,30	Eqn. 2.17	1680
LDG	0	10,20	GRAUP	_	_	0.15,0.2,0.3, 0.45,0.5	1,30	Eqn. 2.17	960
LDG	0	10,20	EXPON	_	_	0.15,0.2,0.1,0.25	1	80000	128
RAIN	0	1,4,10	NGAMMA	-0.1,1.0, 2.0,3.0,4.0	_	0.05,0.1,0.15,0.2, 0.25,0.3,0.35	1,30	1000,5000, 10000,50000, 100000	14580
VI	90	15,30	MPS	_	0.01,0.1,10.	_	1,30	0.05, 0.055, 0.04,0.035	144

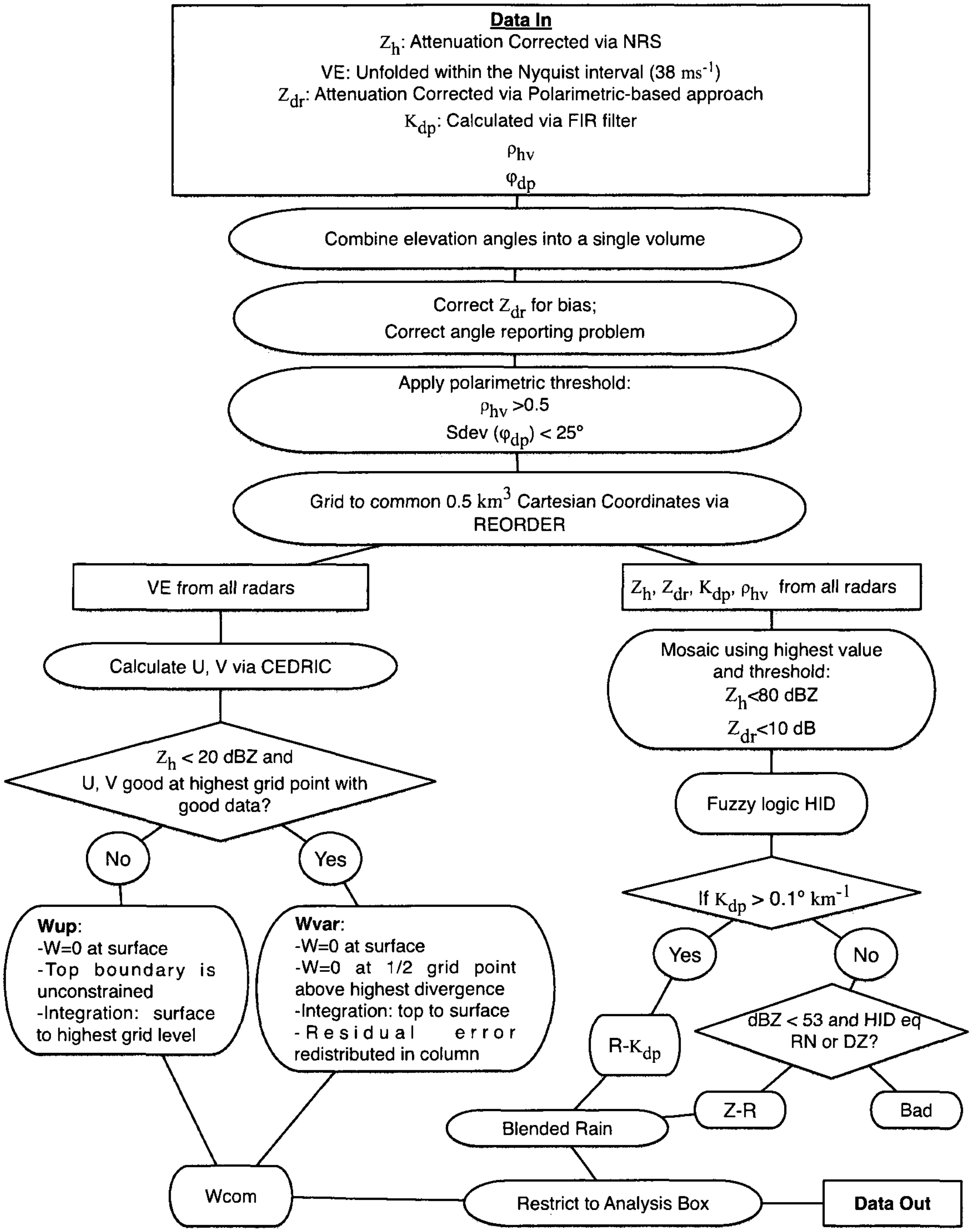

Fig. 2.1: Flow chart for IP1 data processing and quality-control.

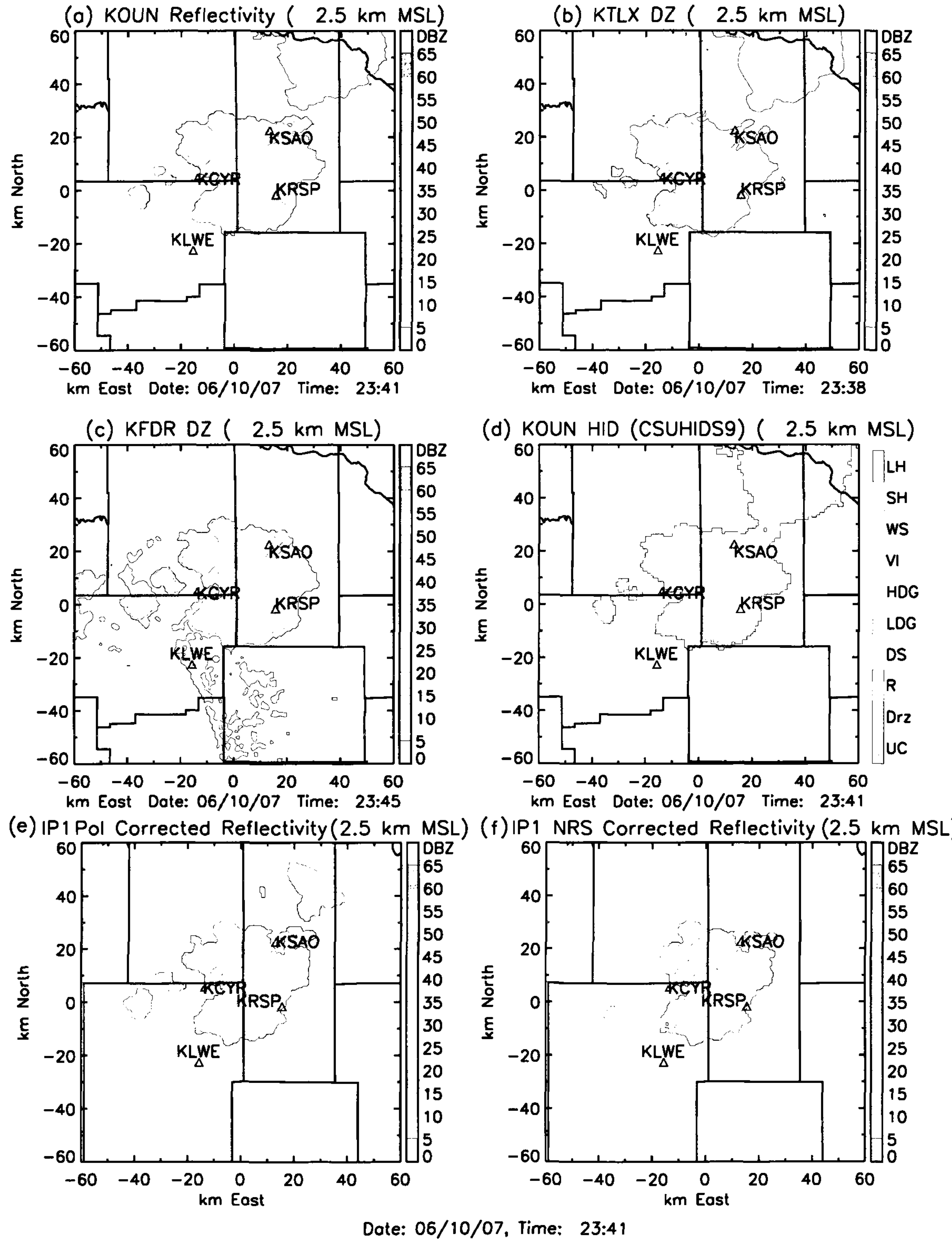

Fig. 2.2: Horizontal CAPPI of reflectivity at 2.5 km MSL from a) KOUN, b), KTLX, c) KFDR, d) KOUN HID, e) IP1 pol corrected, and f) IP1 NRS corrected at approximately 2341 UTC on 10 June 2007. Hydrometeor types in d) are unclassified (UC), drizzle (Drz), rain (R), dry snow (DS), low-density graupel (LDG), high-density graupel (HDG), vertical-aligned ice (VI), wet snow (WS), small hail (SH), and large hail (LH).

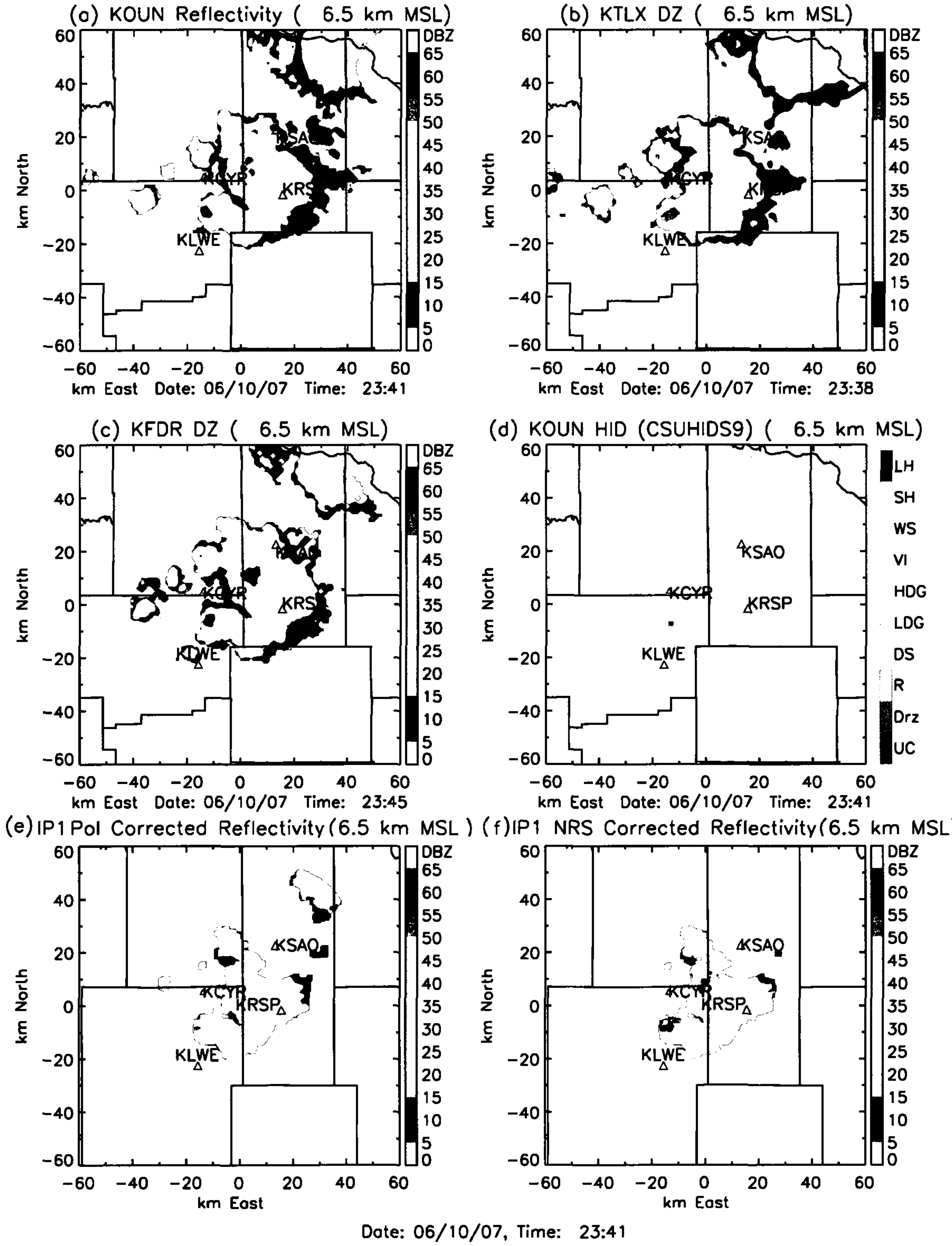

Fig. 2.3: Horizontal CAPPI of reflectivity at 6.5 km MSL from (a) KOUN, b), KTLX, c) KFDR, d) KOUN HID, e) IP1 pol corrected, and f) IP1 NRS corrected at approximately 2341 UTC on 10 June 2007. Categories for panel d) are the same as Fig. 2.2.

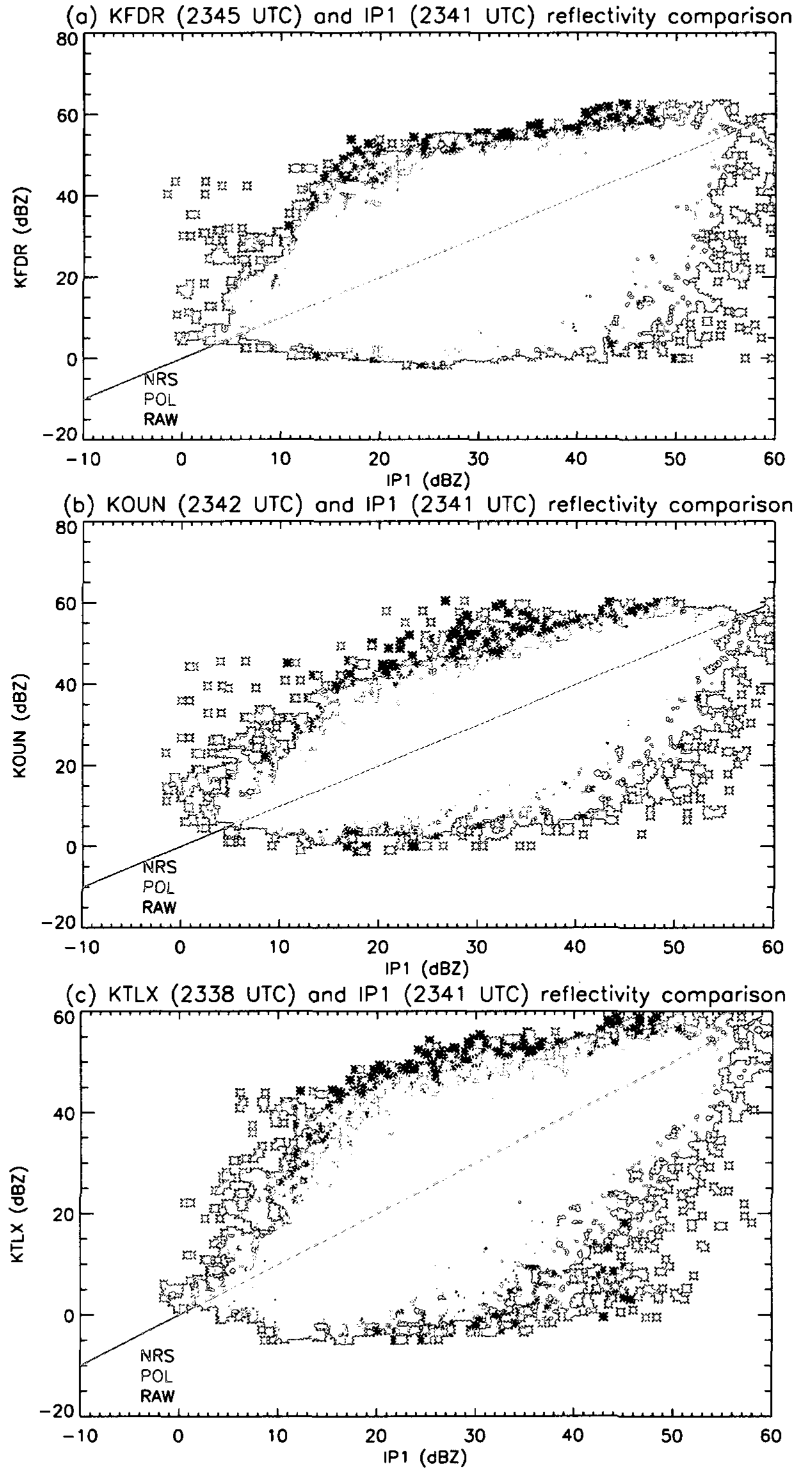

Fig. 2.4: Scatter plots of IP1 data compared to a) KFDR, b) KOUN and c) KTLX for uncorrected (RAW) IP1 reflectivity (black), polimetric-based (POL) corrected reflectivity (green) and NRS corrected reflectivity (red) at approximately 2341 UTC on 10 June 2007.

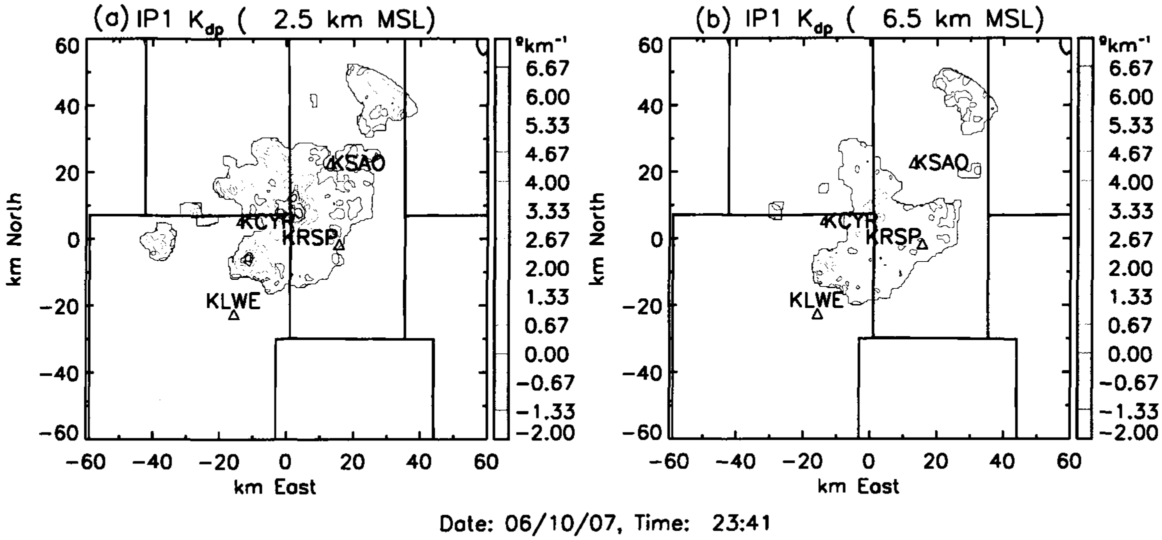

Fig. 2.5: IP1 specific differential phase at a) 2.5 km and b) 6.5 km applied to data from 2341 UTC on 10 June 2007.

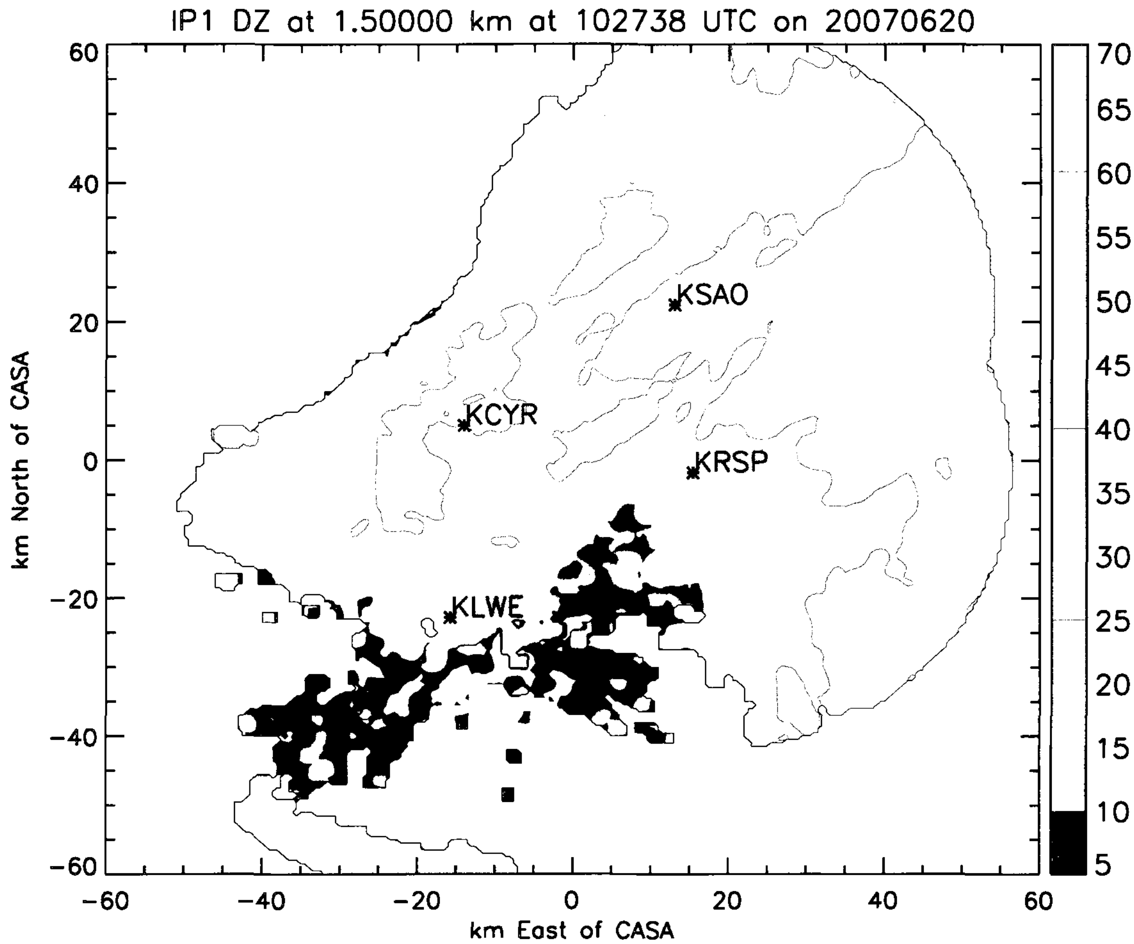

Fig. 2.6: IP1 reflectivity at 1.5 km MSL on 20 June 2007 at 1027 UTC in the trailing strateform region of an MCS.

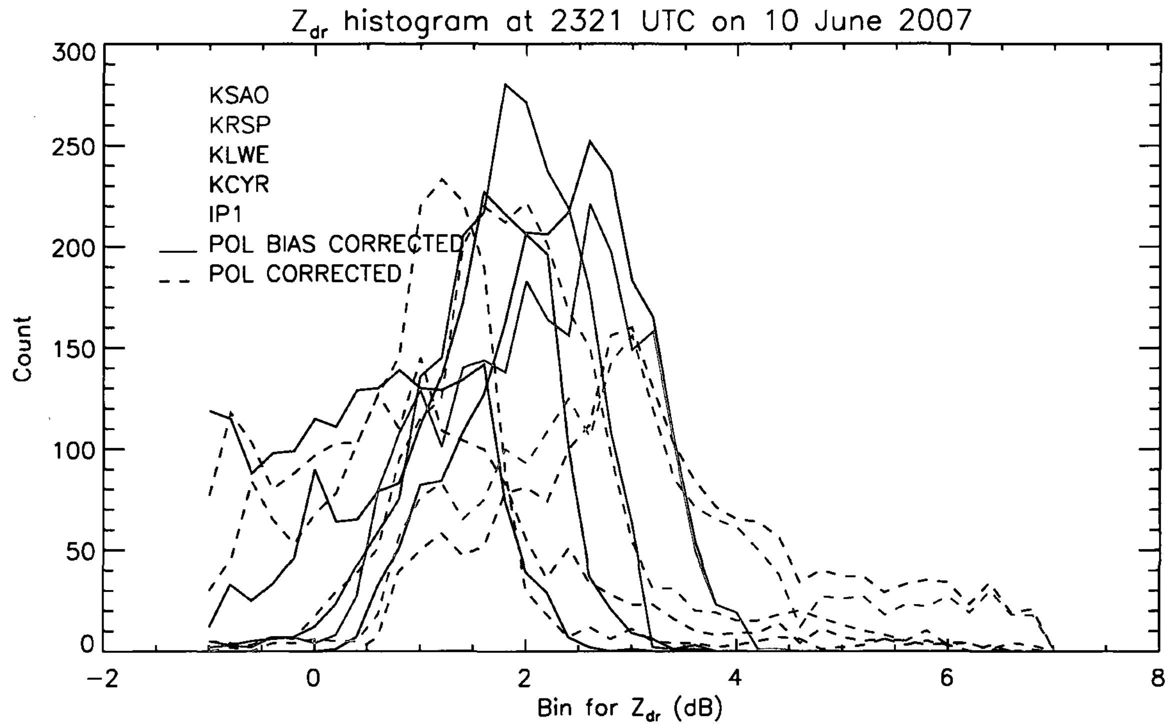

Fig. 2.7: Histograms of biased (dashed) and bias-corrected (solid) differential reflectivites between 0.5 and 3.5 km at 2321 UTC on 10 June 2007.

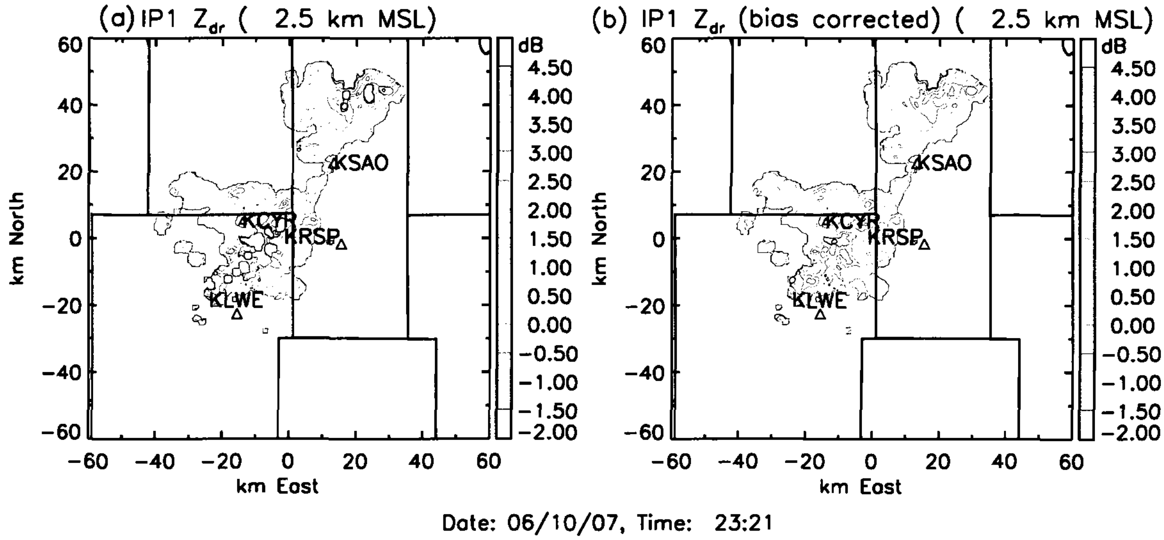

Fig. 2.8: IP1 differential reflectivity CAPPI at 2.5 km MSL a) uncorrected and b) corrected for the bias determined by the 20 June analysis applied to data from 2321 UTC on 10 June 2007.

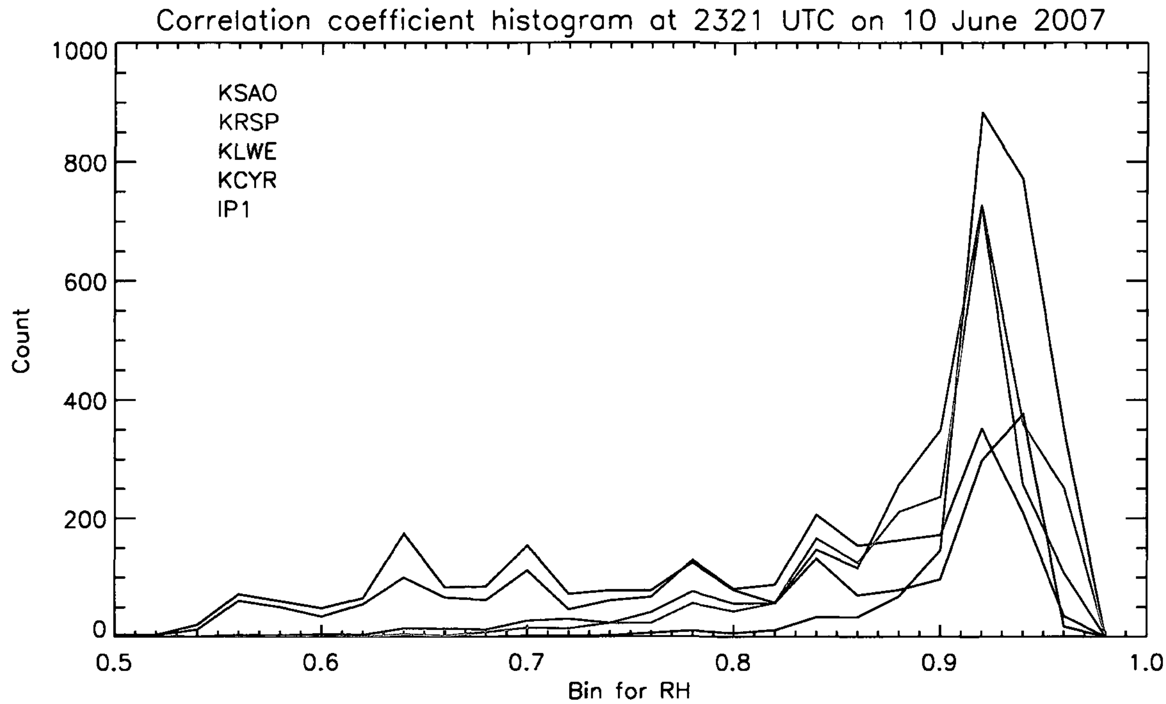

Fig. 2.9: Histogram of correlation coefficient at 2321 UTC on 10 June 2007.

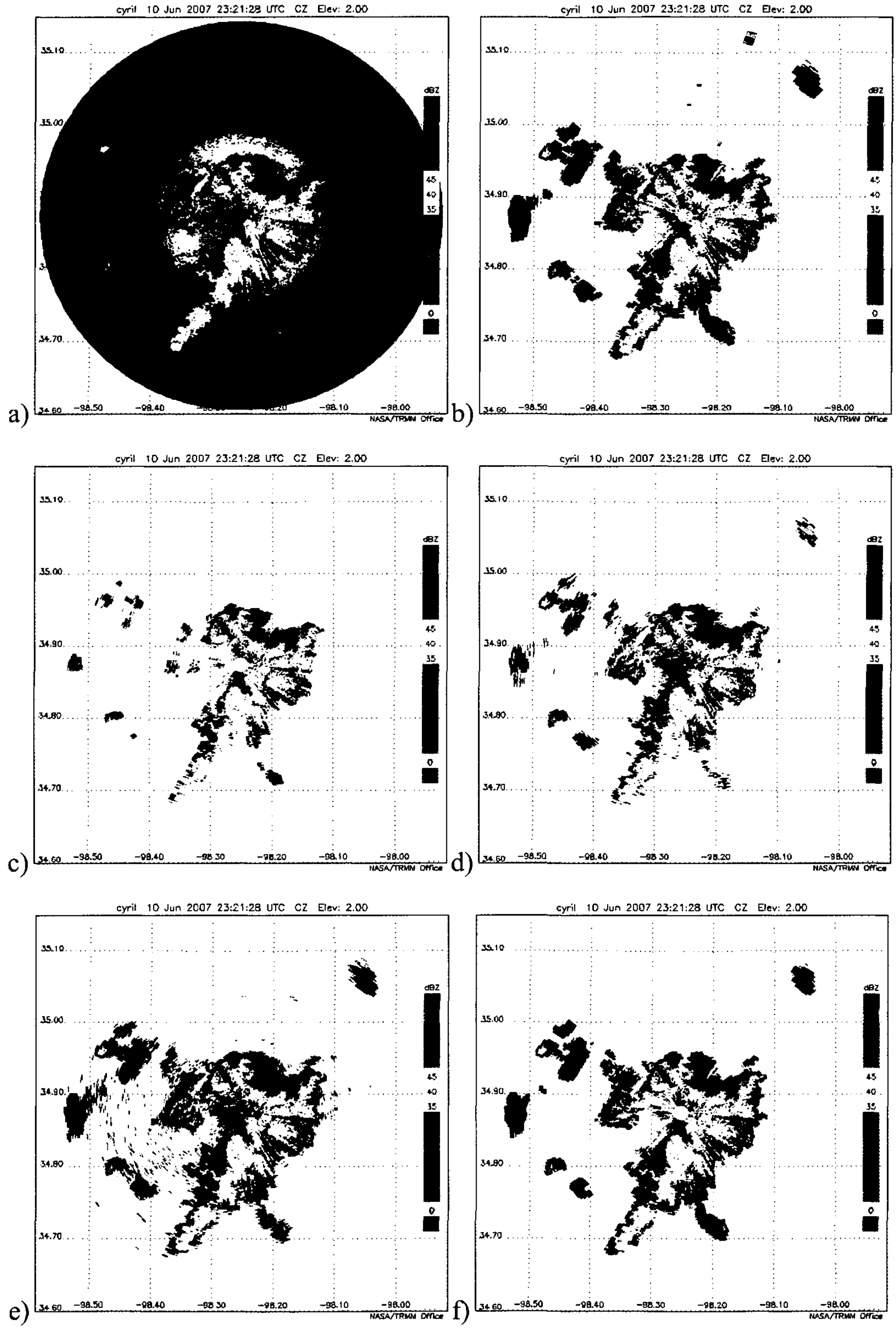

Fig. 2.10: Examples of different thresholds used to quality-control the IP1 data. Data are from KCYR at an elevation of 2°. The quality control thresholds used are in the bottom corner of each image in gray. Thresholds in panels a-c and f are for ρ_{hv} and sdev(Φ_{dp}).

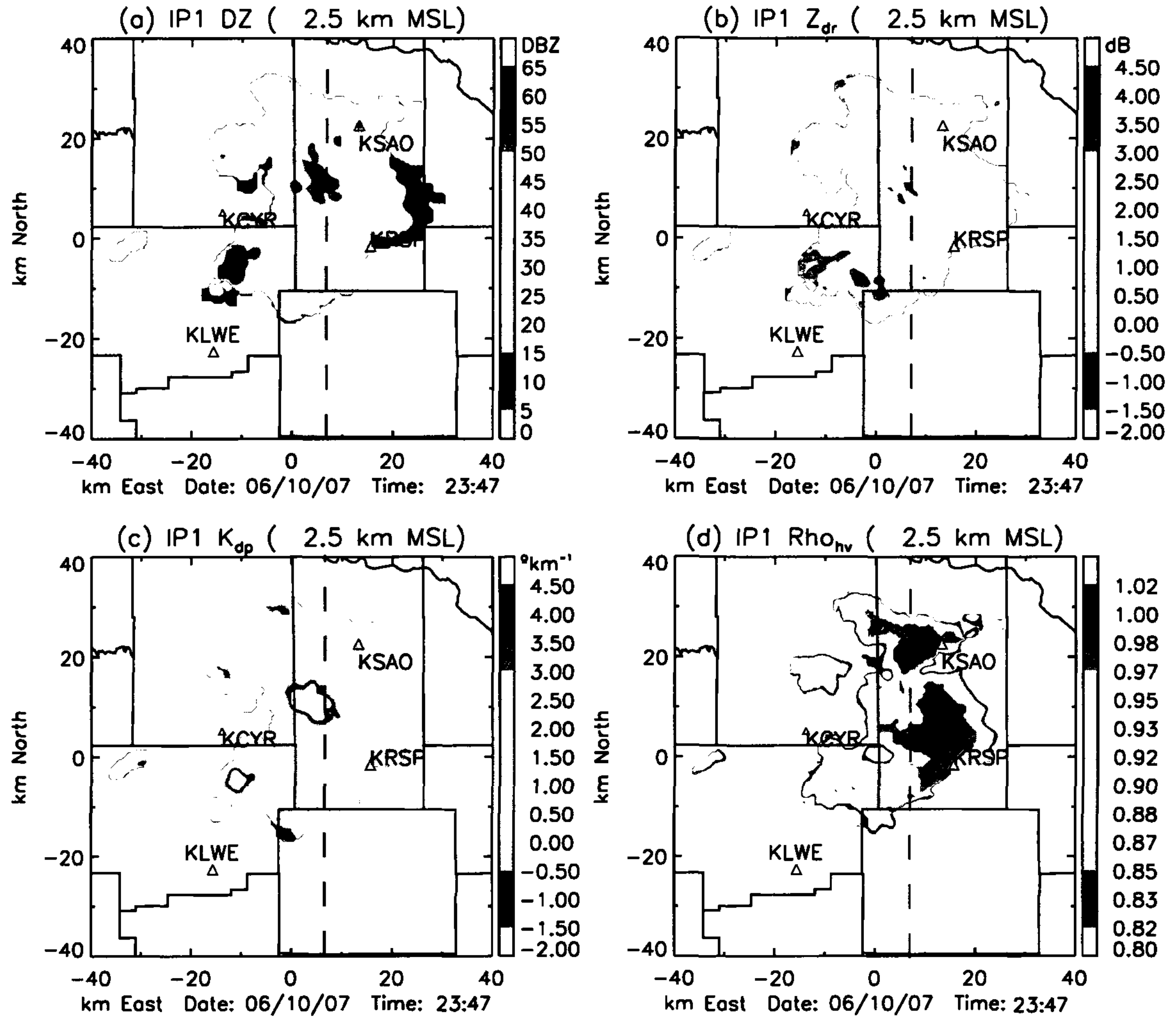

Fig. 2.11: Horizontal cross-sections of gridded, mosaicked IP1 data at 2.5 km MSL at 2347 UTC on 10 June 2007 for a) reflectivity, b) Z_{dr}, c) K_{dp} and d) ρ_{hv}.

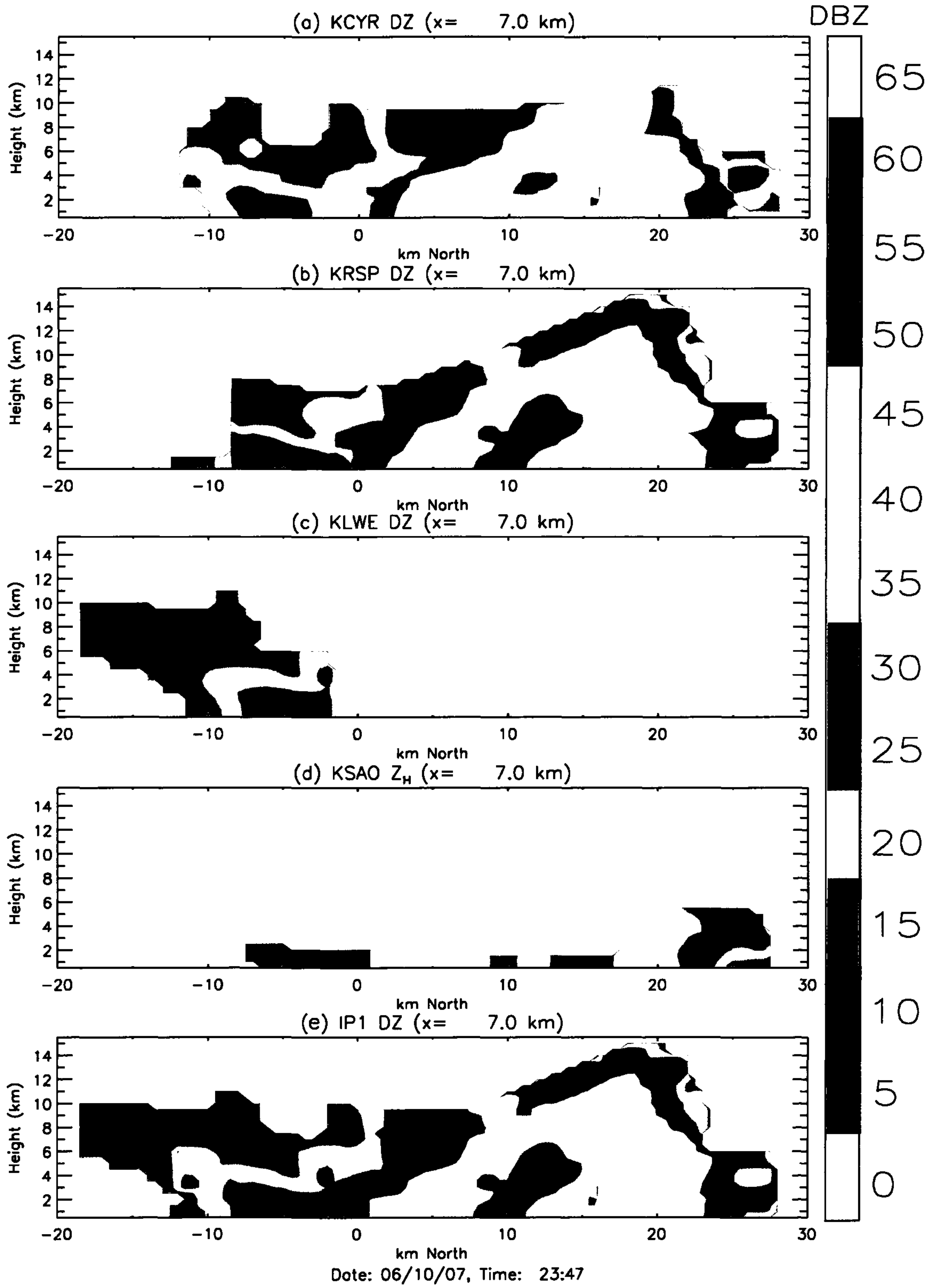

Fig. 2.12: Reflectivity cross-section at x=7.0 km on 10 June 2007 2347 UTC for a) KCYR, b) KRSP, c) KLWE, d) KSAO and e) IP1 mosaic.

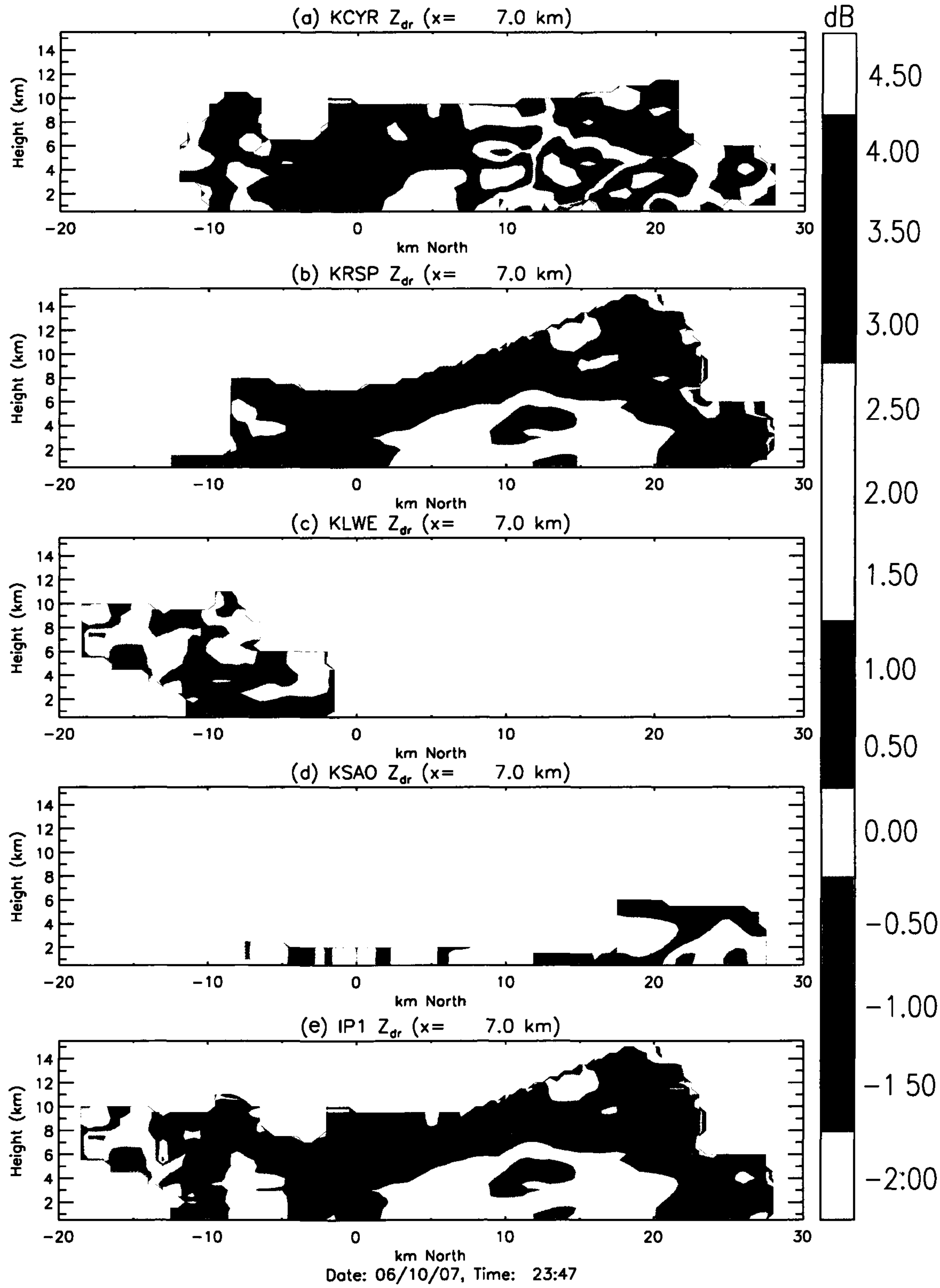

Fig. 2.13: Differential reflectivity cross-section at x=7.0 km on 10 June 2007 2347 UTC for a) KCYR, b) KRSP, c) KLWE, d) KSAO and e) IP1 mosaic.

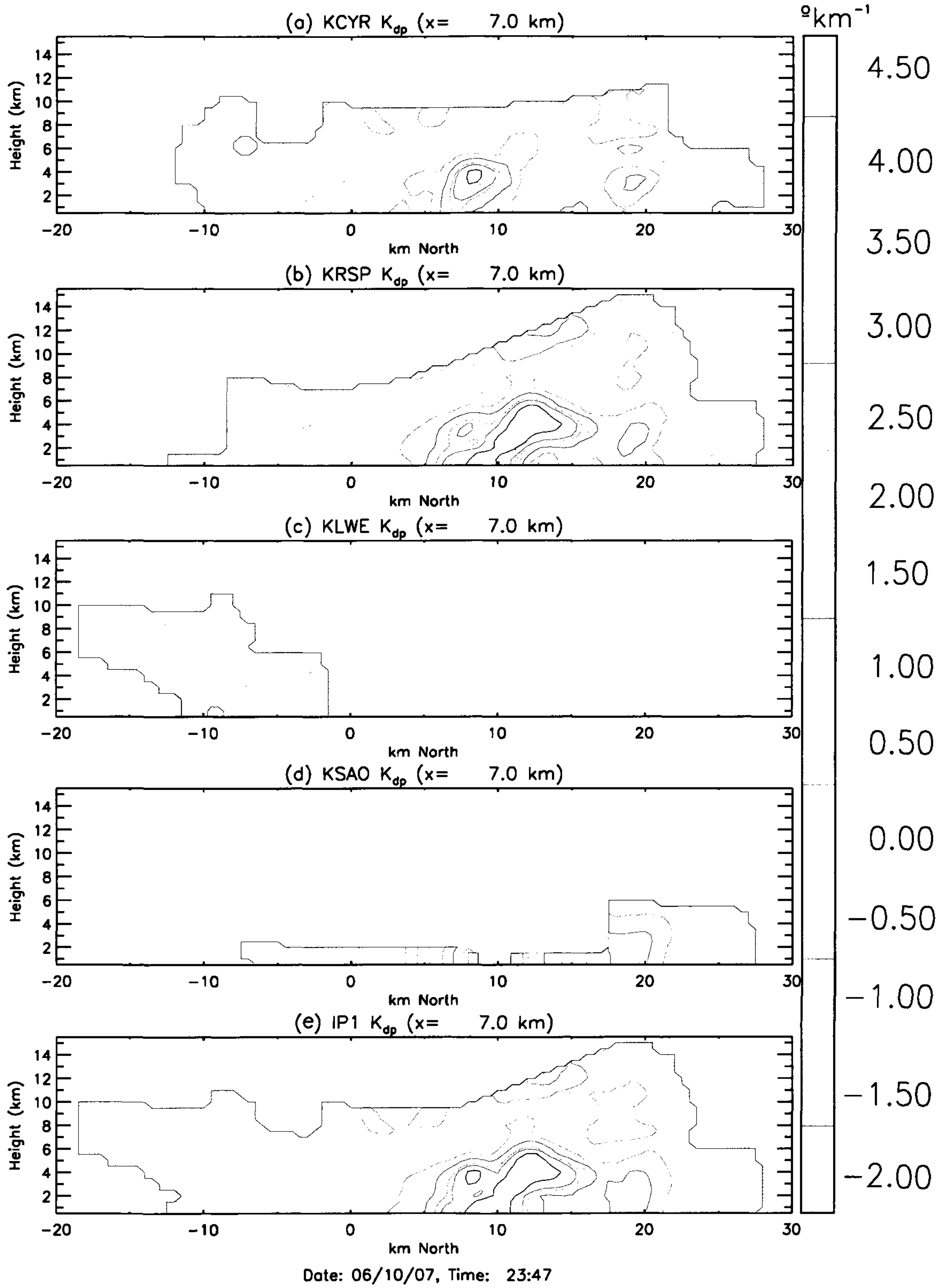

Fig. 2.14: Specific differential phase cross-section at x=7.0 km on 10 June 2007 2347 UTC for a) KCYR, b) KRSP, c) KLWE, d) KSAO and e) IP1 mosaic.

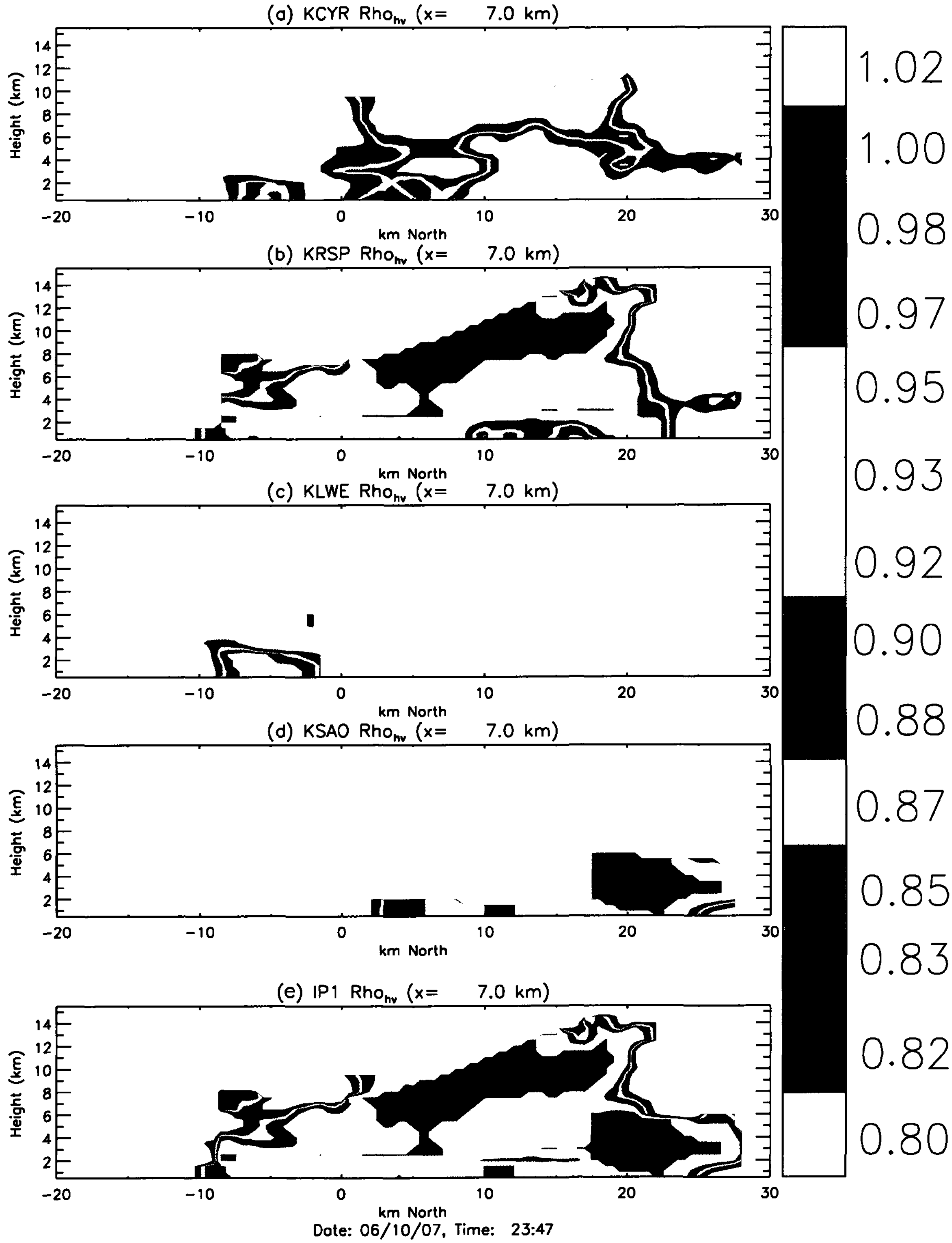

Fig. 2.15: ρ_{hv} cross-section at x=7.0 km on 10 June 2007 2347 UTC for a) KCYR, b) KRSP, c) KLWE, d) KSAO and e) IP1 mosaic.

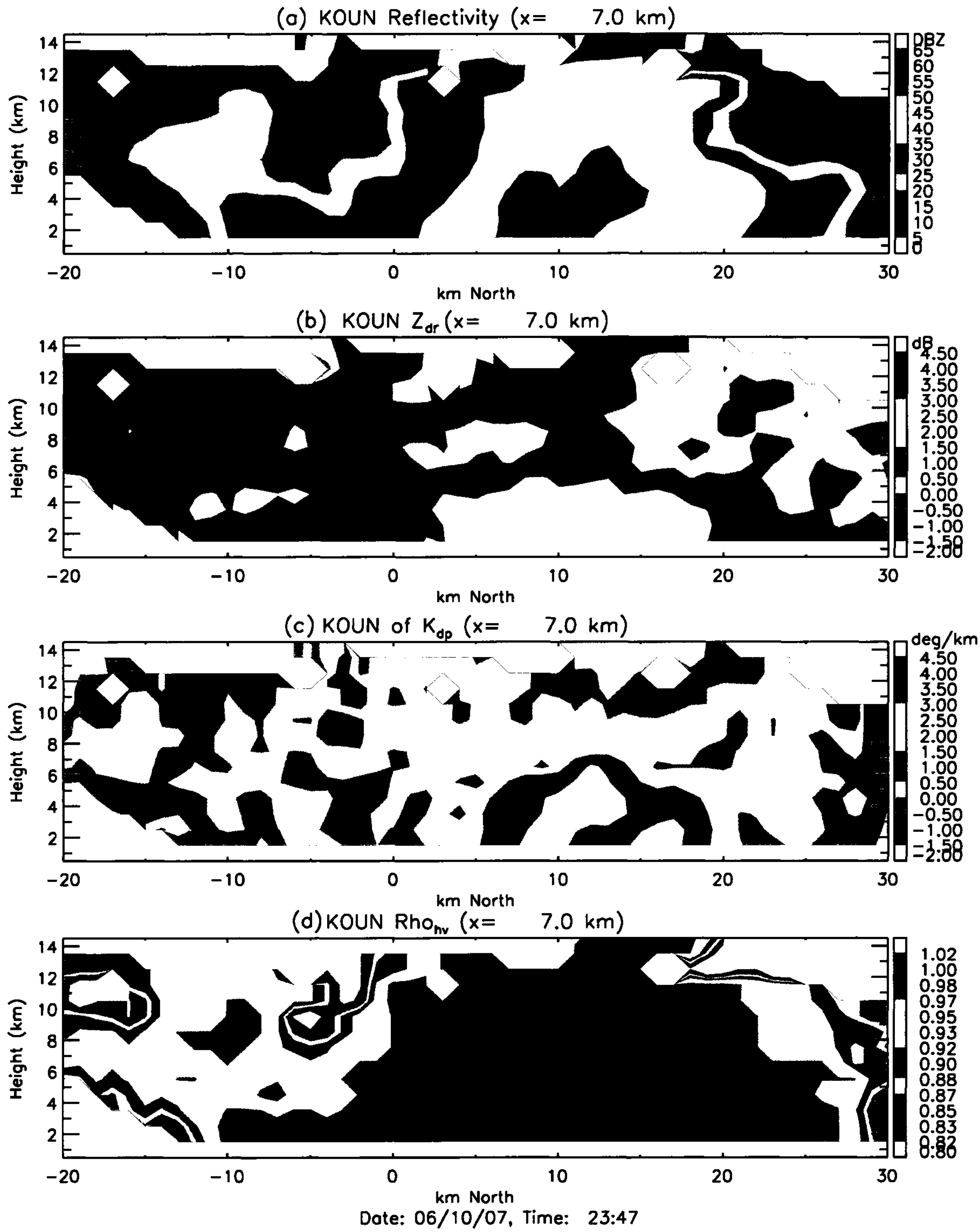

Fig. 2.16: KOUN data from 10 June 2007 at 234705 UTC for a cross-section along x=7.0 km for a) reflectivity, b) Z_{dr}, c) K_{dp}, d) ρ_{hv}.

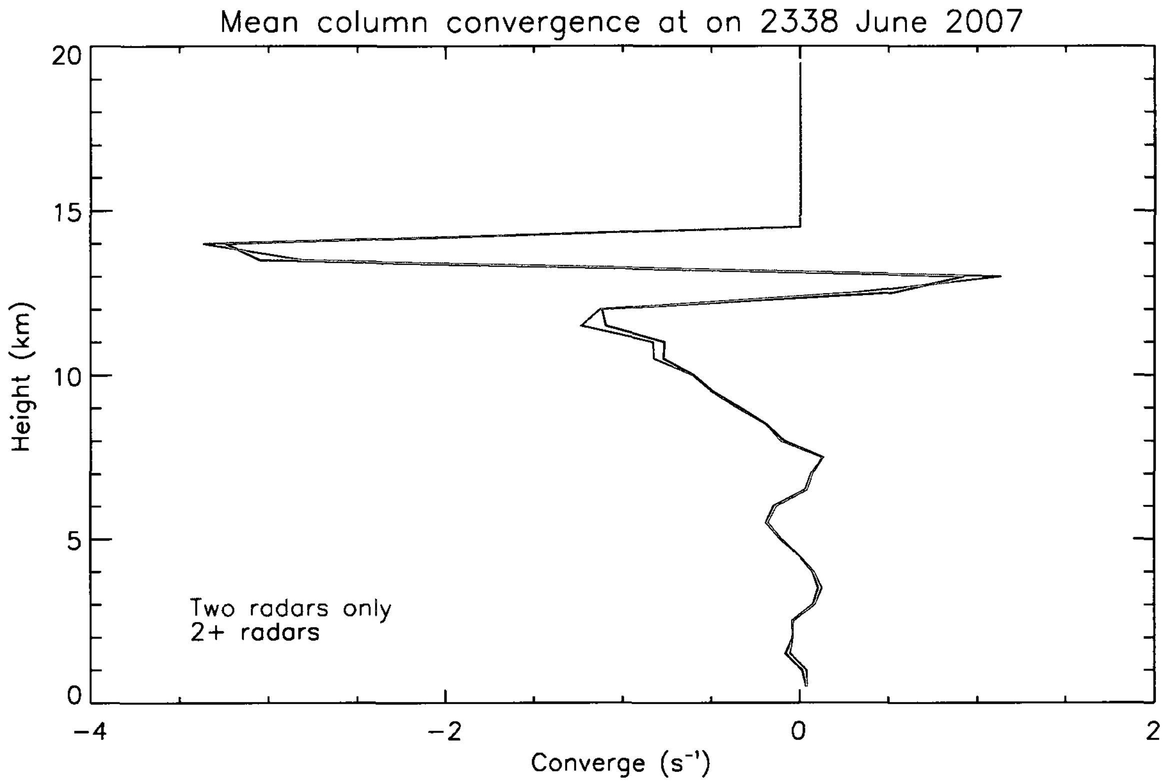

Fig. 2.17: Mean convergence using only two radars to solve for u and v (green), and using 2+ (as many as are available at each grid point; black) at 2338 on 10 June 2007.

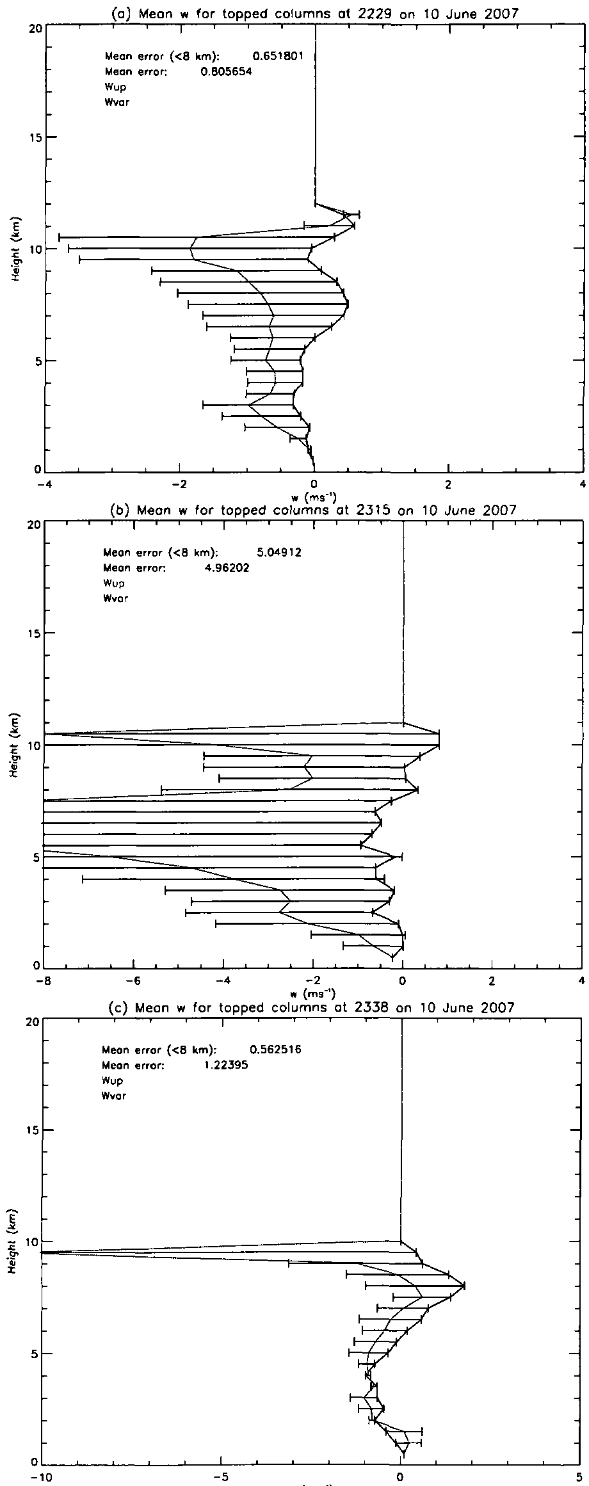

Fig. 2.18: Comparison of W_{up} (green) and W_{var} (black) mean w for columns determined to be "topped" at three different times: a) 2229 UTC, b) 2315 UTC and c) 2338 UTC. Bars represent the average difference between the W_{up} and W_{var} integration methods.

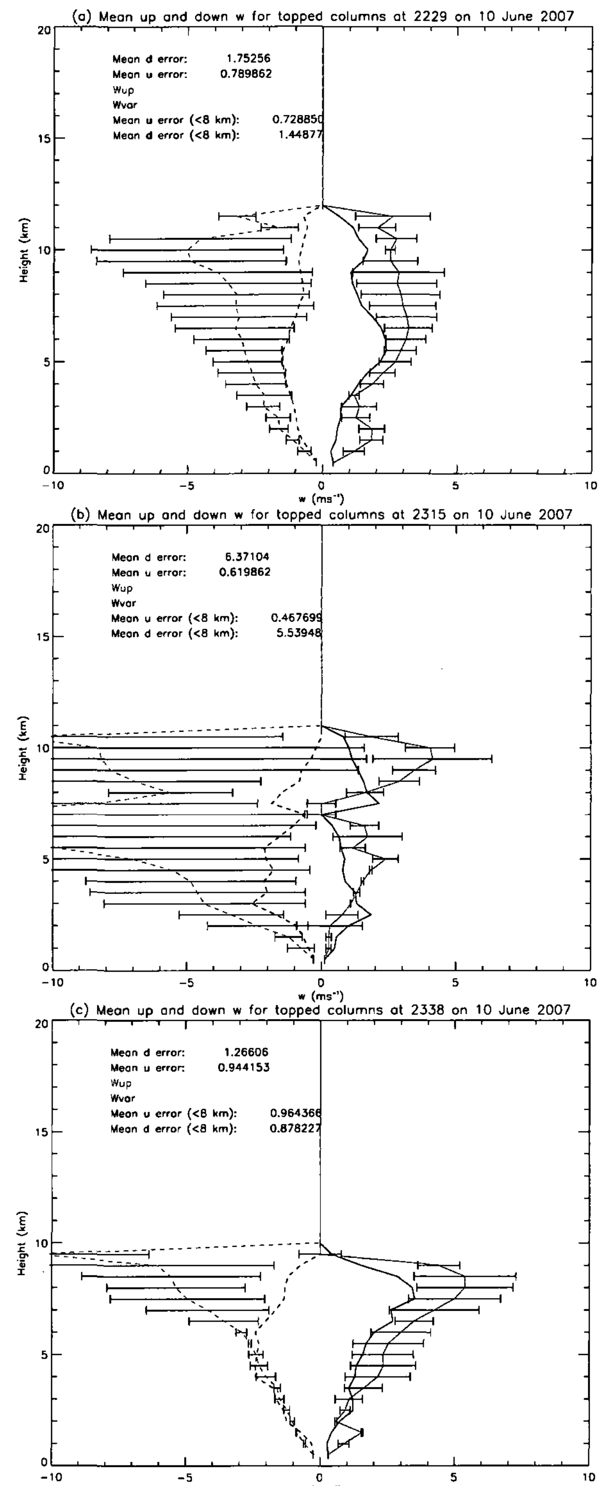

Fig. 2.19: Comparison of W_{up} (green) and W_{var} (black) mean upward and downward velocity for columns determined to be "topped" at three different times: a) 2229 UTC, b) 2315 UTC and c) 2338 UTC. Bars represent the average difference between the W_{up} and W_{var} integration methods.

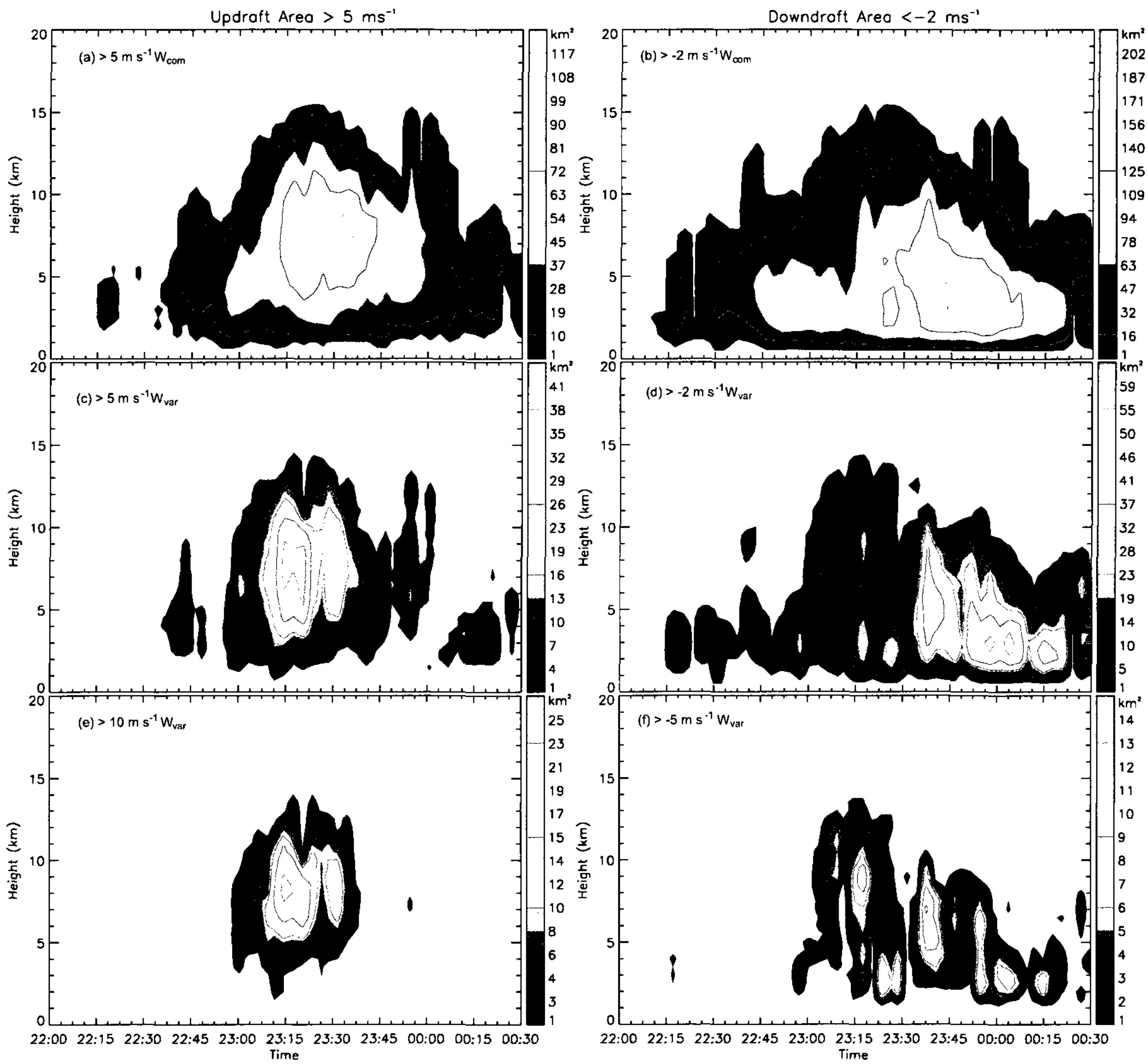

Fig. 2.20: Comparison of the W_{com} and W_{var} dual-Doppler methodologies for updraft (left) and downdraft (right) areas. W_{com} (top) is used on all columns, W_{var} (middle and bottom) is only used on "topped" columns as determined by the methodology outlined in Fig. 2.1.

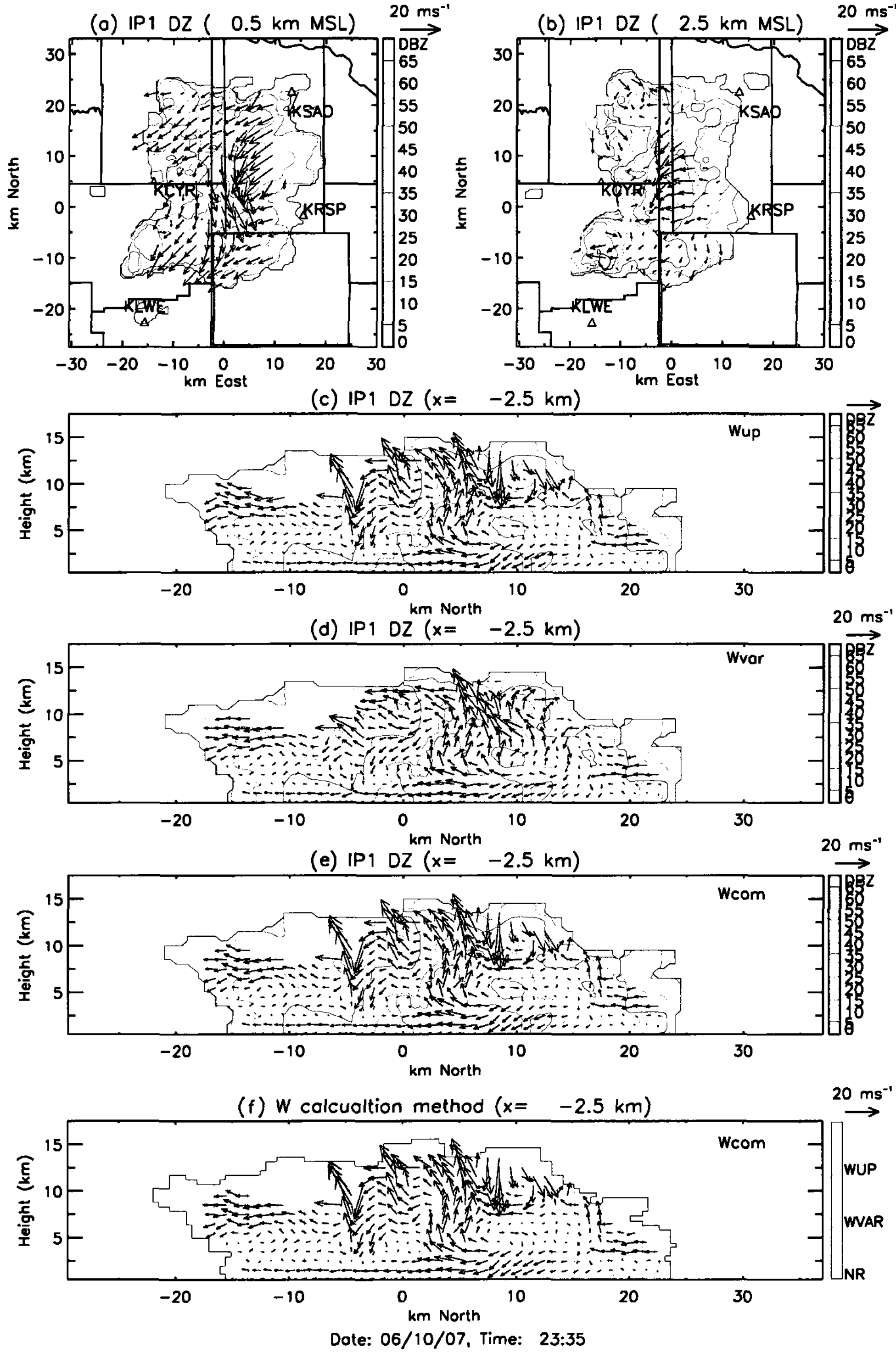

Fig. 2.21: An example comparison of the W_{up}, W_{var}, and W_{com} methods of determining the vertical wind taken at 2335 UTC on 10 June 2007. a) and b) are horizontal cross-sections of IP1 DZ, and c)-f) are vertical cross-sections taken at x=-2.5 km. Vectors are storm-relative winds, using c) W_{up}, d) W_{var}, e) W_{com} and f) W_{com}. f) illustrates the type of integration used in W_{com} on a column-by-column basis.

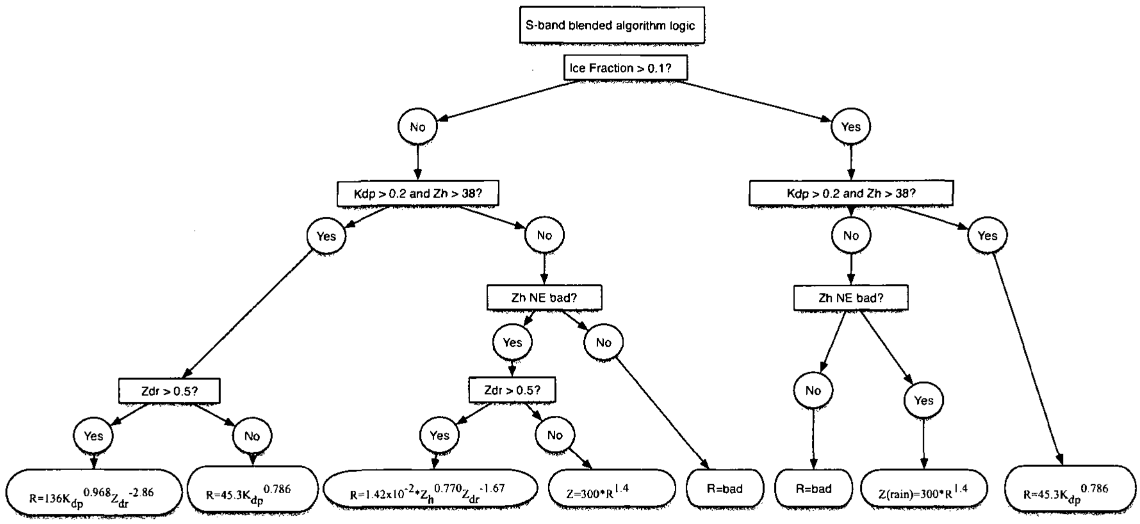

Fig. 2.22: S-band "blended algorithm" methodology for determining rainrate using polarimetric estimation (adapted from Cifelli et al., 2003).

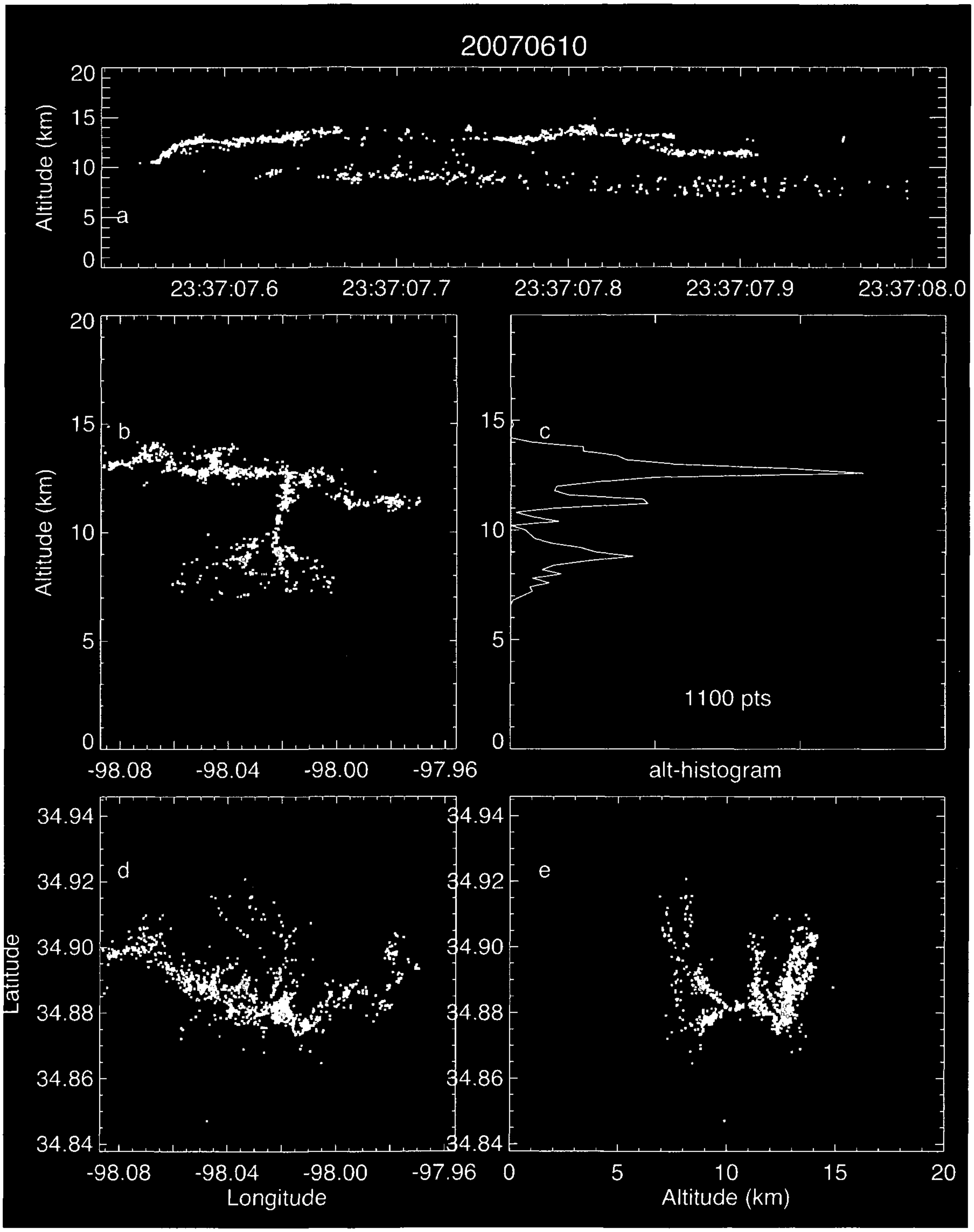

Fig. 2.23: OK-LMA sources for an IC flash occurring at 2337 UTC on 10 June 2007.

Chapter 3

An X-band fuzzy logic-based hydrometeor identification algorithm

3.1 Introduction

Polarimetric radars provide a wealth of information that can be used to estimate microphysical properties within a storm. Bulk classification of hydrometeors using polarimetry can help diagnose hail cores, rain/snow transitions, regions of graupel, and strong electric fields (via vertically aligned ice crystals), among other applications (e.g. Carey and Rutledge, 1998; Vivekanandan et al., 1999; Zrnic et al., 2001; Ryzhkov et al., 2005). To date, polarimetric-based hydrometeor identification algorithms (HID) have been applied to data from primarily S-band (10-11 cm) radars (Vivekanandan et al. 1999; Liu and Chandrasekar, 2000; Straka et al., 2000; Ryzhkov et al., 2005; Tessendorf et al., 2005).

S00 provide an extensive overview of what has been accomplished in terms of bulk hydrometeor classification, particularly at S-band. Their overview presents expected variable ranges for different hydrometeor types based on previous modeling and observational work. S00 characterize a wide variety of hydrometeors in terms of polarimetric radar observables, including hail, graupel-small hail, rain, rain mixed with wet hail, snow crystals, and aggregates. A common technique for synthesizing information from polarimetric variables into a hydrometeor classification scheme is to use a fuzzy logic-based approach (Vivekanandan et al., 1999; Liu and Chandrasekar, 2000; Zrnic et al., 2001). In contrast to a simple decision tree, fuzzy logic allows for soft and overlapping boundaries that can reduce the impact of calibration and measurement errors on the classification (Liu and Chandrasekar, 2000). Fuzzy logic is a four-step process in which the polarimetric radar observations are scored based on how well they fit the membership set for a given hydrometeor type. The hydrometeor type with the highest score is then assumed to be the dominant hydrometeor type in that particular radar volume. The reader is referred to Vivekanandan et al. (1999), Liu and Chandrasekar (2000), and Zrnic et al. (2001) for further discussion of the fuzzy logic process. It should be noted that the fuzzy logic-based method only assigns the hydrometeor type with the highest score to the radar volume. Thus results from fuzzy logic hydrometeor identification (HID) should be considered the dominant type at that particular location.

HID has also been extended to shorter wavelength radars (C-band; Baldini et al., 2005 and others). However, applying HID to even shorter wavelengths (e.g. X-band) encounters challenges due to Mie scattering and attenuation effects, both of which are often negligible at S-band. Although Mie theory describes the scattering of electromagnetic radiation by a sphere, we will use it to approximate all particle shapes for convenience herein. The transition to Mie is a function of wavelength and hydrometeor phase, due to the dielectric response between ice and water. The characteristic diameter for which Rayleigh approximations can be used decreases with decreasing radar wavelength, resulting in a larger range of hydrometeors falling out of the Rayleigh regime at X-band versus that at S-band. For example, the Rayleigh approximation can be used for spherical water targets with diameters less than 7 mm at S-band, which encompasses nearly all rain and graupel particles, with only large raindrops and hailstones falling into the Mie regime. At X-band, rain diameters less than about 2 mm can be considered to be in the Rayleigh regime, resulting in large rain drops and larger graupel and small hail being non-Rayleigh scatterers. Thus, direct application of a S-band HID could lead to improper categorization at shorter wavelengths.

The purpose of this study is to develop a hydrometeor identification algorithm for X-band based on theoretical simulations of radar moments for various hydrometeor types. The theoretical simulations will be used to characterize and understand the Mie scattering and response of meteorological targets to incident X-band radiation. The results of the simulations will be used to develop membership beta functions as part of an X-band fuzzy logic hydrometeor identification scheme that will be applied to IP1 data. Comparisons between X- and S-band will be made to determine the impact of non-Rayleigh scattering on retrieving bulk storm microphysics.

3.2 Scattering Simulation Results

Fig. 3.1 shows the simulated and expected ranges for a) reflectivity (DZ), b) differential reflectivity (Z_{dr}), c) specific differential phase (K_{dp}) and d) correlation coefficient (ρ_{hv}) for the seven different hydrometeor categories described in Sec. 2.3. The results from both the X- and S-band scattering simulations are shown relative to the generally excepted literature values for S-band expressed in S00, as well as values used for the S-band CSUHID algorithm described in Tessendorf et al. (2005). The ranges given in these two studies are used for comparison with the simulated S-band ranges to examine how well the scattering simulations captured the expected variability for the seven hydrometeor types. The other ranges shown in Fig. 3.1 will be discussed in Sec. 3.3

regarding the fuzzy logic HID algorithm development. It should be noted that the CSUHID does not separate aggregates from ice crystals, but rather has a single "dry snow" (DS) category that encompasses these two types. As such, the variable ranges shown for CSUHID in Fig. 3.1 for AG and CR are associated with the DS category.

S-band simulation ranges compare well with S00 and CSUHID for rain, indicating that the parameters used in the simulations were representative of the expected variability of rain. Inter-wavelength comparisons of reflectivity show that X-band simulated reflectivity has a larger maximum and smaller minimum than the S-band reflectivity for the same microphysical input parameters. This is likely due to the increased Mie effects of particles larger than about 2 mm at X-band. As expected, there is very little difference between S- and X-band expected minimum and maximum reflectivity values for the DZ, CR, and VI categories, which have small enough diameters to fall into the Rayleigh regime at both wavelengths. Reflectivity ranges for LDG given by S00 differ from those given by CSUHID, which are on average higher. Simulated LDG ranges for reflectivity encompass both S00 and CSUHID ranges. Simulated HDG values do not extend as low as S00, but maximum values are into the mid 50's, similar to those given by CSUHID. The difference between S00, CSUHID and the simulations are likely due to the definitions of LDG and HDG in terms of the sizes and assumed densities of the particles, but could also be a function of mixtures of particles occurring naturally versus the single particle-type simulations. Non-Rayleigh effects are also noted in LDG and HDG, as well as some minor differences in AG. Under Rayleigh assumptions, the backscattering cross-section depends on λ^{-4}, where λ is wavelength, and therefore for the same radar constant, larger reflectivity values would be expected at X-band compared with S-band (as in the case for RN). However, in all of the frozen hydrometeor types, simulated X-band ranges are lower than simulated S-band (Fig. 3.1a). This is due to the wavelength dependence of the index of refraction, which decreases with increasing frequency, resulting in smaller backscattering cross-sections for X-band versus S-band (Battan, 1973). The smaller index of refraction is due to a reduced dipole response in ice with frequency.

The simulated ranges of Z_{dr} capture the expected S-band ranges relatively well for DZ (Fig. 3.1b). Values given in S00 for the Z_{dr} of RN are allowed to go up to 6 dB, whereas simulated values of S-band RN Z_{dr} maximums were on the order of 3 dB. LDG ranges for Z_{dr} are similar to those of both S00 and CSUHID. Again, S00 and CSUHID report different ranges for HDG Z_{dr} values, but simulated S-band values contain both ranges, though extend to lower minimum values than either S00 or CSUHID. The X-band maximum Z_{dr} value is larger than the S-band values by greater than 0.5 dB in the case of RN and HDG, and a few tenths of a dB in the case of LDG and DZ. Maximum AG Z_{dr} values presented in S00 are slightly less than those modeled at S-band, but S00 CR Z_{dr} ranges are slightly larger than those modeled at S-band. CSUHID, which does not distinguish between CR and AG, shows Z_{dr} values for DS up to 6 dB. Modeled CR maximum values go up to > 5 dB, similar to CSUHID values for DS and S00 values for CR. Minimum simulated Z_{dr} values for CR do not extend to 0, as in the case of CSUHID DS and S00 CR. Modeled values of Z_{dr} for VI are strictly below 0 dB, whereas values given by S00 and CSUHID are centered around zero. As noted by Ryzhkov et al. (1998), larger particles, though less numerous, do not readily align themselves with the electric field and could increase Z_{dr} values while smaller crystals align to give negative K_{dp} values (an effect not captured by the simulations).

Perhaps most notable are the differences in K_{dp} between S- and X-band for the seven hydrometeor types (Fig. 3.1c). Specific differential phase is proportional to the inverse of wavelength (Bringi and Chandrasekar, 2001):

$$K_{dp} = \left(\frac{180}{\lambda}\right) 10^{-3} CW\left(1-\overline{r_m}\right) \tag{3.1}$$

where C is a dimensionless- wavelength-independent constant, W is the mixing ratio for non-spherical particles in g m^{-3}, $\bar{r}_m$ is the mass-weighted mean axis ratio, and λ is in meters. Thus, pure wavelength scaling would result in an increase in K_{dp} between 11 cm (S-band) and 3.2 cm (X-band) by a factor of 3.43. Fig. 3.2 illustrates the variability of X- to S-band K_{dp} ratios observed in the simulations as a function of D_0. X- to S ratios were averaged over all simulated mean diameter (D_0) for each hydrometeor type. The K_{dp} ratio for RN reaches a peak of 3.7 at mean drop diameters of 1.8 mm, and DZ ratios are larger than the expected K_{dp} ratio for all mean diameters. These results are essentially identical to Matrosov et al. (2006), who noted a K_{dp} scaling factor of 3.7 between X- and S-band for rain for drop diameters less than 3.5 mm. LDG and HDG show a clear increasing K_{dp} ratio with increasing mean diameter, while AG shows only slight deviation above the expected 3.43 ratio, and VI and CR have ratios less than or close to the expected 3.43 ratio. The scattering simulations in this study show that ratios can be as large as 4.4 (HDG) and as small as 3.3 (CR and VI) depending on the assumed mean drop diameter and hydrometeor type (Fig. 3.2). These greater than expected differences in K_{dp} can be attributed to resonance and non-Rayleigh effects (Matrosov et al., 2006). It should be noted that simulated values of K_{dp} may differ slightly from observational K_{dp} values which are derived from a highly filtered ϕ_{dp} field.

It is clear from comparison with S00 and CSUHID values that the scattering simulations did not capture the full variability of ρ_{hv} (Fig. 3.1d). A number of factors can decrease ρ_{hv}, including particle size, shape, canting angles, mixtures of hydrometeor types and hydrometeor shape irregularities (Balakrishnan and Zrnic, 1990). Several of these factors were not modeled in the simulations, including mixtures of hydrometeor types and irregular shapes. Although the ranges of values for ρ_{hv} were not completely simulated, non-Rayleigh effects can still be noted at X-band in the simulations (Fig. 3.1d). The co-polar correlation coefficient is influenced by backscattering differential phase, which is wavelength dependent. X-band RN ρ_{hv} values are slightly higher than S-band. HDG, LDG and DZ ranges show the opposite trend, where X-band values are slightly lower than S-band values. Low values of ρ_{hv} for VI were modeled for both X- and S-band, with maximum values not extending to 1.0. This is likely due to the canting angle distribution used, with a mean canting angle of 90°.

Comparisons of simulated S- and X-band variables illustrate their dependence on wavelength (Figs. 3.3 and 3.4). Non-Rayleigh scattering effects can be readily seen in reflectivity and Z_{dr} for rain (Fig. 3.3), as well as drizzle to a smaller extent (Fig. 3.4). Some non-Rayleigh effects are also evident in HDG Z_{dr} comparisons (Fig. 3.3b). Interestingly, HDG and AG reflectivities are smaller at X-band than S-band for higher relative reflectivities (Fig. 3.3a and 3.4a). This results from the complex and oscillatory nature of non-Rayleigh Mie scattering. Smaller deviations are noted in the Z_{dr} values for

VI, CR, and LDG. K_{dp} ratios depart from the expected 3.43 due to resonance effects and non-Rayleigh effects (Matrosov et al., 2006). These variations are especially pronounced for RN and HDG (Fig. 3.3c). Correlation coefficient (ρ_{hv}) RN and HDG values show significant scatter (Fig. 3.3d), and HDG X-band values are lower than S-band HDG ρ_{hv} values. Most rain and drizzle ρ_{hv} values show the same trend, although several X-band rain points are larger than S-band for lower ρ_{hv} (Figs. 3.3d and 3.4d). Ice crystals (CR) as well as oriented ice crystals (VI) trend towards higher X-band values than S-band (Fig. 3.4).

As a consistency check for the simulation output, rainrates were calculated using the assumed drop-size distribution, Z-R and R-K_{dp} relationships for X-band simulations at 20 °C, μ=1.0, and an elevation angle of 1°. The rainrate (R) was calculated from the gamma drop-size distribution using Eqn. 2.11. Two R-K_{dp} relationships derived using different drop-shape model assumptions were used. The first uses the Beard and Chuang (1987) shape model:

$$R=12.32K_{dp}^{0.78} \tag{3.2}$$

The second uses the so-called bridge data (Thurai et al., 2007):

$$R=12.79K_{dp}^{0.77} \tag{3.3}$$

The NWS Z-R relationship was also used (Eqn. 2.5).

Fig. 3.5 shows relatively good agreement between these different rain rate calculation methods. As expected, there is a large difference between the R-K_{dp} and Z-R calculation methods, with R-K_{dp} values falling closer to the rain rates calculated from the DSD. There are also differences of several mm h^{-1} between the R-K_{dp} and DSD estimated rain rates. Only small deviations and overall trends between the DSD calculated rain rates and R-K_{dp} rain rate calculations indicate that the K_{dp} values from the scattering simulations fall within acceptable and expected ranges.

In addition to the hydrometeor simulations described in Tables 2.5 and 2.6, a monodisperse population of raindrops was modeled in order to examine the behavior of reflectivity (Z_h), differential reflectivity (Z_{dr}) and specific differential phase (K_{dp}) for different elevation angles, wavelengths, drop-shape model relationship, and mean diameters (D_0). The parameters used for these studies are given in Tables 3.1 and 3.2.

As expected, the drop-shape model has very little influence on the reflectivity (Fig. 3.6a), although the Jameson (1983) model results in slightly smaller reflectivities for drops greater than 3 mm than the other models. The choice of drop shape model has a significant impact on Z_{dr} and K_{dp} (Fig. 3.6b and c). Again, the J83 shape model results in the smallest values at higher D_0. The Goddard and Cherry (1984) relationship initially shows smaller Z_{dr} for both S- and X-band below 2.5 mm, but results in more oblate larger drops (higher Z_{dr}). The Chuang and Beard (1990) relationship allows for the most oblate small drops, while Pruppacher and Pitter (1971) seems to be a compromise between CB90 and GC84 (Fig. 3.6b). Only very small differences between GC84 and PP71 show up in K_{dp}, and again, J83 deviates from the others, particularly at $D_0 > 5$ mm (Fig. 3.6c). The behavior of Z_{dr} and K_{dp} becomes non-linear at significant mean diameters ($D_0 > 7$ mm). However, it should be noted that mean diameters occurring naturally rarely exceed about 3.5 mm.

For drops greater than 3 mm, it is evident that the X-band reflectivity is larger than the S-band by up to 3.5 dB (Fig. 3.7a). Between 1 mm and 3 mm (Fig. 3.7a), the X-band reflectivity is slightly smaller than the S-band reflectivity by less than 1 dB. These results support the simulations of Tian et al. (2002) and are due to non-Rayleigh scattering effects at X-band. Z_{dr} values are quite varied between X- and S-band (Fig. 3.7b). X-band Z_{dr} values deviate by up to 0.5 dB between 2 mm and 5 mm. As drop diameters increase, S-band Z_{dr} levels off more than X-band, and at really large drop diameters (10 mm), S-band Z_{dr} increases significantly. K_{dp} ratios between X and S show a bimodal trend (Fig. 3.7c), with peak ratios at 2.5 mm and 5 mm. X-band K_{dp} values peak at about 7.5 mm, then fall off rapidly due to the decrease in forward scattering for horizontal polarization compared to the forward scattering in the vertical polarization (a Mie effect), while S-band K_{dp} increases rapidly above 8 mm. These trends support the findings presented by Matrosov et al. (2006).

Z_{dr} and K_{dp} are based on differential measurements between the h and v channels, and as such are highly dependant on the radar viewing angle. To study the relationship between these observables and elevation angle, the monodisperse simulations using the Goddard and Cherry (1984) drop-shape model of rain were conducted for eleven elevation angles ranging from 1 to 90°. Z_{dr} for all drop sizes changed less than 4% between 1 and 10° (Fig. 3.8). By 20° in elevation, changes were 8-14% different than the 1° value. At 30°, the approximate highest elevation angle scanned by the CASA IP1 radars, Z_{dr} had dropped over a quarter of the initial (1°) value for all drop sizes, and drops larger than 6 mm decreased by almost 30%. Again, it is noted that such large drop diameters do not occur regularly in nature. At 45° elevation, Z_{dr} values were half of their original 1° value for all drop diameters. Interestingly, S-band Z_{dr} values decrease more rapidly with elevation angle than X-band Z_{dr} for diameters > 3.5 mm, but X-band K_{dp} decreases much quicker as elevation angle increases compared to S-band K_{dp} (Fig. 3.9). Nearly the same trend is seen with K_{dp} at both X- and S-band, with values reduced by approximately 25% between 1° and 30° elevation (Fig. 3.9).

3.3. Hydrometeor Identification Algorithm

3.3.1 Fuzzy Logic Development

The variable ranges associated with each hydrometeor type derived from the scattering simulations were used as the basis for a theoretically-based fuzzy logic hydrometeor identification algorithm (HID). The HID developed for this study uses one-dimensional membership beta functions (MBF) for the fuzzy logic algorithms (Liu and Chandrasekar, 2000). That is, the membership beta functions define the truth value that relates the observations to the hydrometeor types. MBFs (β) are defined in terms of their width (a), mid-point (m), and slope (b) :

$$\beta = \frac{1}{1+\left[\frac{(x-m)^2}{a}\right]^b} \tag{3.4}$$

where x is the observational data. The simulated variable ranges for each polarimetric variable were converted into beta functions and then applied to IP1 and KOUN data collected on 10 June 2007. Direct conversion of the simulated data into membership beta functions resulted in discontinuous classification with excessive amounts of LDG and little HDG (see Sec. 3.3.3). This is likely due to the overlap between beta functions for frozen hydrometeor types, particularly AG, CR, HDG and LDG. Thus, small modifications to the MBFs were made in order to decrease the degree of overlap between hydrometeor types. Specifically, the minimum LDG values were increased from ~14 dBZ to 20 dBZ, which is between the minimum values given by CSUHID and S00. Because of a large overlap between HDG and RN, S-band RN Z_{dr} values were increased to 5 dB (closer to those reported by S00), and relative differences between X- and S-band were preserved, so X-band values were increased to 5.5 dB. As discussed above, VI Z_{dr} observations could be dominated by larger crystals or plates that do not readily align in an electric field (a physical process not captured by the simulations), and thus Z_{dr} values for VI were increased to a maximum of 0.5 dB. Since comparison with S00 and CSUHID ranges indicate the full variability of ρ_{hv} was not represented by the simulations, ρ_{hv} minimum values were decreased slightly for all categories except VI, where the maximum value was increased to 1.0. Again, the relative differences between X- and S-band were preserved. The modified simulation ranges used in the HID are illustrated in Fig. 3.1 (XMBF and SMBF). We consider these modifications appropriate to the extent that the definitions of dry graupel, wet graupel, small hail, and aggregates are somewhat overlapping, and the simulations include only single hydrometeor types, whereas observed radar volumes are likely mixtures of particles, which could alter observed ranges.

Several different versions of hydrometeor identification algorithms were used to study the representativeness of the theoretically-based HID. Three HID algorithms were applied to the S-band KOUN data: the 6-category CSUHID (henceforth referred to

CSUHIDS 6), the "theoretical" 7-category HID with the modifications described above (where the MBFs were based on the theoretical simulations; henceforth referred to as SS7), and a simple reflectivity and temperature only-based HID, where the weights of the polarimetric variables were set to 0 in the fuzzy sets (referred to as ZTS). Two algorithms were run on X-band IP1 data: the modified theoretical fuzzy logic-based HID (henceforth referred to as CS7), and a simplified X-band fuzzy logic-based reflectivity and temperature only HID (ZTX). The specifics of the five HID algorithms are summarized in Table 3.3.

3.3.2 Application of Algorithm

In order to compare the results of the X-band hydrometeor identification algorithm with more widely-used S-band algorithms (and for comparison with an essentially non-attenuating wavelength), data from IP1 were used in conjunction with S-band polarimetric KOUN data.

For application of the HID algorithms, a temperature profile was acquired from the local 12 Z KOUN sounding. The melting level from the sounding was at 4.3 km MSL. The radar data were first gridded (KOUN data to 1 km^3, and CASA data to 0.5 km^3), then the fuzzy logic HID was applied. In the case of the CASA radars, the individual radar measurements were mosaicked into a single grid by taking the highest value for each variable from the available radars at individual grid points, as described in Sec. 2.1.3. The HID algorithms were then applied to mosaicked, gridded data. Due to the previously described quality of Z_{dr} and ρ_{hv} data during the 2007 CLASIC experiment, the weights for Z_{dr} and ρ_{hv} for the IP1 HID algorithms were set low (0.4 and 0.2, respectively) compared to the weight given to reflectivity (1.5), K_{dp} (1.0), and temperature (0.5) for the fuzzy logic process. Weights applied to KOUN were 1.5 (reflectivity), 1.0 (Z_{dr}), 0.6 (K_{dp}), and 0.5 (temperature and ρ_{hv}).

For various reasons, such as range, resolution, coverage, beam-geometry and of course wavelength, quantitative intercomparisons between KOUN and IP1 HIDs were of little utility. However, intrawavelength quantitative comparisons between HID algorithms applied to each dataset (KOUN and IP1) are possible, and can be used to reveal differences between the theoretical HID, the simple reflectivity and temperature only HID, and the original S-band HID (CSUHID). Quantitative similarities between KOUN theoretical HID (SS7) and CSUHIDS 6 will lend confidence to both the X-band and S-band theoretically-based HID algorithms. Qualitative comparisons between KOUN and IP1 data can also be made to ensure consistency in microphysical characteristics identified by the HID algorithms since no aircraft data are available for validation.

Fig. 3.10-3.13 show data from the five HID algorithms applied to IP1 and KOUN at 2347 UTC on 10 June 2007, during an intense period of the multicellular storm. Horizontal cross-sections at 2.5 km MSL (Fig. 3.10a,b and 3.11a,b) show large regions of rain (RN) surrounded by drizzle (DZ) for both CS7 and SS7. Near the top of the melting layer at 5.5 km (Fig. 3.10c,d and 3.11c,d), both CS7 and SS7 show areas of rain associated with the reflectivity cores, surrounded by graupel (HDG and LDG), and aggregates (AG), with some pristine ice crystals (CR) identified near the edges of the storm and between the two main reflectivity cores. CS7 identifies larger regions of LDG than SS7, both SS7 and CS7 show regions of vertically aligned ice crystals (VI) along the perimeter of the storm.

Vertical cross-sections at x=7 km at 2347 UTC highlight differences between the algorithms. The simulated S-band algorithm (SS7; Fig. 3.12b) shows relatively the same HDG and LDG trends as CSUHIDS 6 (Fig. 3.12c), with a region of HDG associated with the reflectivity core, surrounded by LDG. SS7 appears to identify more HDG, LDG and VI than CSUHIDS 6. SS7 shows a clear distinction between CR and AG around the height of the -20 °C layer (~8 km), adding information about storm microphysics to the otherwise large area of dry snow identified by CSUHIDS 6. Ice crystals are identified in the cold upper-regions of the storms, with aggregates occurring closer to the melting layer, as is expected (Willis and Heymsfield, 1989). The qualitative similarities between CSUHIDS 6 and SS7 lend some degree of confidence to the ability of the theoretically-based HID algorithms to distinguish bulk regions of hydrometeors. The IP1 theoretically-based HID (CS7, Fig. 3.13b) shows similar structure to that observed with the S-band HIDs. Common features reveal rain above the melting layer (lofted by strong updrafts) surrounded by HDG. A large region of LDG can be seen above the layer of HDG, though the areas of graupel are much larger in CS7 than SS7 or CSUHIDS 6. CS7 also shows some CR falling through the AG layer below -20 °C. In general, CS7 qualitatively shows the same features as the KOUN classifications.

In order to understand the contribution of the polarimetric information in the classification, a simplified reflectivity-temperature only algorithm (ZTS) was used. ZTS (Fig. 3.12d) generally demonstrates the same features as CSUHIDS 6 and SS7. There appears to be more drizzle below the melting layer in ZTS, and additionally, slightly less

LDG. Finally, ZTS is unable to identify VI, whereas the polarimetric-based HIDs are able to employ negative K_{dp} values. ZTX (Fig. 3.13c) also has a diminished region of HDG, as well as more DZ below the melting layer than CS7. Though some CR extend below -20 °C in ZTX, CS7 shows much more variability. In this case, X-band polarimetric variables can contribute information for distinguishing AG from CR, and RN from HDG, as well as providing a means to identify vertically aligned ice crystals.

To quantify the differences between CSUHID, the temperature-reflectivity only and theoretically-based HID algorithms, histograms of fractional storm volume for each hydrometeor type during the 2.5 hour lifetime of the 10 June 2007 storm are shown in Fig. 3.14. The KOUN HIDs show similar trends (Fig. 3.14a), with the storm volume being dominated by snow hydrometeor types (DS, AG/CR). The percentage of graupel identified by SS7 was more than twice that identified by CSUHIDS 6, with 12% LDG and 8% HDG for SS7 and 5% LDG and 3 % HDG for CSUHIDS 6. SS7 identified 3% less RN (10%) than CSUHIDS 6 (13%), but approximately the same amount of DZ (11%). For ZTS compared to CSUHIDS 6, DZ and LDG increased, HDG remained at 3% and RN decreased from 14% to 10%. However, when compared to SS7, HDG decreased, LDG and RN were approximately the same, and AG and DZ increased. CR nearly doubled from 16% for SS7 to 31% for ZTS, which is consistent with VI crystals being indistinguishable from CR by ZTS. The IP1 HIDs (Fig. 3.14b) classified nearly half of the grid volume as liquid hydrometeors (DZ and RN). As with the S-band HIDs, the amount of DZ increased when only temperature and reflectivity were used (30%). CR and AG amounts increased slightly for ZTX compared with CS7, while graupel amounts decreased.

Generally, the simulated HID algorithms (SS7 and CS7) identified more graupel, both LDG and HDG, than the CSUHID. Using only temperature and reflectivity altered the relative amounts of all seven hydrometeor types compared with the polarimetric-based algorithms, with the most significant difference being no VI identified and the relative amounts of CR and AG increasing to compensate.

Bulk differences between HID algorithms were calculated by determining on a gridpoint-by-gridpoint basis if each algorithm identified the same hydrometeor type. Then the number of grid points with different classifications was divided by the total number of grid points with classifications, and percentages were taken as an average over the entire 2.5 hour storm lifetime. Only the simulated and ZT algorithms are compared due to the difference in categories for CSUHID. Up to 34% of grid points changed classifications between SS7 and ZTS, and between ZTX and CS7 individual grid point classifications differed by up to 21%. These differences are mostly due to the inability of ZT to distinguish VI from CR. These results suggest that polarimetric variables contribute to greater than 30% of the hydrometeor identification process at S-band, and greater than 20% at X-band for this case compared to reflectivity and temperature only HID.

Several interesting observations can be made when comparing the IP1 and KOUN histograms qualitatively. First of all, both simulated HIDs (SS7 and CS7) identify approximately the same amount of graupel (12% LDG and 7-8% HDG over the total volume). Secondly, there appears to be a much larger percentage of liquid hydrometeor types (DZ and RN) categorized on average by the IP1 HID algorithms (20-30%) than the KOUN HID algorithms (10-15%), and more frozen hydrometeors (VI, AG, CR and DS) are identified by KOUN than IP1. This is likely a reflection of the coverage area and sensitivity of the different radars, not a direct artifact of the different wavelength HIDs. The IP1 radars are focused on the lowest 3 km of the atmosphere (below the melting layer during this case), resulting in the IP1 radars seeing all of the liquid hydrometeors near the surface. The sensitivity of the IP1 radars is approximately 8 dBZ at 30 km range, resulting in the light anvil regions of the storm being missed by the IP1 radars, as well as some of the upper portions of the storm due to the scanning strategy. On the other hand, the KOUN radar is ~75 km from the center of the IP1 network, so due to the curvature of the Earth, KOUN does not sample the lowest 2 km of the storm and therefore misses a relatively large volume of liquid hydrometeors. However, it captures the entire storm volume consistently, resulting in a much larger quantity of frozen hydrometeors on average than the IP1 radars.

3.3.3 Sensitivity Studies

The 10 June 2007 case was chosen in part due to the relatively small amount of hail identified by the CSUHID 9 category HID, which includes categories for large hail (LH), small hail (SH), and wet snow (WS). However, there was hail identified in the southwestern cell, as shown in the KOUN CAPPIs at 6.5 km and 10.5 km MSL (Fig. 3.15). A cross-section through the reflectivity core shows the hail extends from 5.5 km to 10.5 km (Fig. 3.16). Although this is a small fraction of the overall storm, it is important to understand how the hail gets categorized in CS7 and SS7, which do not include hail categories of any type. As can be seen in Fig. 3.16c, the S-band 7 category algorithm classifies the hail portions as HDG, while the X-band 7 category identifies the main hail core as rain, with some points being categorized as HDG (Figs. 3.17 and 3.18). This categorization at X-band is likely due to complex non-Rayleigh effects of hail, which were not studied.

As illustrated in Sec. 2.1.3, multiple radar observations of the same volume can be quite different (Figs. 2.11-2.15). With so many differences between individual radar observations, how does the mosaicked CS7 HID compare to CS7 HID algorithm applied to individual radars? Surprisingly, individual radars identify generally the same bulk hydrometeor types, as illustrated by Fig. 3.19. One noticeable difference in HID is the rain core extending into the HDG region identified in the KRSP HID that is not evident in the KCYR HID, most likely associated with the enhanced reflectivites in the KRSP data. This feature is carried through to the IP1 HID. Additionally, the region of VI at x=-8 km by KLWE is not carried through to the synthesized HID.

It is clear from this example that considering the coverage area, combining information from all of the radars into a single field provides the most complete information about the storm. It appears that although there are some differences between individual radar HID and the mosaicked IP1 HID, the general bulk hydrometeor trends are preserved using this methodology for combining variables and HID.

As suggested in Sec. 3.3.1, the HID went through several stages of development before the MBFs were finalized. The HID using the initial MBFs with exact variable ranges derived from scattering simulations are shown in Fig. 3.20. At S-band, very little CR are identified, while large pockets of LDG are identified outside of the main reflectivity core (Fig. 3.20a). Only a few grid points of VI exist in both the S-band and

X-band HID. The X-band HID is dominated by LDG above the melting layer, with very little CR and a narrow band of HDG between 4.5 and 6 km (Fig. 3.20b). It was determined that this was mostly due to the wide range of LDG reflectivities allowed by the T-matrix model simulations. Additionally, too much overlap between the CR, AG, and VI MBFs resulted in the same score at many points, in which case the point was identified as AG (the first hydrometeor scored in the fuzzy logic methodology). As such, small modifications were made to the MBFs until an improvement (closer to the CSUHIDS 6 identification (Fig. 3.12c) and a much "cleaner" distinction between CR and AG) was obtained. All changes were made proportionately between X- and S-band as determined from the scattering simulations. Results from the final HID are illustrated in Fig. 3.12b and 3.13b.

Several HID sensitivity studies were also performed on the S- and X-band data. The original S-band specific CSUHID 6 was applied to the IP1 X-band data to illustrate why a new X-band specific HID needed to be developed. As can be seen in Fig. 3.21a, applying the S-band HID to X-band data resulted in extensive areas of rain, particularly above the melting layer, and reduced areas of graupel. This is likely due to the higher reflectivities and K_{dp} values observed at X-band. The HDG area was especially diminished compared to the S-band identification (generally these points were categorized as rain at X-band), and a large region of VI was identified along the edge of IP1 coverage in the middle of the storm that was not seen in the S-band HID. These differences clearly indicate that development of an X-band HID was necessary for accurate identification of hydrometeors.

Due to the low confidence in Z_{dr} and ρ_{hv} values during this particular IP1 case, the HID was exercised without using these two variables (Fig. 3.21b). The results indicate that information is being lost with the exclusion of these two variables, which is evident by the lack of VI and diminished regions of HDG compared to the HID CS7 using these variables (Fig. 3.13b). The same study was run with the KOUN S-band algorithm (Fig. 3.22a). Much more CR was identified, indicating that Z_{dr} and ρ_{hv} were important in distinguishing AG and VI from CR. This is because Z_{dr} and ρ_{hv} values determined by the T-matrix simulations for VI were lower than for either AG or CR, while K_{dp} ranges were closer to one another. AG and CR ranges overlap significantly for K_{dp}, but there is more spread in both Z_{dr} and ρ_{hv} to distinguish these hydrometeor types (see MBFs in Sec. 3.3.4). Additionally, much less HDG and DZ were found, again underscoring the importance of these two polarimetric variables in the identification process.

As expected, removing temperature (T) from the fuzzy logic process dramatically influenced the HID categorization (Fig. 3.21c and 3.22b). Although the rain core was picked out in both the X- and S-band HID, very little distinction between the warm and mixed-phase regions of the storm is evident, especially in the S-band HID (Fig. 3.21c, 3.22b). HDG dominates both X- and S-band identifications, while S-band classifies very little LDG and IP1 identifies LDG surrounding the areas of HDG. Drizzle is allowed in the upper regions of the storm and CR and LDG are found at the surface. This illustrates the importance of including temperature in the classification. Even if a full thermodynamic profile is not available, the height of the melting level will help sort out appropriate regions of hydrometeors. As a final sensitivity study, reflectivity was removed from the fuzzy logic scheme (Fig. 3.21d and 3.22c). Again, the results differ significantly from the full fuzzy logic HID (Fig. 3.12b and 3.13b). However, the melting level is clear, identified as a layer of HDG in both X- and S-band. Neither S- or X-band classifies a large amount of AG, but rather small pockets of CR embedded within a large area of LDG. Clearly this study highlights the role of reflectivity in the classification scheme, particularly for distinguishing different ice hydrometeors, although some structure is still evident. These sensitivity studies demonstrate that although reflectivity and temperature are the most important variables for proper hydrometeor identification, the polarimetric variables certainly add value to the classification results. Lerach (2006) found similar results applying a simplified hydrometeor identification algorithm to a 2875 MHz profiling radar and comparing with a fully polarimetric S-band radar.

3.3.4 HID and simulation parameters

The final membership beta functions for the fuzzy logic HID based on scattering simulations are show in Figs. 3.23-3.24. For reference, the original CSUHID MBFs are shown in Fig. 3.25. Clearly, many of the variable ranges overlap, and differences between wavelengths discussed in Sec. 3.2 are also noted. Many of the slopes (b) of the MBFs are relatively small; this was indicative of the uncertainty in the variable ranges. Additionally, the ranges for each of the seven hydrometeor types based on the scattering simulations as well as the finalized HID are shown in Tables 3.4-3.10.

3.4. Discussion

A new fuzzy logic hydrometeor identification algorithm for X-band polarimetric radar data was developed using T-matrix scattering simulations to determine approximate variable ranges for seven different hydrometeor types. S-band simulations were also performed for comparison. Many non-linear Mie effects were seen at the shorter X-band wavelength, particularly in rain and graupel categories. Data from the CASA IP1 network were used to study the functionality of the new hydrometeor identification algorithm in comparison with several other versions of HID, and results were also qualitatively evaluated against similar HID algorithms applied to S-band data from KOUN. It was shown that a S-band simulation-based algorithm was similar to current literature, *in situ* and experience-based HID algorithms at S-band, lending some credence to the theoretically-based HID algorithms. The theoretically-based X-band algorithm performed relatively well and showed many similar microphysical characteristics to the S-band algorithms, despite non-Rayleigh effects noted at X-band. The addition of aggregate and ice crystal categories to replace the CSUHID dry snow category assists in increasing the detail of microphysical processes. Although a simple reflectivity-temperature HID also reveals bulk microphysical structures within a storm, the polarimetric variables enable the distinction between frozen hydrometeors, such as graupel and vertically aligned ice, and alter the identification of hydrometeors by 20-34% compared to just using temperature and reflectivity.

Table 3.1: Scattering simulation inputs for the T-matrix model for monodisperse rain studies.

HID	Type	a/b	Temp (°C)	D_{min} (mm)	D_{max} (mm)	Δd
RAIN	Rain	CB90, PP71, J83, GC84, BC87	10	0.5	10	0.05

Table 3.2: Scattering simulation inputs for the Mueller-matrix model for monodisperse rain studies.

HID	θ_m(°)	σ(°)	Distribution type	D_0	Elevation Angle (°)	n_0 ($cm^{-1}\ m^{-3}$)	#
RAIN	0	4	MONO	0.05,0.1,0.15,0.2, 0.25,0.3,0.35,0.4, 0.45,0.5,0.55,0.6, 0.65,0.7,0.75,0.8, 0.85,0.9,0.95, 1.0	1,10,20,30, 40,45,50,60, 70,80,90	80000	1100

Table 3.3: Summary of hydrometeor identification algorithms applied in this study.

HID algorithm	Description	Hydrometeor types included	Radar data used	Source
CSUHIDS 6	Original S-band MBFs	DZ, RN, DS, LDG, HDG, VI	KOUN	Tessendorf et al. (2005), Straka et al. (2000), Carey and Rutledge (1998), Liu and Chandrasekar (2000)
SS7	Theoretically-based S-band HID	DZ, RN, AG, CR, LDG, HDG, VI	KOUN	Theoretical simulations of hydrometeors at 11 cm described in Section 2.3
ZTS	Fuzzy-logic based reflectivity and temperature classification	DZ, RN,AG, CR, LDG, HDG, VI	KOUN	Same as SS7, but without Z_{dr}, K_{dp}, and ρ_{hv}
CS7	Theoretically-based X-band HID	DZ, RN, AG, CR, LDG, HDG, VI	CASA	Theoretical simulations of hydrometeors at 3.2 cm described in Section 2.3
ZTX	Fuzzy-logic based reflectivity and temperature classification	DZ, RN, DS, LDG, HDG, VI	CASA	Same as CS7, but without Z_{dr}, K_{dp}, and ρ_{hv}

Table 3.4: Rain ranges for simulations (SIM) and final HID (MBF) for S- and X-band, as well as S-band ranges reported by CSUHID and S00.

	DBZ		Z_{dr}		K_{dp}		ρ_{hv}	
	Min	Max	Min	Max	Min	Max	Min	Max
XSIM	25	59	0.07	3.6	0.004	25.5	0.983	1.0
SSIM	26	57	0.07	3.1	0.001	7.35	0.983	1.0
S00	28	60	0.7	6	0.03	6	0.95	1.0
XMBF	25	59	0.1	5.6	0.0	25.5	0.98	1.0
SMBF	26	57	0.1	5.1	0.0	7.4	0.98	1.0
CSUHID	24	61	0.6	7.4	0.05	5.95	0.945	1.0

Table 3.5: Drizzle ranges for simulations (SIM) and final HID (MBF) for S- and X-band, as well as S-band ranges reported by CSUHID and S00.

	DBZ		Z_{dr}		K_{dp}		ρ_{hv}	
	Min	Max	Min	Max	Min	Max	Min	Max
XSIM	-27	31	0.0	0.9	0.0	0.06	0.993	1.0
SSIM	-27	31	0.0	0.7	0.0	0.02	0.997	1.0
S00	0	28	0.0	0.7	0.0	0.03	0.97	1.0
XMBF	-27	31	0.0	0.9	0.0	0.06	0.985	1.0
SMBF	-27	21	0.0	0.7	0.0	0.02	0.99	1.0
CSUHID	-28	28	0.05	0.65	-0.1	0.1	0.965	1.0

Table 3.6: Aggregate ranges for simulations (SIM) and final HID (MBF) for S- and X-band, as well as S-band ranges reported by CSUHID and S00.

	DBZ		Z_{dr}		K_{dp}		ρ_{hv}	
	Min	Max	Min	Max	Min	Max	Min	Max
XSIM	-0.3	33	0.0	1.3	0.0	0.3	0.9979	1.0
SSIM	-0.1	35	0.0	1.3	0.0	0.1	0.998	1.0
S00	--	<35	0.0	1.0	0.0	0.2	0.95	1.0
XMBF	-1.0	33	0.0	1.4	0.0	0.4	0.978	1.0
SMBF	0	34	0.0	1.2	0.0	0.08	0.978	1.0
CSUHID*	-35	35	-0.1	6.1	-0.05	0.65	0.945	1.0

* Values given are for a Dry Snow category which includes both ice crystals and aggregates.

Table 3.7: Ice crystal ranges for simulations (SIM) and final HID (MBF) for S- and X-band, as well as S-band ranges reported by CSUHID and S00.

	DBZ		Z_{dr}		K_{dp}		ρ_{hv}	
	Min	Max	Min	Max	Min	Max	Min	Max
XSIM	-25	19	0.6	5.8	0.0	0.3	0.9635	0.9998
SSIM	-25	19	0.6	5.7	0.0	0.1	0.9636	0.9998
S00	--	<35	0.0	6.0	0.0	0.6	0.95	1.0
XMBF	-25	19	0.6	5.8	0.0	0.3	0.97	1.0
SMBF	-25	19	0.0	5.8	0.0	0.09	0.98	1.0
CSUHID*	-35	35	-0.1	6.0	-0.05	0.65	0.945	1.0

* Values given are for a Dry Snow category which includes both ice crystals and aggregates.

Table 3.8: LDG ranges for simulations (SIM) and final HID (MBF) for S- and X-band, as well as S-band ranges reported by CSUHID and S00.

	DBZ		Z_{dr}		K_{dp}		ρ_{hv}	
	Min	Max	Min	Max	Min	Max	Min	Max
XSIM	14	44	-0.7	1.3	-1.4	2.8	0.999	1.0
SSIM	15	45	-0.5	1.1	-0.4	0.8	0.999	1.0
S00	20	35	-0.5	1.0	-0.5	0.5	0.95	1.0
XMBF	24	44	-0.7	1.3	-1.4	2.8	0.985	1.0
SMBF	25	45	-0.5	1.1	-0.4	0.8	0.99	1.0
CSUHID	30	46	-0.5	1.00	-0.5	0.5	0.955	1.0

Table 3.9: HDG ranges for simulations (SIM) and final HID (MBF) for S- and X-band, as well as S-band ranges reported by CSUHID and S00.

	DBZ		Z_{dr}		K_{dp}		ρ_{hv}	
	Min	Max	Min	Max	Min	Max	Min	Max
XSIM	31	55	-1.3	3.7	-2.5	7.6	0.992	1.0
SSIM	32	57	-0.9	2.9	-0.6	1.7	0.996	1.0
S00	30	50	-0.5	2.0	0.0	1.5	0.95	1.0
XMBF	32	54	-1.3	3.7	-2.5	7.6	0.965	1.0
SMBF	32	58	-0.9	2.9	-0.6	1.7	0.975	1.0
CSUHID	40	55	-0.5	3.0	-0.5	2.0	0.94	1.0

Table 3.10: Vertical ice ranges for simulations (SIM) and final HID (MBF) for S- and X-band, as well as S-band ranges reported by CSUHID and S00.

	DBZ		Z_{dr}		K_{dp}		ρ_{hv}	
	Min	Max	Min	Max	Min	Max	Min	Max
XSIM	-25	17	-2.1	-0.3	-0.1	0.0	0.9518	0.9983
SSIM	-25	18	-2.1	-0.3	-0.04	0.0	0.9517	0.9982
S00	--	<35	-0.5	0.5	-0.6	0.0	0.95	1.0
XMBF	-25	32	-2.1	0.5	-0.15	0.0	0.93	1.0
SMBF	-26	32	-2.1	0.5	-0.04	0.0	0.93	1.0
CSUHID	-35	35	-0.5	0.5	-1.0	-0.25	0.945	1.0

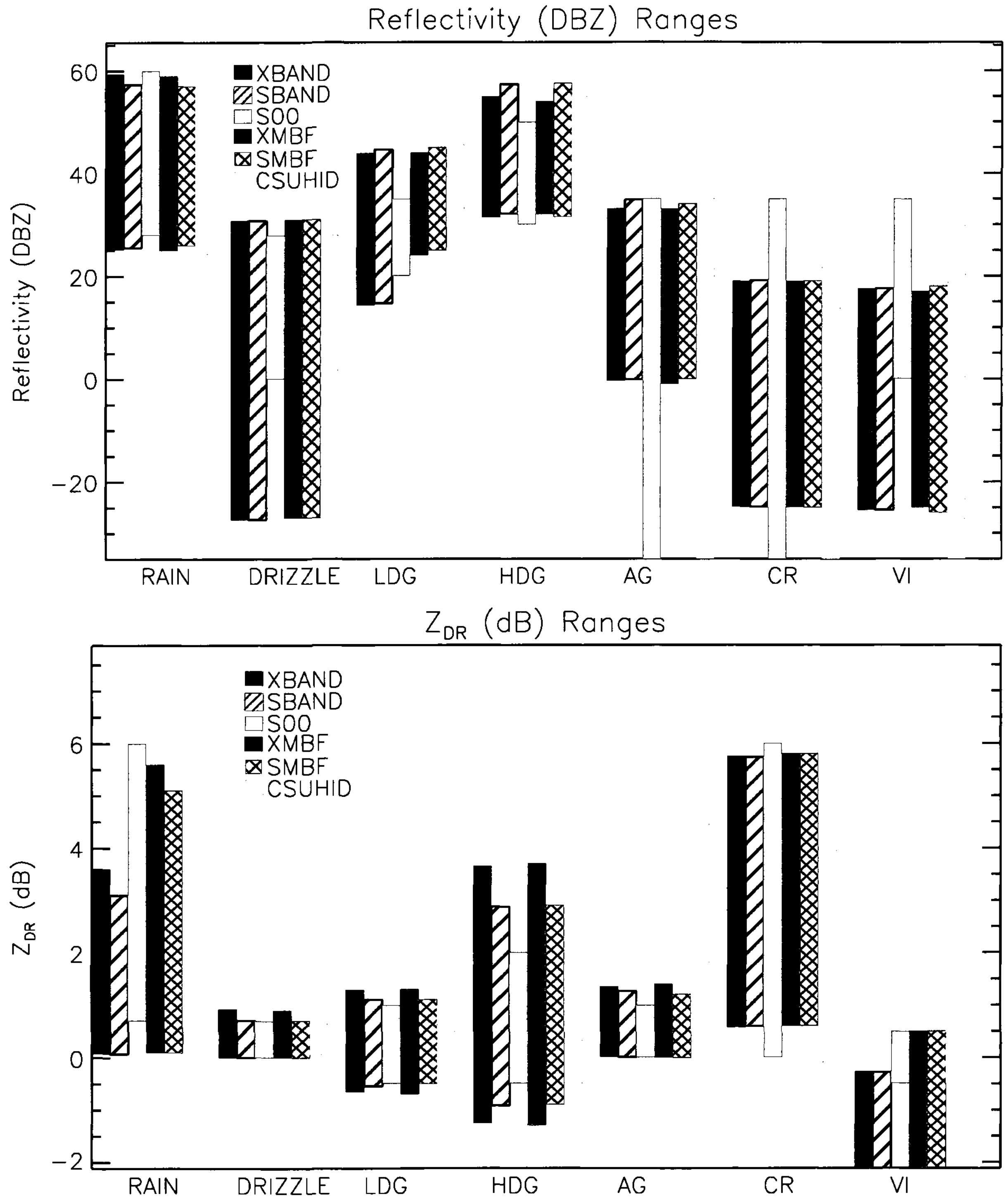

Fig. 3.1: Variable range derived from scattering simulations for six different hydrometeor types for a) reflectivity and b) differential reflectivity. Ranges for XMBF, SMBF, and CSUHID are discussed in Section 3.3.1. Note: CSUHID values for AG and CR are both taken from the DS category. Shades of gray from left to right correspond to the legend values from top to bottom.

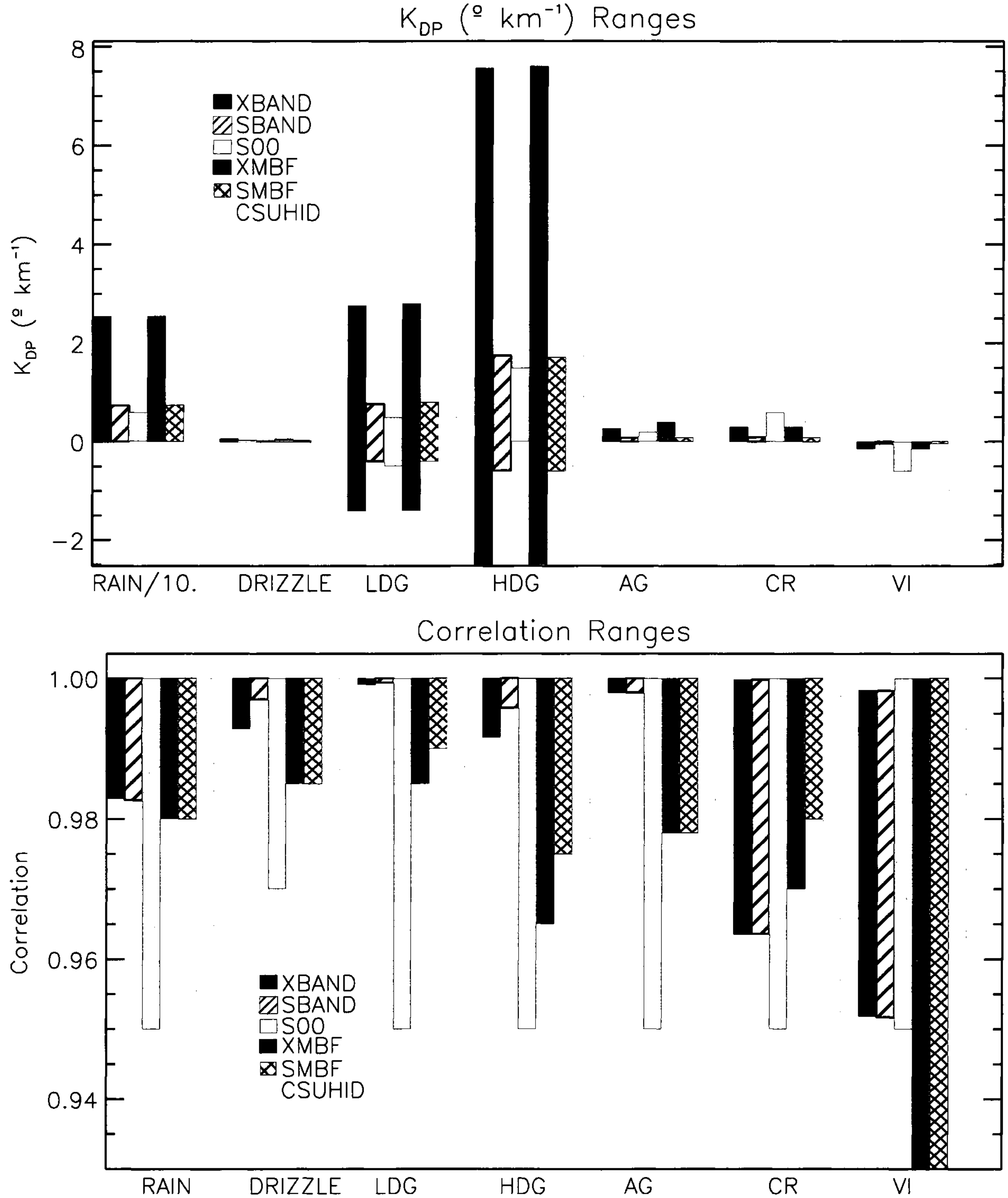

Fig. 3.1 (continued): c) specific differential phase and d) correlation coefficient. Values of K_{dp} for rain are divided by 10.

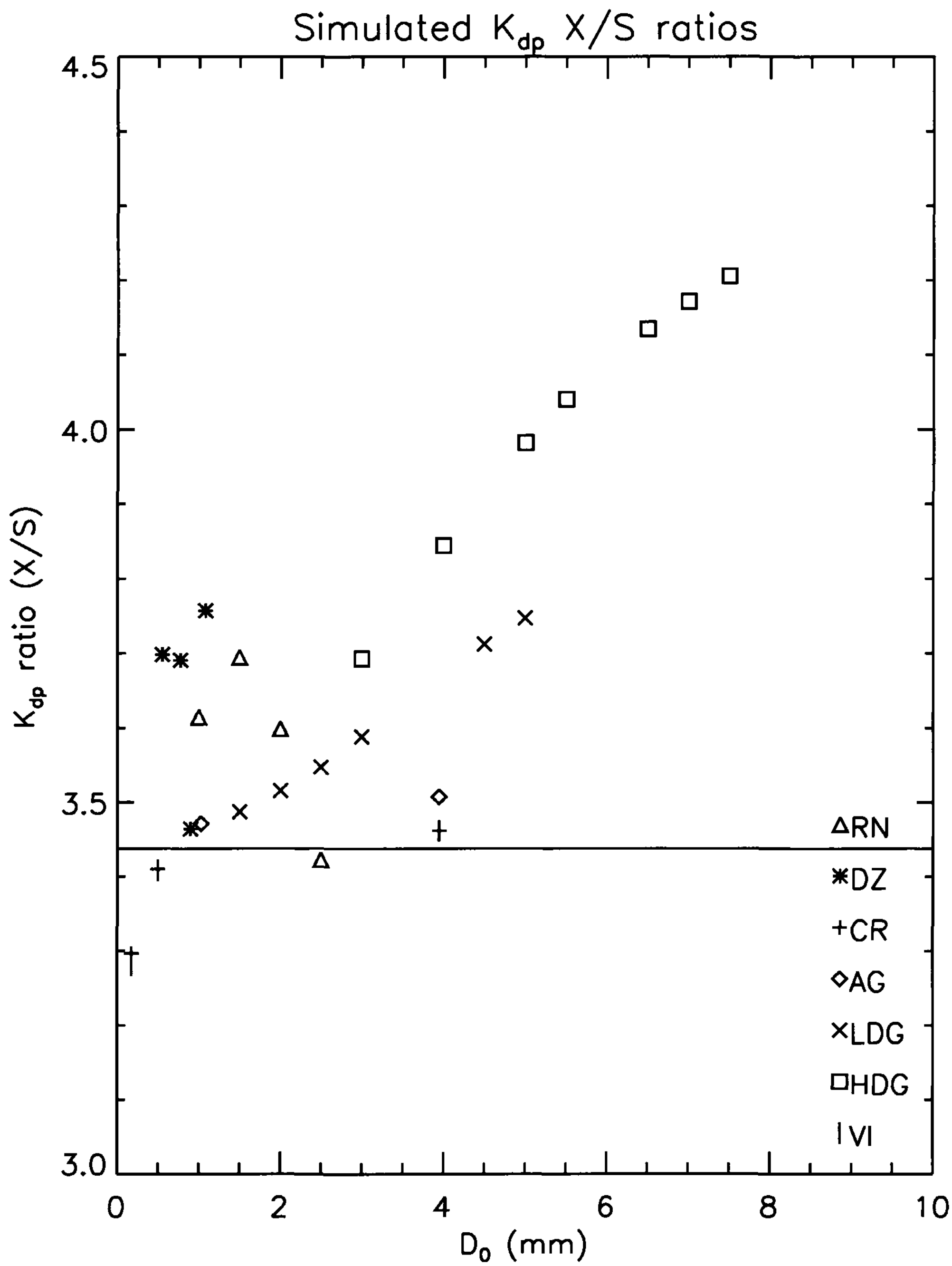

Fig. 3.2: Simulated K_{dp} ratios (X/S) between X-band and S-band for the seven hydrometeor categories as a function of median drop diameter. The thick black line denotes the 3.43 ratio expected by pure wavelength scaling.

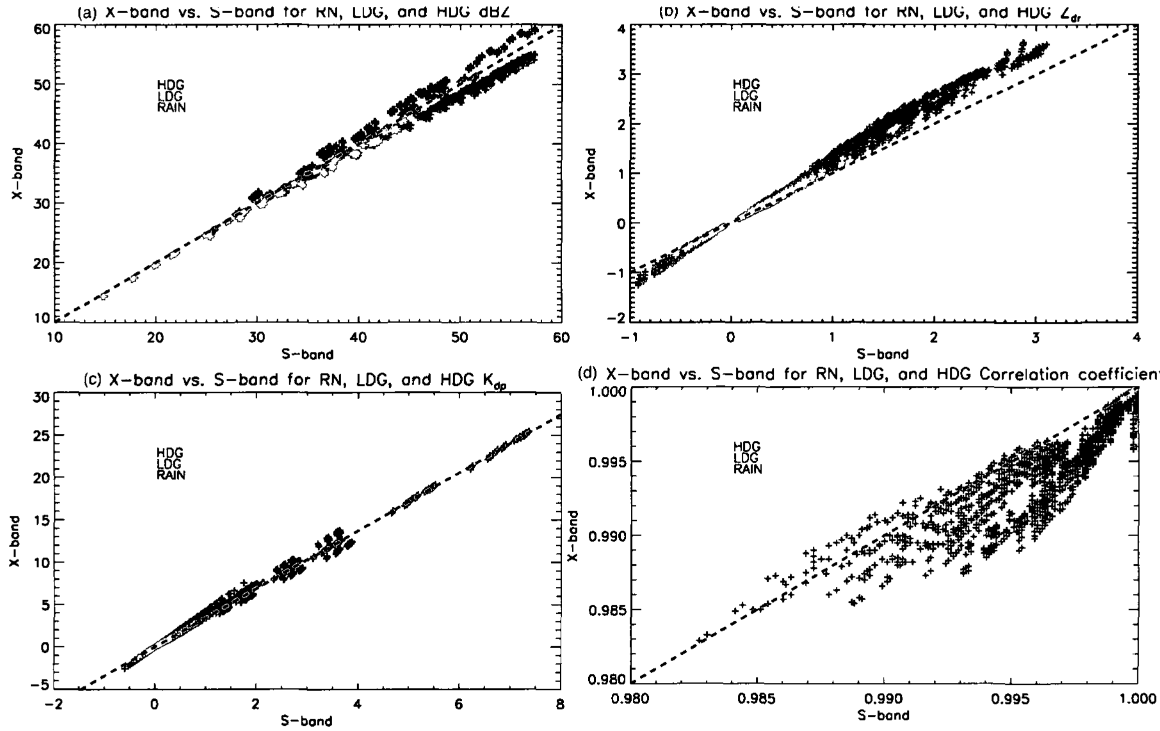

Fig. 3.3: S-band and X-band comparisons for scattering simulations of rain (blue), low-density graupel (green) and high-density graupel (red) for a) DZ, b) Z_{dr}, c) K_{dp} and d) ρ_{hv}. The dashed black line denotes a 1:1 relationship; in the case of K_{dp} it represents 1:3.43, which would be the expected relationship due to wavelength scaling.

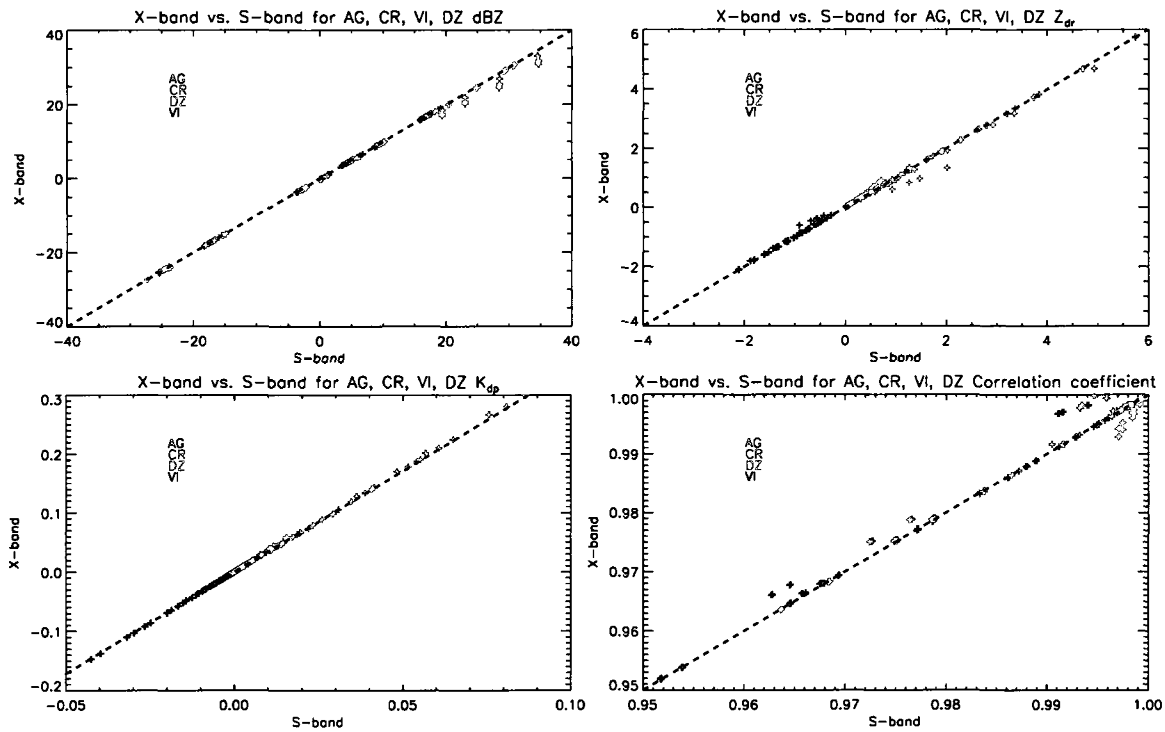

Fig. 3.4: S-band and X-band comparisons for scattering simulations of drizzle (blue), aggregates (red), ice crystals (green), and vertically aligned ice crystals (purple) for a) DZ, b) Z_{dr}, c) K_{dp} and d) ρ_{hv}. The dashed black line denotes a 1:1 relationship; in the case of K_{dp} it represents 1:3.43, which would be the expected relationship due to wavelength scaling.

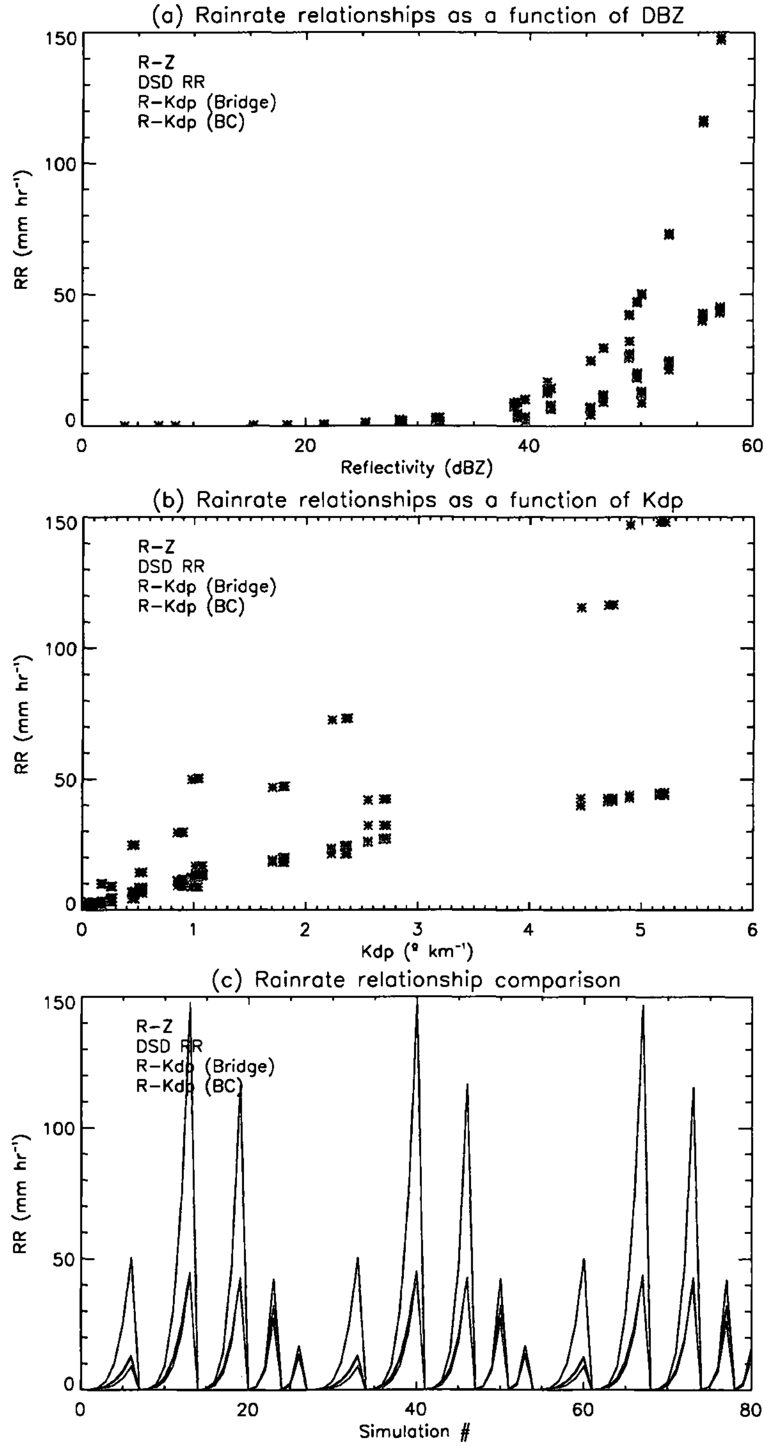

Fig. 3.5: Comparison of rainrate relationships from T-matrix simulations. a) Reflectivity versus rainrate for Z-R relationship, R-K_{dp} using the bridge-shape model ('Bridge') of Thurai et al. (2007), R-K_{dp} using the Beard and Chuang (1987) drop-shape model ('BC'), and the rainrate calculated from the drop-size distribution used in the simulations (DSD RR). b) K_{dp} versus rainrate, and c) rainrate as a function of simulation number.

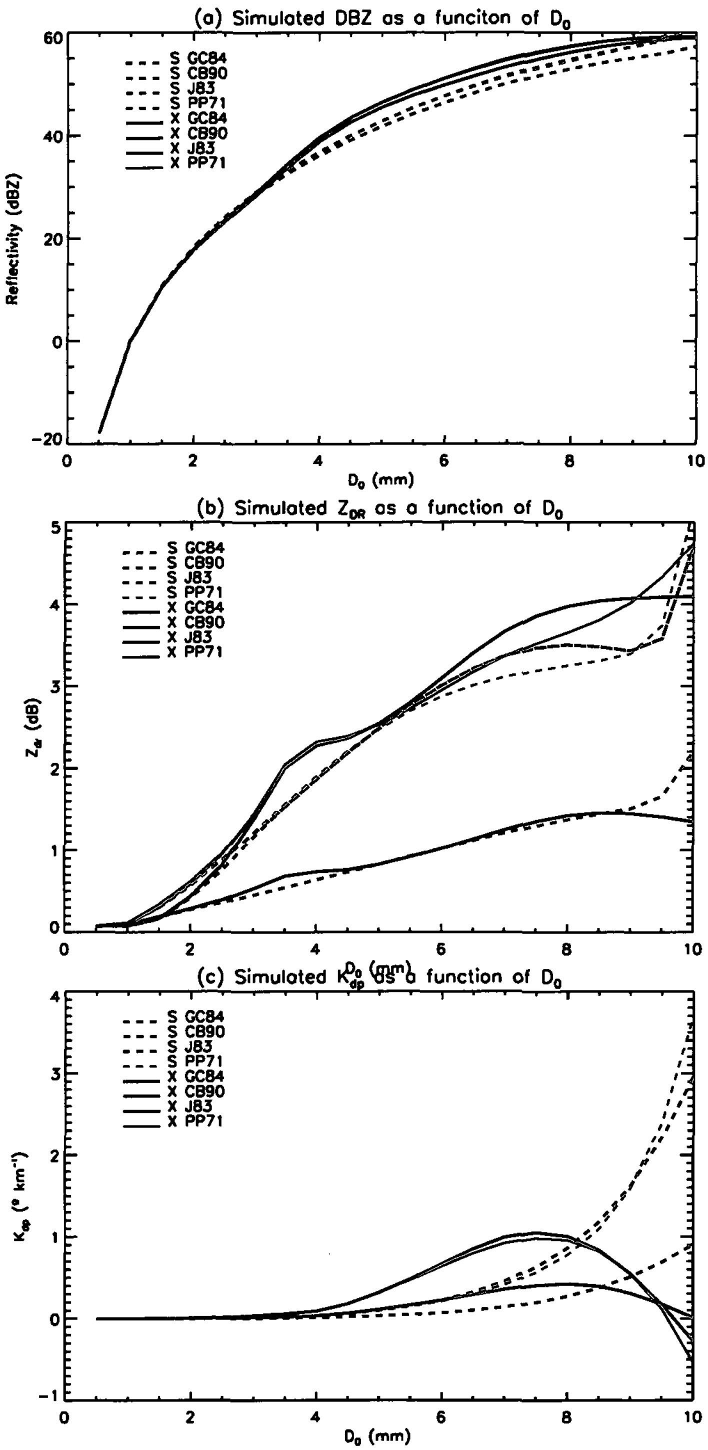

Fig. 3.6: Drop-shape model dependence of a) reflectivity, b) differential reflectivity, and c) specific differential phase both X- (solid) and S- (dashed) band as a function of mean drop diameter (D_0) for monodisperse populations of rain.

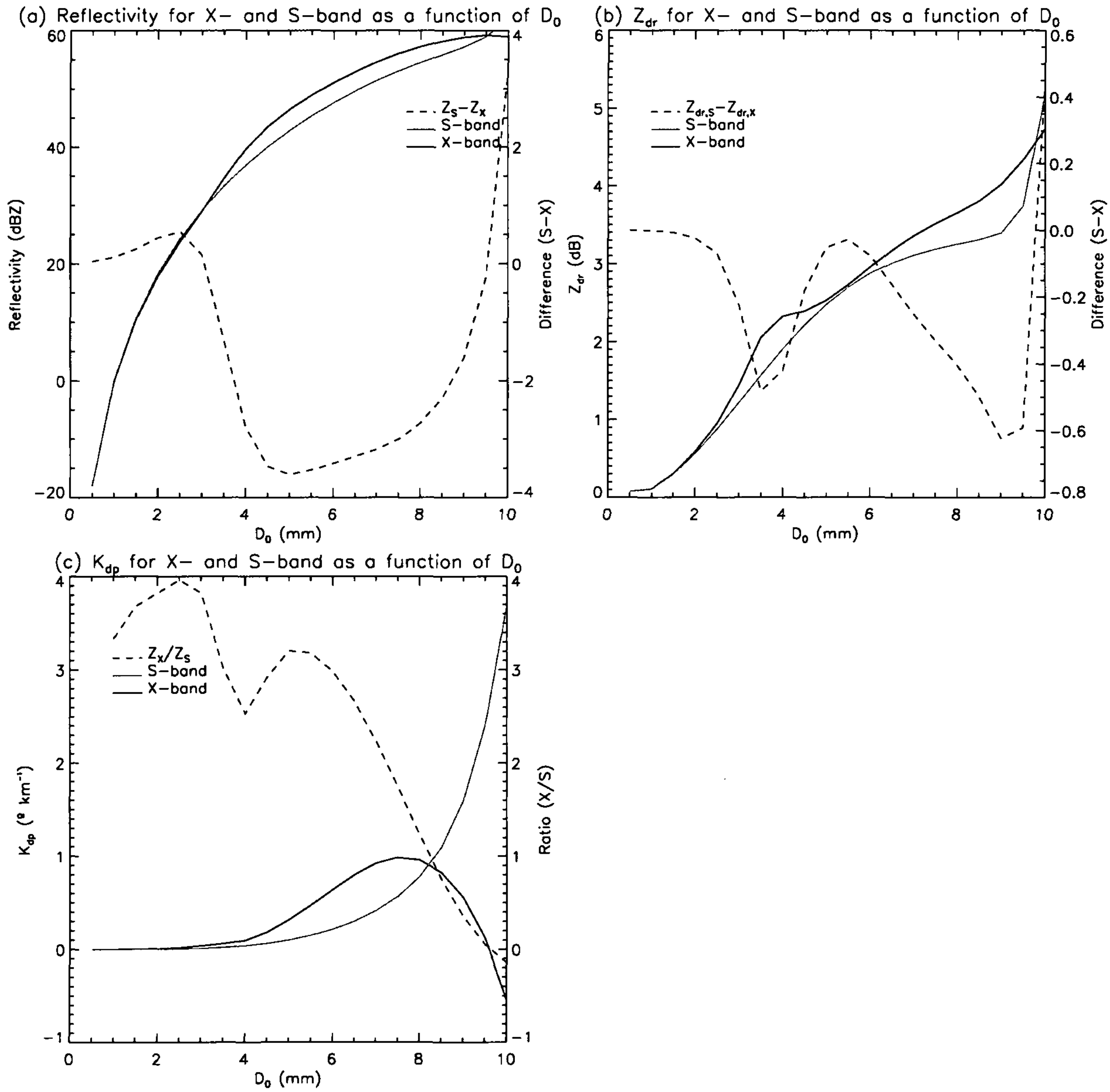

Fig. 3.7: X-band (black) and S-band (gray) simulated values as a function of drop diameter for a) reflectivity, b) Z_{dr}, and c) K_{dp} for a monodisperse population of rain drops using the GC84 shape model. The dashed line indicates the difference between S- and X-band (a and b) and the ratio of X- to S-band (c).

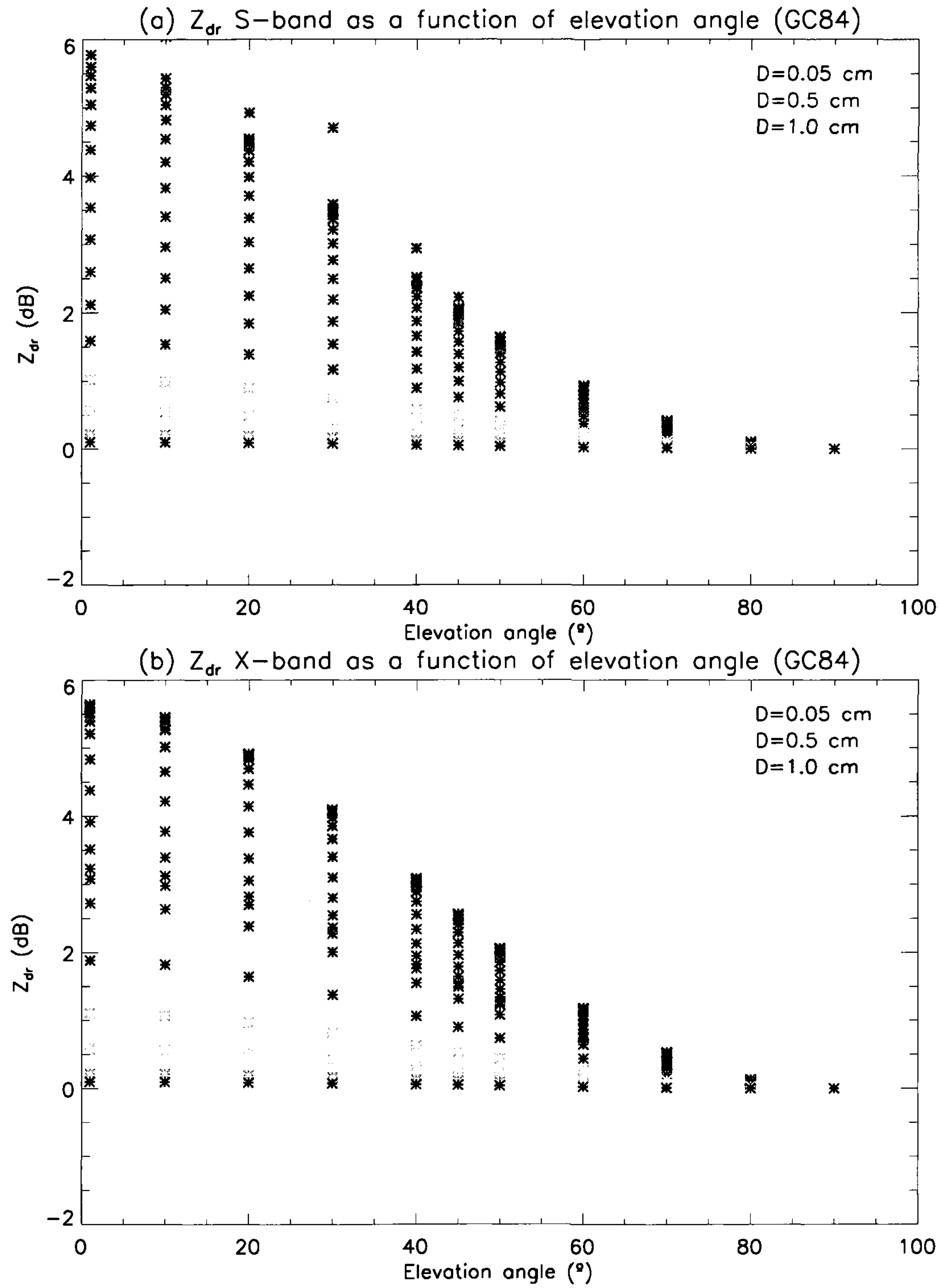

Fig. 3.8: Z_{dr} as a function of radar elevation angle for a) S-band and b) X-band. Symbol color indicates relative drop size, with warmer colors being smaller diameters and cooler colors relating to larger drop sizes. Simulations are of a mono disperse volume of rain drops. The Goddard and Cherry (1984) drop-shape model was assumed.

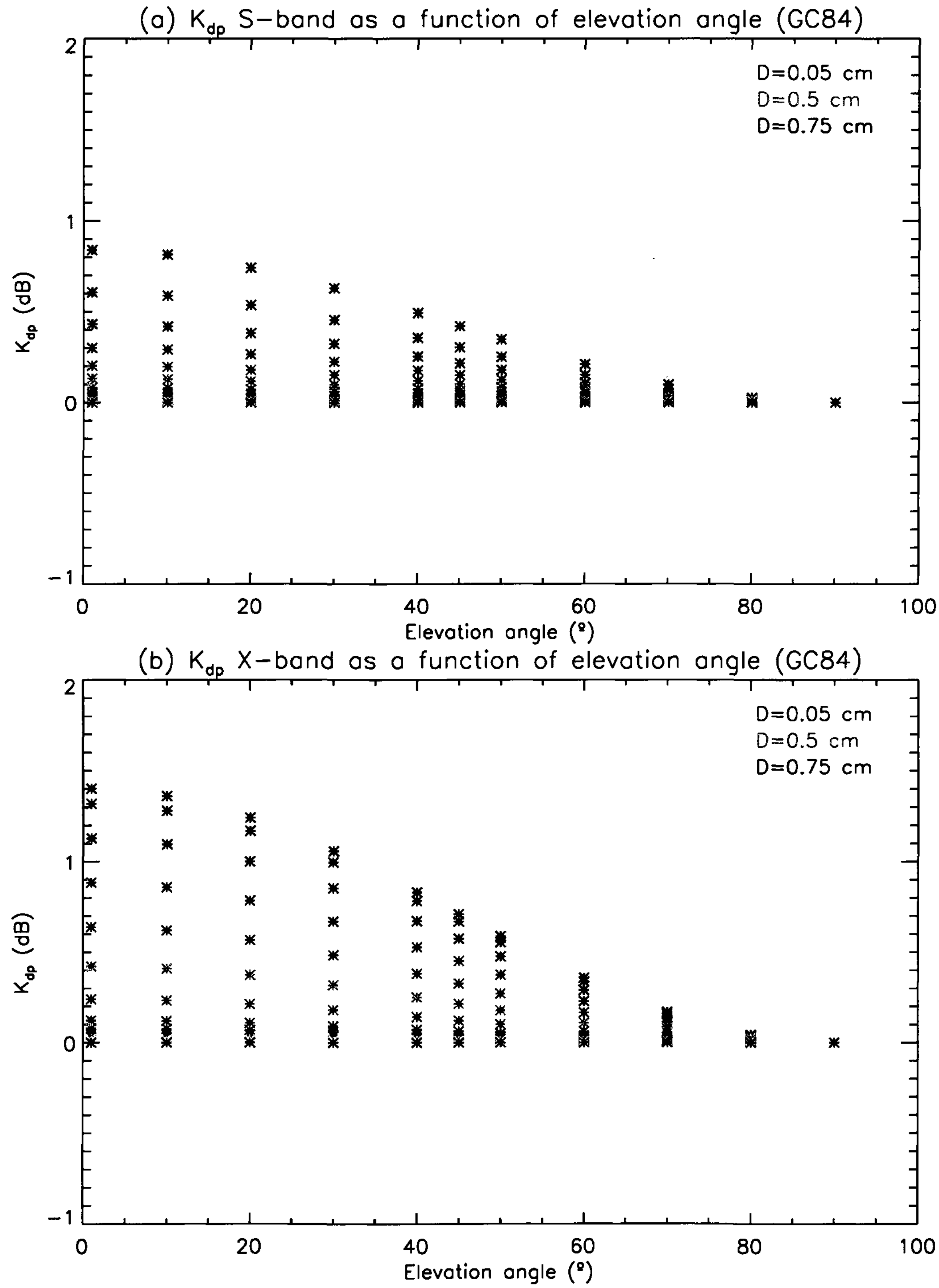

Fig 3.9: K_{dp} as a function of radar elevation angle for a) S-band and b) X-band. Symbol color indicates relative drop size, with warmer colors being smaller diameters and cooler colors relating to larger drop sizes. Simulations are of a mono disperse volume of rain drops. The Goddard and Cherry (1984) drop-shape model was assumed. Only mean diameters less than 0.8 are shown due to the non-linearities occuring at larger mean diameters (see Fig. 3.7).

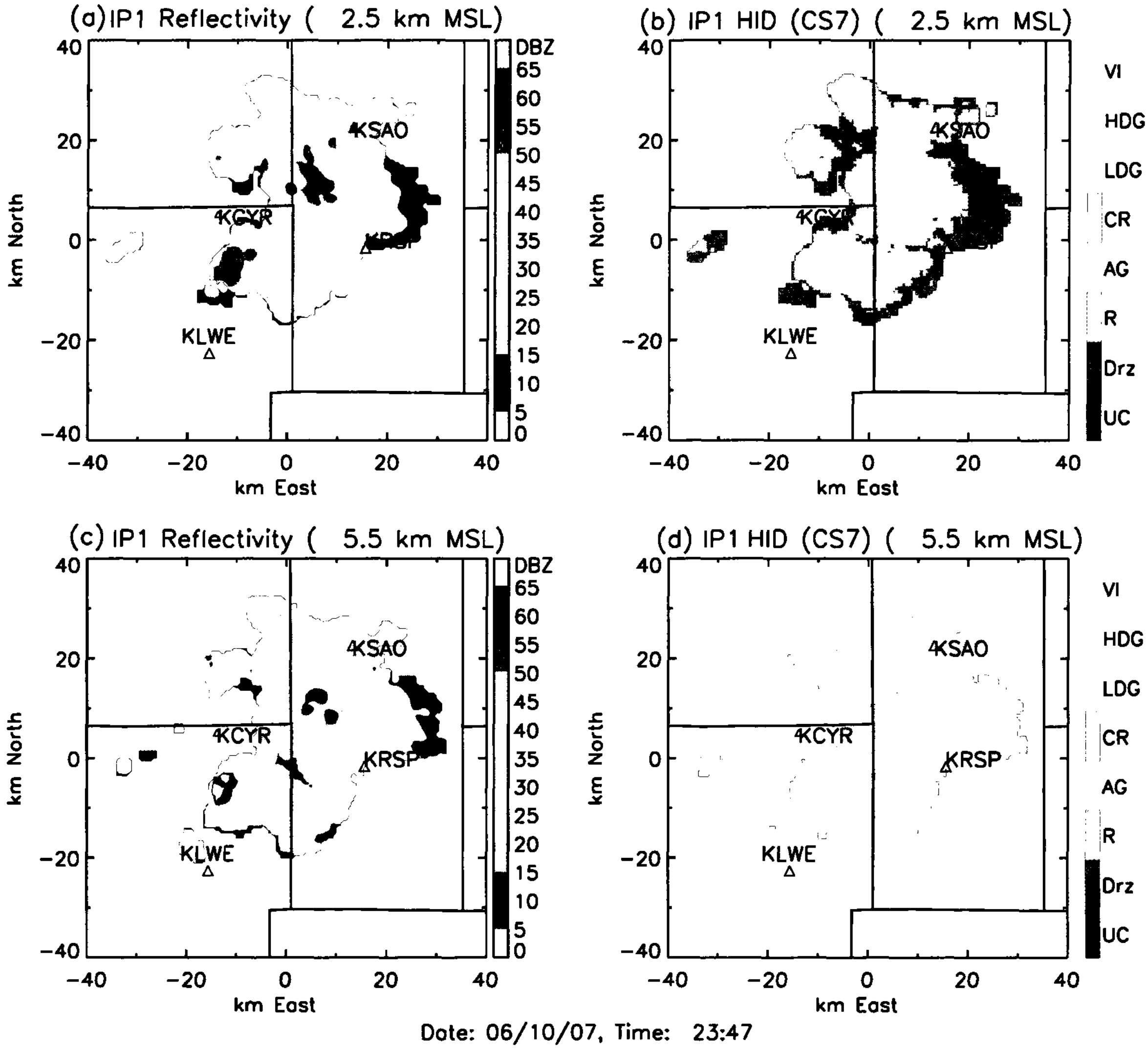

Fig. 3.10: Horizontal cross-section of mosaicked IP1 data at 2347 UTC on 10 June 2007. The upper figures (a and b) are at 2.5 km, and the lower figures (c and d) are at 5.5 km MSL. The left images (a and c) are reflectivity and the right images (b and d) are hydrometeor classifications using the X-band theoretical HID (CS7).

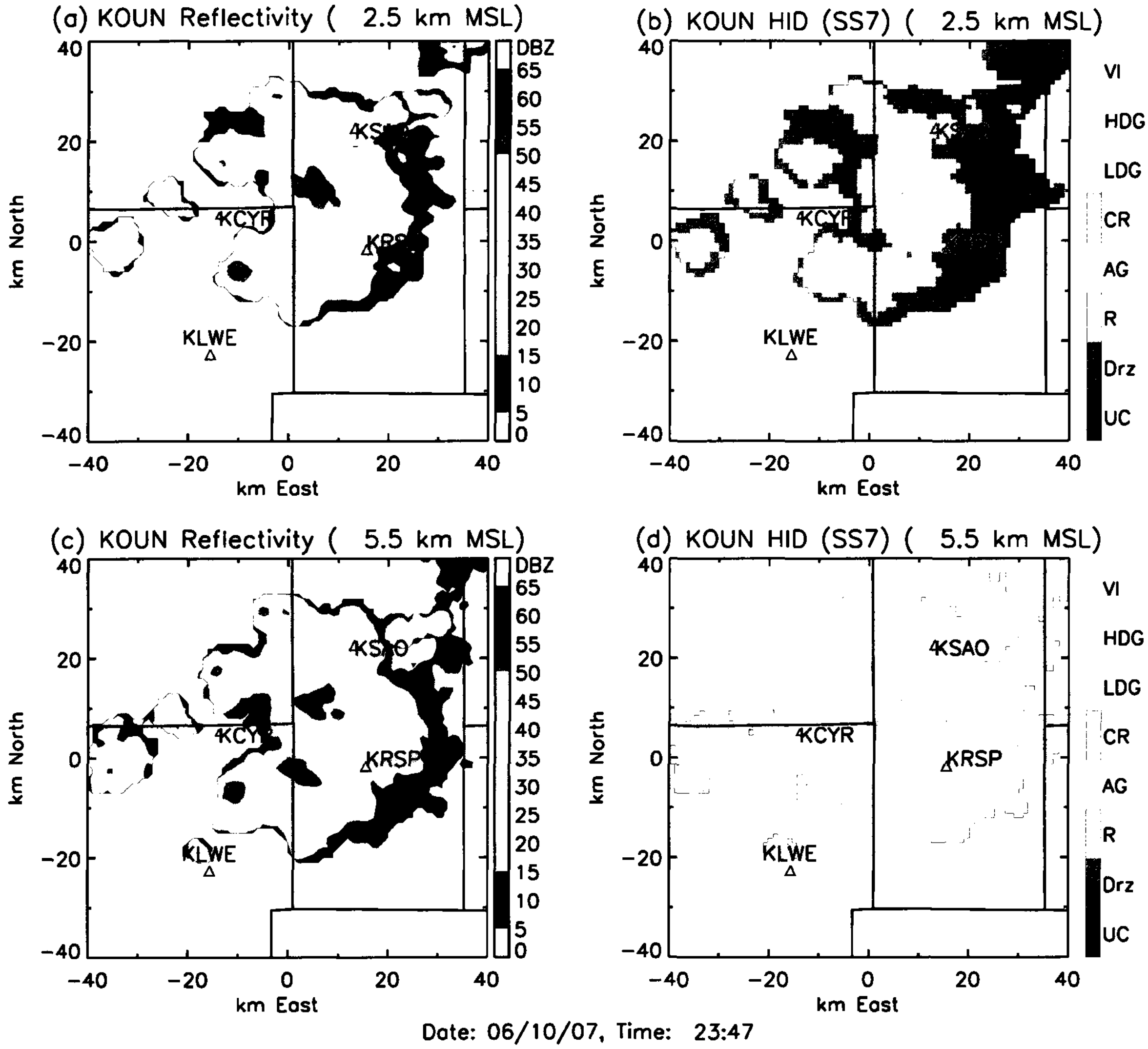

Fig. 3.11: Horizontal cross-section of mosaicked KOUN data at 2347 UTC on 10 June 2007. The upper figures (a and b) are at 2.5 km, and the lower figures (c and d) are at 5.5 km. The left images (a and c) are reflectivity and the right images (b and d) are hydrometeor classifications using the theoretical S-band HID (SS7).

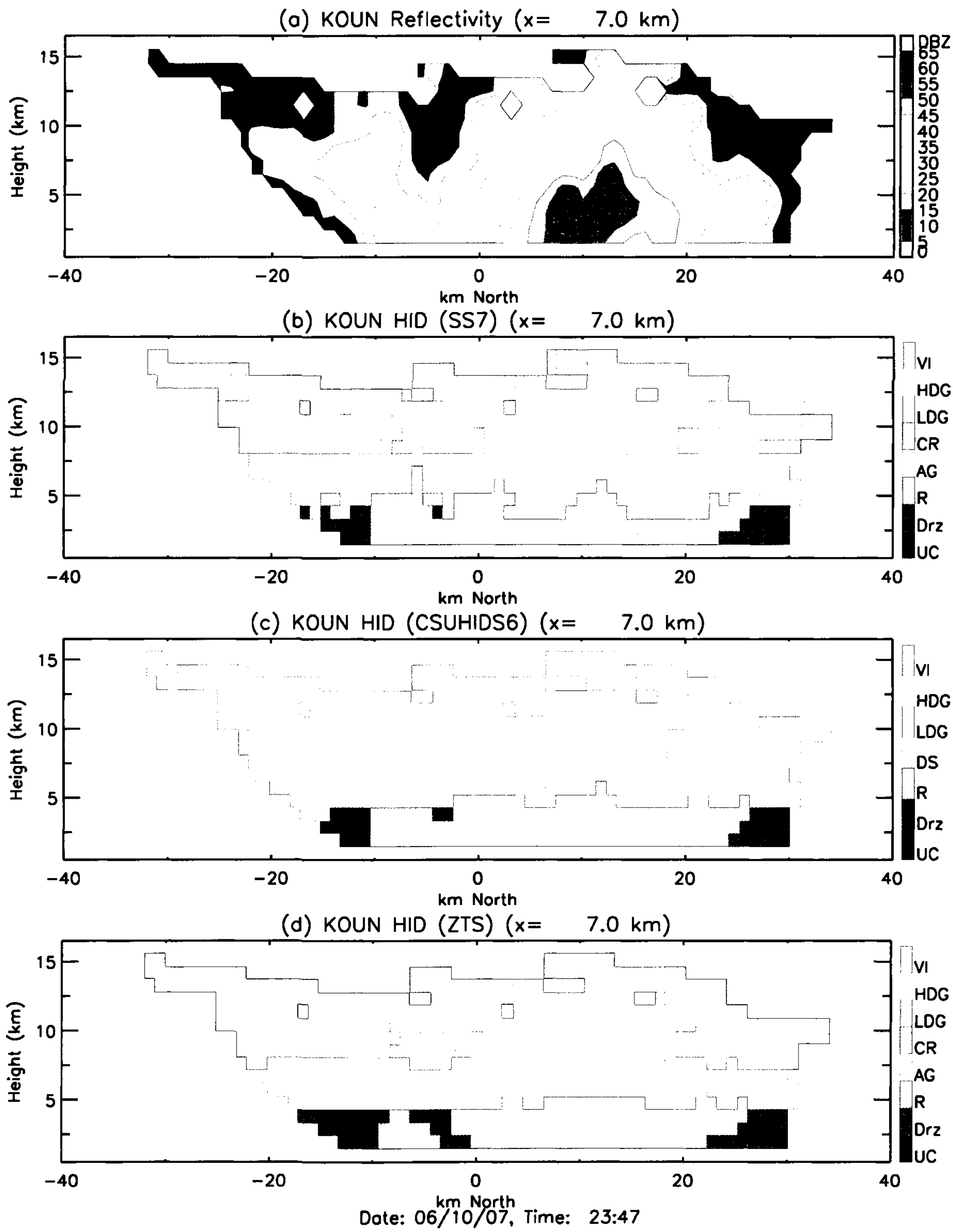

Fig. 3.12: Vertical slices at x=7.0 km through KOUN data at 2347 UTC on 10 June 2007. Cross-sections illustrate a) reflectivity, b) S-band modified theoretical HID (SS7), c) CSUHIDS 6, and d) S-band fuzzy Z-T only (ZTS).

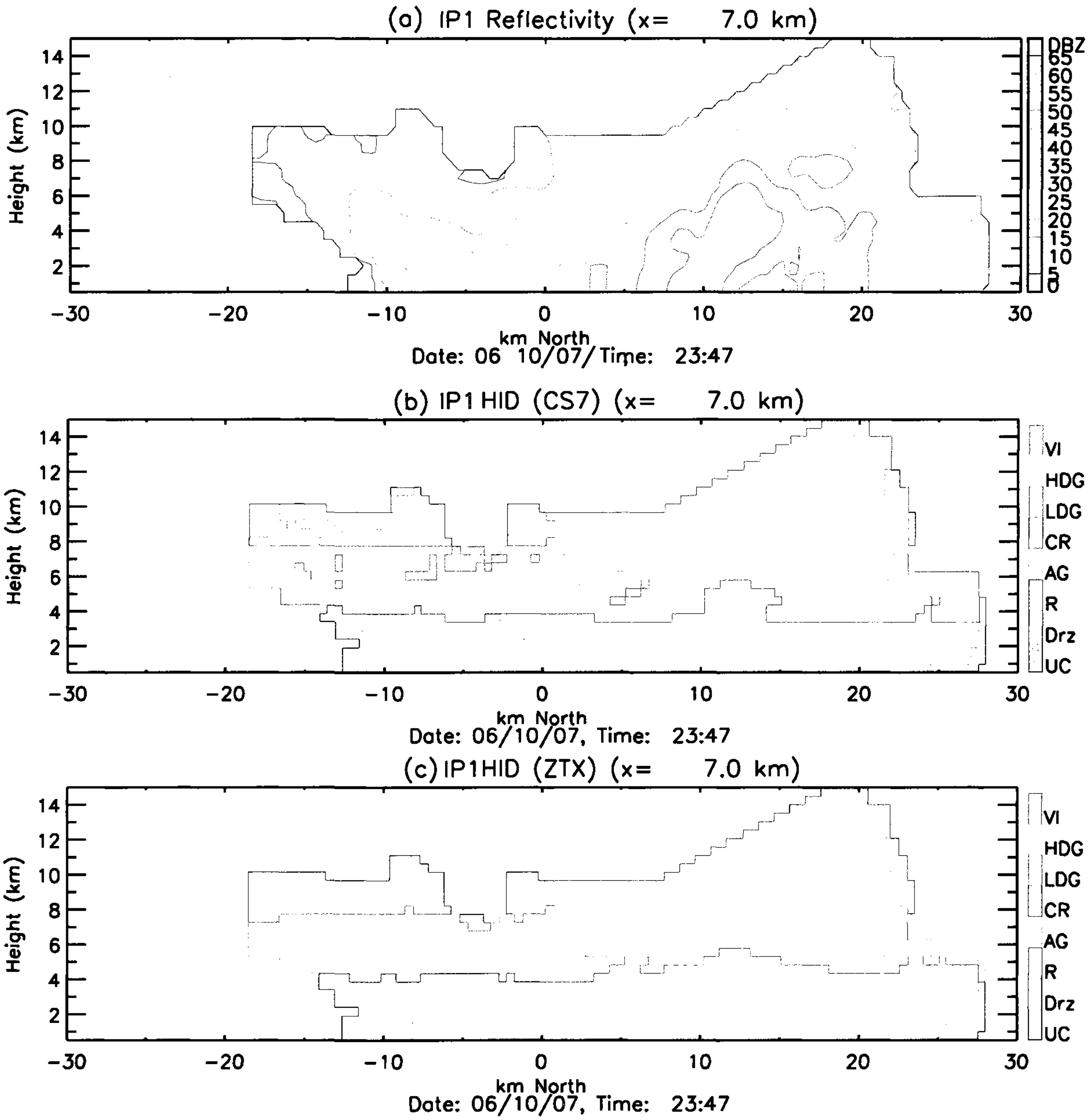

Fig. 3.13: Vertical slices at x=7.0 through mosaicked IP1 data at 2347 UTC on 10 June 2007. Cross-sections illustrate a) reflectivity, b) X-band simulated HID (CS7), and c) X-band fuzzy Z-T only HID (ZTX).

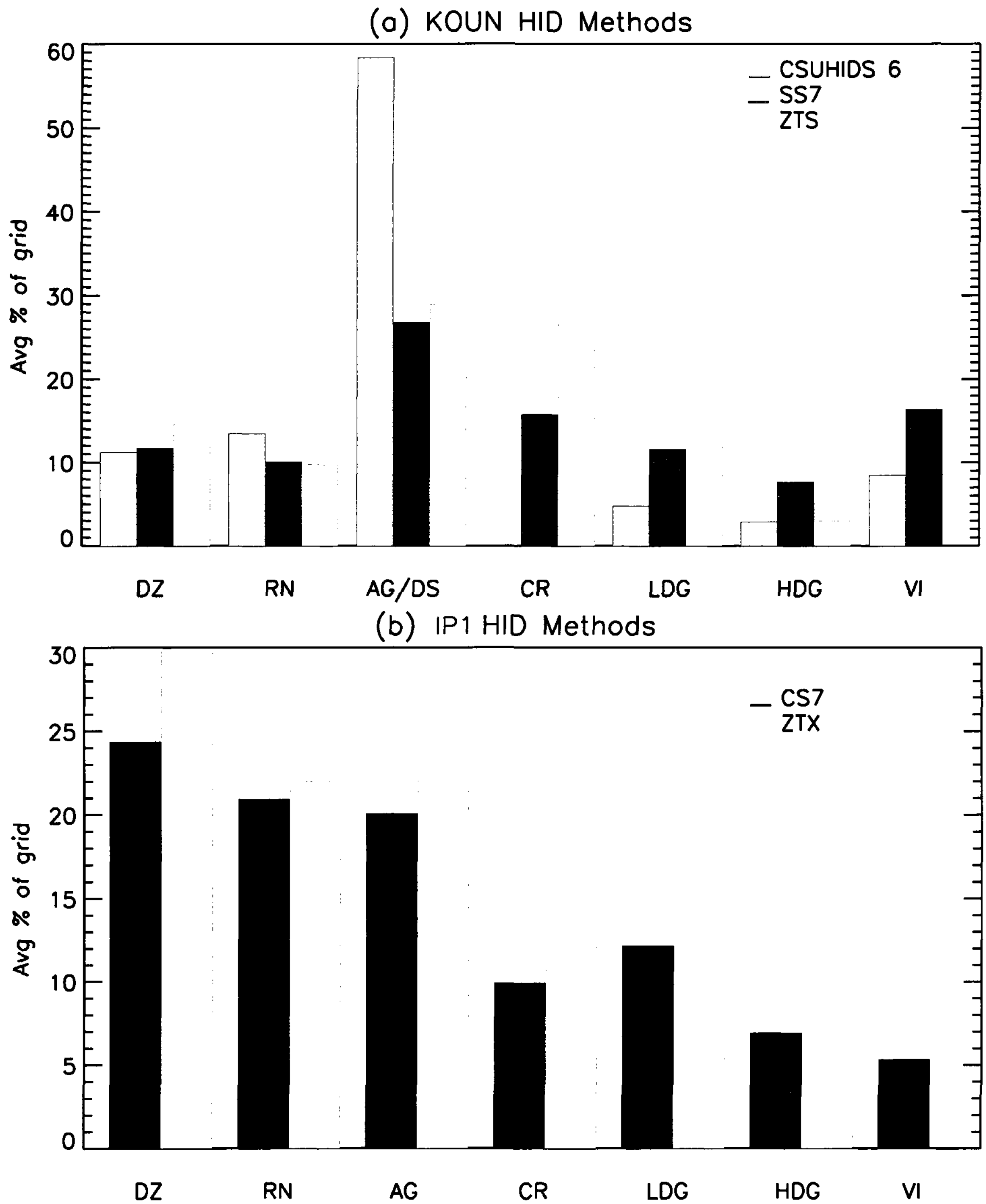

Fig. 3.14: Histograms of different HID methods applied to a) KOUN and b) IP1 data on 10 June 2007. Bars illustrate the relative percentage of the storm volume classified as each hydrometeor type averaged throughout the 2.5 hour lifetime of the storm.

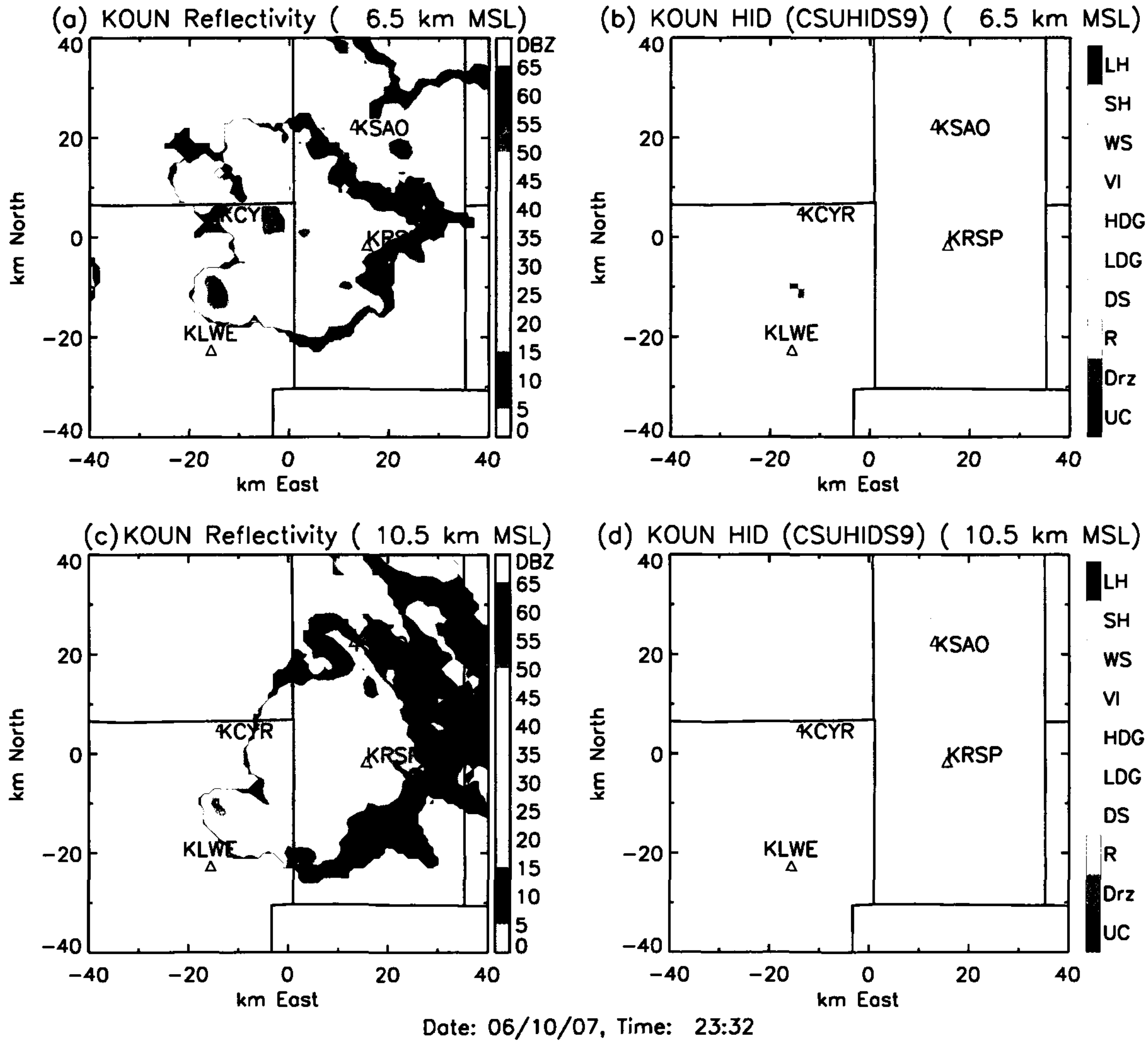

Fig. 3.15: Horizontal cross-sections of KOUN a) and c) reflectivity and b) and d) HID using CSUHIDS 9 at 2332 UTC on 10 June 2007. Upper panels are taken at 6.5 km MSL, and the lower panels at 10.5 km MSL. Note the large hail (LH) and small hail (SH) in the southwestern cell.

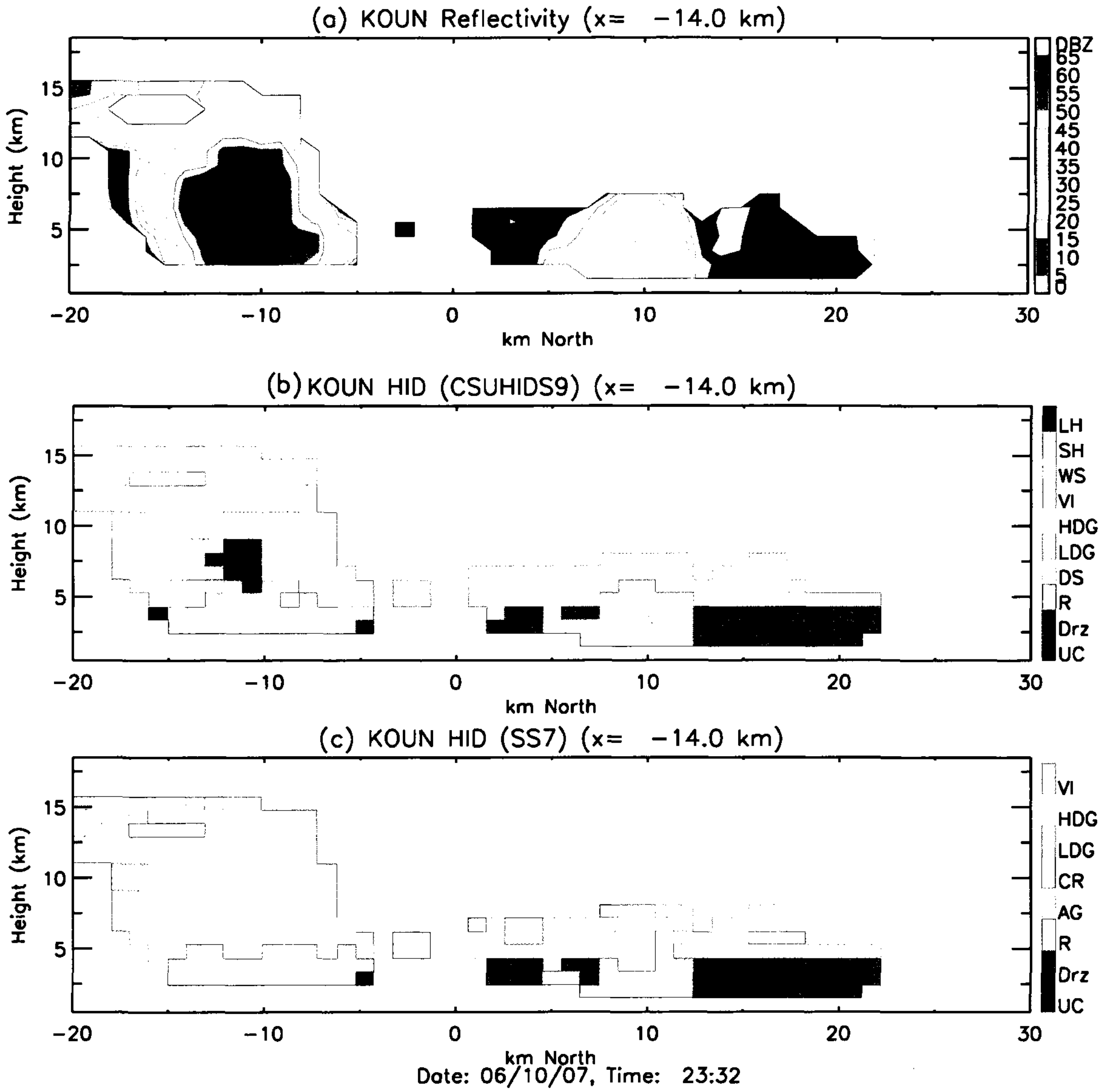

Fig. 3.16: Vertical cross-section at x=-14 km of KOUN a) reflectivity, b) HID from the CSU 9 category algorithm, and c) HID from SS7 at 2332 UTC on 10 June 2007.

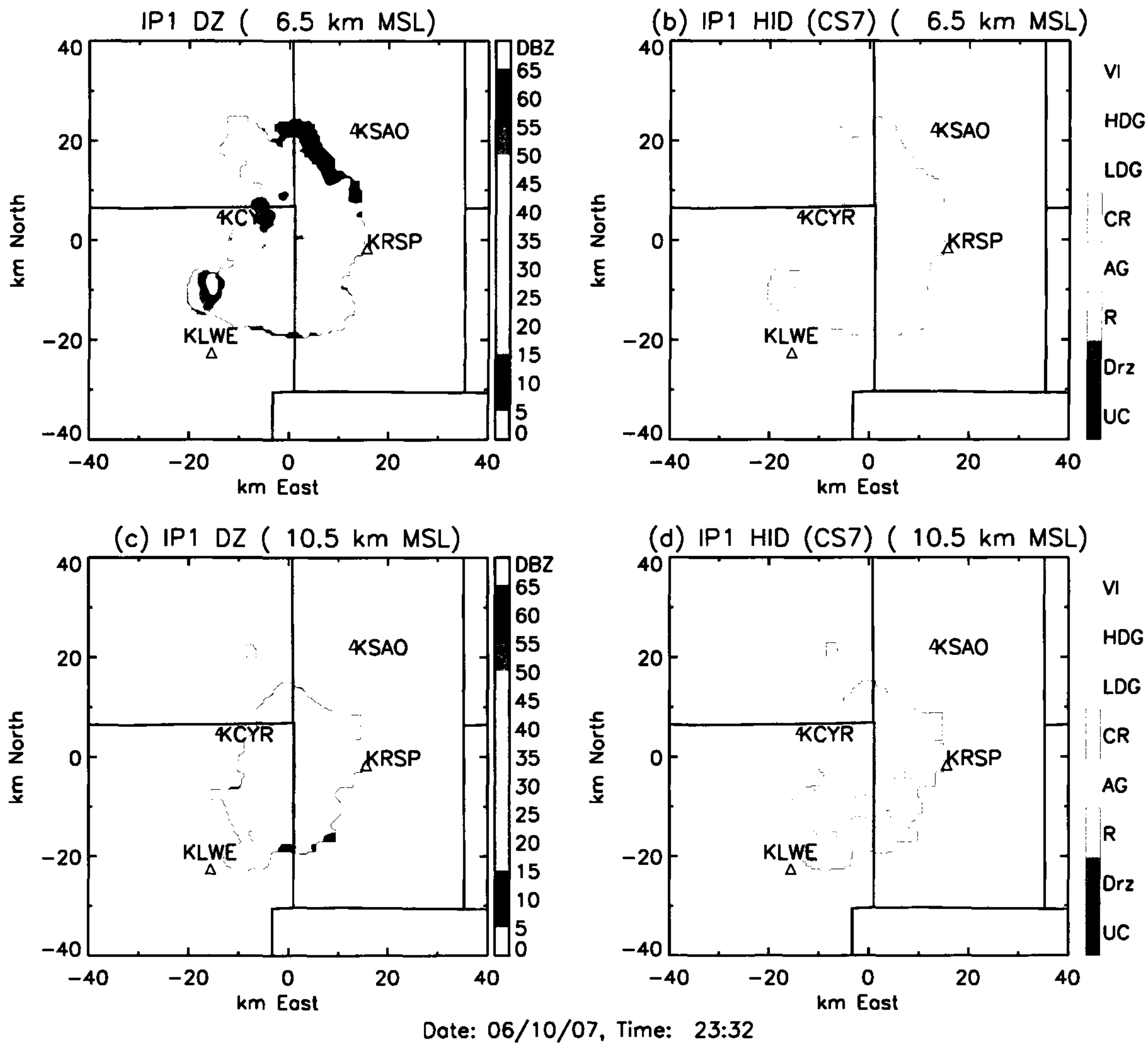

Fig. 3.17: Horizontal cross-sections of IP1 a) and c) reflectivity and b) and d) HID using CS7 HID at 2332 UTC on 10 June 2007. Upper panels are taken at 6.5 km MSL, and the lower panels at 10.5 km MSL.

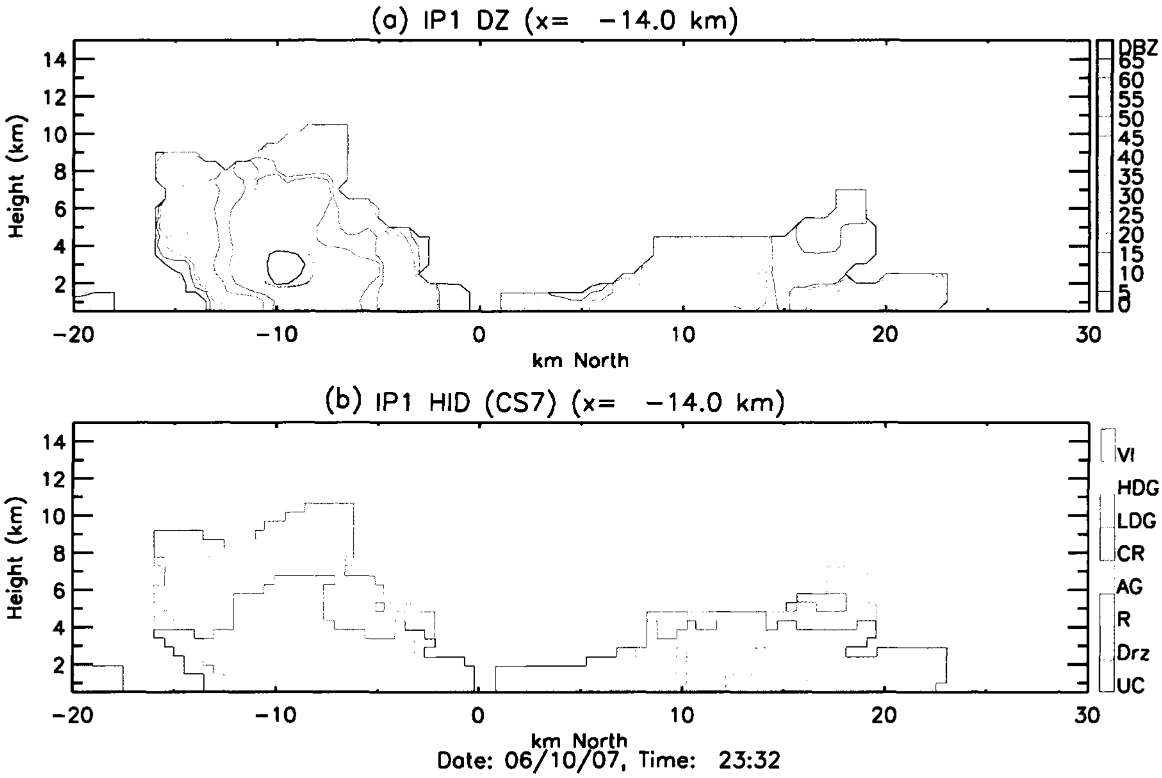

Fig. 3.18: Vertical cross-section at x=-14 km of IP1 a) reflectivity and b) HID from CS7 at 2332 UTC on 10 June 2007.

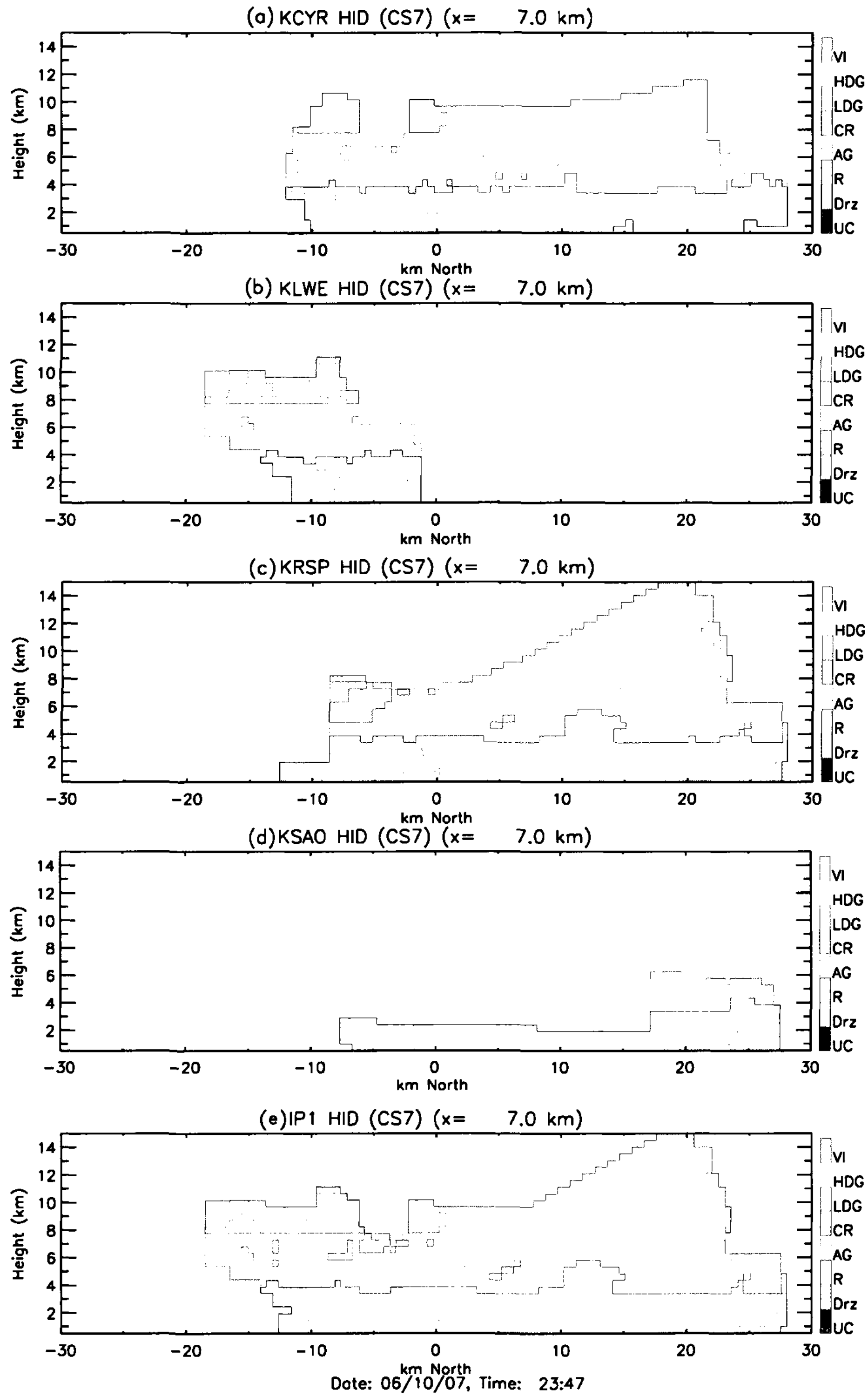

Fig. 3.19: Comparison of individual radar X-band HID (CS7) cross-section at x=7.0 km on 10 June 2007 2347 UTC for a) KCYR, b) KRSP, c) KLWE, d) KSAO and e) IP1 mosaic.

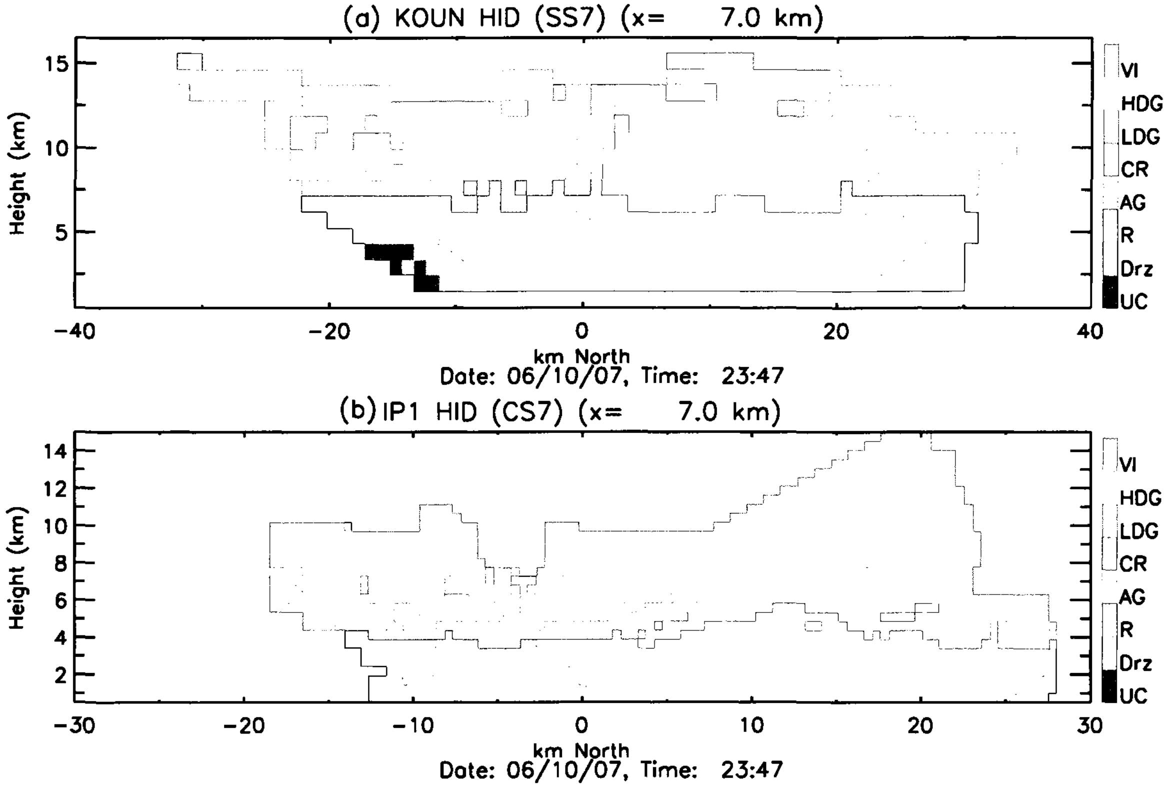

Fig. 3.20: HID classifications based on the strict ranges derived from the scattering simulations for a) KOUN (SS7) and b) IP1 (CS7).

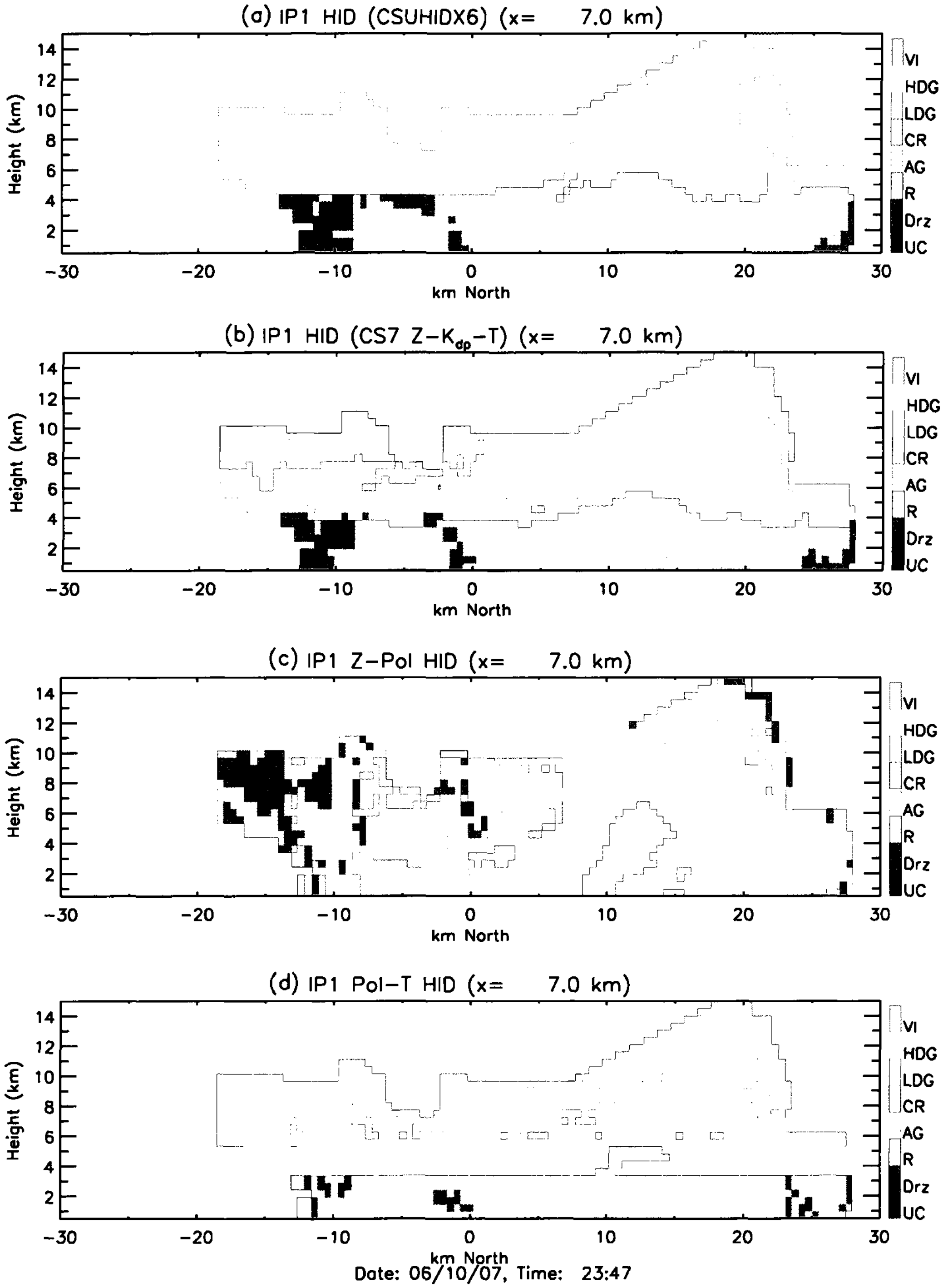

Fig. 3.21: IP1 data from 10 June 2007 at 234705 UTC for a cross-section along x=7.0 km for HID using modified boundaries from scattering simulations for a) CSUHID 6, b) using Z, K_{dp} and T only, c) X-band using only Z and the polarimetric variables (no temperature), d) using the polarimetric variables and temperature only (no reflectivity).

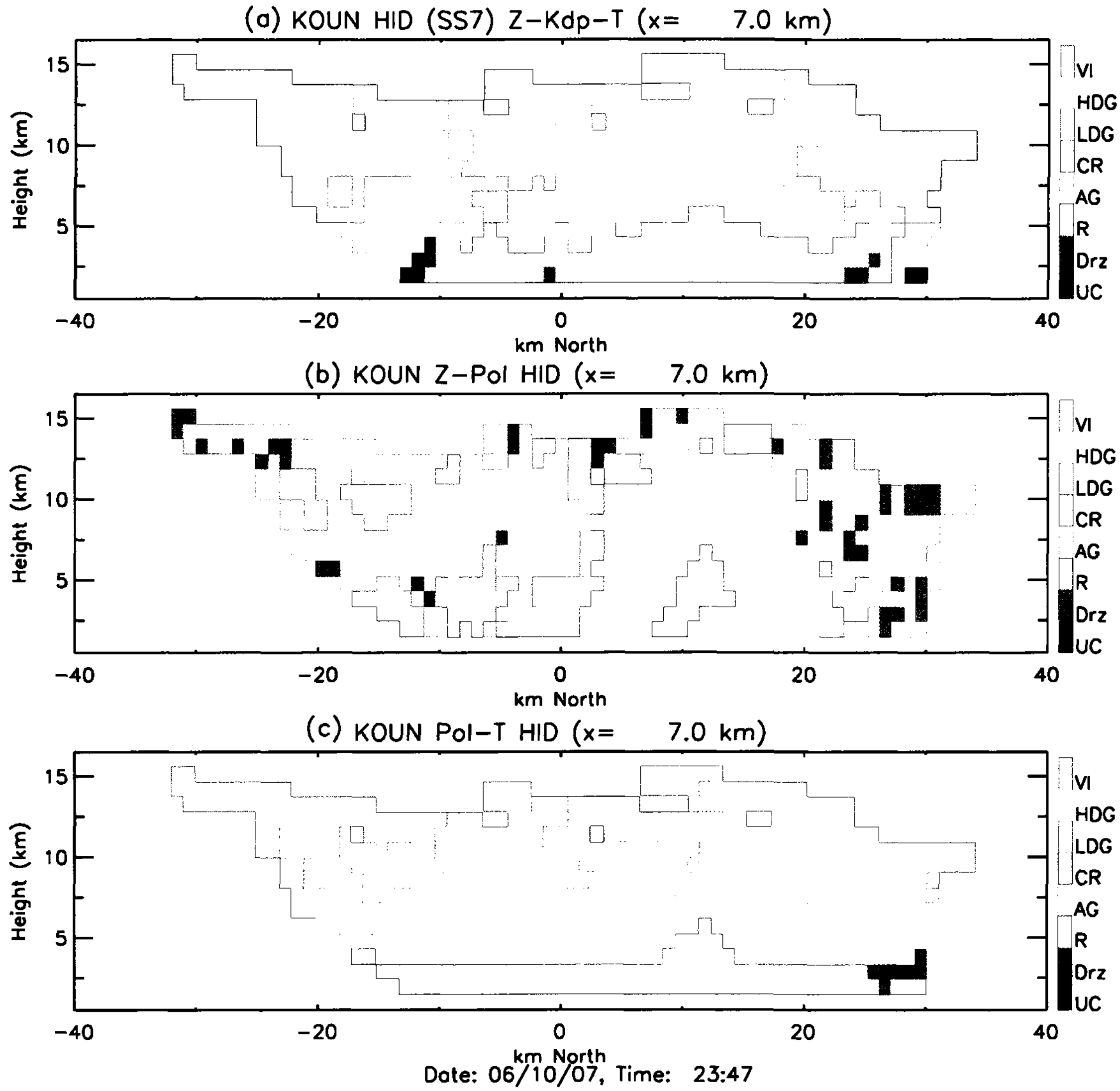

Fig. 3.22: KOUN data from 10 June 2007 at 234705 UTC for a cross-section along x=7.0 km for HID using modified boundaries from scattering simulations for a) using only Z, K_{dp} and T, b) using only Z and the polarimetric variables (no temperature), and c) using only the polarimetric variables and temperature (no reflectivity).

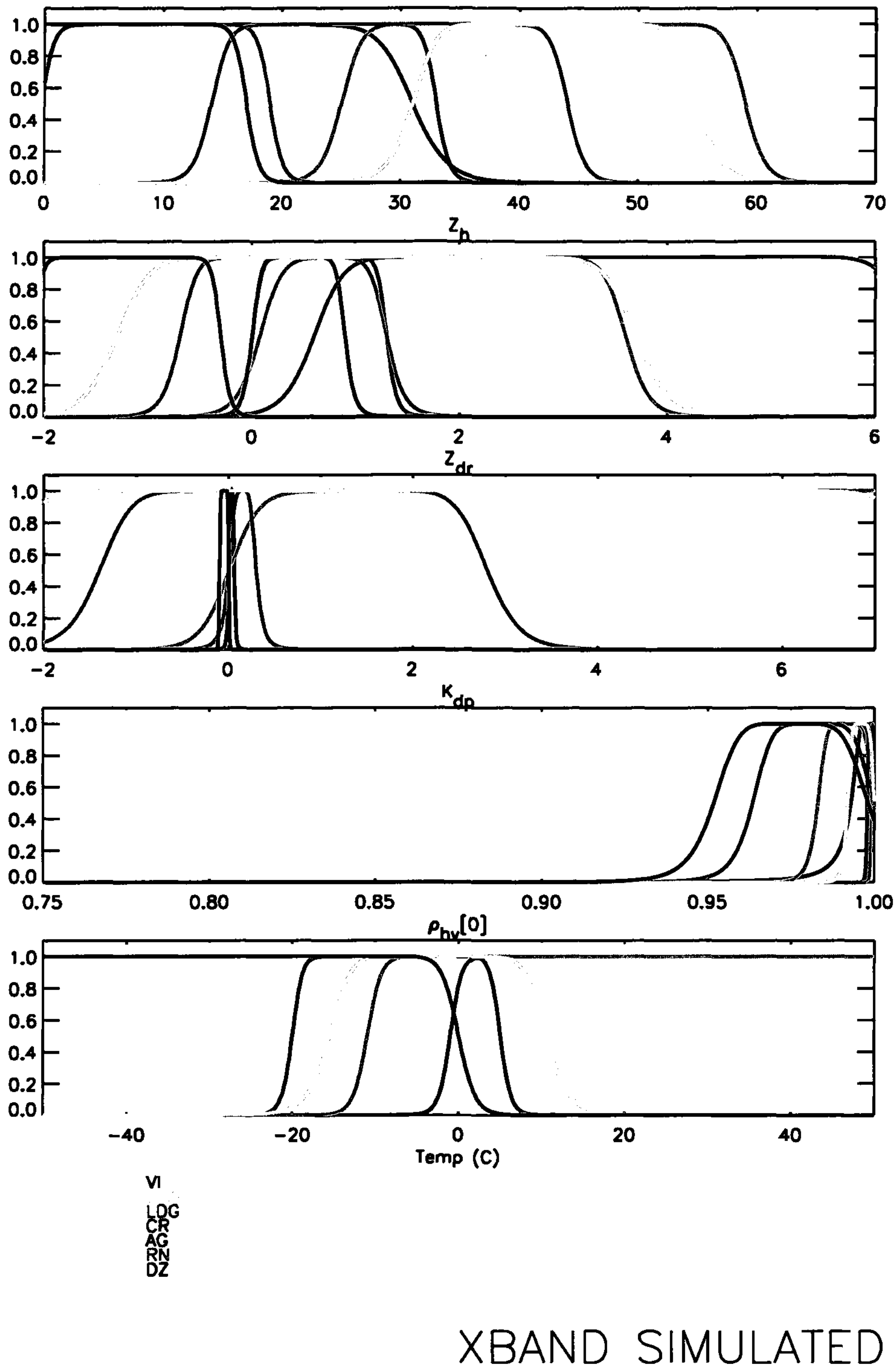

Fig. 3.23: Membership beta functions for the seven categories and five variables associated with the X-band theoretical HID.

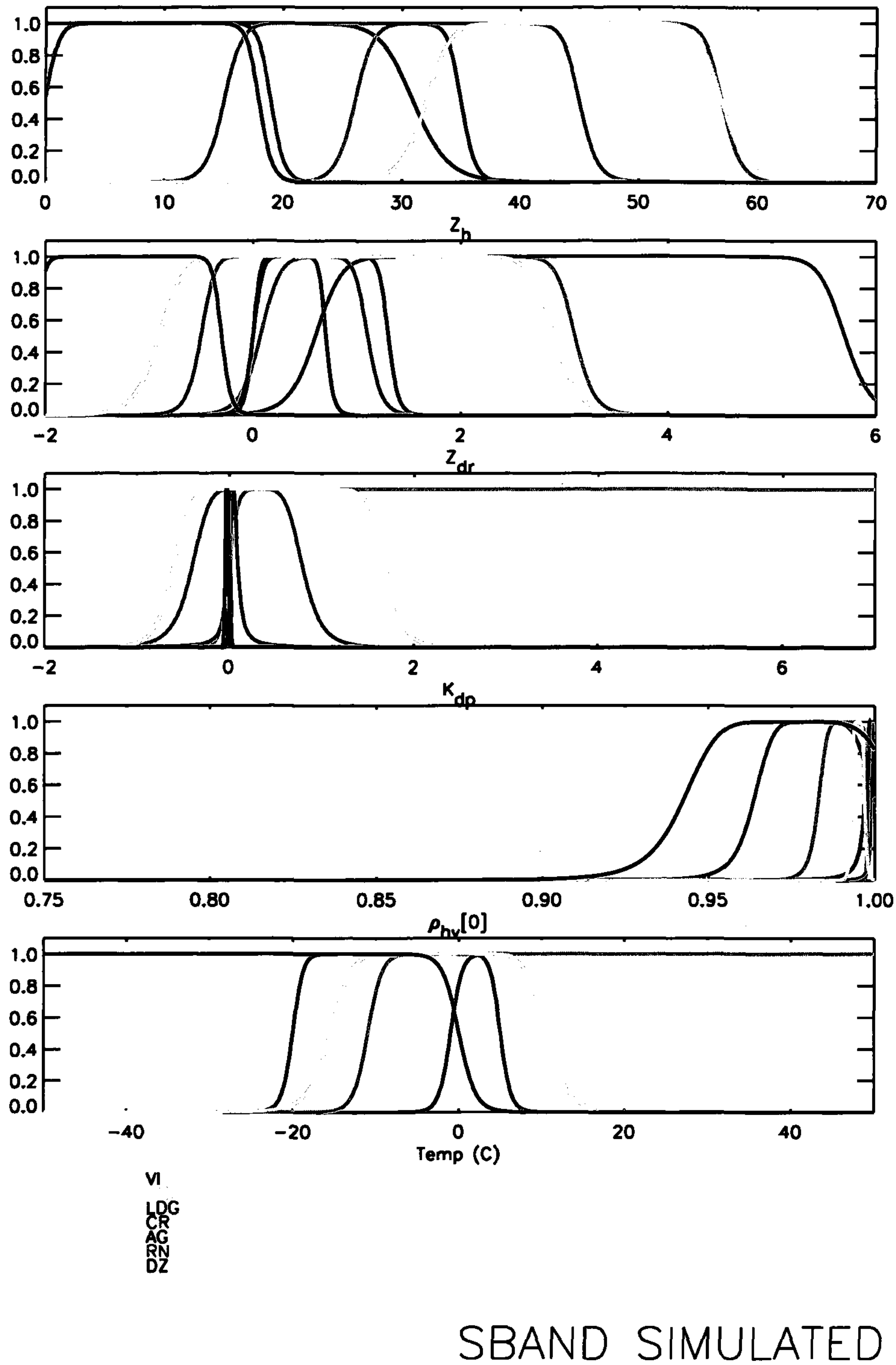

Fig. 3.24: Membership beta functions for the seven categories and five variables associated with the S-band theoretical HID.

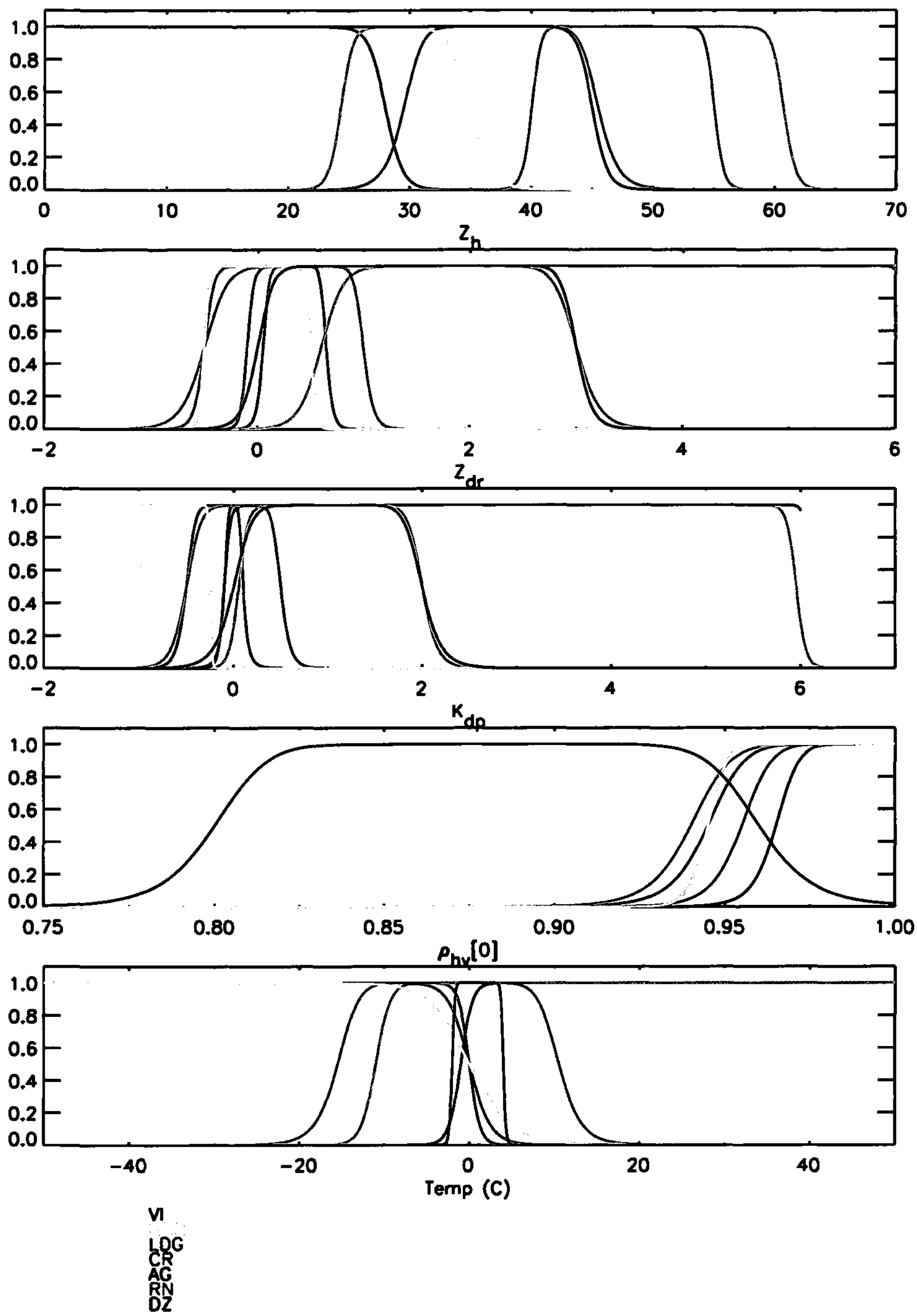

ORIGINAL

Fig. 3.25: Membership beta functions for the six categories and five variables associated with the CSUHIDS 6 (note: the DS category is represented by CR and AG, which are identical).

Chapter 4

Kinematic, Microphysical, and Lightning Observations in a Convective Storm Using the CASA IP1 X-band Radar Network

4.1 Introduction

It is estimated that roughly one-quarter of the troposphere below 3 km in the United States is scanned by the current WSR-88D network of radars. Hence about 75% of this volume is not observed by NEXRAD given the current radar spacing, beam blockage, and Earth curvature considerations (McLaughlin, 2001). As described before, CASA seeks to employ new low-cost, short-range, adaptively scanning networks of radars aimed at improving low-level sampling. To accomplish this, compact X-band radars have been designed that may be installed on cell towers and existing structures, and adaptive scanning techniques have been developed.

The so-called Distributed Collaborative Adaptive Sensing (DCAS) technology determines how to scan the radars based on the current weather situation within the IP1 network (McLaughlin, 2001). The Meteorological Command and Control (MC&C) determines the type of echoes in the network based on storm identification algorithms and allocates radars in order to scan those features (Zink et al., 2008). The MC&C decides which radars to use, the sector size for each, and the number of elevation angles for each. The rapid and adaptive scanning strategy can optimize the coverage for particular types of meteorological events and change in real-time to accommodate changing weather situations. This means that during each volume scan interval the sector size, number of elevation angles, and focus area can change.

A benefit of a low-looking network of radars situated in Oklahoma is the ability to pinpoint the location of tornados, providing information to increase reliability and lead-time for warnings, ingest the radar data into forecast models and study tornadogenesis. However, the IP1 network posses several qualities that could be beneficial for studying more general storm morphology, specifically the high-temporal resolution has potential for relating radar-derived microphysics and dynamics to lightning and electrification.

As previously discussed, however, the IP1 radars have limitations to overcome for such an analysis. The purpose of this study is to do a preliminary evaluation of the capability of the IP1 network for storm interaction studies, and to use the data collected from IP1 to investigate the relationships between kinematics, microphysics and electrification. Data are compared with KOUN to place the IP1 network in a larger context and to compare with an essentially unattenuated wavelength.

IP1 data were quality controlled and processed using the methodology described in Sec. 2.1 (Fig. 2.1). KOUN data were subjected to the quality-control measures outlined in Sec. 2.2.1. The SS7 and CS7 HID algorithms were used for the microphysical analysis, and the W_{com} methodology was employed for the kinematic studies. Echo volumes (i.e. graupel, ice, updraft) were arrived at by multiplying the number of grid points meeting the requirements (i.e. HID equal to LDG or $w > 5$ m s^{-1}) by the grid point volume (0.5 km^3 for IP1, 1.0 km^3 for KOUN).

Data from the National Lightning Detection Network (NLDN; Cummins et al., 1998) provided cloud-to-ground (CG) flash rates, as well as CG polarity (positive or negative). The OK-LMA was used to calculate intracloud (IC) flashrates, as well as infer bulk charge structure. Between these two lightning detection networks, the total flash rate (TFR), CG flash rate, and IC flash rates can be estimated.

For the purposes of this study, the rain rate estimation will be used only for diagnosing areas of heavy, moderate and light rainfall. The blended algorithm described in Sec. 2.1.4.3 was employed for rain rate estimation using IP1, and the S-band blended algorithm detailed in Sec. 2.2.1 was applied to KOUN data. A HIDRR field uses the HID for altitudes above 2.5 km, and divides the RN and DZ HID at 2.5 km and below into four rain categories based on the blended algorithms. The four rain categories are light rain (LTRN; < 2.5 mm h^{-1}), moderate-light rain (MLTRN; 2.5 - 25 mm h^{-1}), moderate-heavy rain (MHVYRN; 25 - 50 mm h^{-1}) and heavy rain (HVYRN; > 50 mm h^{-1}).

4.2 Case overview

On 10 June 2007, a multi-cellular storm developed to the southwest of the IP1 network and moved through the network to the northeast, allowing IP1 to capture nearly the entire 2.5-hour lifetime of the storm. The storm began as several reflectivity cores (Fig. 4.1a) that eventually joined around 2300 UTC to form a linear complex (Fig. 4.1b), and by 2320 UTC began to separate into two reflectivity cores (Fig. 4.1c), one to the southwest (A) and one to the northeast (B). Cell B continued to remain intense through

0020 UTC on 11 June 2007, while cell A reached a reflectivity maximum at 2340 UTC, and rapidly dissipated after 0000 UTC on 11 June 2007 (Fig. 4.1d). Fig. 4.2 shows the IP1 and KOUN reflectivity swaths associated with the overall storm complex, as well as cells A and B, with the cloud-to-ground lightning detected by NLDN overlaid. Due to the proximity to other storms on this day (not shown), a moving analysis box was drawn around the storm of interest and all data were then limited to within the analysis grid.

No severe weather was reported for this storm, and KOUN identified only a small amount of hail during the most intense period of the storms lifecycle (see Sec. 3.3.3), making it an ideal case to study with IP1 in order to minimize complications from non-Rayleigh effects. Maximum reflectivities reached >65 dBZ (KOUN) and > 75 dBZ (IP1). The 12 Z 10 June 2007 sounding from Norman, OK (Fig. 4.3) shows counter-clockwise shear in the lowest levels, with strong westerly winds at the surface. The sounding indicates 2324 J kg^{-1} of surface-based CAPE, and 18 J kg^{-1} of CIN. The 700 mb "steering wind" was 13 m s^{-1} from 210°. These parameters were used for storm advection in the dual-Doppler analysis.

In order to understand the impact of coverage area on the results discussed below, Fig. 4.4a shows a time-height series of the relative echo area of IP1 reflectivities >20 dBZ compared to the total reflectivity area > 20 dBZ observed by KOUN. Due to scanning considerations, IP1 has limited coverage (10-40%) of heights above 3 km until approximately 2300 UTC when IP1 scanning began to cover 60-90% of the upper levels. The best coverage occurs between 2315 and 0000 UTC. Fig. 4.4b illustrates the dual-Doppler coverage area compared to the IP1 reflectivity area > 20 dBZ. During the early (2200-2230 UTC) and late (2350-0030 UTC) periods of the storm, dual-Doppler analysis could be performed on nearly the entire area covered by IP1. Between 2230 and 2350 UTC, a large volume of the storm passed through the KLWE-KCYR and KSAO-KRSP baselines, where winds could not be retrieved. This results in dual-Doppler wind retrievals in only 25-75% of the IP1 area, with particularly degraded coverage in heights above 5 km. The variable coverage area of IP1 will impact the ability to retrieve the 3-D wind field, as well as kinematic and microphysical analysis by decreasing the volume of vertical winds and hydrometeor types, especially above 3 km.

4.3 Kinematic analysis

Many previous studies have employed dual-Doppler methodologies to study the kinematic characteristics of storms (e.g. Ray et al., 1978; Rutledge et al., 1988; Carey and Rutledge, 1996; Cifelli et al., 2002). Kinematic intensity (defined by updraft area and strength) has been linked to severe weather and electrification (e.g. Ray, 1978; Nelson, 1983; Williams et al., 1989; Carey and Rutledge, 1996; Lang and Rutledge, 2002; Wiens et al., 2005). Updrafts are responsible for lofting particles into a "balance layer", where the particle fall speed matches the updraft speed, leading to accumulations of particles in the mid-levels (Williams et al., 1989) which has important implications for electrification.

The combined method (W_{com}) of deriving the vertical wind from dual-Doppler analysis was applied to IP1 data from this case. The mean vertical wind speed at different times throughout the storm lifetime are shown in Fig. 4.5. At 2310 UTC when the storm is developing, a large layer of mean upward motion is noted in the mid-levels between 4 and 8 km (Fig. 4.5a). Large negative w above 10 km are likely an artifact of the columns using W_{up}. Twenty-five minutes later at 2338 UTC, the profile of mean w illustrates that the mean upward motion has weakened and extended slightly higher to 10 km. By 0012 UTC, the mean vertical motion is dominated at all levels by downward motion (Fig. 4.5a). Mean upward speeds below 10 km peak at 7 ms^{-1}, while mean downward speeds below 10 km peak at 9 ms^{-1} (Fig. 4.5b). Both updraft and downdraft speeds increase with height, likely due to the upwards integration method used as part of the W_{com} methodology. Low-level speeds are on the order of 2-3 ms^{-1}, while mid-level speeds range from 3-7 ms^{-1} for both upward and downward motion (Fig. 4.5b).

The dual-Doppler derived updraft echo volume > 5 ms^{-1} (U5) starts at 2235 UTC (Fig. 4.6). A threshold of 5 ms^{-1} was applied in order to delineate areas of strong upward motion, consistent with where graupel production would be expected, with accompanying electrification. The evolution of downdraft echo volume < -2 ms^{-1} (D2) is also illustrated in Fig. 4.6. Cell A has a much smaller U5 volume than cell B after the storm split at 2318 UTC, and is generally dominated by downdrafts. The U5 volume for cell A peaks at 2335 UTC, and has dissipated by 0000 UTC. Cell B, however, continues to have a large U5 volume until 0000 UTC, with the peak occurring just after the split at 2320 UTC and possibly a second peak at 2352 UTC, although this peak corresponds to the time of increased dual-Doppler coverage (Fig. 4.4). The D2 volume peak is coincident with the U5 peak for cell B, as well as the several subsequent secondary peaks. For cell A, the U5 and D2 volumes have a raw correlation of 0.9, and a detrended (storm volume removed) lag correlation of 0.8 with U2 leading D2 by 2 time steps (6 minutes; Table 4.1). This would be consistent with formation of the updraft first, followed by development of the downdraft. Cell B U5 and D2 volumes have the highest correlation at 0 lag of 0.6 (Table 4.1).

Perhaps a more enlightening illustration of the kinematic storm evolution is through time-height cross-sections, allowing for the determination of the height-evolution of various features. Time-height series of U5 and D2 areas reveal interesting characteristics of the storm dynamics (Fig. 4.7). The U5 area shows two distinct peaks, one occurring at 2320 UTC between 5 and 8 km, and the other slightly higher at 7-9 km at 2333 UTC. By separating the cells into A and B (Fig. 4.7c and e), it is clear that the first large area of U5 is associated with cell B, while the higher second peak occurs in cell A, although cell B has a large area of U5 between the time of splitting (2318 UTC) and 2338 UTC. The D2 time-height areas reveal a descending trend in the downdraft volume (Fig. 4.7b). The D2 area rapidly increases after the storm split, and a continuous area of large D2 area begins at 2335 UTC, and extends from the mid-levels (9.5 km) down to the low-levels (2 km). The D2 area reaches a maximum at 2347 UTC between 2 and 5 km, about 15 minutes after the U5 peak in the mid-levels. Cell A D2 area is centered higher (5 km) than the D2 area related to cell B, whereas cell B D2 peaks mostly below 5 km (Fig. 4.7d, f). The D2 peak for cell A is at 2340 UTC, just a few minutes after the cell A U5 peak. Cell B D2 reaches a maximum area at 2358 UTC, about 40 minutes after the U5 peak. As discussed previously, however, the dual-Doppler coverage was limited between 2245 and 2353 UTC, which could influence the locations and timing of the greatest updraft areas. However, the D2 threshold of < -2 ms^{-1} biases the downdrafts to the mid- and low-levels, which are still relatively well covered by dual-Doppler scanning during this time period. These series of up- and downdrafts highlight one of the features of the

IP1 radars, that is, the ability to resolve both updrafts and downdrafts due the high temporal resolution which aids in resolving these structures.

4.4 Microphysics

The total effect of coverage, radar sensitivity and differences in the HID algorithms (e.g. different variable weights for X- and S-band; see Sec. 3.3.2) is illustrated in Fig. 4.8. Although IP1 and KOUN data show similar trends in hydrometeor heights, KOUN clearly reveals a larger volume of ice crystals (CR and VI), as well as aggregates. This is a result of the reduced sensitivity of the IP1 radars relative to KOUN (Fig. 4.9), as well as reduced upper level coverage by IP1. Both radar volumes show a peak in ice crystals (CR) at 9 km, with a secondary peak at 5 km. The lower coverage of IP1 allows it to detect rain to very near the surface, while KOUN tapers off significantly below 2.5 km due to the range from KOUN to the echoes (Fig. 4.8a). Interestingly, LDG and HDG volumes between the two radars are strikingly similar with a few subtle differences (Fig. 4.8b). IP1 shows the peak in aggregation at 4.5 km, at the same level as the melting layer, while KOUN indicates peak aggregates much higher, around 7 km. The subtle differences between HDG and LDG (not discussed) and the more significant differences in AG could be a function of the coarser resolution of the KOUN data that smears out trends over 1 km in the vertical. The general trends indicate the potential for better observations of the low- to midlevels with IP1 compared to longer wavelength radars when operating at longer ranges. These capabilities of IP1 were also noted in Sec. 3.3.2.

The microphysical evolution of the storm can be inferred by employing the HID to look at the formation of different types of hydrometeors throughout the lifetime of the storm. The KOUN VI volume increases rapidly at 2307 UTC, and reaches an absolute maximum at 2339 UTC (Fig. 4.10a). IP1 generally captures much less VI volume due to coverage and sensitivity, but the VI volume peaks approximately every 20 minutes beginning at 2307 and ending at 2345 UTC (Fig. 4.10a). IP1 VI volumes for cell A and B both peak at 2345 UTC, while KOUN VI for cell B peaks much earlier at 2325 UTC. Both IP1 and KOUN do not show significant volumes of VI associated with cell A until 2338 UTC, which is consistent with the peak in U5 area for cell A. If we assume that the height of the 40 dBZ echo can be used as a measure of the intensity of a storm, KOUN 40 dBZ echo heights start at 8.5 km and increase to about 14 km by 2325 UTC (Fig. 4.10b). IP1 sees a similar trend. Both IP1 and KOUN show that the 40 dBZ height for cell A is slightly lower than storm B after the split, and rapidly falls to 4 km by 0000 UTC, while cell B heights remain greater than 12 km until early on 11 June 2007.

For simplicity, HDG and LDG have been combined into a single category termed "graupel". Time-height contours of graupel echo area derived from the HID analysis are shown in Fig. 4.11. General trends observed by IP1 show a rapid onset of graupel volume beginning at 2237 UTC. KOUN graupel trends are smoother, indicate the presence of graupel sooner than IP1, and reach a maximum at 2322 UTC. The difference in the onset of graupel is likely a result of the storm coverage during the early times of the storm. KOUN and IP1 graupel areas show similar trends, with two relative maxima at 8 km and between 5 and 6 km that are associated with the two types of graupel (Fig. 4.11a and b). Separate analysis confirms that the upper maximum at 8 km is LDG, while the lower maxima is related to HDG. The maximum area of KOUN LDG occurs at 2333 UTC, while the IP1 LDG peak occurs 5 minutes later at 2337 UTC. The KOUN HDG maximum is smaller than the KOUN LDG and occurs at the same time as the peak in LDG. The HDG maximum area identified by IP1 is larger than the peak in LDG and occurs 7 minutes later, at 2345 UTC. However, as noted in Fig. 4.4, the relative IP1 coverage above 5 km peaks at this time and may cause the increased area. In comparing cell A and cell B, it is clear that cell B dominates the overall storm trend, with two distinct layers associated with LDG and HDG. The peak in graupel areas identified by both IP1 and KOUN for cell A is around 8 km, indicating that cell A has a larger area of LDG than HDG. KOUN graupel area for cell B indicates more LDG early in the lifecycle, while IP1 shows more area of HDG later in the storm. Both KOUN and IP1 have high correlations between LDG and HDG, with HDG leading LDG by anywhere from 0 to 3 timesteps (Table 4.1). Correlations between the two are improved by breaking the overall storm into the two cells (Table 4.1).

The U5 area peaked at 6-8 km, and the LDG area is greatest towards the top of this layer (8-9 km). In fact, U5 and graupel echo volume are highly correlated for all cells, with a tendency for U5 to lead the graupel volumes by 1 timestep (3 minutes), which supports the theory of the updraft strengthening and lofting graupel into the upper levels of the storm (Table 4.1). As graupel accumulates in the upper-levels, precipitation loading drives the development of the downdraft. This is illustrated in the time-height figures for graupel and D2 (Fig. 4.11 and Fig. 4.7, respectively), as well as in the correlations. The detrended correlations for cell A shows a strong lag correlation (0.8) with graupel leading the downdraft by 1 timestep (3 minutes; Table 4.1). The correlation for cell B is weaker and negative (meaning D2 volume reaches a maximum as graupel reaches a minimum), but still with graupel leading D2 by several minutes (Table 4.1). The peak in graupel area occurs from 2335 to 2347 UTC, while the D2 area reaches a max area 6 minutes later at 2352 UTC.

Qualitative examples of the combined microphysics and kinematics are illustrated in Figs. 4.12 and 4.13. The storm-relative winds derived from the dual-Doppler synthesis have been overlaid on IP1 observations. The HIDRR fields are shown, where the rain and drizzle categories below 2.5 km have been broken into four categories based on the blended algorithm rainrate calculations.

Fig. 4.12 shows a cross-section at 2321 UTC, just as the linear-organized storm began to split into cell A and cell B. Storm-relative surface flow is from the northeast (Fig. 4.12a and b). As the air enters the leading edge of the storm, some of it begins to lift, forming new cells (Fig. 4.12c). The main updraft is located above 5 km at 30 km range along the vertical cross-section, which is along the direction of propagation. This region of strong upward motion is characterized by large areas of both HDG and LDG, as well as RN identified above the nominal melting layer. Behind the main updraft the motions are weaker, mostly characterized by downward motion below 3.5 km and upward motion above 5 km. Surface rain rates are largest (> 50 mm h^{-1}) to the southwest of the main updraft, and are coincident with relatively strong downward motion. KOUN cross-sections from four minutes earlier demonstrate two main reflectivity cores (Fig. 4.12e), which are not as distinct in the IP1 data. General HID trends are similar between the two wavelengths (Fig. 4.12d, f), with IP1 providing details of smaller scale features. The KOUN area of heavy rain is located in the same region along the cross-section as IP1. KOUN identifies large regions of VI along the upper-level edges of the storm that are not seen by IP1.

Fifteen minutes later at 2347 UTC, the reflectivity core is significantly tilted towards the direction of propagation (Fig. 4.13). Surface horizontal flow is diffluent away from the main reflectivity center and area of heavy rain (Fig. 4.13a). Although dual-Doppler wind analysis is not available in the leading edge of the cross-section, upward motion prevails to the southwest of the main reflectivity core. Cell A, at 10 km along the cross-section, still has high elevated reflectivities in both KOUN and IP1 data (Fig. 4.13c and e), but dual-Doppler winds indicate the core is dominated by downward motion. Both KOUN and IP1 HID analysis show similar large regions of HDG surrounding the core, identified as rain but likely supercooled liquid water (Fig. 4.13d and f). IP1 identifies more RN above 5 km in cell A than KOUN.

These qualitative observations support some of the quantitative findings described above, and illustrate some of the advantages and disadvantages of the IP1 radar network. For example, the coverage area and artifacts from the mosaicing and W_{com} procedures are apparent, but the increased resolution compared to KOUN in this case is also notable. The low-level coverage is also clearly providing information about winds and precipitation at the surface that cannot be seen by KOUN at longer ranges.

4.5 Lightning

Thunderstorms have been shown to often have a dipole or tripole charge structure (Williams, 1989; Williams, 2001). A so-called "normal dipole" generally exhibits negative charge near -10 °C, with the positive charge residing above the negative, above approximately -30 °C (Williams, 1985, Williams et al., 1994). A "normal tripole" has a smaller region of positive charge near the 0 °C isotherm (Williams, 1989). This type of charge structure is thought to be the result of non-inductive ice-ice collision mechanisms. The non-inductive charging theory proposes that as graupel and ice crystals fall with differential fall velocities, they collide with each other and transfer charge. The amount and polarity transferred between particles is dependant on the riming rate and temperature at which the collisions occur (Takahashi, 1978; Saunders and Peck, 1998, Berdeklis and List, 2001). In a normal dipole, graupel generally acquires negative charge and ice crystals a positive charge. In this case the graupel particle is growing by riming and its surface is in a sublimational state with respect to vapor transfer (Williams et al., 1991; Williams et al., 1994).

During the 10 June 2007 case, the NLDN detected 333 ground strikes. The LMA identified upwards of 4000 total flashes, making the average IC/CG ratio 12. This is much higher than Price and Rind (1993) ratio of 3 for the latitude of IP1 (35° N), but it is similar to the ratio observed in a Colorado multicellular complex by Carey and Rutledge (1996). Peak IC flash rates reached 80 min^{-1}, while peak CG flash rates were 2 min^{-1}. The IC component accounted for 92% of the total lightning.

The three-minute (corresponding to the IP1 scan interval) total lightning flash rate (TFR) timeseries exhibits a trimodal trend, dominated by the intra-cloud (IC) flash rate (Fig. 4.14). The three peaks occur at 2307, 2322, and 0010 UTC with the largest peak at 2322 UTC. IC lightning onset begins at 2222 UTC, and markedly increases at 2245 UTC. The CG flash rate starts nearly a half an hour after the IC at 2250 UTC, although only five minutes after the rapid increase of IC at 2245. The onset of IC prior to the beginning of CG flashes is a general trend in storm electrification noted by many authors (e.g. Carey and Rutledge, 1996; Goodman et al., 1988; Williams et al., 1989). Two minimums in TFR occur at 2315 and 2348 UTC. While both cell A and B were clearly dominated by IC flashes, cell A had nearly twice the percentage of CG flashes (13%) compared to cell B (7 %).

Using the LMA for charge analysis, it was clear that this storm exhibited normal polarity with two distinct regions of charge: mid-level negative charge and upper level positive charge. Pockets of lower positive charge below the negative source region were also observed, providing the source region for negative cloud-to-ground flashes. The LMA VHF source density for the storm complex is color contoured in Fig. 4.15. Temperature data from the 12 Z Norman sounding (Fig. 4.3) indicate that the negative source region resides between -10 and -25 °C with the positive region above the negative, which is consistent with the normal dipole storm structure (Fig. 4.15; Williams, 2001). Graupel echo area contours overlaid on the LMA source density reveal the negative source regions are generally associated with the largest area of graupel as identified by both IP1 and KOUN (Fig. 4.15). The KOUN ice echo area (VI and CR) shows the positive source region containing the greatest area of ice crystals (Fig. 4.15b), an observation consistent with several of the non-inductive charging mechanism studies (Takahashi, 1978; Saunders and Peck, 1998).

An interesting feature noted in this storm was the apparent increase in initial flash discharge height and general increase in height of the maximum source density from 9 km at 2230 UTC to nearly 12 km by 0000 UTC on 11 June 2007. The increase of lightning initiation height pushed the upper level positive charge to heights of 12-15 km, while deepening the mid-level negative source region. The inferred charge regions are indicated in orange in Fig. 4.15. This elevated dipole structure was first described by MacGorman et al. (1989) and studied further by Lang et al. (2000). MacGorman et al. (1989) postulated that the elevated dipole situation was the result of an intense updraft that would loft particles higher and cause the non-inductive charging to occur at higher levels, and such charge situations favor IC flashes over CG. Following the increase in initiation height was a burst of IC activity, resulting in the third peak in flashrate, although CG flashrates remained low (Fig. 4.14). Although the cause of the increase and secondary peak in IC flashrate are not readily apparent, there are several radar-identified features that accompany the increase. The IP1 U5 area suddenly increases to heights of 14 km around 2355 UTC, with a second peak at 2358 UTC up to 12 km (Fig. 4.15a). These updraft pulses could indicate an additional growth phase that is not entirely captured by the IP1 radar network, consistent with the charge elevation hypothesis of MacGorman et al. (1989). This conclusion is also supported by a rapid peak in 40 dBZ heights for both IP1 and KOUN at 2358 UTC, where KOUN heights reach up to 15.5 km and IP1 heights up to 14 km (Fig. 4.10b). Interestingly, IP1 vertical ice areas reach their maximum peak about 15 minutes before the third peak in IC flashrate (Fig. 4.10a and

4.14). Finally, IP1 and KOUN graupel echo area contours at 13-15 km show a minor lift in height coincident with the time of increased height in source density, at 0005 UTC 11 June (Fig. 4.15).

When the storm is broken into the two main cells (A and B), it is clear that the elevated positive source region is associated with cell B, while cell A has a large density of VHF sources between 8 and 13 km (likely indicating positive charge at these altitudes) before rapidly dissipating (Fig. 4.16). It is also interesting to note that there are no sources below 4.5 km (roughly the 0° C isotherm) in cell B after 0015 UTC, at which point the CG flashrate essentially drops to zero (Fig. 4.14). MacGorman et al. (1989) and Lang and Rutledge (2002) speculated that an elevated charge structure, such as that seen in this case, could lead to a predominately IC lightning profile, due to the preferential breakdown between the upper charge levels rather than discharge to ground. This could be responsible for the decreased CG to IC ratio noted in this storm, particularly in cell B. Clearly cell B underwent a secondary kinematic intensification around 2355 UTC, as evidence by the U5 area time-height contours and 40 dBZ heights, both readily seen with IP1 data, as well as the electrical activity. Unfortunately, the storm moved out of the dual-Doppler coverage area shortly after 0000 UTC preventing further up- and down-draft analysis.

Previous studies have found that graupel peaks before the peak in IC lightning (Carey and Rutledge, 1996), which is a trend also found in this study with the highest correlations occurring when graupel leads the TFR (which is dominated by TIC) by 5-15 minutes (Table 4.1). The peak in IP1 VI volume at 2345 UTC (Fig. 4.10a) corresponds to the minima in the IC flash rate, which is consistent with an increasing local electric field, aligning ice crystals in the vertical. It is difficult to say if this is the case, because negative correlations between IP1 VI volume and IC are low (-0.3 to -0.4) with lag of 1 (Table 4.1). Although the same "pulsing" is not obvious in the KOUN timeseries, correlations are mixed, with negative correlations for individual cells and a high positive correlation for the overall storm (0.8). Lags range from VI leading by ten minutes in cell B to TIC leading by ten minutes in the overall storm volume (Table 4.1). Interestingly, the mean heights associated with VI as identified by KOUN are centered between 10-13 km (Fig. 4.8a), the same region as the highest density of OK-LMA sources.

4.6 Discussion

The unique network of X-band polarimetric adaptively scanning radars employed by CASA IP1 has been used to examine the evolution, microphysics and dynamics of a multi-cellular storm. These parameters were examined in relation to one another, as well as to lightning data. Data from the nearby S-band polarimetric KOUN radar were also used to put the IP1 observations into a larger context.

Qualitative analysis of the timeseries suggests that the storm evolution loosely follows that described in Carey and Rutledge (1996) and Williams et al. (1989) where the updraft develops, leading to graupel formation several minutes later, followed by the onset of IC lightning shortly thereafter. The IC flash rates quickly increase as the graupel and updraft volumes increase. CG flashes begin once HDG is present in the 5-7 km heights (Williams et al., 1989). As more graupel is suspended in the mid-levels by the updraft, the downdraft starts to form, bringing precipitation to the surface. Although IC flash rates in this case resurge as the storm is dissipating, CG flash rates cease as the graupel volume drops off. IP1 data did show significant correlations between graupel and U5, as well as graupel and TFR. It should be noted that multicellular storms could inherently have weak correlations due to the different cells in different phases of storm lifetime. The IP1 network also allowed for kinematic comparisons with lightning and graupel formation, highlighting the evolution of the updraft relative to the development of the upper-level microphysics and subsequent charging leading to electrification. The better spatial resolution of IP1 also allowed finer time-height contouring compared to the coarser resolution of KOUN, although this is a result of the arrangement of the radars and not necessarily indicative of general IP1 advantages.

IP1 data were used to infer the development of the downdraft due to precipitation loading from graupel in the mid-levels, and that the updraft leads the graupel echo volume by several minutes. The IP1 time-height contours showed some interesting characteristics of the storm evolution, with HDG developing around the melting layer in the developmental stages of the storm, then large volumes of both LDG and HDG forming during the mature stage, followed by an increase in downdraft area in the low-levels. IP1 was able to show kinematic intensification (corroborated by KOUN data) behind the increase in height of the positive charge region and subsequent burst of IC flashes, even despite limited coverage of the high levels of the storm.

One significant drawback revealed in this study was the lack of consistent coverage by the radars. The adaptive scanning strategy is an important aspect of balancing high temporal resolution, resources in the network, and total coverage area of the networked radars. However, inconsistent storm coverage results in ambiguities regarding real fluctuations in storm parameters versus changes in the scanning strategy, making quantitative analysis difficult. The lack of coverage in the upper levels reduces the overall storm coverage, but also decreases the understanding of ice-phase processes that are important for lightning and electrification. The lack of upper level coverage also limits the quality of the dual-Doppler derived vertical winds, impacting the quantitative analysis of updraft and downdraft dynamics, as well as vertical wind magnitudes.

Table 4.1: Correlations among kinematic, microphysics, and lightning parameters. Values outside the parentheses are raw correlations, while values inside the parentheses are the best detrended lag correlations (the storm volume identified by each radar, respectively, was removed from both x and y). Positive lag values correspond to y leading x.

X	Y	Storm IP1	Storm KOUN	Cell A IP1	Cell A KOUN	Cell B IP1	Cell B KOUN
D2	U5	0.8 (-0.4@-3)	--	0.9 (0.8@2)	--	0.9 (0.6@0)	--
LDG	HDG	0.9 (0.6@1)	0.7 (0.9@3)	0.9 (0.8@1)	0.97 (0.95@0)	0.98 (0.8@0)	0.98 (0.9@0)
U5	GRAUPEL	0.9 (0.8@-1)	--	0.9 (0.8@0)	--	0.9 (0.8@0)	--
D2	GRAUPEL	0.9 (-0.3@-5)	--	0.9 (0.8@1)	--	0.9 (-0.3@2)	--
TIC	VI	0.5 (-0.3@1)	0.9 (0.8@-2)	0.01 (-0.4@0)	0.1 (-0.7@-1)	0.4 (-0.4@1)	0.8 (-0.6@2)
TFR	GRAUPEL	0.6 (-0.4@-5)	0.6 (0.6@-1)	0.5 (0.7@-3)	0.7 (0.9@-1)	0.5 (-0.6@0)	0.9 (-0.4@1)
TCG	TIC	0.8 (0.6@0)	0.9 (0.8@0)	0.8 (0.8@0)	0.9 (0.9@0)	0.7 (0.7@-2)	0.9 (0.6@1)

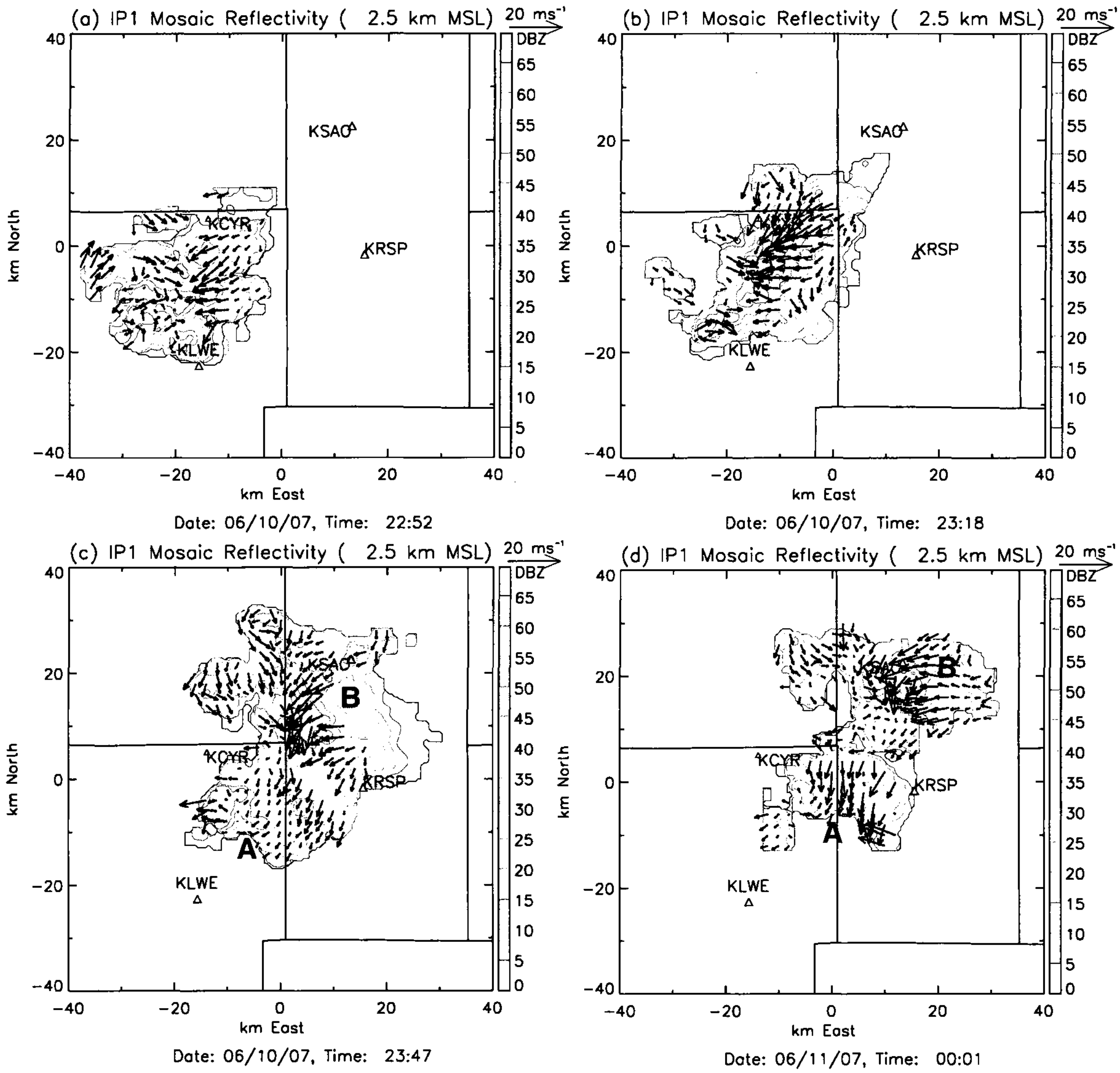

Fig. 4.1: Horizontal cross-section of IP1 reflectivity at 2.5 km MSL for 4 different times a) 2252 UTC, b) 2318 UTC, c) 2347 UTC and d) 0001 UTC. Storm relative dual-Doppler derived winds are overlaid. Cells A and B are indicated after the split, in panels c) and d).

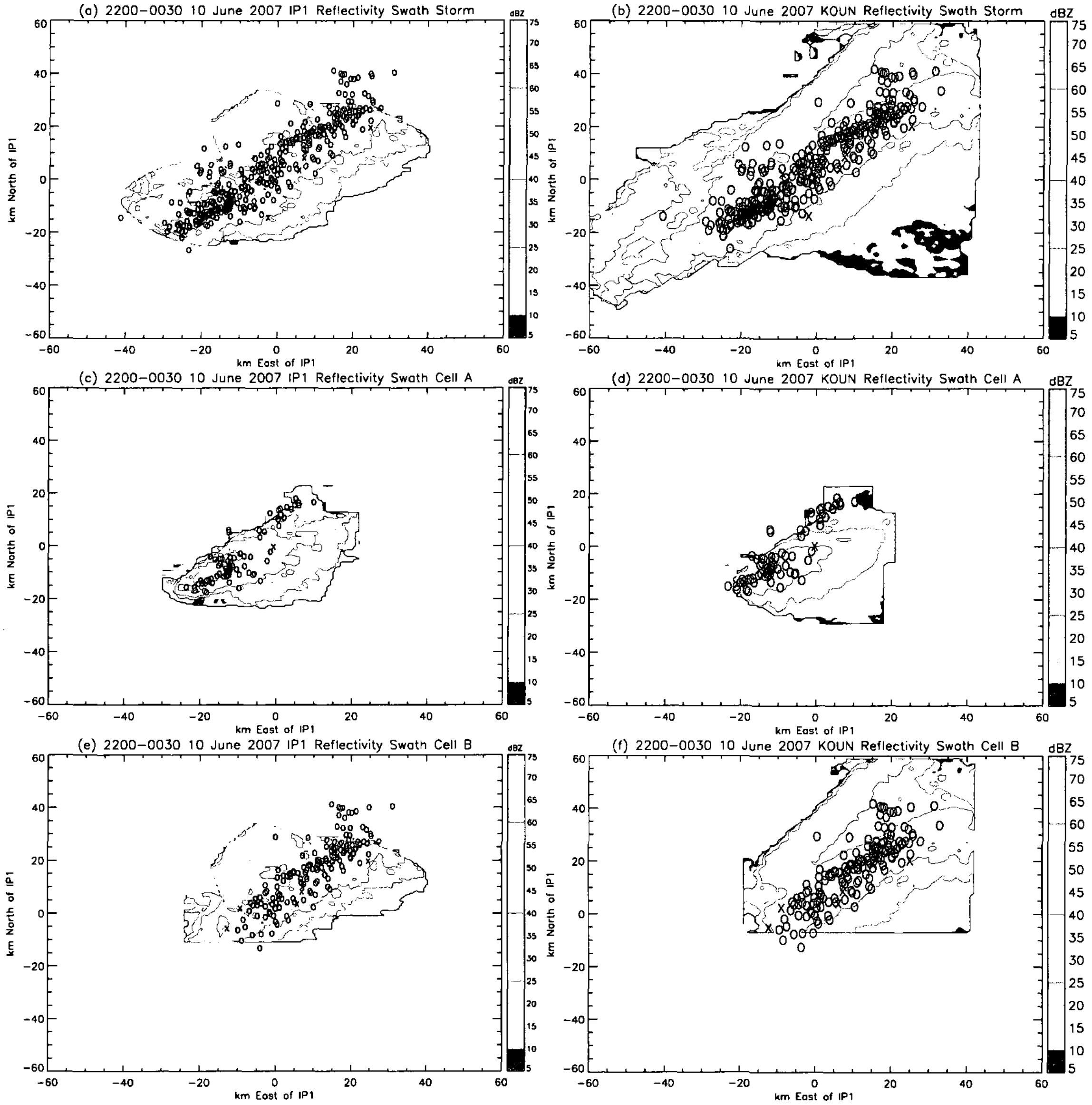

Fig. 4.2: Reflectivity swath of IP1 mosaicked data from 2200-0030 UTC during the 10 June 2007 case for a), b) storm complex; c), d) cell A, and e), f) cell B. Locations of NLDN detected CG lightning overlaid. ‘O’ denotes negative CGs and ‘+’ denotes positive CGs.

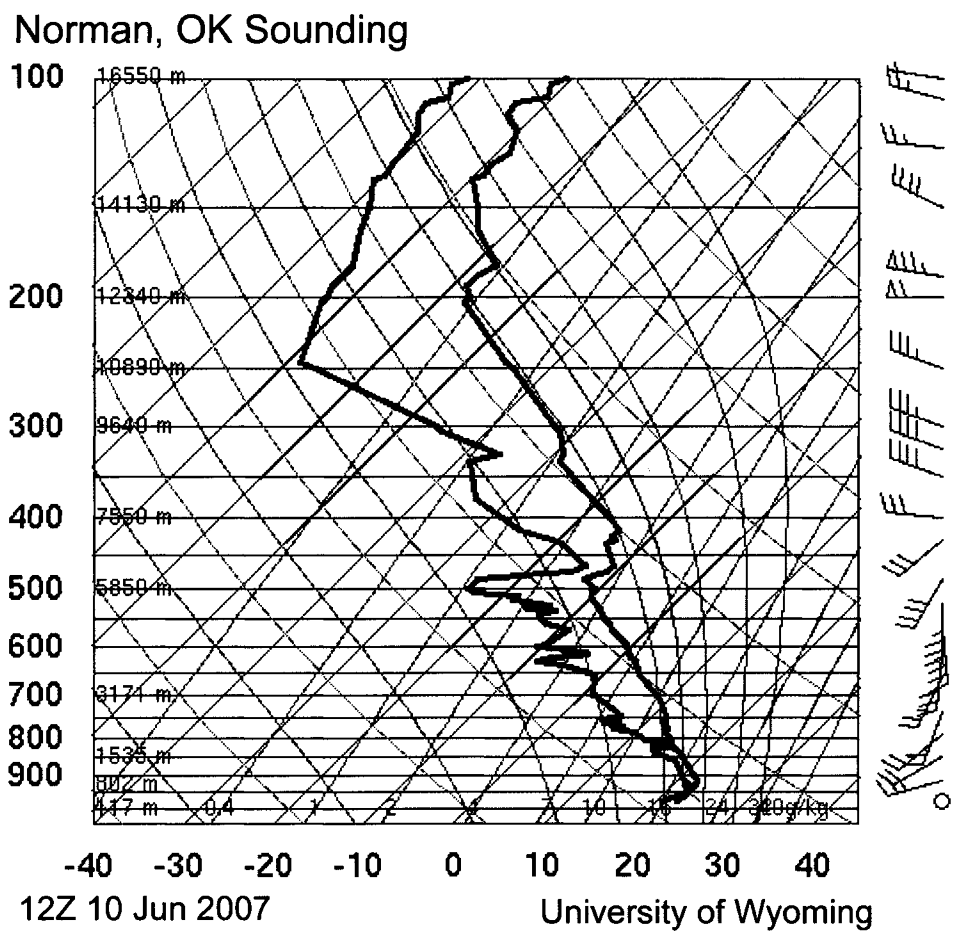

Fig. 4.3: The Norman (OUN), OK sounding at 12 Z on 10 June 2007.

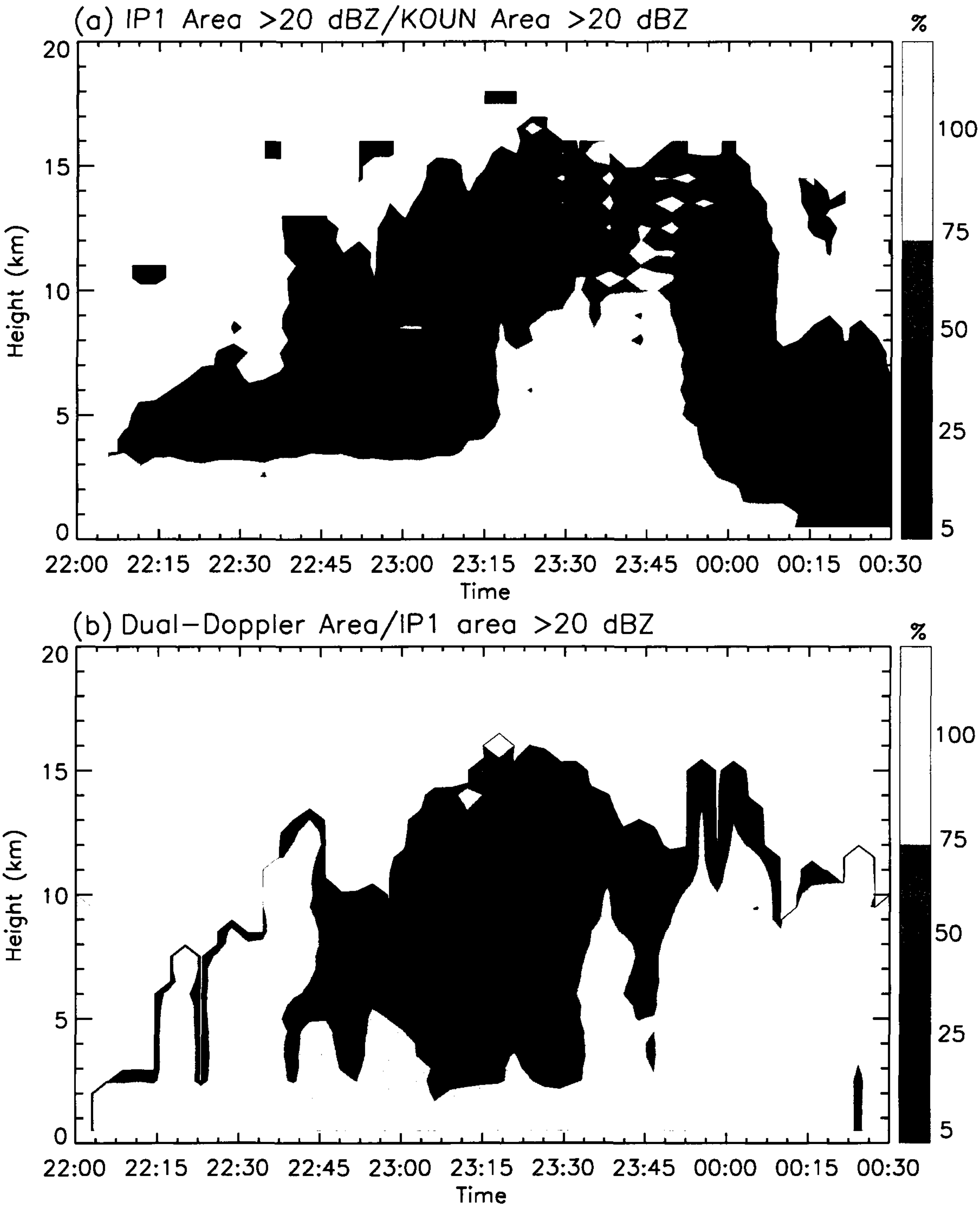

Fig. 4.4: Time-height cross-section of a) percentage of IP1 area > 20 dBZ compared to KOUN area > 20 dBZ, and b) percentage of dual-Doppler coverage as a function of IP1 reflectivity area > 20 dBZ.

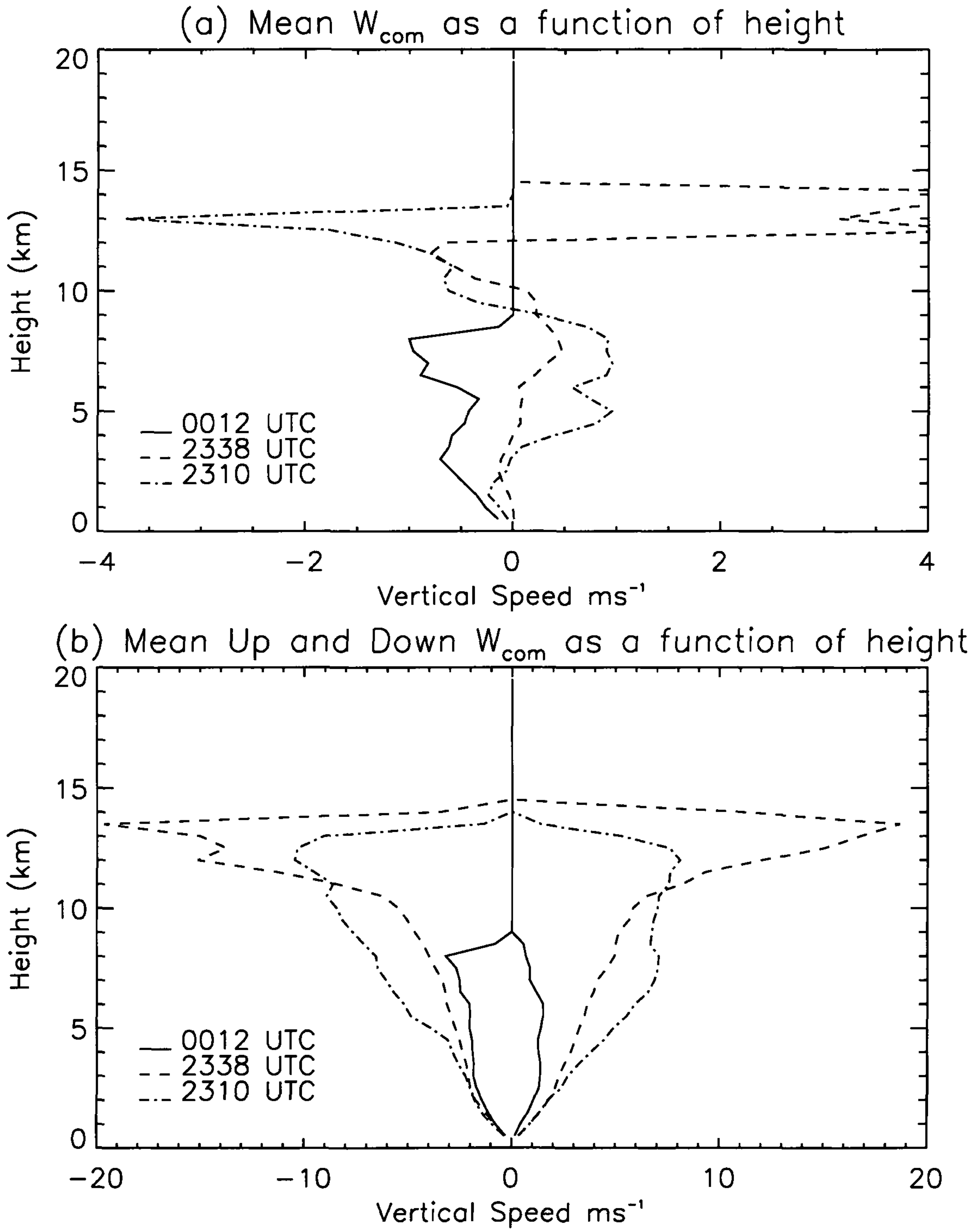

Fig. 4.5: Mean vertical wind using the W_{com} methodology as a function of height (a), and broken into up- and downward motion (b) at three time during different stages of evolution.

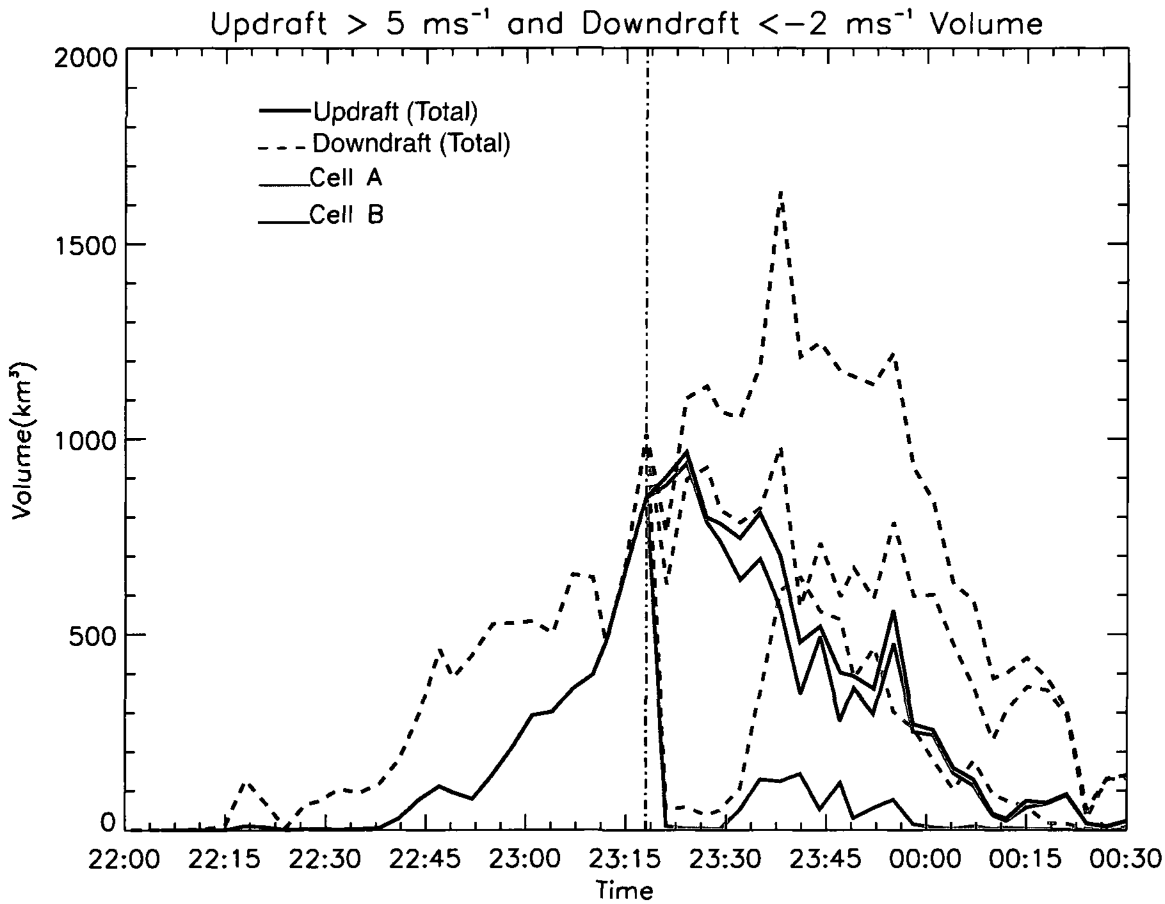

Fig. 4.6: Timeseries of updraft volume > 5 ms^{-1} and downdraft volume < -2 ms^{-1}. The beginning of the storm split is marked with a dashed-dot line (2318 UTC).

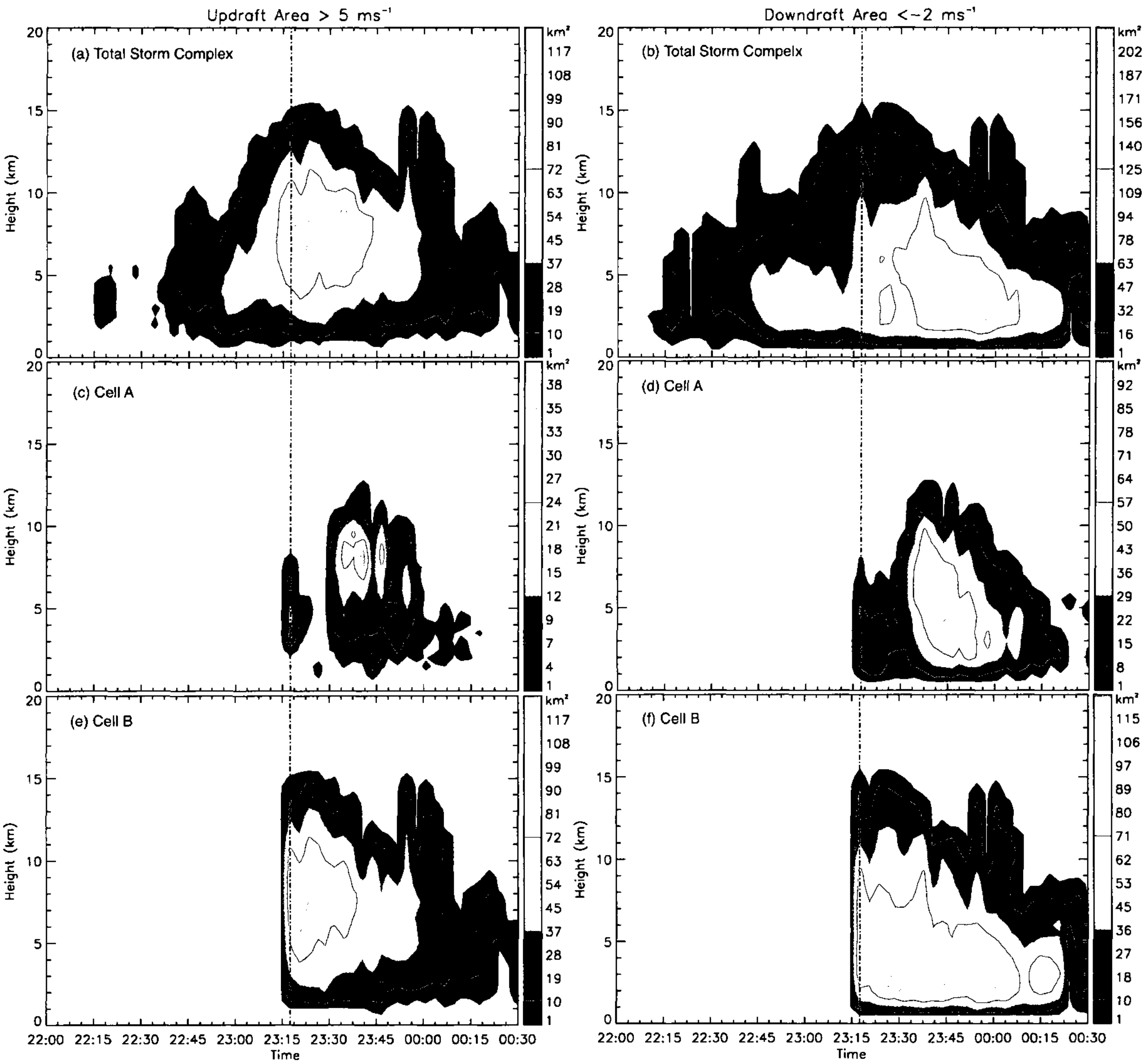

Fig. 4.7: Time-height cross-section of updraft area > 5 ms^{-1} (left) and downdraft area < -2 m s^{-1} (right) for the storm complex (top), cell A (center) and cell B (bottom). The beginning of the split into cell A and B is indicated with the dashed-dot line (at 2318 UTC).

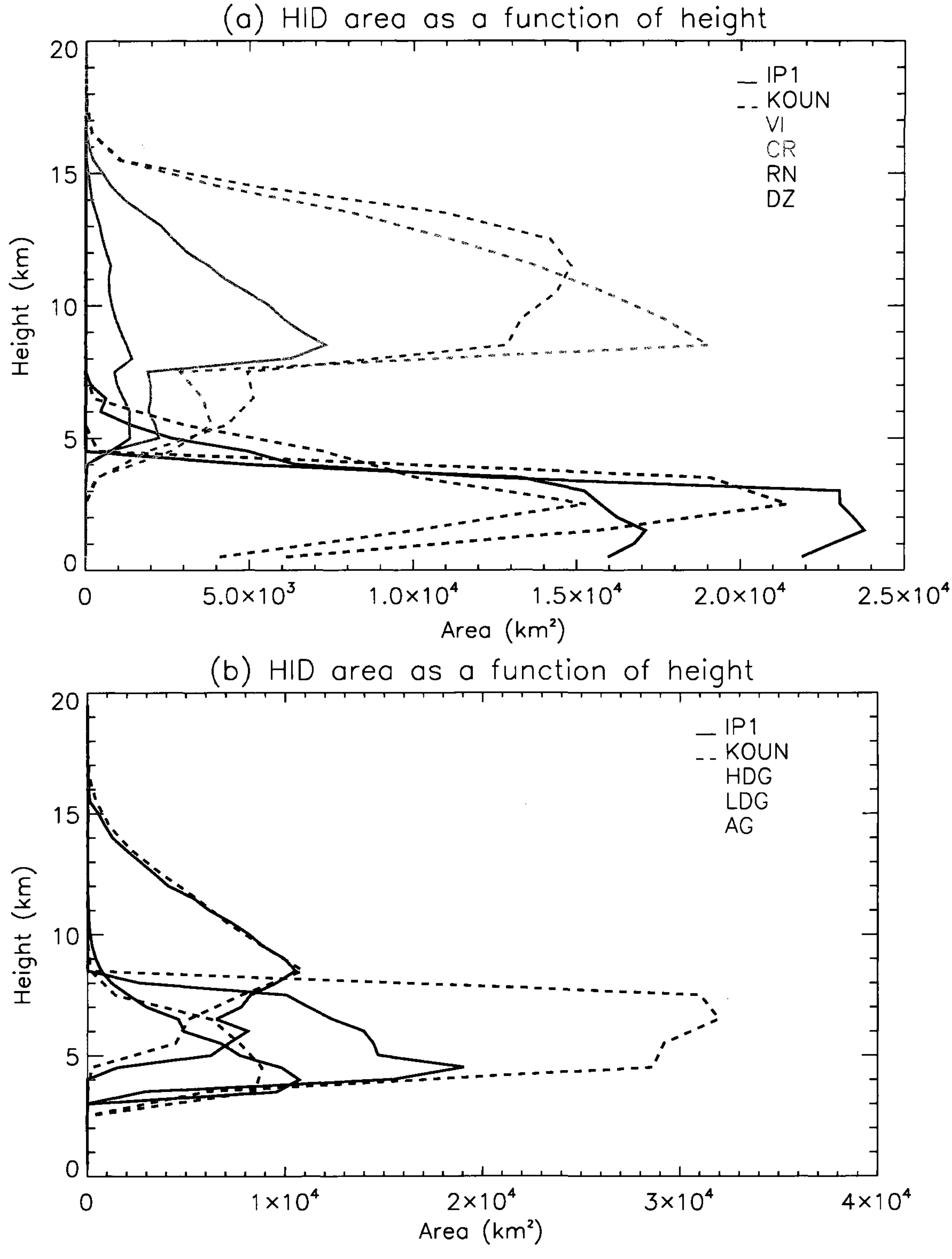

Fig. 4.8: Total HID echo area for different hydrometeors as identified by IP1 (solid) and KOUN (dashed) over the entire storm lifetime. a) Vertically aligned ice crystlas (light green), pristine ice crystals (orange), rain (dark blue), and drizzle (purple); b) high-density graupel (red), low-density graupel (green), and aggregates (light blue).

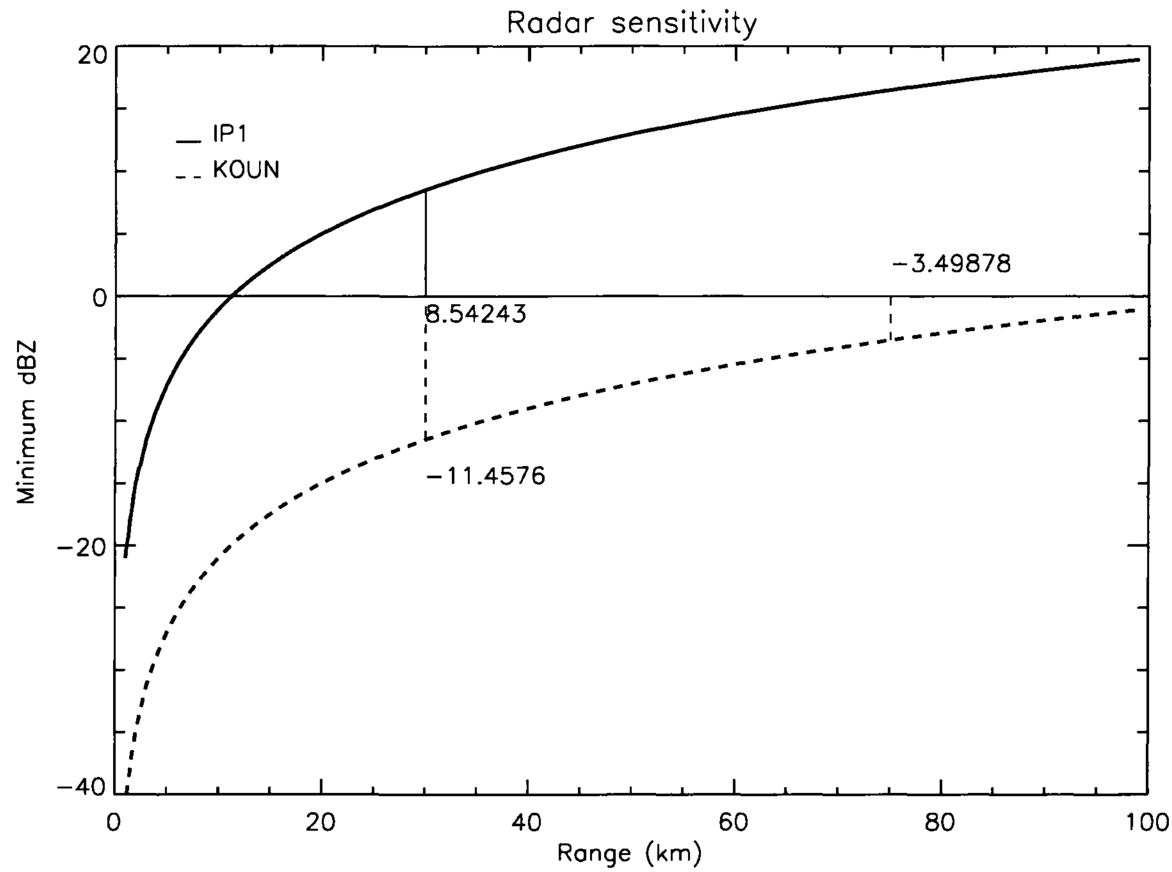

Fig. 4.9: Comparison of radar sensitivity for IP1 and KOUN. The KOUN and IP1 sensitivity at the IP1 maximum range (30 km) and the KOUN sensitivity at the approximate disance to IP1 (75 km) are indicated.

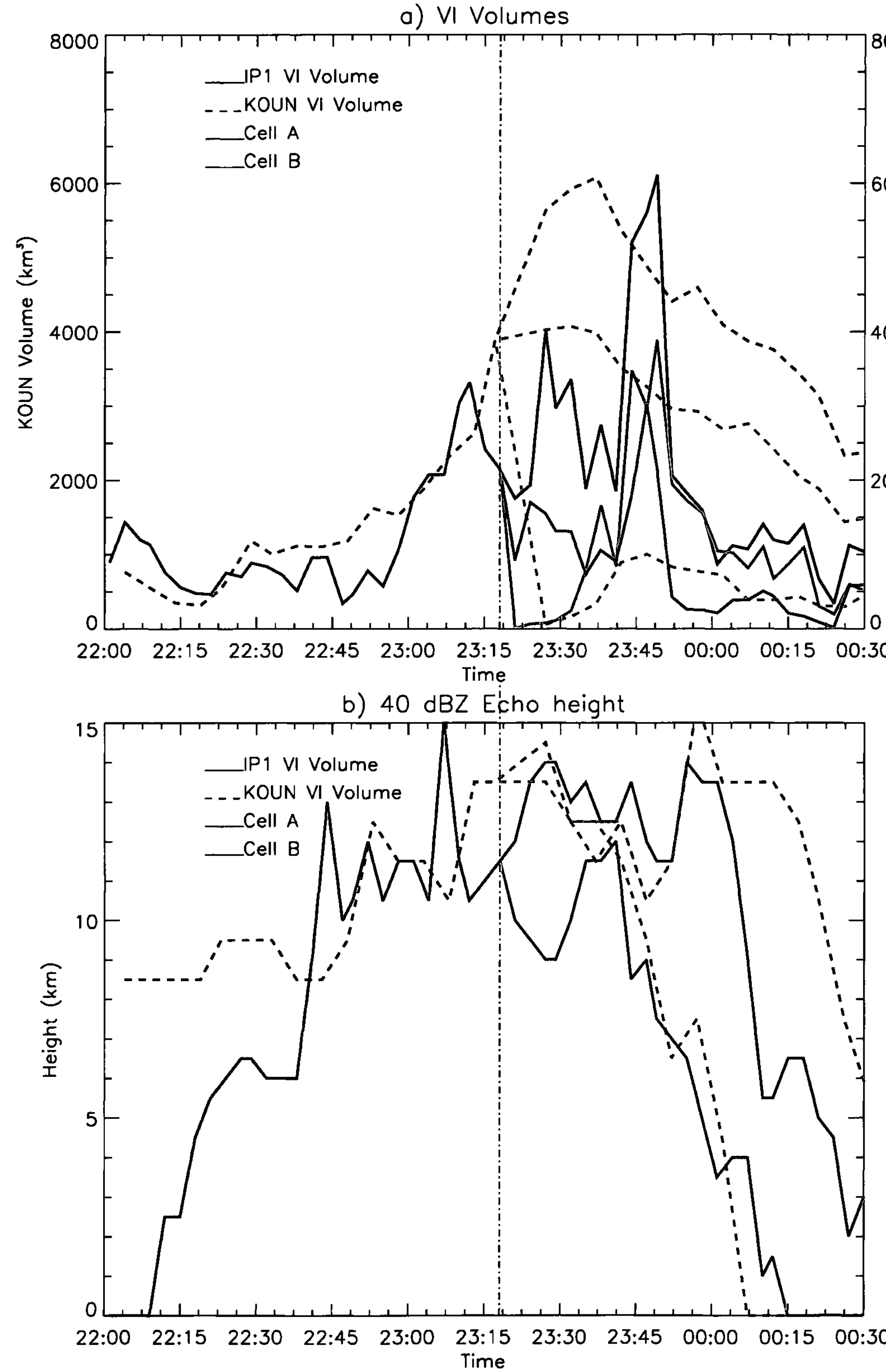

Fig. 4.10: Timeseries of a) VI volumes and b) 40 dBZ echo top height for IP1 and KOUN.

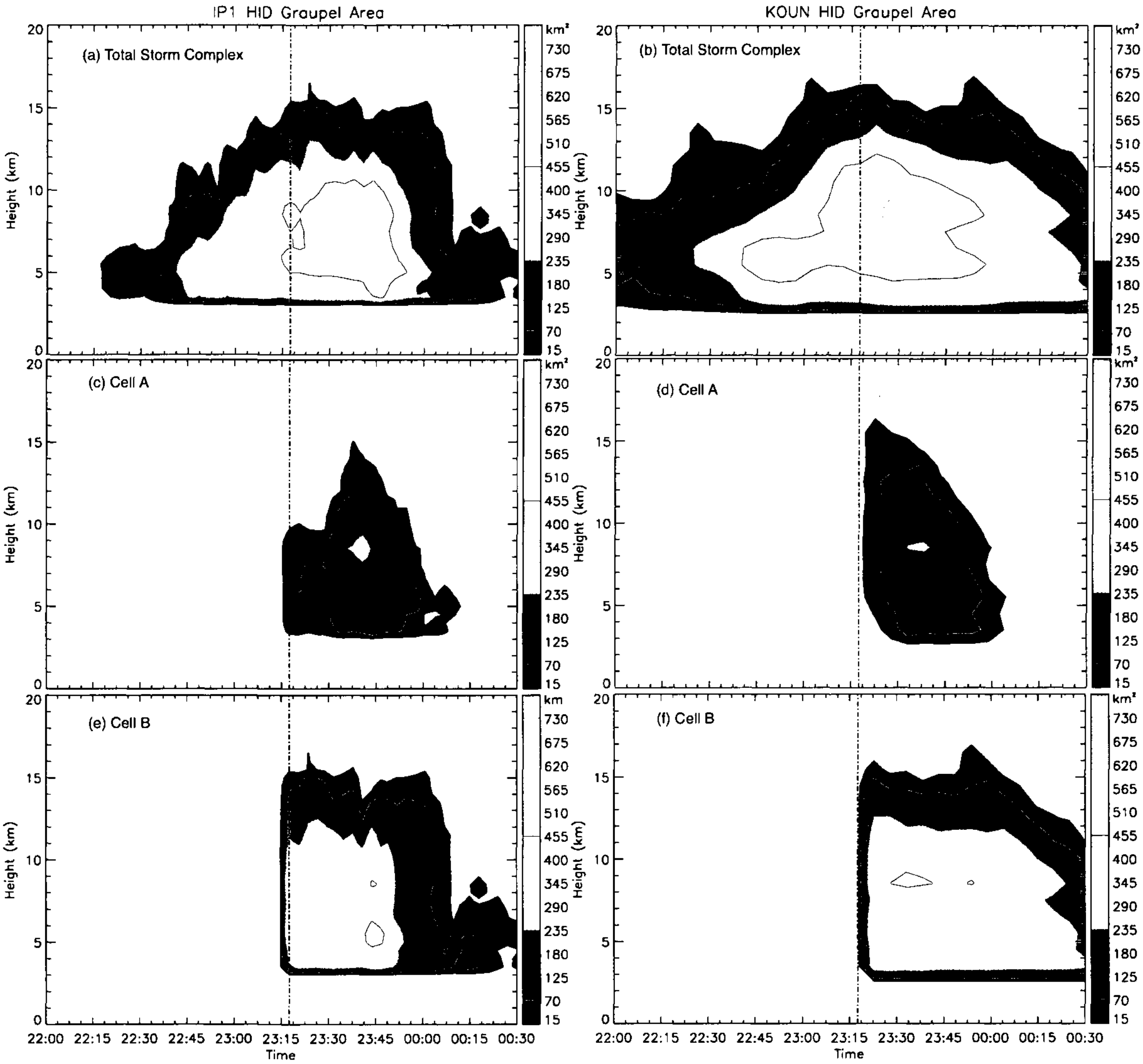

Fig. 4.11: Time-height cross-section of graupel area for IP1 (left) and KOUN (right) for the storm complex (top), cell A (middle), and cell B (bottom). The beginning of the storm split is marked with a dashed-dot line.

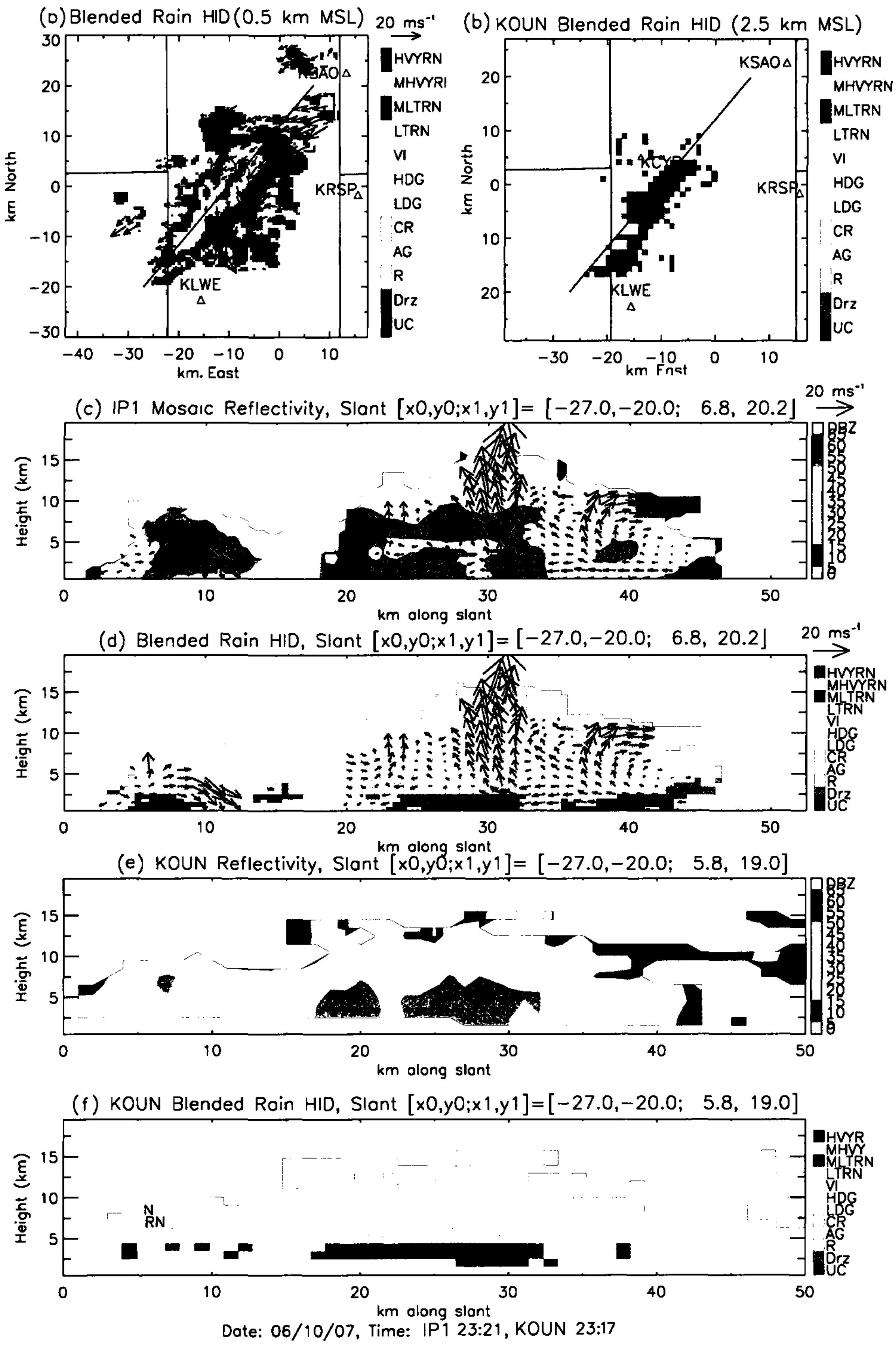

Fig. 4.12: Microphysical and kinematic observations at 2321 UTC by IP1 (a-d) and KOUN (e and f). The expanded HID analysis utilizing the X-band blended rain algorithm to determine surface rain rates below 2.5 km is illustrated in a) and d), and the expanded KOUN HID rain is shown for comparison in f. The vertical cross-sections (c - f) were taken along the direction of propagation, as illustrated by the line in a) and b). Vectors are storm relative winds derived from dual-Doppler analysis.

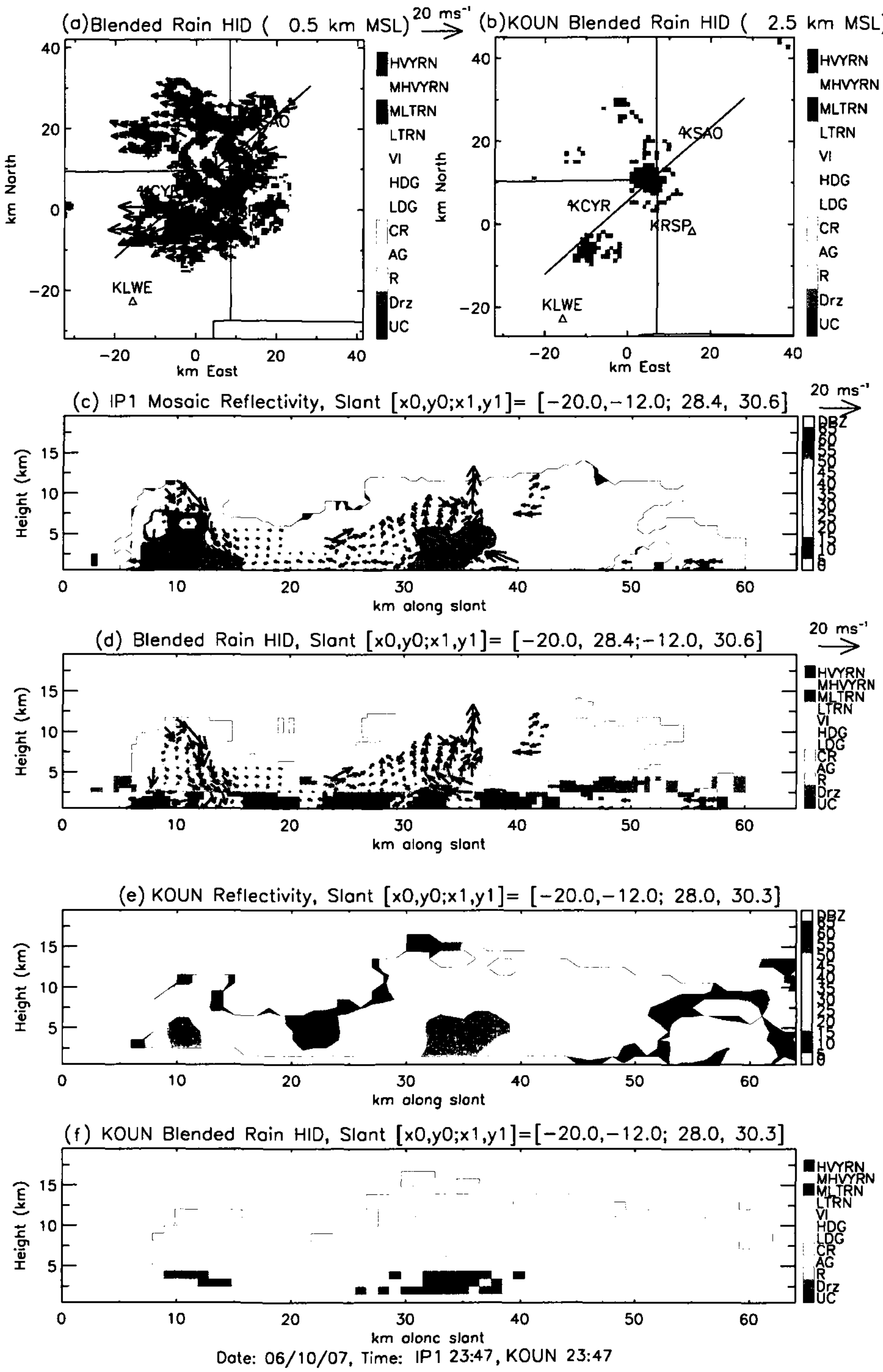

Fig. 4.13: Same as Fig. 4.12, but at 2347 UTC.

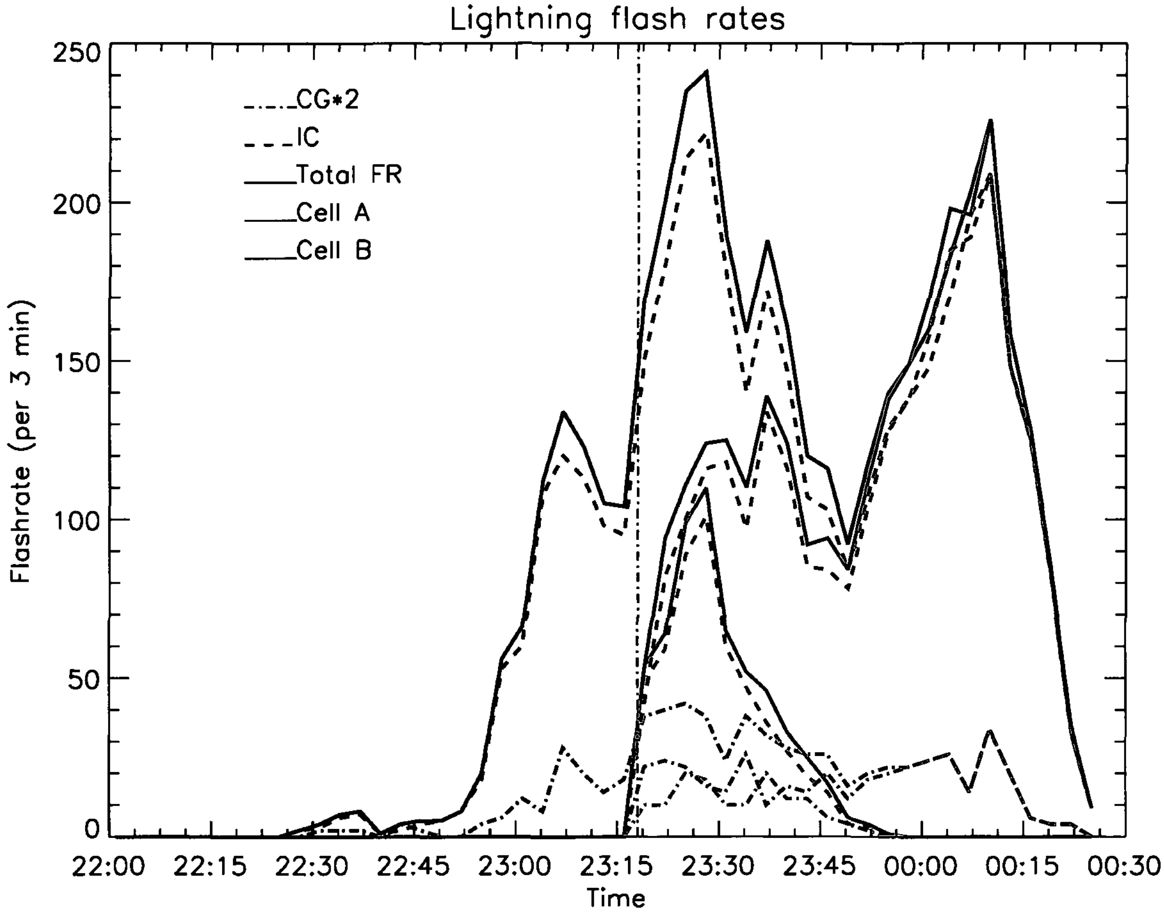

Fig. 4.14: Timeseries of three-minute lightning flash rates for cloud-to-ground (CG) identified by NLDN, intracloud (IC) identified by the OK-LMA, and total flash rate (TFR).

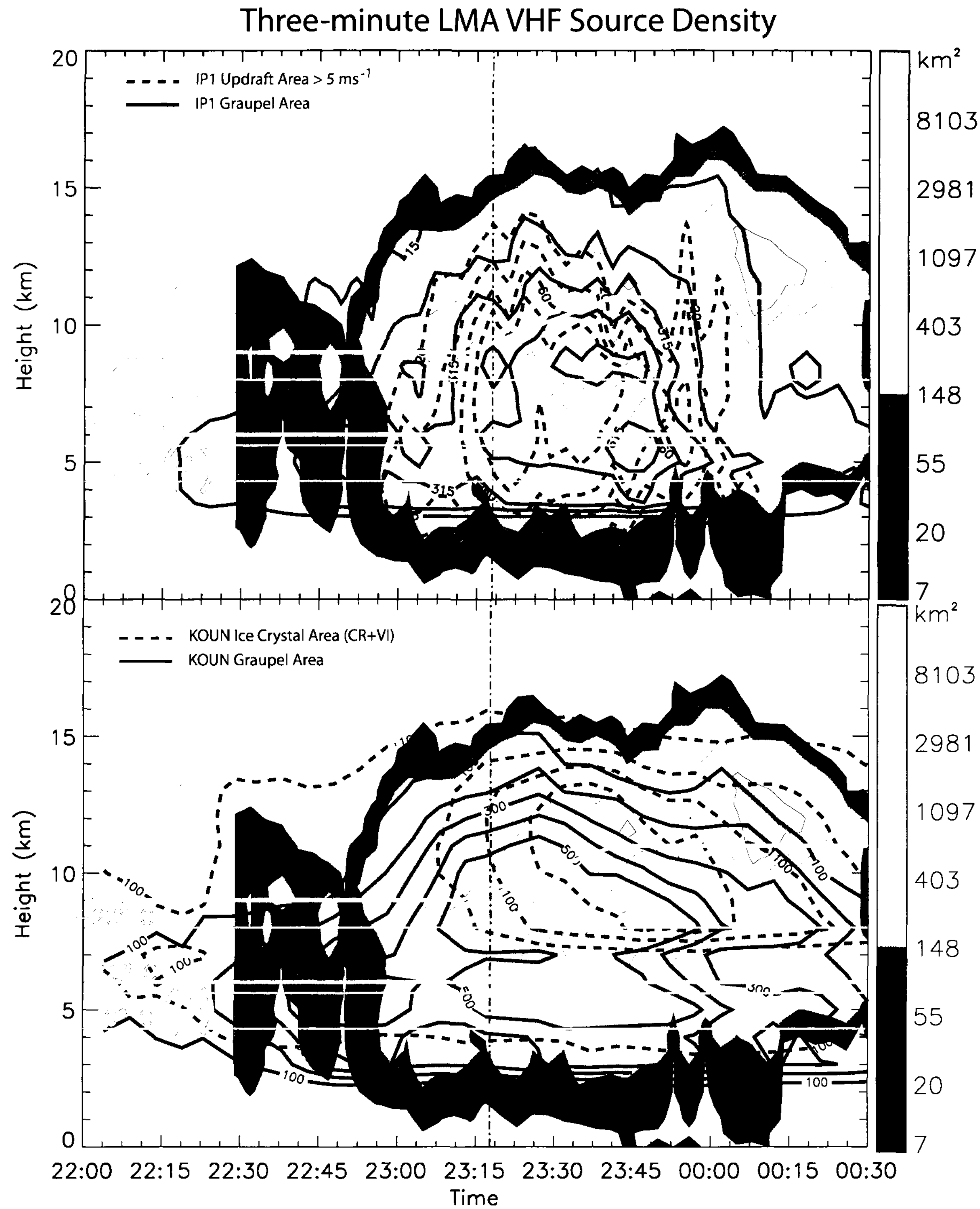

Fig. 4.15: Time-height contours of three-minute OK-LMA VHF source density for the 10 June 2007 storm with contours of top: IP1 Updraft area > 5 m s^{-1} (dashed black line) and graupel area (solid black line) and bottom: KOUN ice crystal area (dashed black line). The inferred charge layers are indicated in orange and the temperature from the 12 Z 10 June 2007 sounding is denoted in gray. The time of storm split is indicated by the dashed-dot line at 2318 UTC.

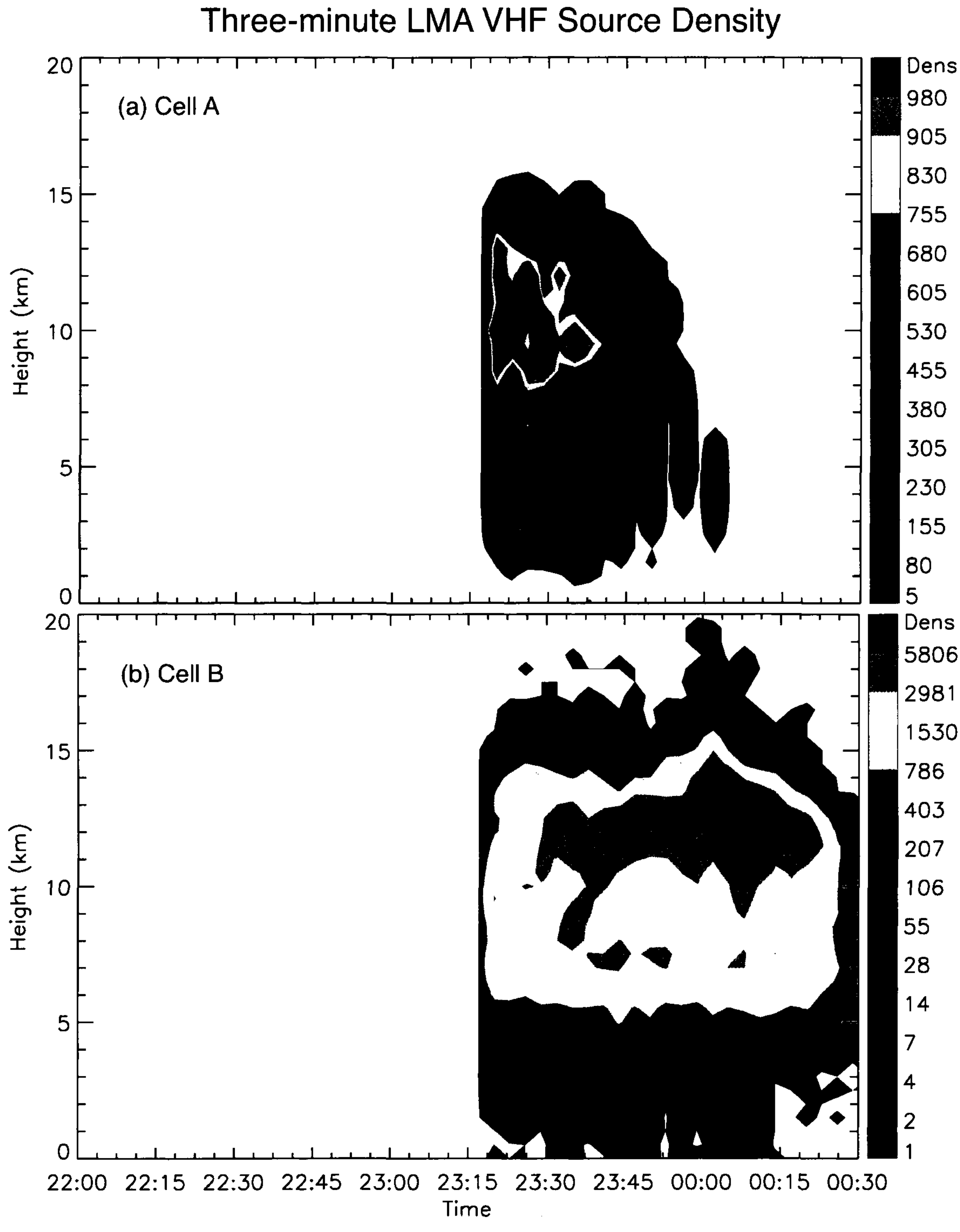

Fig. 4.16: OK-LMA three-minute VHF source density time-height contours for cell A (a) and cell B (b).

Chapter 5

Rainfall Estimation

5.1 Background

Quantitative Precipitation Estimation (QPE) using polarimetric radar has been a topic of interest for at least several decades (Bringi and Chandrasekar, 2001). Polarimetric-based rainfall algorithms have been shown to improve rainfall estimates compared to traditional reflectivity-based algorithms (e.g. Matrosov et al., 1999; Petersen et al., 1999; Brandes et al., 2001; Matrosov et al., 2002; Ryzhkov et al., 2005). K_{dp}, specific differential phase, is relatively insensitive to the drop-size distribution (DSD), contamination from hail, and absolute radar calibration (Zrnic and Ryzhkov, 1996), and therefore could improve rain estimation compared to Z-R relations that are prone to such errors. Many studies have historically used S-band or C-band (e.g. Chandrasekar et al., 1990; Ryzhkov and Zrnic, 1995; Zrnic and Ryzhkov, 1996; May et al., 1999; Brandes et al., 2001) to reduce or eliminate attenuation and non-Rayleigh effects that can occur in moderate and heavy rainfall at shorter wavelengths. However, with the development of better attenuation correction techniques, especially using polarimetric information (e.g. Testud et al., 2000; Park et al., 2005), the use of X-band radars for hydrological applications is now more common (e.g. Jameson, 1991; Jameson, 1994; Matrosov et al., 2002; Anagnostou et al., 2004), due to the portability, compactness, and relatively lower-cost of X-band systems.

A benefit of using X-band for QPE is stronger differential phase shifts, which result in larger specific differential phase (K_{dp}) values at X-band. It was shown in Sec. 3.2, as well as in Matrosov et al. (2006), that K_{dp} is on average 3.7 times greater at X-band than S-band (for the same liquid water path), which is larger than wavelength scaling would predict. Matrosov et al. (2006) showed that the larger differential phase shifts allow for the use of R-K_{dp} estimates of rain rate down to about 2.5-3.0 mm h^{-1}, whereas S-band R-K_{dp} methods are only applicable above 8-10 mm h^{-1}. Although R-K_{dp} relationships are relatively insensitive to DSD assumptions, the coefficient is quite dependant on the equilibrium shape model assumed (Matrosov et al., 2002). As such, Matrosov et al. (2002) proposed including Z_{dr} to help estimate drop oblateness. Z_{dr} provides an estimate of the shape factor that relates drop aspect ratio to drop diameter (Gorgucci et al., 2001). Matrosov et al. (2006) concluded that X-band provides the best rainfall estimates in light- to moderate rain rates, and found that X-band R-K_{dp} rainfall estimators could be used in much lighter stratiform rain than similar S-band estimators due to the enhanced specific differential phase. However, George (2007) performed a similar study that showed no substantial benefit to rainfall estimation using X-band compared to well-tuned, calibrated S-band polarimetric algorithms

5.2 Rain rate algorithms

Since Z_{dr} data during the 10 June 2007 case were uncalibrated, a simplified blended algorithm was applied to CASA IP1 data, as described in Sec. 2.1.4.3. Because R-K_{dp} relationships are significantly influenced by the individual equilibrium drop-shape model chosen, several proposed relationships were compared to determine the best fit for our dataset. Matrosov et al. (2006) derived a relationship based on data from a Joss-Waldvogel disdrometer and an assumed shape factor (that relates the drop aspect ratio to diameter) of 0.56 cm^{-1} (hereafter referred to as R-K_{dp} Matrosov).

$$R=15K_{dp}^{0.76} \tag{5.1}$$

where K_{dp} is in ° km^{-1} and r is in mm h^{-1}. George (2007) built on the R-K_{dp} Matrosov relationship and modified it based on data from the Global Precipitation Mission (GPM) Ground Validation (GV) project conducted in Colorado in 2004. George (2007) used the so-called "bridge shape model" proposed by Thurai and Bringi (2005), resulting in the following R-K_{dp} relationship (hereafter called R-K_{dp} George):

$$R=12.8K_{dp}^{0.77} \tag{5.2}$$

Bringi and Chandrasekar (2001) suggest that wavelength scaling arguments can be applied to R-K_{dp} relationships. They find the exponent of 0.85 and coefficient of 129 for S-band using the Beard and Chuang (1987) shape model, resulting in an X-band R-K_{dp} of

$$R=19.3K_{dp}^{0.85} \tag{5.3}$$

(hereafter referred to as R-K_{dp} BC01). Application of the scaling argument to the S-band R-K_{dp} relationship found during JPOLE (Ryzhkov et al., 2005) results in Equation 2.5, which will be referred to as R-K_{dp} JS. The S-band rain rate estimation algorithms (NSSL, blended, Z-R, and R-K_{dp}) applied to KOUN are described in Sec. 2.2.1.

The four X-band R-K_{dp} functions are plotted in Fig. 5.1. R-K_{dp} BC01 results in the largest rain rate for a given K_{dp} value, while R-K_{dp} George yields the smallest rain rate. At the highest K_{dp} value observed during this case (12° km^{-1}), R-K_{dp} George and

Matrosov result in maximum rain rates of 85 and 99 mm h^{-1}, respectively. R-K_{dp} BC01 yields the highest rain rates, with a maximum of 159 mm h^{-1}, while the R- K_{dp} JS curve falls between the others at 123 mm h^{-1}. For relatively small K_{dp} values (< 2° km^{-1}), differences between the relationships are less substantial, on the order of 5 mm h^{-1}. With the exception of R-K_{dp} BC01, the exponents are similar, indicating that the assumed shape model (indicated by the coefficient used) plays a significant role in the rain rate retrieval.

A rain rate histogram of data at 2.5 km MSL from IP1 and KOUN during the 10 June 2007 case is shown in Fig. 5.2. Data were binned into 2.0 mm h^{-1} bins, with the minimum bin set to 3.0 mm h^{-1}, corresponding to the approximate minimum rain rate measurable with a K_{dp} threshold of 0.1 ° km^{-1} at X-band. The four X-band R-K_{dp} relationships are relatively similar below rain rates of 40 mm h^{-1}, at which point they begin to deviate significantly due to the exponential nature of the relationships. Again, it is clear that R-K_{dp} BC01 results in the largest number of high rain rates, while the R-K_{dp} George results in an insignificant percentage of rain rates above 70 mm h^{-1}. The most logical choice of R-K_{dp} relationship is the Oklahoma-tuned R-K_{dp} scaled to X-band (R-K_{dp} JS), since it likely accounts for the drop shapes found in that environment.

Choice of the R-K_{dp} JS is supported by comparison with rain rate histograms derived from S-band KOUN data. The IP1 R-K_{dp} JS provides the closest match to both the KOUN NSSL and KOUN blended curves (Fig. 5.2). IP1 R-K_{dp} George and Matrosov fall short of the KOUN NSSL and blended curves, while R-K_{dp} BC overshoots both significantly. Interestingly, the JPOLE R-K_{dp} applied to KOUN is biased towards higher rain rates compared with both the KOUN NSSL and blended algorithms.

5.3 Rain rate comparisons between S- and X-band

The relative rain rate histogram (Fig. 5.2) also allows for comparisons between wavelengths. The Z-R relationship applied at both X and S-band shows relatively good agreement from low to moderate rain rates, but then begins to deviate significantly around 80 mm h^{-1}, with X-band tending toward a larger portion of higher rain rates (Fig. 5.2a). This could be due to the increased reflectivity at X-band compared to S-band due to non-Rayleigh backscattering (see Sec. 3.2), or a factor of taking the highest value for IP1 before calculating the rain rate, or possibly the grid resolution difference between KOUN and IP1. The X-band blended algorithm using R-K_{dp} JS relationship closely follows the R-K_{dp} JS curve, although the blended curve is slightly biased towards higher rain rates resulting from the use of the Z-R relationship. The S-band blended algorithm is also surprisingly similar to the X-band blended rain rate, but is even more biased towards higher rain rates, and shows a smaller percentage of occurrences of rain rates below 15 mm h^{-1}. Generally the S-band algorithms capture more heavy rain grid points and fewer light rain grid points (< 15 mm h^{-1}; Fig. 5.2b). This could be the result of many factors, including attenuation of the X-band signal in extremely heavy rain (> 100 mm h^{-1}) resulting in a smaller percentage of heavy rainrates. The KOUN R-K_{dp} trend deviates from the other S-band algorithms, particularly in light rain rates (Fig. 5.2b), due to K_{dp} values at S-band. A very small percentage of rain rates below 7 mm h^{-1} are observed by KOUN R-K_{dp}, while the other S-band algorithms see a larger percentage of small rain rates, with the relative percentage decreasing with increasing rain rate. Additionally, X-band algorithms using K_{dp} identify large percentages of rain rates less than 7 mm h^{-1}

where the S-band R-K_{dp} does not. This supports the conclusion drawn by Matrosov et al. (2006) that the more reliable K_{dp} data at X-band (due to larger differential phase shifts) can increase the usability of R-K_{dp} estimators down to rain rates less than 8 mm h^{-1}, which is where S-band R-K_{dp} estimates become noisy or unobtainable.

The relative frequency of rain estimators used in the blended algorithms as a function of reflectivity is shown in Fig. 5.3a. At X-band, the frequency distribution of both relationships is a well-defined bimodal distribution, with a cross-over from R-Z to R-K_{dp} at 28 dBZ. That is, when the reflectivity is small, spherical or nearly spherical drops produce little to no differential phase shift, making R-K_{dp} of little use. The S-band blended algorithm frequency distributions are more complicated, since five rain estimators are employed. Below 18 dBZ, the straightforward Z-R relationships are used most often, again due to the small differential backscattering for nearly spherical drops at small reflectivities. Between 18 and 36 dBZ, the modified R-Z relationship using only the reflectivity due to rain identified using the difference reflectivity field is most commonly chosen. This method assumes there is some amount of contamination in reflectivity due to ice, which is removed using a rain line calculation (see discussion in Sec. 2.2.1). Above 36 dBZ, estimators using the differential polarimetric information are most frequently used, with R-K_{dp}-Z_{dr} chosen over 80% of the time for reflectivities over 50 dBZ. S-band K_{dp} estimators (R-K_{dp} and R-K_{dp}-Z_{dr}) are not used below reflectivities of 36 dBZ. Again, this is consistent with the finding of Matrosov et al. (2006), who showed the extension of R-K_{dp} rain estimators down to lighter rainrates at X-band. A cumulative distribution function (CDF) was constructed for reflectivity, and using the results of the relative frequency histogram, the most frequently used rainrate algorithms for given reflectivity ranges are indicated (Fig. 5.3b) for both X- and S-band. It is clear that although the X-band blended algorithm uses R-Z for 50% of reflectivities, it is far less than at S-band, which uses R-Z based methods for nearly 80% of reflectivities. At S-band, differential polarimetric information (K_{dp} and Z_{dr}) are only utilized for the highest 20% of reflectivity.

A comparison of instantaneous rain rates at 2344 UTC 0.5 and 2.5 km MSL derived from the X-band blended, Z-R, and R-K_{dp} JS relationships are shown in Fig. 5.4. The corresponding DZ, K_{dp} and HID fields are shown in Fig. 5.5 for reference. The difference between maximum rain rates utilizing K_{dp} versus Z-R is immediately evident. The IP1 blended and R-K_{dp} indicate small areas with maximum rain rates of 85 mm h^{-1}, while the Z-R maximum exceeds 100 mm h^{-1} in wide areas of the storm, particularly in the southwestern cell (cell A). The location of the maximum rain rates from the R-K_{dp} and blended algorithms at 0.5 km MSL are offset to the northwest from the maximum rain rate derived from the Z-R relationship, an important discrepancy for hydrological applications. The KOUN rain rates, DZ, HID and K_{dp} at the same time at 2.5 km MSL are shown in Fig. 5.6. Due to the distance from the center of the network to KOUN, complete coverage is not available at 0.5 km, and as such, 2.5 km was used to compare with IP1. KOUN R-K_{dp} shows very little area of rain rates below 10 mm h^{-1}, and shows maximum rain rates in the northeastern cell (cell B) of 75 mm h^{-1}, and greater than 108 mm h^{-1} in the southwestern cell (cell A). Comparisons of the S- and X-band R-K_{dp} reveals that IP1 has greater coverage of the light rain rates surrounding the main reflectivity core. With the exception of the blended algorithm, all of the KOUN rain rates show a targeted area of maximum rain rates occurring at approximately x=5 km and y=10 km. The KOUN blended algorithm is offset to the northwest from the other algorithms. Again, the Z-R algorithm yields the largest areas of maximum rain rates, with rain rates exceeding 108 mm h^{-1}, while the NSSL and blended algorithms show similar maximums of 75 mm h^{-1} in the northeastern cell (cell B), but deviate significantly in the southwestern cell (cell A).

It is interesting to compare the X-band and S-band blended algorithms to determine which method is selected most often. Fig. 5.7a shows a relative histogram of the number of grid points at which each method is used for the X-band and S-band algorithm. At X-band, the R-K_{dp} method is used more often than the R-Z method (64% versus 46%). In fact, the R-Z method is utilized even more than would be expected because the K_{dp} threshold of 0.1 ° km^{-1} is only met in 64% of grid points. A CAPPI at 2344 UTC (Fig. 5.5g and h) of the method used in the rain rate calculation illustrates that the majority of points utilizing R-Z fall along the edges of the storm where K_{dp} is ≤ 0. This is an artifact of the K_{dp} calculation method, where K_{dp} around the edges of the storm are noisy due to the filtering method. However, the HID indicates many of these points are drizzle, meaning that the volume could be comprised of small, nearly spherical drops which result in little to zero K_{dp}. If the rain volume (taken to be the total of all rain rates) is considered, than it is clear that R-K_{dp} is responsible for the majority of the rainfall volume at X-band (Fig. 5.7b).

The KOUN blended algorithm, interestingly, uses R- K_{dp} the least, and the R-Z-Z_{dr} and R-Z_{rain} methods the most (Fig. 5.7a). The polarimetric variables are invoked in less than half of the grid points (42%) to aide in the rain rate calculation. The excessive use of the R-Z_{rain} method could result from the ice fraction calculation, which tends to be anomalously high when reflectivity is low due to small differences in the h and v reflectivities that lead to large difference reflectivity values (Z_{dp}; R. Cifelli, personal communication, 2008). Considering the rain volume accounted for by each S-band calculation method, the R-K_{dp}-Z_{dr} method alone is responsible for > 50%, while R-Z and R-Z_{rain} actually contribute little to the overall rain volume. Thus, the polarimetric rain estimators contribute the bulk of the total rain volume compared to the power-based estimators.

The total rainfall accumulation swath for the IP1 blended, R-K_{dp} JS, and Z-R algorithms is shown in Fig. 5.8. Using Z-R clearly results in a much wider swath of rainfall greater than 40 mm over the 2.5-hour lifetime of the storm. The R-K_{dp} JS and blended swaths look similar, with small differences. This is expected since R-K_{dp} accounted for the majority of rain volume, as shown in Fig. 5.7b. The IP1 blended swath shows the rainfall maximum at x=-10 km and y=-5 km. A wide area of accumulations from 0.5 to 5.0 mm is evident around the storm. For reference, the swaths of DZ and K_{dp} are provided (Fig. 5.9).

The KOUN total accumulation swaths are shown in Fig. 5.10. The KOUN blended and NSSL algorithms show striking similarities, although the NSSL algorithm produces more rainfall than the blended algorithm. Both algorithms show two maxima, although the blended algorithm suggests the peak is to the west of the NSSL peak at x=-10 km, y=-7 km. The KOUN Z-R relationship, like the IP1 counterpart, identifies a large area of rainfall accumulation greater than 40 mm, and generally has higher accumulations than KOUN blended or NSSL. KOUN R-K_{dp} is not as smooth as any of the other methods, and does not generally show the same rainfall pattern as the other algorithms. Compared with the X-band R-K_{dp}, the IP1 rainfall retrieval is much smoother and does not accumulate large areas of rainfall. The IP1 R-K_{dp} also shows distinct areas of 0.5-1.0 mm accumulations around the edges of the storm, while KOUN R-K_{dp} is much patchier. The KOUN K_{dp} swath (Fig. 5.11b) reveals that this is due to a relatively noisy K_{dp} field. The smoother retrieval from IP1 highlights a strength of X-band, in that differential phase shifts are larger, and therefore less noisy when filtered into a range derivative field compared to S-band, resulting in more homogeneous rainfall retrievals.

Time-height cross-sections of the rainmass flux integrated over the horizontal domain derived from the IP1 and KOUN blended rain rate methodologies are shown in Figs. 5.12 and 5.13. The IP1 blended algorithm illustrates a wide column of rain during the period from 2323-2355 UTC, with the largest flux occurring at the surface between 2327 UTC and 2337 UTC. An interesting peak occurs between 2.5 and 4.0 km just after 2300 UTC. Comparing with the graupel area cross-sections (Fig. 4.11), it is apparent that the largest rainmass fluxes are associated with times where the graupel areas above are the largest. This is an illustration of a mixed-phase precipitation process, whereby rainmass at the surface is supported by graupel falling through the melting layer to form liquid precipitation below the melting layer. The IP1 Z-R method produces a much larger rainmass flux than the blended or R-K_{dp} methods, and the peak occurs between 2 and 4 km at 2333 UTC, reaching the surface a few minutes later at 2338 UTC. The KOUN blended rain mass flux shows the largest flux slightly earlier than IP1 between 2300 and 2340 UTC. The largest KOUN rainmass fluxes occur between 2.5 km and 4.5 km, while the IP1 fluxes are maximized below 4 km. This is a result of the lack of coverage of KOUN below 2.5 km during the initial storm period. The lag between IP1 and KOUN is most likely due to the time it takes for particles to fall between a height of 4 km and 0.5 km. The KOUN NSSL rainmass flux time-height series shows the second peak in mass flux occurring between 4 and 5 km at 2325 UTC. KOUN Z-R shows a similar trend to the KOUN blended algorithm, while the KOUN R-K_{dp} illustrates a tri-modal structure with the second peak occurring at 2.5 m at 2318 UTC.

5.4 Comparison with surface gauge measurements

As discussed in Sec. 2.2.3, several surface-based rainfall observations were available for this storm. The locations of the NSSL 2DVD and four Mesonet sites are illustrated in Figs. 5.4-5.6.

Three minute instantaneous accumulations were calculated from the minute data provided by the 2D-VD. The three and five minute instantaneous accumulations using IP1 and KOUN data, respectively, calculated over the gauge are shown in Fig. 5.14a. The 2D-VD rain trace shows the smallest instantaneous accumulation, while KOUN algorithms generally show the highest, most likely due to the height difference of 2.5 km versus the surface. KOUN algorithms also show the rain starting nearly 15 minutes before the 2D-VD shows any accumulation, and 7-10 minutes before IP1 detects any accumulation. Assuming a constant fall velocity of 6 ms^{-1}, it would take approximately 5.5 minutes on average for raindrops observed by KOUN at 2.5 km to fall 2.0 km to the IP1 observation at 500 m. Thus, the timing differences could be due to the fallout time of rain, as well as time resolution differences between KOUN, IP1 and the surface gauges.

The IP1 instantaneous accumulation trace shows coincident peaks in accumulation with the 2D-VD, but in some cases the accumulation is larger as detected by IP1. IP1 also shows a small peak occurring about three minutes before the 2D-VD shows any significant accumulation. Although the height difference is small between IP1's lowest level and the gauge at the surface (500 m and 300 m, respectively), there could be some amount of evaporation or advection of drops between the two observation platforms, although this effect is probably small. Instantaneous accumulations over the Mesonet stations generally show the same trend, with the 5-minute peak accumulation identified by the tipping bucket occurring later compared to either radar (Fig. 5.14b-e). This is especially true of the CHIC and NINN sites (Figs. 5.14b, e). The timing difference is most likely due to the five-minute time resolution of the tipping bucket gauges. With the exception of the ACME site (Fig. 5.14c), instantaneous accumulation timeseries show that the different radar-based rainfall methods generally follow the same trend, but with different amplitudes, and the tipping bucket gauges have much less structure than the radar-based calculations, due to the sampling resolution.

The total cumulative rainfall distributions clearly show the delay between KOUN, IP1 and the surface sensors (Fig. 5.15). It is clear that although the timing of the peaks in rain rate were similar, differences in the magnitude translate into large differences in the total accumulated rainfall. The total rainfall measured by the 2D-VD over this time period is 13.5 mm, while the IP1 blended algorithm at 0.5 km calculates 22.0 mm and the KOUN blended algorithm at 2.5 km estimates 20.6 mm (Table 5.1). At the CHIC Mesonet station in the north part of the CASA IP1 network, the story is quite a bit different. The gauge total measures 17.5 mm (Table 5.1), and all other methods, with the exception of KOUN Z-R, measure a smaller amount of total rainfall. The IP1 blended algorithm estimates 12.2 mm, IP1 Z-R 10.5, KOUN blended 12.2 mm, and KOUN Z-R with highest total of 20.5 mm. The KOUN NSSL has the closest total to the gauge, with 14.6 mm. At both NINN and ACME, all of the radar algorithms overestimate the gauge-measured accumulation. In both cases, the KOUN blended and NSSL algorithms come the closest to the gauge value. At APAC, where the IP1 Z-R relation was not available, the IP1 blended algorithm (using only R-K_{dp}) provides the best estimate to the gauge measured rainfall, while the KOUN algorithms underestimate the total.

The mean relative bias and standard deviation between the gauge and radar accumulations was calculated for each rain algorithm (Table 5.1, Matrosov et al., 2002). The IP1 blended and R-K_{dp} algorithms had lower biases and standard deviations than the IP1 Z-R, but all three algorithm's errors were much higher than any of the KOUN methods. At both wavelengths, including polarimetric information decreases the overall standard bias and standard deviation compared with the ground measurements. Although the errors are high, comparison between a radar volume measurement and point measurements at the surface is always a difficult problem, due to sampling differences such as temporal resolution, time of measurement, and height of measurement (Matrosov et al., 2002). Comparisons between radars with unmatched beams are also difficult due to similar sampling issues (Matrosov et al., 2006). Additionally, radar measurements in strong reflectivity gradients, or near edges are often noisy and can lead to noisy K_{dp} fields, leading to noisy rain rates that translate into large variability in total rainfall accumulation.

5.5 Discussion

Qualitative results from this case study illustrate the benefits of the IP1 X-band network for rainfall estimation. That is, in this case the IP1 radars observe closer to the ground and can therefore provide a better estimate of the actual surface rain rates compared to KOUN, which due to the distance from the analysis area, is only able to see down to 1.5-2.5 km. The larger differential phase shifts at X-band also provide a smoother, more reliable K_{dp} field that translates into less noisy rainfall fields. The improved temporal resolution of the IP1 radars (3 minutes vs. 5 minutes) also allows for better pinpointing of areas of heavy rainmass flux and surface rain rates. This study also showed, as many previous studies have, that using the information contained in the polarimetric variables can improve the rain estimation. Quantitative analysis showed that the IP1 R-K_{dp} could be used down to rain rates of 2.5-3 mm h^{-1}, whereas S-band R-K_{dp} estimated rain rates were not available below 8 mm h^{-1}. Cumulative distribution functions illustrated the applicability of different rain rate estimators as a function of reflectivity. The X-band polarimetric rain rate estimator (R-K_{dp}) was used most frequently above 28 dBZ, corresponding to nearly half of all reflectivity points, while Z-R was used for lower reflectivities. The S-band blended algorithm used power-based estimators (Z-R and R-Z_{rain}) for all reflectivities below 36 dBZ, representing over 80% of all reflectivity points. Polarimetric-based estimators (R-Z_h-Z_{dr}, R-K_{dp}, and R-K_{dp}-Z_{dr}) were almost exclusively used for reflectivities greater than 36 dBZ.

However, quantitative analysis over several gauge sites during this case showed that the IP1 errors were much larger than the KOUN errors, despite the height difference in the measurements. The NSSL algorithm had the lowest bias and standard error compared with ground-based gauges. The dependence of R-K_{dp} on assumed drop shape model was also illustrated, underscoring the need to choose a relationship representative of the environment being investigated. The large standard error associated with the IP1 rain estimators could be due to a number of different sources, including the greatest value gridding method, the calculation of K_{dp}, the short duration of the rainfall, low-level beam-blockage, and the calculation of rainfall from a single grid point.

It should be emphasized that this is one case; many more would be needed to conclusively show the advantages and disadvantages of using an X-band network such as IP1 for QPE. Adding Z_{dr} into the X-band blended algorithm could also improve the rainfall retrievals, as Matrosov et al. (2002) and Anagnostou et al. (2004) showed the effectiveness of so-called "combined estimators", which utilize K_{dp} and Z_{dr}, for X-band QPE. The short duration of rainfall over many of the gauge locations also makes quantitative comparison difficult; a longer period of rainfall would produce more robust comparisons.

Table 5.1: Mean relative bias and standard deviations between the surface-based rainfall observations and the radar-derived accumulations.

	NINN (mm)	CHIC (mm)	DVD (mm)	ACME (mm)	APAC (mm)	Bias	Sdev
GAUGE	8.13	17.5	13.5	0.51	5.33	-	-
IP1 Blend	10.7	12.2	22.0	2.0	6.0	75%	84%
IP1 ZR	19.1	10.5	23.2	1.5	-	99%	109%
IP1 KD	10.5	11.9	22.0	1.7	6.0	68%	75%
KOUN Blend	9.9	12.2	20.6	1.1	2.5	39%	53%
KOUN ZR	11.0	20.5	28.6	1.4	4.1	63%	72%
KOUN NSSL	8.6	14.6	22.6	1.1	2.5	23%	51%

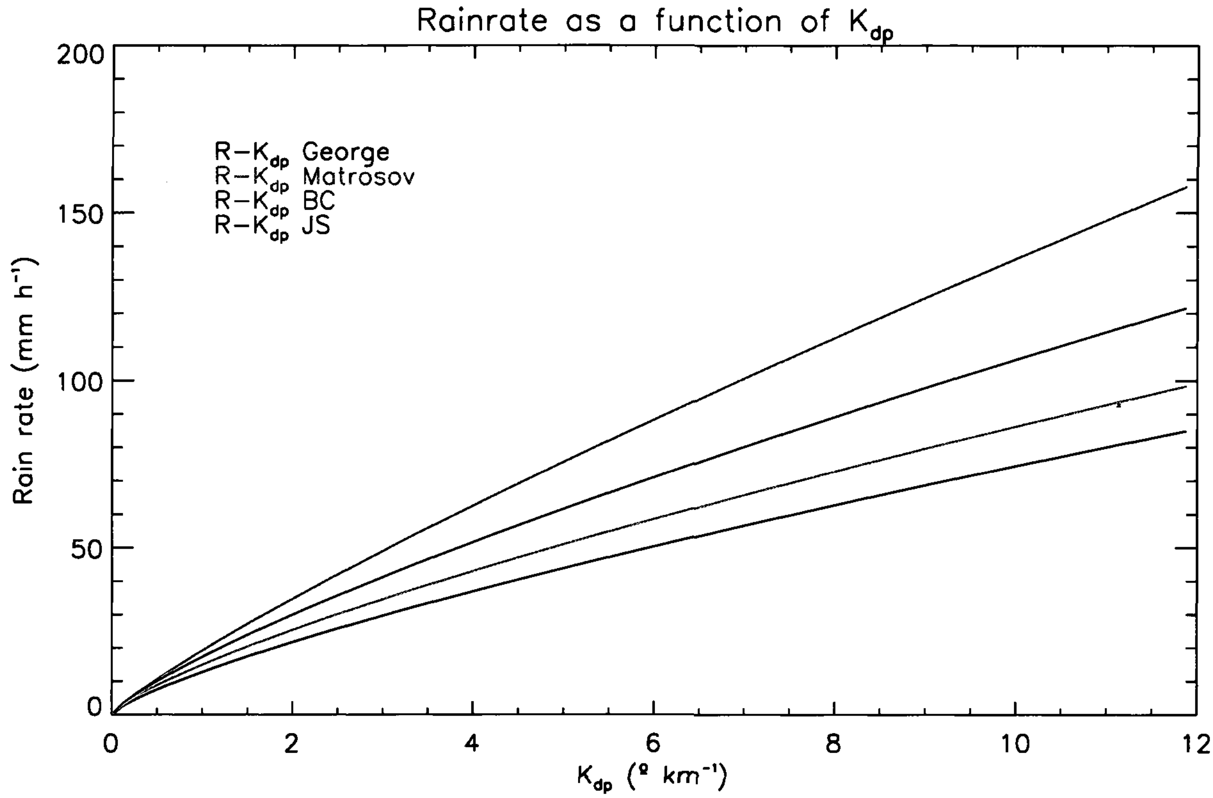

Fig. 5.1: Rain rate (mm h^{-1}) as a function of K_{dp} (° km^{-1}) for different R-K_{dp} X-band relationships.

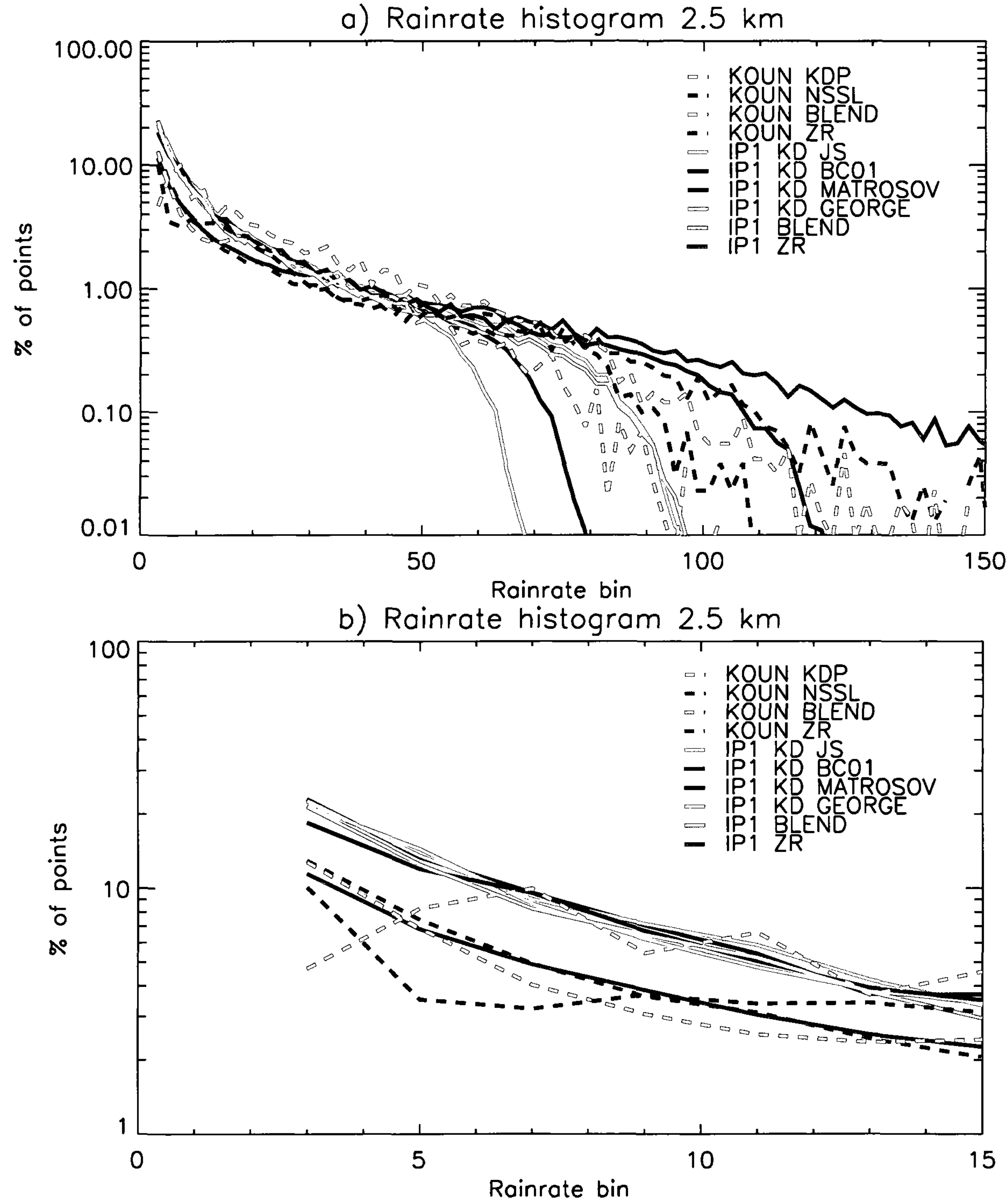

Fig. 5.2: Relative frequency of rain rates occurring during the 10 June 2007 case. Data were taken at 2.5 km during the entire 10 June 2007 event and binned into 2 mm h^{-1} bins starting at 3 mm h^{-1}. a) is plotted on a logarithmic scale, b) is zoomed in on light rain rates (0-15 mm h^{-1}).

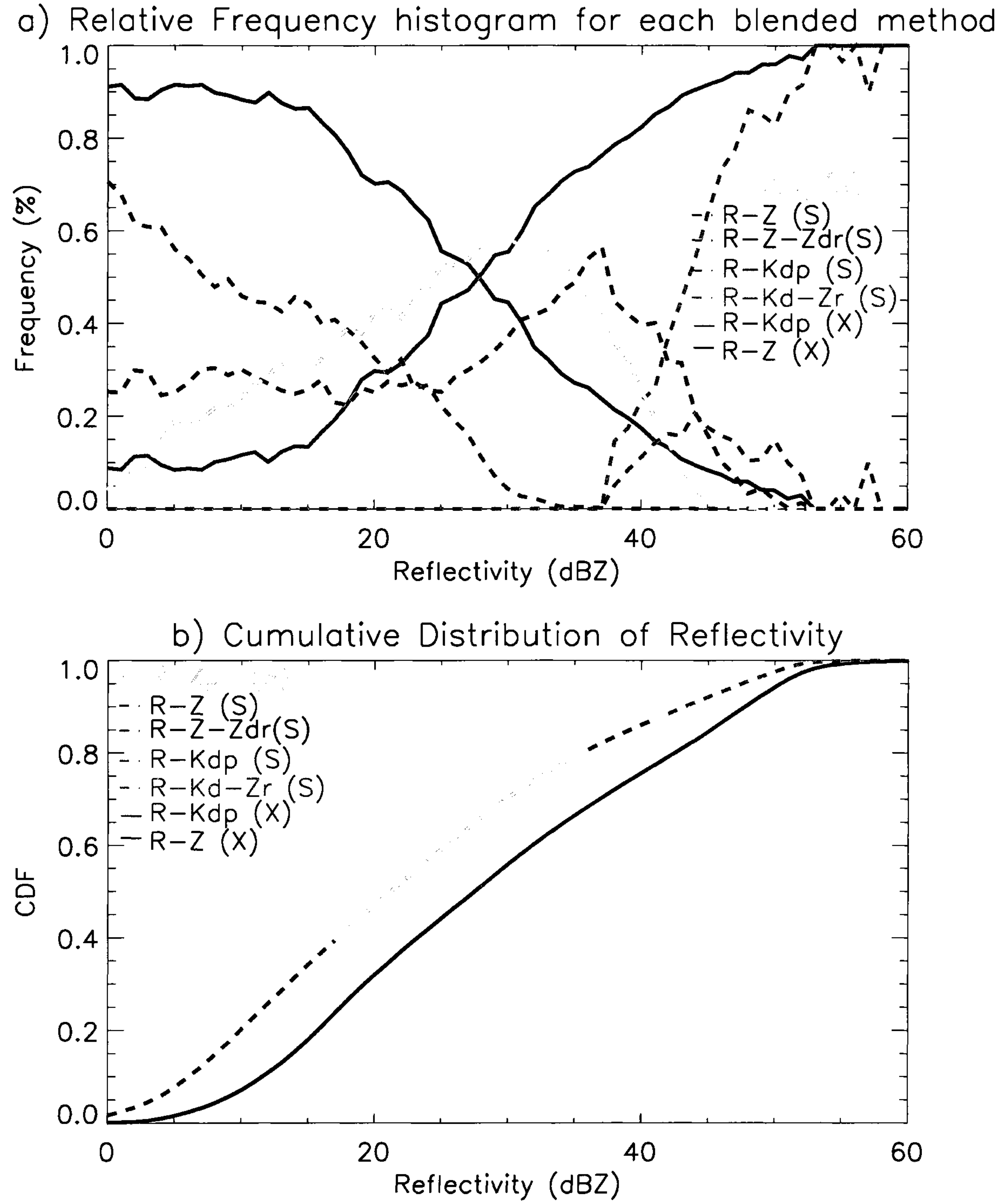

Fig. 5.3: a) Relative frequency of different rain estimators used in the X- and S-band blended algorithms (reflectivity bins are 1 dBZ). b) Cumulative distribution function for reflectivity at 2.5 km during the 10 June 2007 case. The relationship most frequently used for each reflectivity bin is indicated by color.

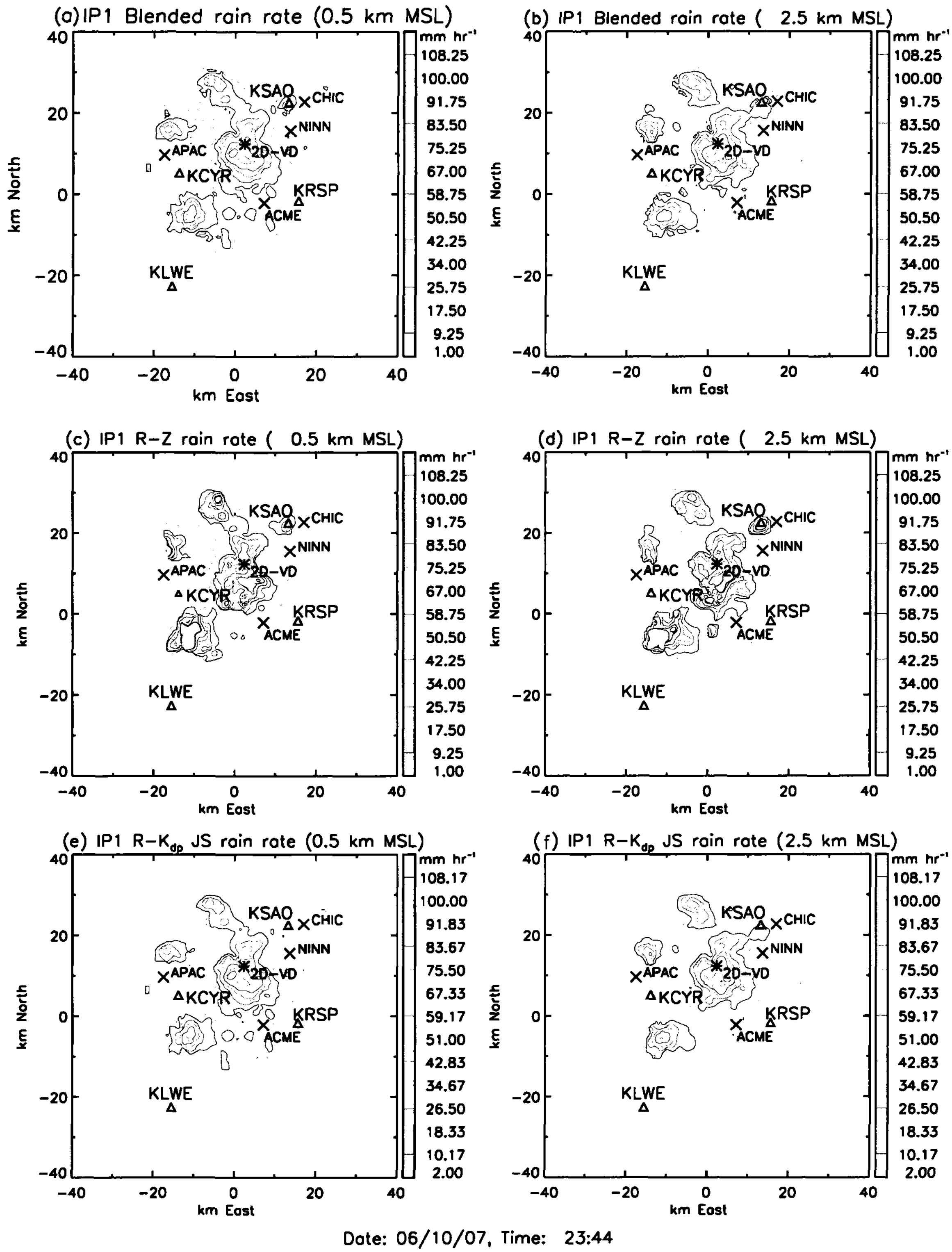

Fig. 5.4: IP1 instantaneous rainrate CAPPIs at 2344 UTC on 10 June 2007 at 0.5 km (left) and 2.5 km (right) using the blended (top), R-Z (middle) and R-K$_{dp}$ (JS) (bottom) estimators.

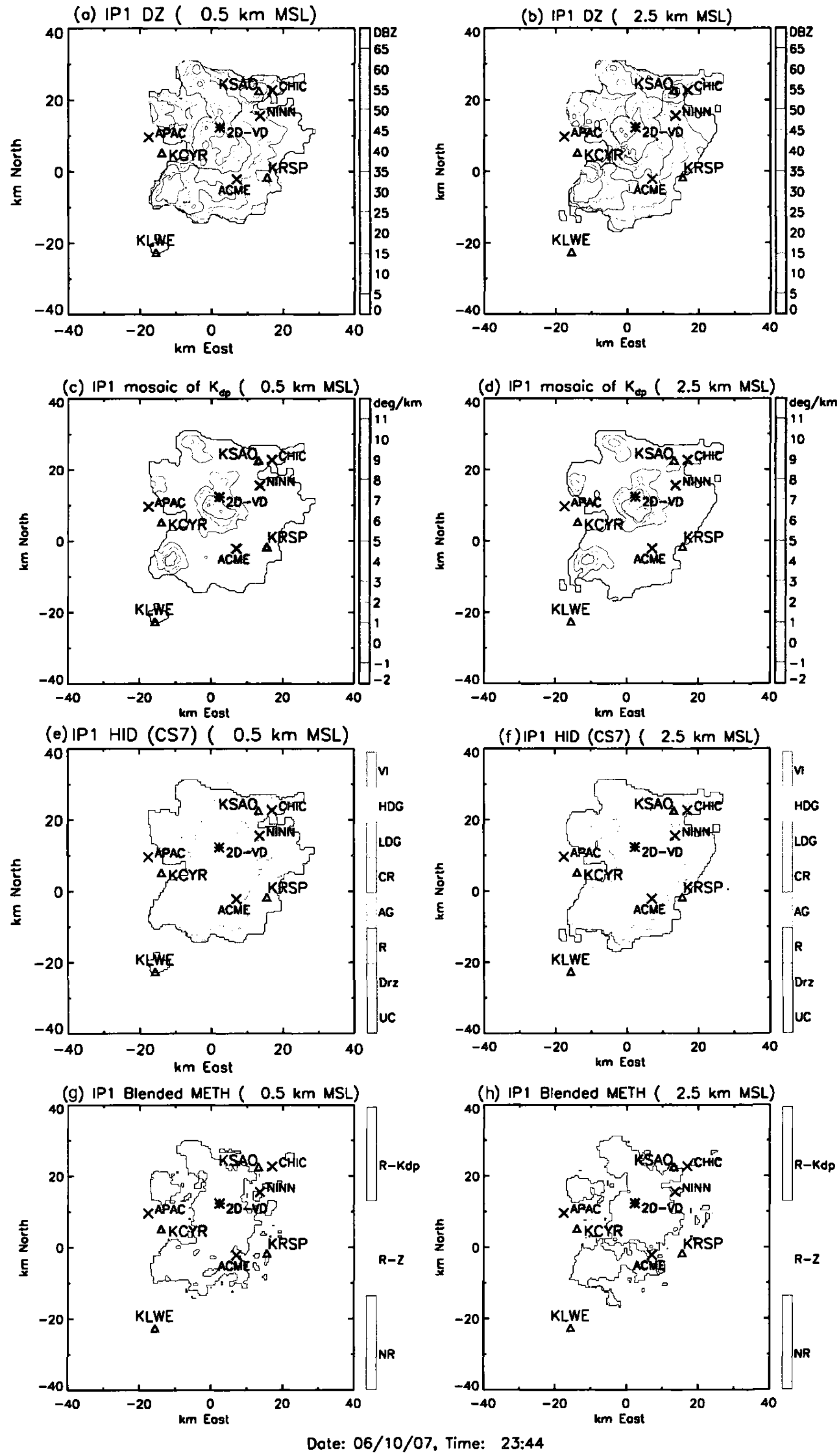

Fig. 5.5: IP1 CAPPIs at 2344 UTC on 10 June 2007 for reflectivity (top), K_{dp} (middle top), HID CS7 (middle bottom) and rainrate calculation method (METH) for the blended algorithm (bottom). CAPPIs on the left are taken at 0.5 km and 2.5 km on the right.

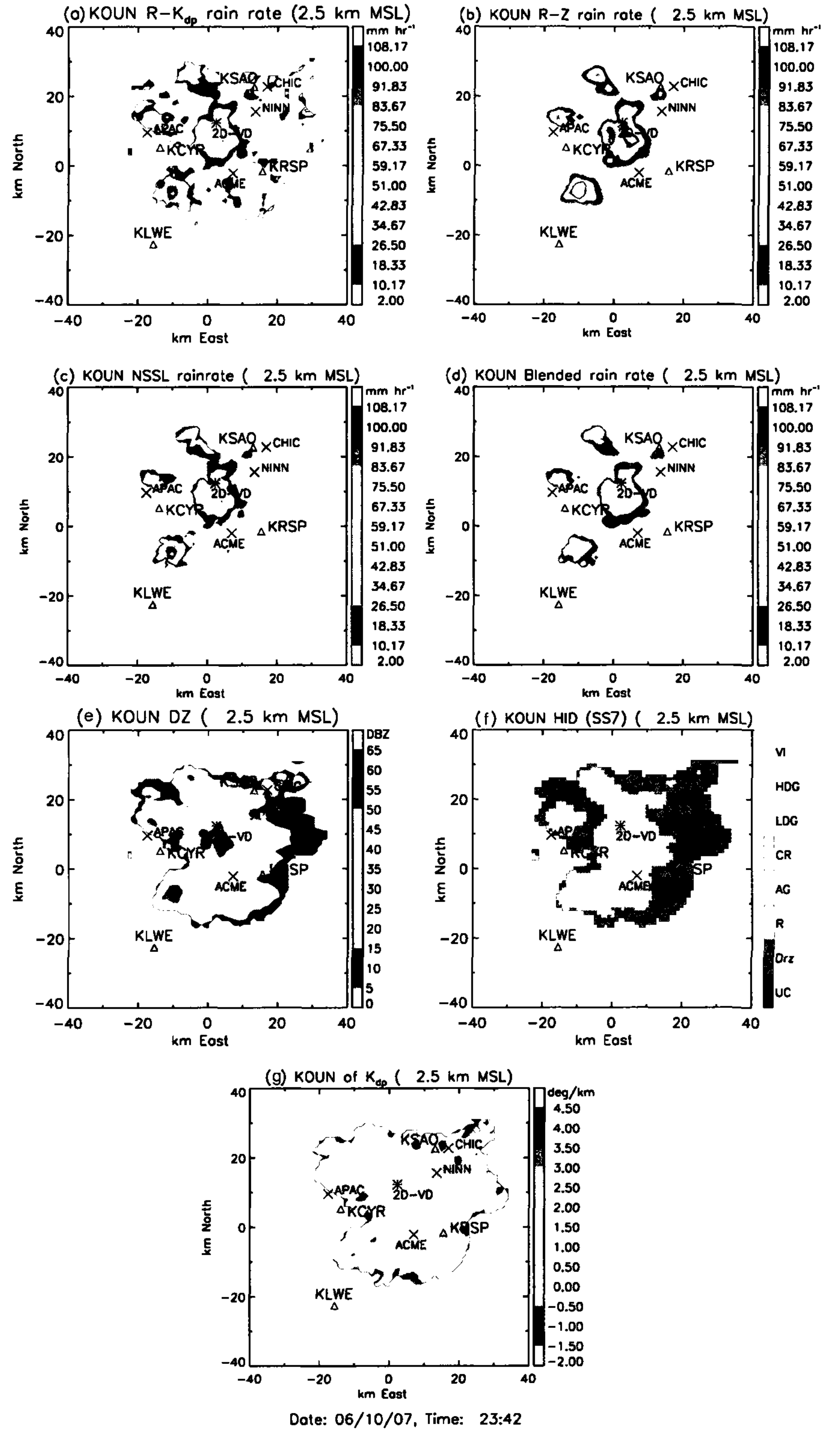

Fig. 5.6: KOUN CAPPIs at 2.5 km at 2342 UTC on 10 June 2007 for rainrates using a) R-K_{dp}, b) R-Z, c) NSSL and d) blended algorithms. Panel e) is reflectivity, f) HID SS7, and g) K_{dp}.

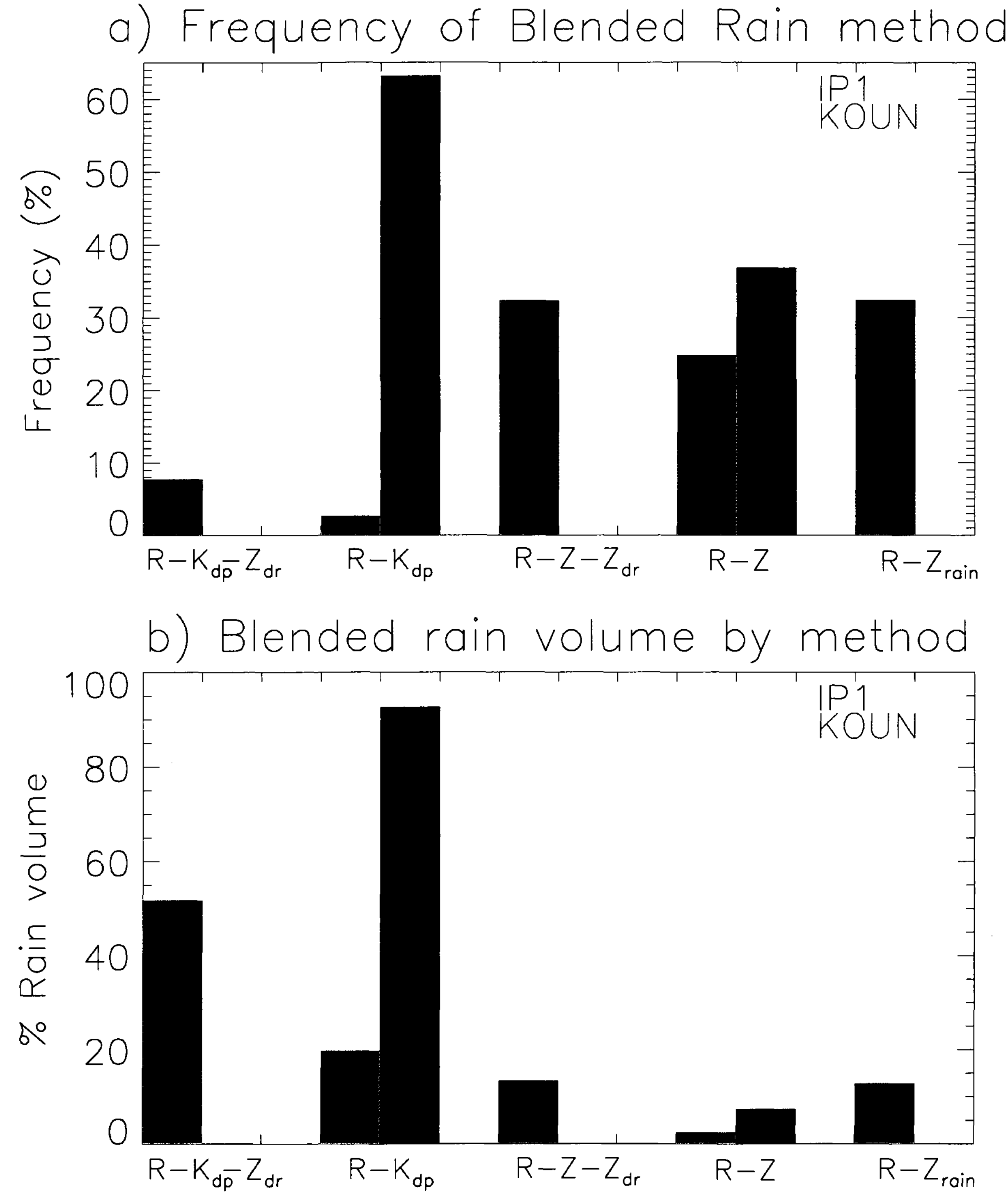

Fig. 5.7: a) Relative occurance of the blended algorithm rainrate method and b) rain volume contributed by each method in the blended algorithm.

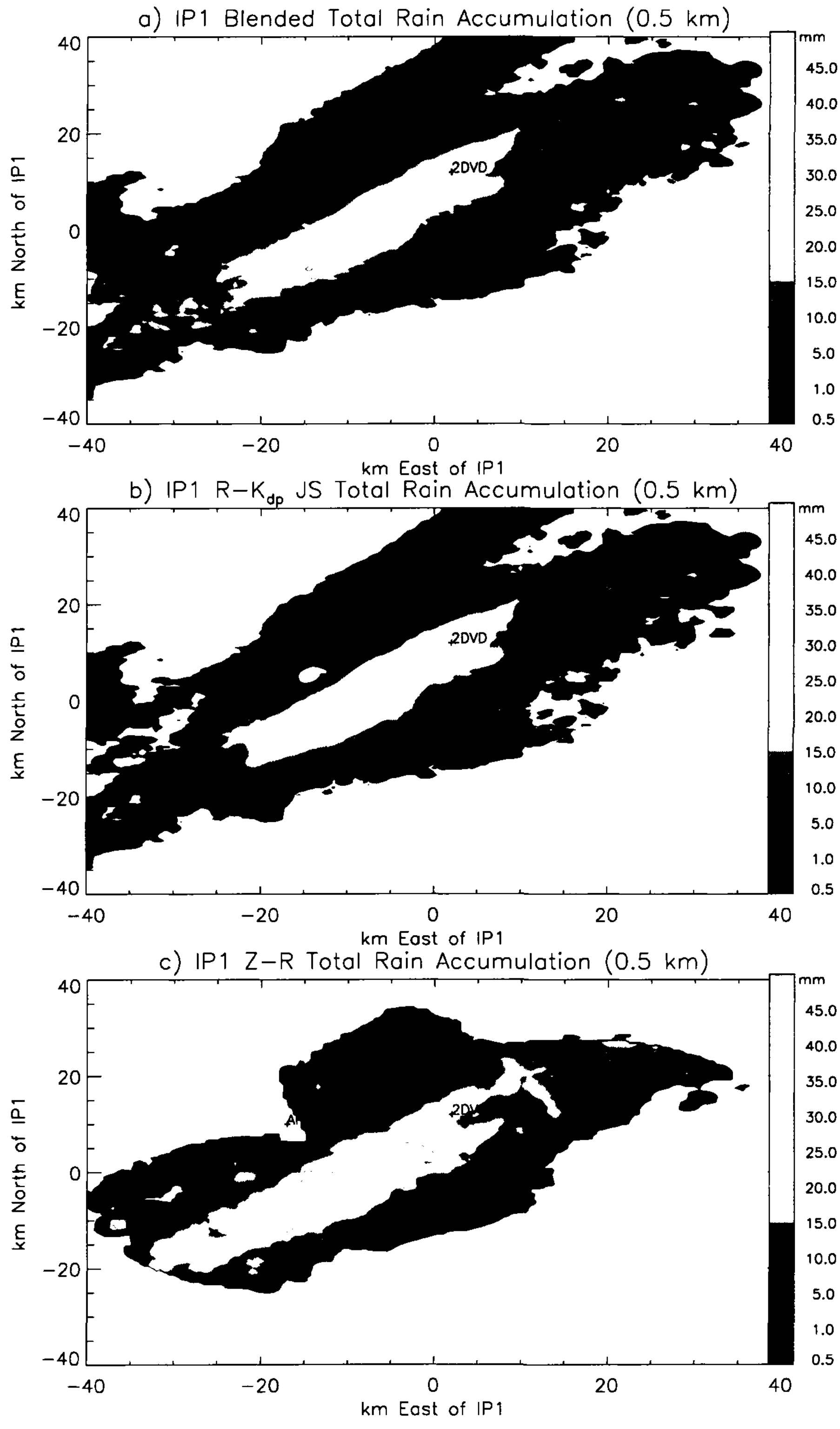

Fig. 5.8: IP1 total rainfall accumulation swaths at 0.5 km for the 10 June 2007 event using a) blended, b) R-K_{dp} JS, and c) Z-R rain rate estimators .

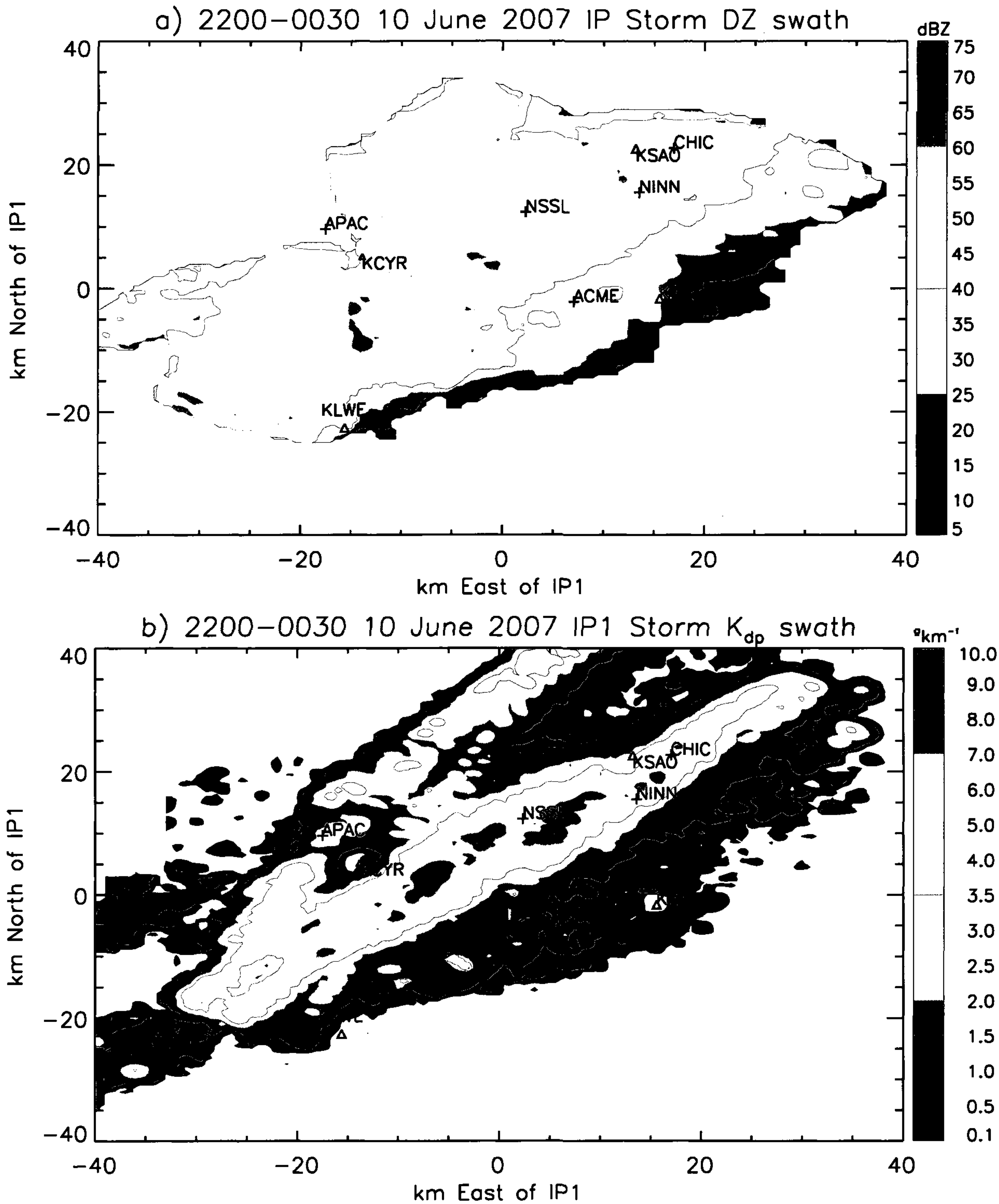

Fig. 5.9: a) IP1 reflectivity and b) K_{dp} swath at 0.5 km associated with the 10 June 2007 event.

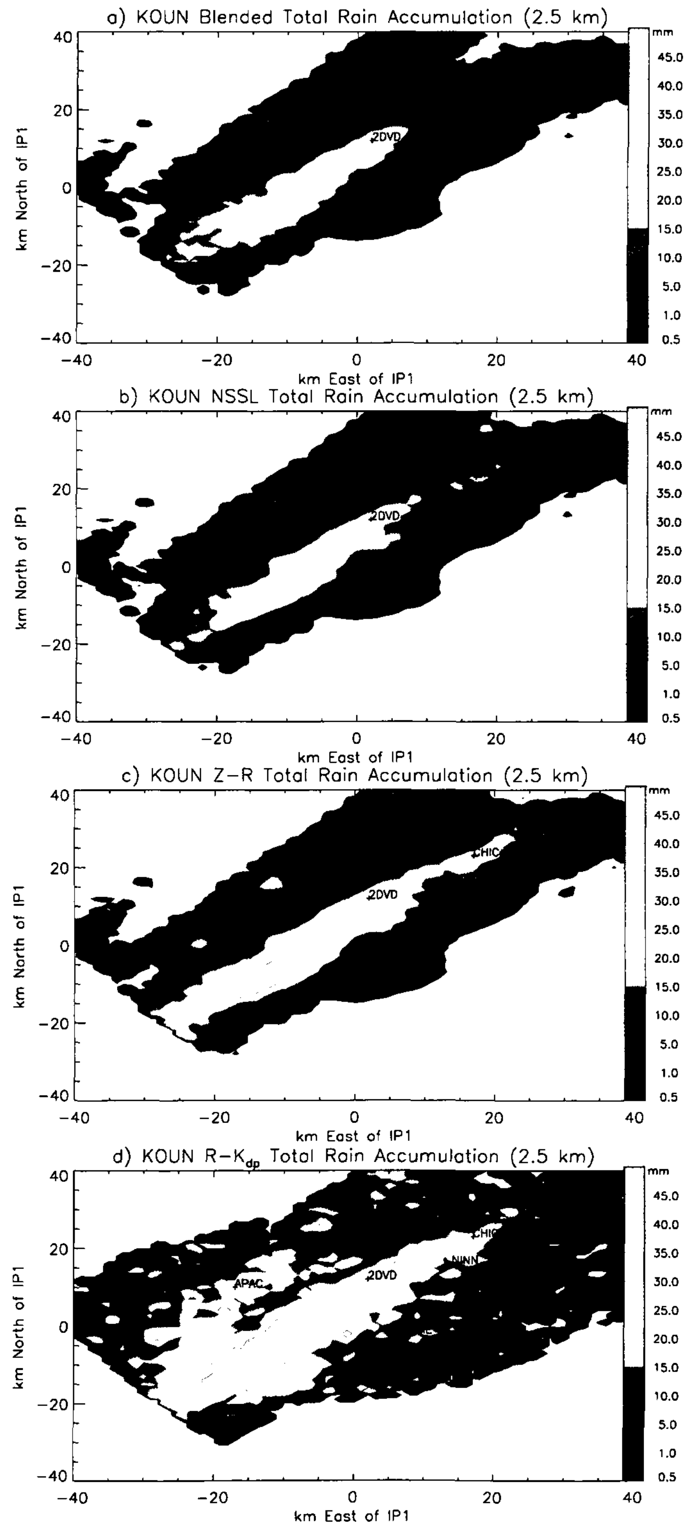

Fig. 5.10: KOUN total rainfall accumulation swaths at 2.5 km for the 10 June 2007 event using a) blended, b) NSSL, c) Z-R and d) R-K$_{dp}$ rain rate estimators.

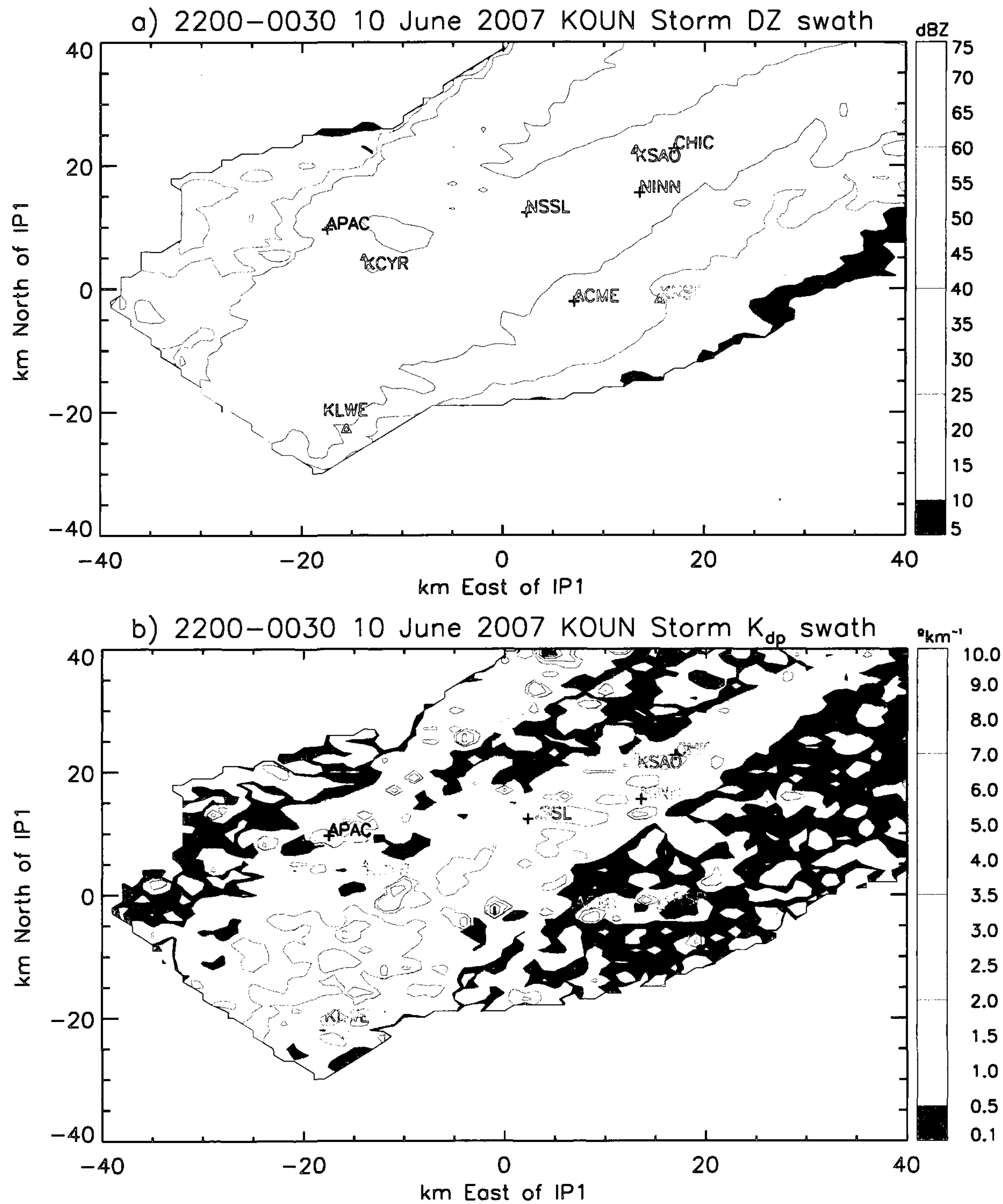

Fig. 5.11: Same as Fig. 5.9, but using KOUN data at 2.5 km.

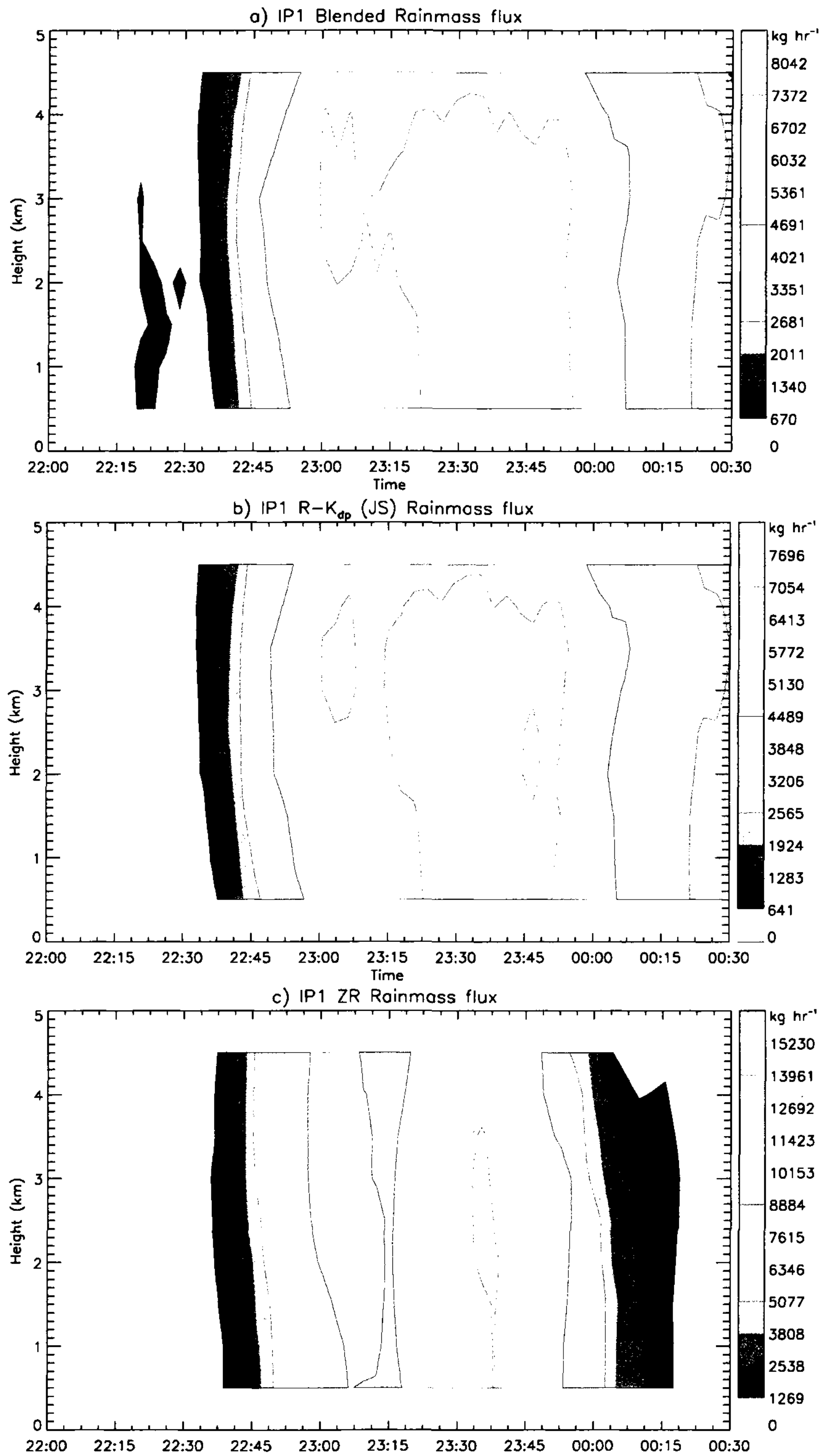

Fig. 5.12: IP1 rainmass flux time-height contours for the 10 June 2007 event using a) blended, b) R-K_{dp}, and c) Z-R algorithms for calculating the rainrate.

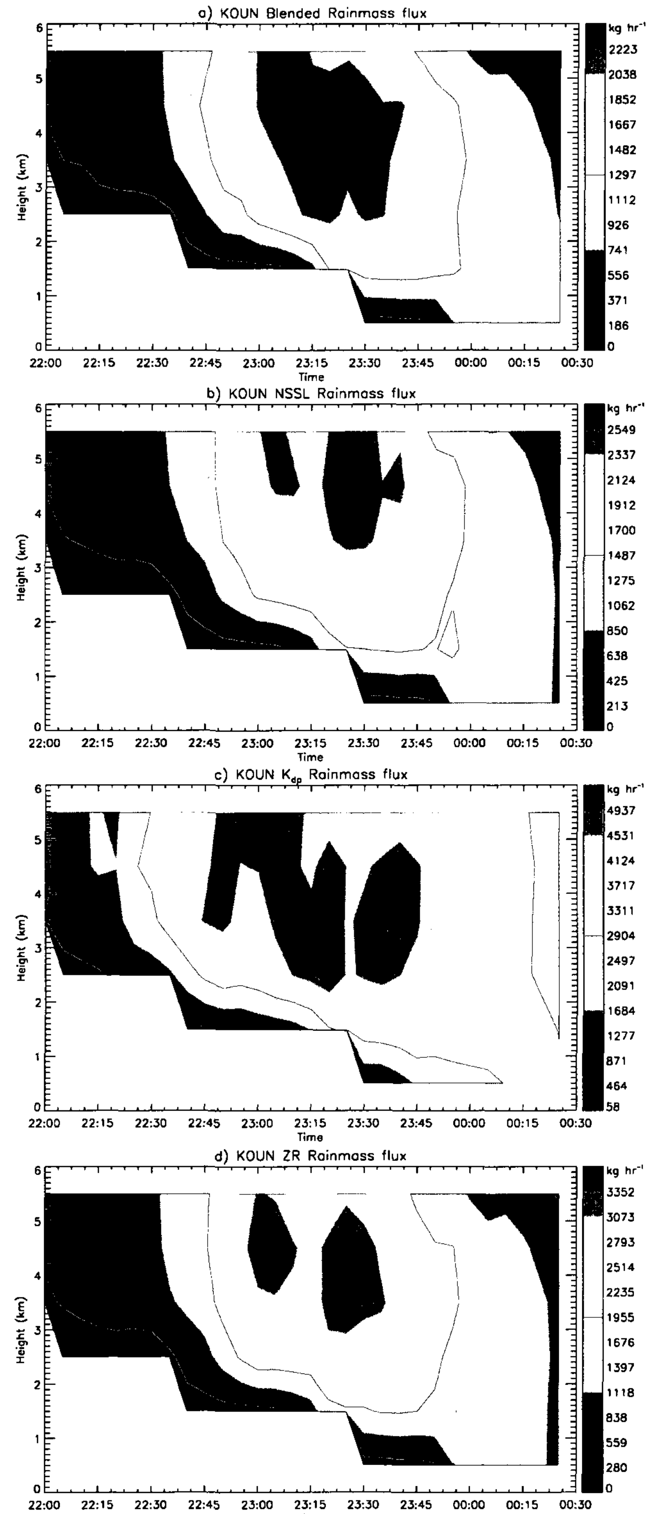

Fig. 5.13: KOUN rainmass flux time-height contours for the 10 June 2007 event using a) blended, b) NSSL, c) R-K_{dp}, and d) Z-R rainrate estimators.

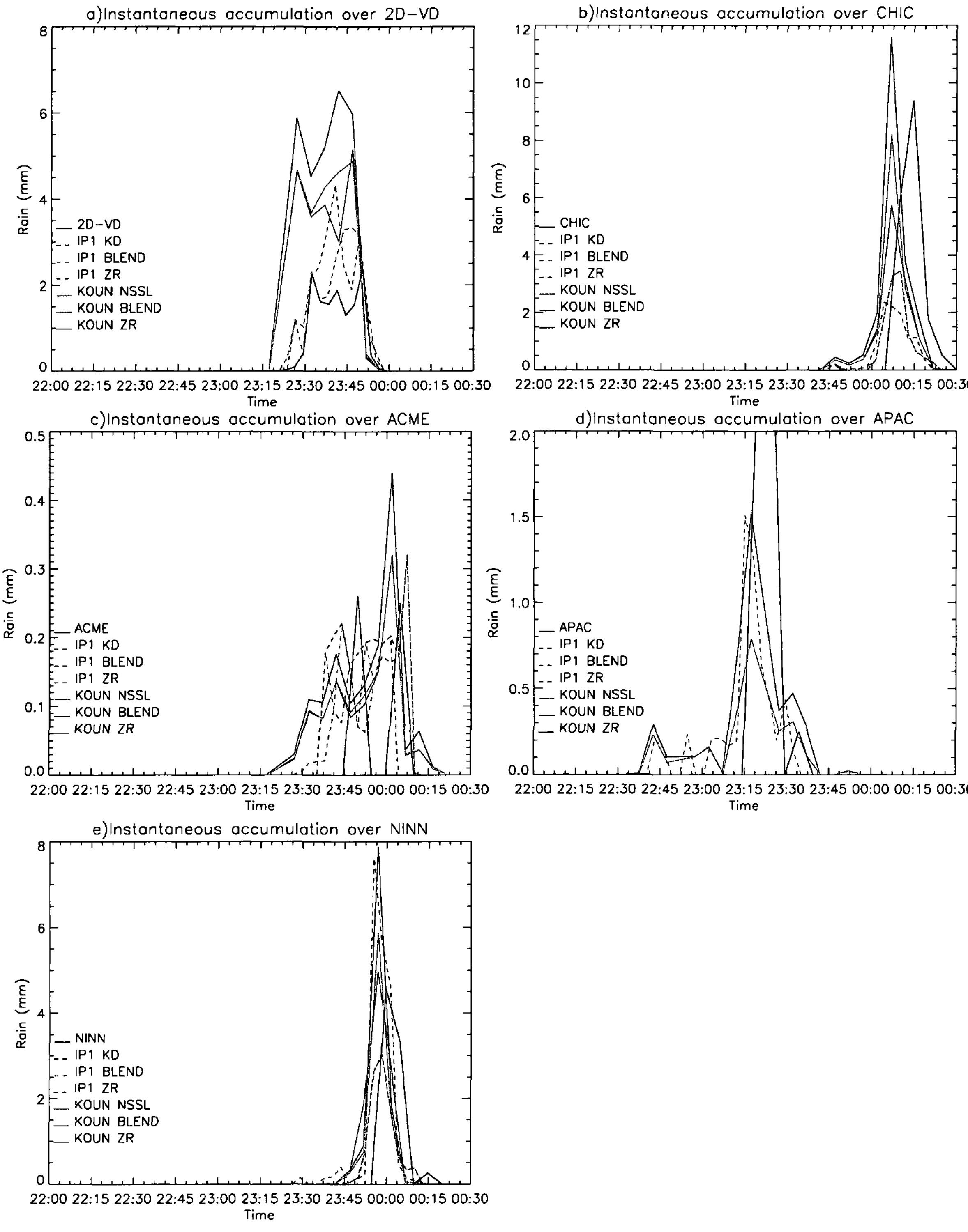

Fig. 5.14: Three (IP1 and 2D-VD) and five (KOUN and Mesonet stations) minute instantaneous rainfall accumulations over a) 2D-VD, b) CHIC, c) ACME, d) APAC, and e) NINN ground-based stations.

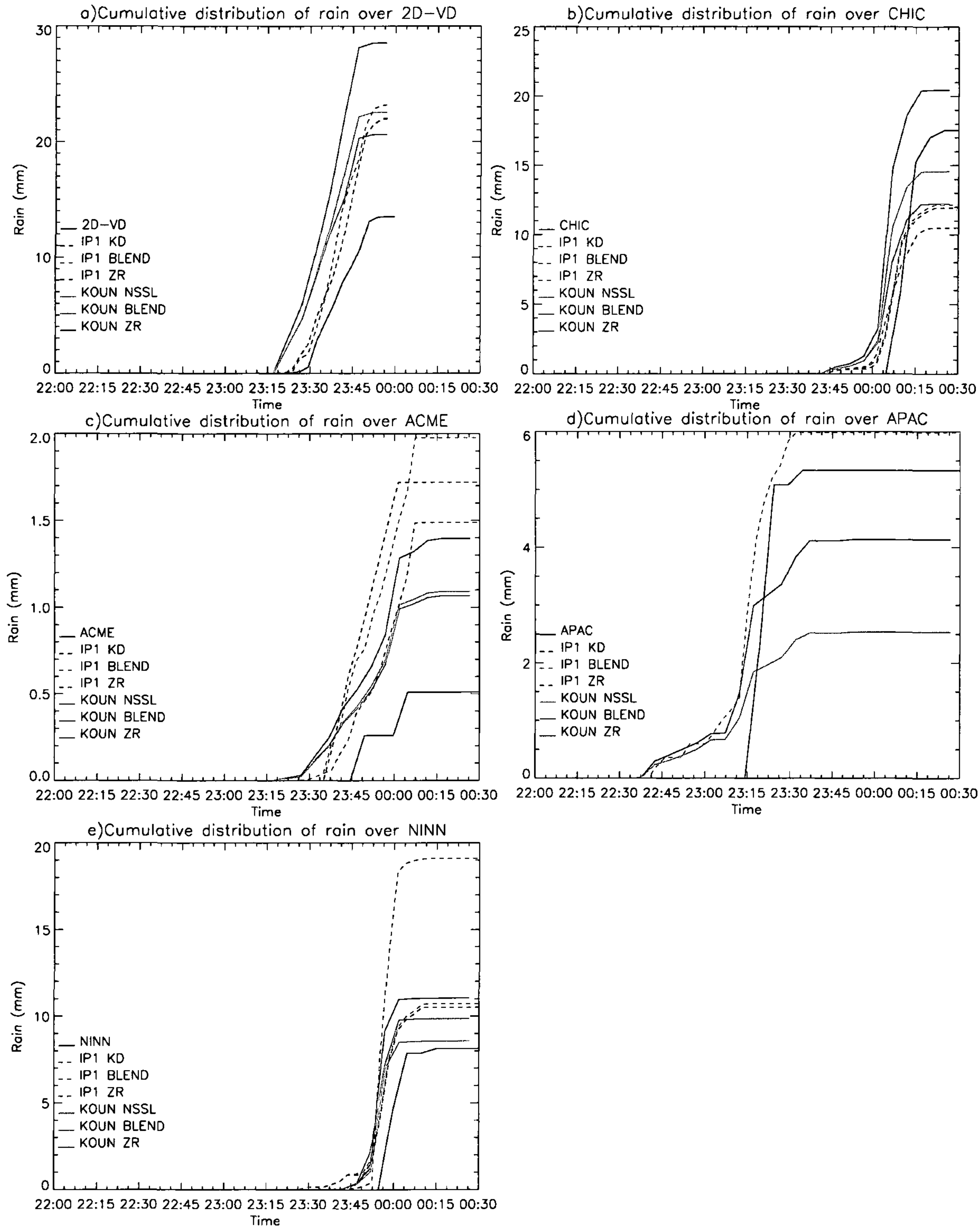

Fig. 5.15: Same as Fig. 5.14, but for cumulative rainfall.

Chapter 6

Conclusions

6.1 Summary of Results

The NSF Engineering Research Center for Collaborative Adaptive Sensing of the Atmosphere (CASA) has deployed a network of four X-band, polarimetric, adaptively scanning radars in southwestern Oklahoma. This radar network is unique in its ability to adaptively and rapidly scan echoes based on user specifications. The dual-polarization capability and network configuration of IP1 have potential for use in research studies of interactions between kinematics and microphysics. The complications of attenuation and non-Rayleigh scattering at X-band have been examined relative to understanding bulk microphysics. The potential for taking the IP1 radars beyond the fundamental objective of low-level observation was assessed, and data from the IP1 radars was examined from a case collected on 10 June 2007.

6.1.1 Microphysical and kinematic retrievals using X-band

The T-matrix model was used to investigate the scattering properties of seven hydrometeor categories: rain (RN), drizzle/light rain (DZ), ice crystals (CR), aggregates (AG), low-density graupel (LDG), high-density graupel (HDG), and vertically aligned ice crystals (VI). Non-Rayleigh effects were observed at X-band, particularly for rain and graupel, for power-based measurements (Z_h and Z_{dr}). These effects impact the potential for retrieving parameters of the particle size distribution such as D_0, and also impact the identification of hydrometeors using bulk fuzzy-logic schemes. It was hypothesized that X-band LDG and HDG reflectivity values were smaller than S-band values due to the complex nature of non-Rayleigh scattering. However, Z_{dr} values for LDG and HDG were amplified compared to S-band due to non-Rayleigh scattering. One of the advantages of X-band is the increased differential phase shift, which was determined by scattering simulations to be generally larger than the 3.43 predicted by wavelength scaling for all hydrometeor types modeled except for VI and CR, which had ratios closer to 3.43. The larger X-band K_{dp} values (compared to S-band) provided robust R-K_{dp} estimates of rain rate even at low to moderate intensities.

Simulated values of each variable were used to create a fuzzy logic hydrometeor identification algorithm (HID) for both S- and X-band. Comparisons between the simulation-based HID and other currently employed S-band algorithms showed good similarity, as did comparisons between S-band and X-band simulated HIDs. Splitting dry snow in the CSUHIDS 6 HID into two separate categories (ice crystals CR and aggregates AG) increased the microphysical information provided by the HID. Several sensitivity studies were performed and illustrated the contribution of different variables to the HID retrieval. Although temperature and reflectivity were clearly the most important variables for producing a realistic picture of the storm microphysics, inclusion of Z_{dr}, K_{dp}, and ρ_{hv} improved the overall categorization, especially regarding identification of VI and for distinguishing different snow types.

T-matrix scattering simulations and development of a new theoretically-based X-band hydrometeor identification algorithm showed that there are sometimes significant non-Rayleigh effects that can occur at 3.2 cm wavelength in rain and graupel. However such effects did not appreciably decrease the performance of a X-band specific fuzzy logic hydrometeor identification compared to a similar S-band specific fuzzy logic HID. Thus, despite the complications from non-Rayleigh scattering at X-band, bulk hydrometeor identification is physically plausible. However, it should be noted that hail, specifically large and wet hail, were not considered in this study. Hail could have excessive non-Rayleigh effects that may make identification via fuzzy logic difficult, and could complicate bulk microphysical retrievals.

Considerable attenuation is also a drawback to using X-band for studies of storm physics. The case studied herein exhibited extensive attenuation, although very little complete extinction of the signal. Two methods of attenuation correction were examined; the first being a polarimetric-based differential phase correction, and the second a technique exploiting the network configuration of the IP1 design (NRS). In this particular case, the NRS applied to horizontal reflectivity appeared to perform better than the polarimetric-based algorithm when compared to the local S-band polarimetric radar, KOUN. A limitation of the network-based attenuation correction is that it can only be applied in areas where two or more radars observe the same volume, and as such, the network coverage area is reduced. However, once the correction was applied, data compared well with local S-band radars (both KOUN and local NEXRADs), though a bias toward high reflectivities due to non-Rayleigh scattering was observed.

Comparisons of rain rate estimators showed that R-K_{dp} could be used at X-band for rain rates greater than 2.7 mm h^{-1}, while S-band R-K_{dp} could be used only above 8 mm h^{-1}, supporting the findings of other studies (Matrosov et al., 2006). Cumulative distribution functions revealed that R-K_{dp} was most often used above 28 dBZ at X-band, while power-based estimators were used most frequently applied below 36 dBZ in the S-band blended algorithm. The improved temporal and spatial resolution of the IP1 radars did a better job pinpointing timing and regions of heavy rain at the surface compared with the 5 minute KOUN observations. Intercomparisons between KOUN, IP1 and surface-based rain gauges showed that the KOUN NSSL rainfall algorithm provided the closest match and smallest error to the surface measurements. While standard errors for X-band algorithms were all high, the X-band blended algorithm had smaller bias and standard deviations than the Z-R relationship.

Quantitative comparisons of rainfall between ground based sensors and radar observations showed no significant benefits of X-band compared to S-band estimators employing polarimetric information (blended and NSSL algorithms). George (2007) found similar results in a study of several storms during the GPM GV project in Colorado in 2004. However, X-band algorithms employed polarimetric-based estimators (R-K_{dp}) in a larger percentage of grid points than S-band, and direct comparison of only R-K_{dp} relationships showed better retrievals at X-band due to the more sensitive and smoother K_{dp} field. The rather significant dependence of R-K_{dp} estimators on the assumed drop-shape model was also illustrated.

6.1.2 Microphysical and kinematic retrievals using the IP1 Network

The IP1 network demonstrated several advantages and disadvantages for scientific study of storm interactions. First, the network configuration increased storm coverage compared to any single radar in the network, resulting from both the scanning methodology and the short range of the radars. However, combining information from four radars was difficult due to intra-radar Z_{dr}, Z_h, ρ_{hv} and K_{dp} calibration and biases.

The unique adaptive scanning strategy employed by the CASA IP1 radars is advantageous but also has drawbacks. The adaptive technology allows for rapid update times, as well as implementation of specific dual-Doppler scanning strategies (i.e., high priority coverage of dual-Doppler regions). However, compromises between sector size, number of elevation angles, maximum elevation angle, and volume scan update time made during the 10 June 2007 case resulted in insufficient coverage of the upper levels. The lack of coverage of the upper levels was less than ideal for dual-Doppler analysis of the 3D wind field. The lack of upper level coverage is partially the result of a hardware limitation on the maximum elevation angle (31°), while some of the limited dual-Doppler retrievals were due to radar baselines along which the wind field cannot be derived, as well as the 30 km maximum range constraint (a data collection consideration). Sparse coverage of the upper levels of the storm, combined with the radar sensitivity, led to diminished coverage of regions of vertical ice, which has implications for storm electrification. Additionally, overall mapping of ice crystals was diminished compared with the longer wavelength KOUN. Comparisons with KOUN showed that the IP1 coverage was enough to accurately identify graupel areas in the mid levels, which have an influence on the downdraft development, electrification, and rain processes. As a result of the radar configuration, IP1 had increased coverage of the lower levels (< 3 km) over the more distant KOUN, and thus better identification through HID of low-level precipitation. Despite the lack of consistent upper-level coverage, the low level coverage provided by the IP1 radars has significant benefits for rainfall estimation, melting layer and surface dynamics. The IP1 radars observe low level convergence and divergence, which is associated with downdrafts. These types of observations could help detect downbursts in future cases, as well as strong areas of outflow.

Although the more desirable variational integration method (W_{var}) for calculating the vertical component of the wind was available in less than 50% of scanned columns, use of the more error-prone upward integration method (W_{up}) still produced the same general vertical wind tendencies as W_{var}. As such, evolution of the up- and downdraft were derived from IP1 data, although accurate wind speeds were not available.

The most valuable aspect of the IP1 network for kinematic and microphysical studies was the temporal resolution (3 minutes). This allowed for resolution of the up- and downdrafts, as well as correlations between storm parameters such as lightning flash rate, graupel echo volume, and intense updraft echo volumes. The greatest drawback from the IP1 network was the inconsistent coverage. The variable coverage area limited the quantitative analysis that could be performed, and it was difficult to determine if small fluctuations in storm parameters were due to changing storm coverage or actual processes occurring within the storm.

6.1.3 IP1 observations of storm interactions

IP1 data were used to observe the evolution, microphysics, and dynamics of an ordinary multi-cellular storm that passed through the network on 10 June 2007. Observations from the nearby KOUN S-band polarimetric radar were used for comparison, and lightning data from NLDN and OK-LMA were used to infer lightning flash rates and charge structure. IP1 data showed that updraft development preceded graupel production by several minutes, with IC flashes lagging graupel volume by 5-15 minutes. As graupel volumes increased, the downdraft formed, bringing precipitation to the surface, and as the graupel volume dropped off, CG flash rates ceased. High correlations were observed between updraft volumes and graupel echo volume, as well as between graupel echo volume and total lightning flash rate. The charge inferred from the OK-LMA data indicated a normal dipole with some pockets of lower-level positive charge. The negative charge regions corresponded to the regions where HID identified graupel, while the upper positive was associated with ice crystals, consistent with non-inductive charging theory (Takahashi, 1978; Saunders and Peck, 1998). An increase in height of the upper level positive charge and subsequent burst of IC lightning after the storm split was found to be related to a kinematic intensification inferred from an increase in the 40 dBZ echo height and a small elevation of the U5 volume (MacGorman et al., 1989; Lang et al., 2000). Many of these observations were corroborated by KOUN, although no wind information could be retrieved using KOUN data. The scanning strategy and location of the IP1 radars compared to KOUN also allowed for better temporal and spatial resolution that was evident in the lag correlations and time-height contours.

6.2 Recommendations for CASA

The following recommendations are intended to improve the applicability of the IP1 radars for research studies of storm microphysics, kinematics and morphology based on the conclusions from this 2007 case study. Some of the following have already been implemented, in part as a result of the research conducted herein.

1. *Calibrated Z_{dr}.* The benefits of calibrated Z_{dr} include improved distinction between frozen hydrometeor types (such as ice crystals versus aggregates), and could benefit rainfall estimation through a combined rain rate estimator as explored by Matrosov et al. (2006) and Anagnostou et al. (2004).

2. *Improved dual-Doppler scanning rules.* Although the general trends of vertical wind could be retrieved using a combined upward and variational integration methodology, 3-D wind retrievals would be greatly improved if a majority of columns within a storm were topped by two or more radars. Improvements to the scanning strategy could include using more distant radars to reach the top of storms to overcome the 30° elevation angle (hardware) constraint, increasing the elevation stepping (at the expense of vertical resolution) in order to include higher elevation angles in the same three minute update time, and choosing radars with the greatest viewing angle difference (i.e., 90°) instead of the closest radars to decrease gaps resulting from radar baselines (Wang et al., 2008). Periodic RHIs could help determine the maximum echo heights to be scanned and therefore direct the necessary elevation angles.

3. *Integrated dual-Doppler scanning.* The dual-Doppler scanning strategy used during the 2007 CLASIC experiment was separate from the normal IP1 operational

scanning strategy. The dual-Doppler rules should be integrated with other end-user rules to provide kinematic and microphysical observations during all IP1 operations. The possibility of setting dual-Doppler rules for one-minute heartbeats should be explored, possibly by increasing the elevation angle stepping or decreasing the number of elevation angles. Dual-Doppler scans could then be scheduled every other or every third heartbeat to maintain a high temporal resolution of kinematics and microphysics while still allowing for other, low-level objectives and end-user requests to be met.

4. *More consistent scanning.* Unfortunately, one of the greatest drawbacks to using the IP1 network for studying storm kinematics and microphysics was inconsistent coverage, since accurate quantitative analysis was not possible with variable radar coverage. This will be the most challenging obstacle to overcome with the adaptive scanning technology, which is inherently going to change based on user needs and features in the network. However, much like the consistent 360° elevation angle at 2° included in every heartbeat, perhaps a set volume scan could be carried out every five minutes to provide an overall assessment of the storm volume. Additionally, completely reaching storm top and improving sector scan size and direction determination to minimize cutting off the edges of echoes will alleviate some of the fluctuating echo volume coverage.

5. *Extended range.* By extending the maximum range of stored data beyond 30 km, not only will network coverage expand, but more overlap between radars will lead to enhanced dual-Doppler coverage area (particularly in the upper levels) and extend the area for application of the network-based attenuation correction. Additionally, longer

maximum ranges would decrease gaps in the derived wind field resulting from radar baselines.

6.3 Future work

Time constraints only allowed for detailed analysis of a single case collected by the IP1 radars for this study. The obvious next step would be application of the HID, dual-Doppler and rainfall algorithms to more cases. Additionally, as stated previously, some of the above recommendations resulting from the 2007 CLASIC experiment were implemented during the 2008 spring storm season. The maximum ranges of the radars were extended to 40 km, and some data were collected using modified dual-Doppler scanning techniques (Wang et al., 2008). The impact of these improvements on retrievals of storm physics and evolution needs to be assessed.

This study specifically did not include hail due to the complicated non-Rayleigh scattering, and as such the case study was chosen due to the small amount of hail identified by KOUN CSUHIDS 9. X-band observations of hail should be modeled using T-matrix with a variety of sizes, water-coatings, and sponginess to judge the impact on hydrometeor identification at X-band. X-band and S-band should be then compared to quantify the extent of this potential complication.

The short duration of rainfall over many of the ground-based gauges during the 10 June 2007 storm limited quantitative comparisons between radar algorithms and the gauges. A climatological study of radar and gauge rain estimations using a wide range of rain rates will allow for more accurate assessment of different algorithms and inter-wavelength comparisons of rainfall retrievals. Inclusion of Z_{dr} in the X-band blended algorithm may improve X-band estimates of rainfall (Matrosov et al., 2002; Anagnostou et al., 2004). Other methods of compositing the data should also be investigated, as taking the greatest value may have biased the measurements high and influenced the precipitation estimates.

The complex nature of multi-cellular storms may also have caused inconclusive correlations between parameters. Other types of storms, including isolated cells, squall lines, frontal passages, and winter storms, should be examined to evaluate the full potential of the IP1 network for microphysical and kinematic studies. Winter storms appear to be ideal cases to study with IP1 due to the lower echo tops, weaker kinematics and reduction of non-Rayleigh scattering effects.

References

Anagnostou, E. N., M. N. Anagnostou, W. F. Krajewski, A. Kruger, and B. J. Miriovsky, 2004: High-resolution rainfall estimation from X-band polarimetric radar measurements. *J. Hydrometeor.*, **5**, 110-128.

Anagnostou, E. N., M. Grecu, and M. N. Anagnostou, 2006: X-band polarimetric radar rainfall measurements in Keys Area Microphysics Project. *J. Atmos. Sci.,* **63**, 187-203.

Auer, A. H., 1971: Distribution of graupel and hail with size. *Mon. Wea. Rev*, **100**, 325-328.

Aydin, K., and T. A. Seliga, 1984: Radar polarimetric backscattering properties of conical graupel. *J. Atmos. Sci.,* **41,** 1887–1892.

Balakrishnan, N. and D. S. Zrnic, 1990: Use of polarization to characterize precipitation and discriminate large hail. *J. Atmos. Sci.*, **47**, 1525-1540.

Baldini, L., E. Gorgucci, V. Chandrasekar, and W. Petersen, 2005: Implementations of CSU hydrometeor classification scheme for C-band polarimetric radars. Preprints, *32nd Int. Conf. on Radar Meteor.,* Albuquerque, NM, Amer. Meteor. Soc., P11.4.

Barber, P., and C. Yeh, 1975: Scattering of electromagnetics waves by arbitrarily shaped dielectric bodies. *Appl. Opt.*, **14**, 2864-2872.

Barthazy, E., and R. Schefold, 2003: Properties of snowflakes of different riming degree and crystal types. Preprints, *31st Conf. on Radar Meteor.,* Seattle, WA, Amer. Meteor. Soc., 124-127.

Battan, L. J., 1964: Some observations of vertical velocities and precipitation sizes in a thunderstorm. *J. Appl. Meteor.*, **3**, 415-420.

Battan, L. J., 1973: *Radar Observation of the Atmosphere.* University of Chicago Press, 323 pp.

Battan, L. J. and J. B. Theiss, 1972: Observed Doppler spectra of hail. *J. Appl. Meteor.*, **11**, 1001-1007.

Battan, L. J. and J. B. Theiss, 1973: Wind gradients and variance of Doppler spectra in showers viewed horizontally. *J. Appl. Meteor.*, **12**, 688-693.

Beard, K. V. and A. R. Jameson, 1983: Raindrop Canting. *J. Atmos. Sci.*, **40**, 448-454.

Beard, K.V. and Chuang, C., 1987: A new model for the equilibrium shape of raindrops, *J. Atmos. Sci.*, **44**, pp1509-1524.

Berdeklis, P., and R. List, 2001: The ice crystal-graupel charging mechanism of thunderstorm electrification. *J. Atmos. Sci.*, **58**, 2751-2770.

Bluestein, H. B. and R. M. Wakimoto, 2003: Mobile radar observations of severe convective storms. *Meteor. Monographs*, **30**, 105-105.

Bluestein, H. B., M. M. French, R. L. Tanamachi, S. Frasier, K. Hardwick, F. Junyent, and A. L. Pazmany, 2007a: Close-range observations of tornadoes in supercells made with a dual-polarization, X-band Doppler radar. *Mon. Wea. Rev.*, **135**, 1522-1543.

Bluestein, H. B., C. C. Weiss, M. M. French, E. M. Holthaus, R. L. Tanamachi, S. Frasier, and A. L. Pazmany, 2007b: The structure of tornadoes near Attica, Kansas, on 12 May 2004: High-resolution, mobile, Doppler radar observations. *Mon. Wea. Rev.*, **135**, 475-506.

Braham, R. R., 1963: Some measurements of snow pellet Bulk-densities. J. Appl. Met., 2, 498-500.

Brandes, E. A., A. V. Ryzhkov and D. S. Zrnic, 2001: An evaluation of radar rainfall estimates from specific differential phase. *J. Atmos. Oceanic Technol.,* **18**, 363-374.

Brandes, E. A., G. Zhang, and J. Vivekanandan, 2002: Experiments in rainfall estimation with a polarimetric radar in a subtropical environment. *J. Appl. Meteor.*, **41**, 674-685.

Brandes, E. A., K. Ikeda, G. Zhang, M. Schenhuber, and R. M. Rasmussen, 2006: A statistical and physical description of hydrometeor distributions in Colorado snow storms using a video disdrometer. *J. Appl. Meteor.*, **46**, 634-650.

Bringi, V.N., V. Chandrasekar, N. Balakrishnan, and D. S. Zrnic, 1990: An examination of propagation effects in rainfall on polarimetric variables at microwave frequencies. *J. Atmos. Oceanic Technol.*, **7**, 829–840.

Bringi, V. N., and V. Chandrasekar, 2001: *Polarimetric Doppler Weather Radar: Principles and Applications.* Cambridge University Press, 636 pp.

Carey, L. D., and S. A. Rutledge, 1996: A multiparameter radar case study of the microphysical and kinematic evolution of lightning producing storm, *Meteorol. Atmos. Phys.*, **59**, 33-64.

Carey, L.D., and S. A. Rutledge, 1998: Electrical and multiparameter radar observations of a severe hailstorm. *J. Geophys. Res.,* **103,** 13979-14000.

Chandrasekar, V., V. N. Bringi, N. Balakrishnan, and D. S. Zrnic, 1990: Error structure of multiparameter radar and surface measurements of rainfall. Part III: Specific differential phase. *J. Atmos. Oceanic Technol.*, **7**, 621-629.

Chandrasekar, V., E. Gorgucci, and G. Scarchilli, 1993: Optimization of multi-parameter radar estimates of rainfall. *J. Appl. Meteor.,* **32**, 1288-1293.

Chandrasekar, V., E. Gorgucci, and L. Baldini, 2002: Evaluation of polarimetric radar-rainfall algorithms at X-band. Proc. Second European Conf. on Radar Meteorology, Delft, Netherlands, European Meteorological Society, 277–281

Chandrasekar, V., S. Lim, and E. Gorgucci, 2006: Simulation of X-band rainfall observations from S-band radar data. *J. Atmos. Ocean. Tech.,* **23**, 1195-1205.

Chandrasekar, V. and S. Lim, 2008: Retrieval of reflectivity in a networked radar environment. *J. Atmos. Ocean. Tech.*, 2008 early online release, DOI: 10.1175/2008JTECHA1008.1.

Chandrasekar, V., D. McLaughlin, J. Brotzge, M. Zink, B. Philips, and Y. Wang, 2008: Evaluation of Distributed Collaborative Sending in a Four-node Radar Network: Integrated Project 1. Preprints, IGARRS, Boston.

Cheng, L and M. English, 1983: A relationship between hailstone concentration and size. *J. Atmos. Sci.*, **40**, 204-213.

Cheng, L., M. English, and R. Wong, 1985: Hailstone size distributions and their relationship to storm thermodynamics. *J. Appl. Meteor.*, **24**, 1059-1067.

Chuang. C. C. and K. V. Beard, 1990: A numerical model for the equilibrium shape of electrified raindrops. *J. Atmos. Sci.,* **47**, 1374-1389.

Cifelli, R., W. A. Petersen, L. D. Carey, S. A. Rutledge, and M. A. F. da Silva Dias, 2002: Radar observations of the kinematic, microphysical, and precipitation characteristics of two MCSs in TRMM LBA. *J. Geophys. Res.,* **107**, Doi: 10.1029/2000JD0000264.

Cifelli, R., D. Barjenbruch, D. Brunkow, L. Carey, C. Davey, N. Doesken, C. Gimmestad, T. Huse, P. Kennedy, and S. A. Rutledge, 2003: Evaluation of an operational polarimetric rainfall algorithm. AMS 31st Conference on Radar Meteorology, Seattle, WA, 6-12 August 2003, P2B.14.

Cressman, G. P., 1959: An operational objective analysis system. *Mon. Wea. Rev.,* **87,** 367-374.

Cummins, K. L., M. J. Murphy, E. A. Bardo, W. L. Hiscox, R. B. Pyle, and A. E. Pifer, 1998: A combined TOA/MDF technology upgrade of the U. S. National Lightning Detection Network. *J. Geophys. Res.,* **103**, 9035-9044.

Dolan, B. and S. A. Rutledge, 2008: An X-band fuzzy logic-based hydrometeor identification algorithm. *J. Atmos. Oceanic Tech.*, submitted August 2008.

Doviak, R. J., and D. S. Zrnic, 1993: *Doppler Radar and Weather Observations.* Academic Press, 562 pp.

Federer, B. and A. Waldvogel, 1975: Hail and raindrop size distributions from a Swiss multicell storm. *J. Appl. Meteor.*, **14**, 91-97.

Field, P. R., 1999: Aircraft observations of ice crystal evolution in an altostratus cloud. *J. Atmos. Sci.*, **56**, 1925-1941.

Fletcher, N. H., 1962: *The Physics of Clouds,* 2nd Ed., Clarendon Press, Oxford, 671 pp.

Fulton, R. A., J. P. Breidenbach, D. J. Seo, D. A. Miller, and T. O'Bannon, 1998: The WSR-88D Rainfall Algorithm. *Wea. and Forecasting*, **13**, 377–395.

George, K., 2007: *Polarimetric-based Rainfall Rates Using S- and X-band Radars in the GPM-GV Pilot Project.* Master's thesis, Colorado State University, Fort Collins, 81 pp.

Goddard, J.W.F. and Cherry, S.M., 1984: Quantitative precipitation measurements with dual linear polarisation radar, 22nd Conference on Radar Meteorology of A.M.S., Zurich, Switzerland.

Golestani, Y., V. Chandrasekar, and V. N. Bringi, 1989: Intercomparison of multiparameter radar measurements. Proceedings of 24th Conference on Radar Meteorology, pp 309-314, Am. Meteorlog. Soc., Boston, MA.

Gorgucci, E. , G. Scarchilli, V. Chandraskear, and V. N. Bringi, 2001: Rainfall estimation from polarimetric radar measurements: Composite algorithms immune to variability in raindrop shape-size relation. *J. Atmos. Oceanic Technol.*, **18**, 1773-1786.

Gorgucci, E. and V. Chandrasekar, 2005: Evaluation of attenuation correction methodology for dual-polarization radars: Application to X-band systems. *J. Atmos. Oceanic Tech.*, **22**, 1195-1206.

Gorgucci, E., V. Chandrasekar, and L. Baldini, 2006: Correction of X-band radar observation for propagation effects based on the self-consistency principle. *J. Atmos. Oceanic Technol.*, **23**, 1668-1681.

Gorgucci, E., V. Chandraskear, and L. Baldini, 2008: Microphysical retrievals from dual-polarization radar measurements at X-band. *J. Atmos. Oceanic Technol.*, **25**, 729-741.

Gosset, M. and I. Zawadzki, 2001: Effect of Nonuniform Beam Filling on the Propagation of the Radar Signal at X-Band Frequencies. Part I: Changes in the *k*(*Z*) Relationship. *J. Atmos. Oceanic Technol.*, **18**, 1113-1126.

Goodman, S. J., D. E. Buechler, P. D. Wright, and W. D. Rust, 1988: Lightning and precipitation history of a microburst producing storm. *Geophys. Res. Lett.*, **15**, 1185-1188.

Gunn, K. L. S. and J. S. Marshall, 1958: The distribution with size of aggregate snowflakes. *J. Atmos. Sci.*, **15**, 452-461.

Hendry, A., G. C. McCormick, and B. L. Barge, 1976: The degree of common orientation of hydrometeors observed by polarization diversity radars. *J. Appl. Meteor.*, **15**, 633-640.

Heymsfield, A., 1972: Ice crystal terminal velocities. *J. Atmos. Sci.*, **29**, 1348-1357.

Heymsfield, A. J., 1978: The characteristics of graupel particles in Northeastern Colorado cumulus congestus clouds. *J. Atmos. Sci.*, **35**, 284-295.

Heymsfield, A. J., A. Bansemer, C. Schmitt, C. Twohy, and M. R. Poellot, 2004: Effective Ice Particle Densities Derived from Aircraft Data. *J. Atmos. Sci.*, **61**, 982–1003.

Hobbs, P. V., S. Chang, and J. D. Locatelli, 1974: The dimensions and aggregation of ice crystals in natural clouds. *J. Geo. Res.*, **79**, 2199-2206.

Hogan, R. J., A. J. Illingworth, and H. Sauvageot, 2000: Measuring crystal size in cirrus using 350 and 94-GHz radars. *J. Atmos. Oceanic Tech.*, **17**, 27-37.

Iwanami, K., R. Misumi, M. Maki, T. Wakayama, K. Hata, and S. Watanabe, 2001: Development of a multiparameter radar system on mobile platform. Preprints, 30th Int. Conf. on Radar Meteorology, Munich, Germany, Amer. Meteor. Soc., 104–106.

Jameson, A. R., 1983: Microphysical interpretation of multi-parameter radar measurements in rain. Part I: Interpretation of polarization measurements and estimation of raindrop shapes. *J. Atmos. Sci.*, **40**, 1792-1802.

Jameson, A. R., 1991: Polarization radar measurements in rain at 5 and 9 GHz. *J. Appl. Meteor.*, **30**, 1500–1513.

Jameson, A. R., 1992: The effect of temperature on attenuation-correction schemes in rain using polarization propagation differential phase shift. *J. Appl. Meteor.*, **31**, 1106–1118.

Jameson, A. R., 1994: An alternative approach to estimating rainfall rate by radar using propagation differential phase shift. *J. Atmos. Oceanic Technol.*, **11**, 122-131.

Kasemir, H. W., 1960: A contribution to the electrostatic theory of lightning discharge. *J. Geophys. Res.*, **65**, 1873-1878,

Keeler, R. J., and R. E. Passarelli, 1990: Signal Processing for Atmospheric Radars. *Radar in Meteorology*, D. Atlas, Ed., Amer. Meteor. Soc., 287-315.

Kruger, A. and W. F. Krajewski, 2002: Two-dimensional video disdrometer: A description. *J. Atmos. Oceanic Tech.*, **19**, 602-617.

Lang, T. J., S. A. Rutledge, J. E. Dye, M. Venticinque, P. Laroche, and E. Defer, 2000: Anomolously low negative cloud-to-ground lightning flash rates in intense convective storms observed during STERAO-A. *Mon. Wea. Rev.*, **128**, 160-173.

Lang, T. J. and S. A. Rutledge, 2002: Relationships between convective storm kinematics, precipitation and lightning. *Mon. Wea. Rev.,* **130**, 2492-2506.

Lerach, D., 2006: *Vertical Structure and Kinematics of Tropical Monsoon Precipitation Observed from a 2875-MHz Profiler during NAME.* Master's thesis, Colorado State University, Fort Collins, 105 pp.

List, R., 1958: Kennzzeichen atmosphärischer Eispartikeln, Part 1. *Z. Angew. Math. Phys.*, **9a**, 180-192.

List, R. and R. S. Schemenauer, 1971: Free-Fall Behavior of Planar Snow Crystals, Conical Graupel and Small Hail. *J. Atmos. Sci.,* **28**, 110-115.

Liu, H., and V. Chandrasekar, 2000: Classification of hydrometeors based on polarimetric radar measurements: Development of fuzzy logic and neuro-fuzzy systems, and in situ verification. *J. Atmos. Oceanic Tech.,* **17,** 140-164.

Liu, Y., V. N. Bringi and M. Maki, 2006: Improved rain attenuation correction algorithms for radar reflectivity and differential reflectivity with adaptation to drop shape model variation. Preprints, IEEE International Geoscience and Remote Sensing Symposium, Denver, Colorado, July 31-August 4.

Locatelli, J. D., and P. V. Hobbs, 1974: Fall speeds and masses of solid precipitation particles. *J. Geophys. Res.,* **79,** 2185–2197.

MacGorman, D. R., D. W. Burgess, V. Mazur, W. D. Rust, W. L. Tayler, and B. C. Johnson, 1989: Lightning rates relative to tornadic storm evolution on 22 May 1981. *J. Atmos. Sci.*, **46**, 221-250.

Magano, C., 1954: Aon the falling velocities of solid precipitation elements, *Sci. Pre. Yokohama Nat. Univ., Sect. 1*, no. 3, 33.

Maki, M., S.-G. Park, and V. N. Bringi, 2005: Effect of natural variations of rain drop size distributions on rain rate estimators of 3 cm wavelength polarimetric radar. J. Meteor. Soc. Japan, **83,** 871-893.

Mansell, E. R., D. R. MacGorman, C. L. Ziegler, and J. M. Straka, 2002: Simulated three-dimensional branched lightning in a numerical thunderstorm model. *J. Geophys. Res.,* **107**, 4052, doi:10.1029/2000JD000024.

Marshall, J. S., and W. M. Palmer, 1948: The distribution of raindrops with size. *J. Meteor.*, **5**, 165-166.

Martner, B. E., K. A. Clark, S. Y. Matrosov, W. C. Campbell and J. S. Gibson, 2001: NOAA/ETL's polarization-upgraded H-band 'HYDRO" radar. Preprints *30th Int. Conf. on Radar Meteorology*, Munich, Germany, Amer. Meteor. Soc., 101-103.

Matrosov, S. Y., R. F. Reinking, R. A. Kropfli, and B. W. Bartram, 1996: Estimation of ice hydrometeor types and shapes from radar polarization measurements. *J. Atmos. Oceanic. Tech.,* **13**, 85-96.

Matrosov, S. Y., R. A. Kropfli, R. F. Reinking, and B. E. Martner, 1999: Prospects of measuring rainfall using propagation differential phase in X- and K_a-radar bands. *J. Appl. Meteor.*, **38**, 766–776.

Matrosov, S. Y., K. A. Clark, B. E. Martner, and A. Tokay, 2002: X-band polarimetric radar measurements of rainfall. *J. Appl. Meteor.*, **41**, 941-952.

Matrosov, S. Y., D. E. Kingsmill, B. E. Martner, and F. M. Ralph, 2005: The Utility of X-Band Polarimetric Radar for Quantitative Estimates of Rainfall Parameters. *J. Hydrometeor.*, **6**, 248-262.

Matrosov, S. Y., R. Cifelli, P. C. Kennedy, S. W. Nesbitt, S. A. Rutledge, V. N. Bringi and B. E. Martner, 2006: A Comparative Study of Rainfall Retrievals Based on Specific Differential Phase Shifts at X- and S-Band Radar Frequencies. *J. Atmos. Oceanic Tech.*, **23**, 952–963.

May, P. T., T. D. Keenan, D. S. Zrnic, L. D. Carey and S. A. Rutledge, 1999: Polarimetric radar measurements of tropical rain at a 5-cm wavelength. *J. Appl. Meteor.*, **38**, 750-765.

McLaughlin, D., 2001: *Presentation to Committee on weather radar technology beyond NEXRAD*. Washington, D.C., National Research Council.

McPherson, R. A. and co-authors, 2007: Statewide monitoring of the mesoscale environment: A technical update on the Oklahoma Mesonet. *J. Atmos. Oceanic. Tech.,* **24**, 301-321.

Miller, M. A., and co-authors, 2007: SGP Cloud and Land Surface Interaction Campaign (CLASIC): Science and Implementation Plan. U. S. Dept. Energy, DOE/SC-ARM-0704.

Mohr, C. G., and L. J. Miller, 1983: CEDRIC – A software package for Cartesian space editing, synthesis and display of radar fields under interactive control. *Preprints, 21st Conf. On Radar Meteorology,* Boston, *Amer. Meteor. Soc.,* 569-574.

Nelson, S., 1983: The influence of storm flow structure on hail growth, *J. Atmos. Sci*, **40**, 1965-1983.

Nelson, S. P., and R. A. Brown, 1987: Error sources and accuracy of vertical velocities computed from multiple-Doppler radar measurements in deep convective storms. *J. Atmos. Oceanic Technol.* **4, 233-238.**

Nissen, R., D. Hudak, S. Laroche, R. de Elia, I. Zawadzki, and Y. Asuma, 2001: 3D wind field retrieval applied to snow events using Doppler radar. *J. Atmos. Oceanic Technol.*, **18**, 348-362.

O'Brien, J.J., 1970: Alternative solutions to the classical vertical velocity problem. *J. Appl. Meteor.,* **9,** 197-203.

Ono, A., 1970: Growth mode of ice crystals in natural clouds. *J. Atmos. Sci.*, **27**, 649-658.

Park, S.-G., V. N. Bringi, V. Chandrasekar, M. Maki, and K. Iwanami, 2005: Correction of radar reflectivity and differential reflectivity for rain attenuation at x band. Part I: Theoretical and empirical basis. *J. Atmos. Oceanic Technol.,* **22**, 1621-1632.

Petersen, W. A., L. D. Carey, S. A. Rutledge, J. C. Knievel, N. J. Doesken, R. H. Johnson, T. B. McKee, T. Vonder Haar and J. F. Weaver, 1999: Mesoscale and radar observations of the Fort Collins Flash Flood of 28 July 1997. *Bull. Amer. Meteorol. Soc.,* **80,** 191-216.

Price, C., and D. Rind, 1993: What determines the cloud-to-ground lightning fraction in thunderstorms? *Geophys. Res. Lett.*, **20**, 463-466.

Pruppacher, H. R., and K.V. Beard, 1970: A wind tunnel investigation of the internal circulation and shape of water drops falling at terminal velocity in air. *Quart. J. Roy. Meteor. Soc.*, **96**, 247.

Pruppacher, H.R. and R.L. Pitter, 1971: A Semi-Empirical Determination of the Shape of Cloud and Rain Drops. *J. Atmos. Sci.*, **28**, 86-94.

Pruppacher, H. R. and J. D. Klett, 1997: Microphysics of clouds and precipitation, 2nd Ed., Kluwer Academic Publishers, Dordrecht, The Netherlands, 954 pp.

Ray, P. S., K. K. Wagner, K. W. Johnson, J. J. Stephens, W. C. Bumgarner, and E. A. Mueller, 1978: Triple-Doppler observations of a convective storm. *J. Appl. Meteor.*, **17**, 1201-1212.

Rison, W., R. J. Thomas, P. R. Krehbiel, T. Hamlin, and J. Harlin, 1999: A GPS-based three-dimensional lightning mapping system: Initial observations in central New Mexico. *Geophys. Res. Lett.,* **26**, 3573-3576.

Rogers, D. C., 1974: Observational study of aggregation. *Bull. Amer. Met. Soc.,* **55**, 676-676.

Rottner, D. and G. Vali, 1974: Snow Crystal Habit at Small Excesses of Vapor Density over Ice Saturation. *J. Atmos. Sci.,* **31**, 560–569.

Rutledge, S. A., R. A. Houze Jr., M. I. Biggerstaff, and T. Matejka, 1988: The Oklahoma-Kansas Mesoscale Convective System of 10-11 June 1985: Precipitation structure and single-Doppler radar analysis. *Mon. Wea. Rev.,* **116**, 1409-1430.

Ryzhkov, A. V., V. B. Zhuravlyov, and N. A. Rybakova, 1994: Preliminary results of X-band polarization radar studies of clouds and precipitation. *J. Atmos. Oceanic Tech.*, **11**, 132-139.

Ryzhkov, A. V., and D. S. Zrnic, 1995: Comparison of dual-polarization radar estimators of rain. *J. Atmos. Oceanic Technol.*, **12**, 249-256.

Ryzhkov, A. and D. S. Zrnic, 1998: Discrimination between ran and snow with a polarimetric radar. *J. Appl. Meteor.*, **37**, 1228-1440.

Ryzhkov, A., D. S. Zrnic, B. A. Gordon, 1998: Polarimetric method for ice water content determination. *J. Appl. Meteor.*, **37**, 125-134.

Ryzhkv, A., S. E. Giangrande, and T. J. Schuur, 2003: Rainfall measurements with the polarimetric WSR-88D radar. National Severe Storms Laboratory Rep., 98 pp.

Ryzhkov, A. and D. Zrnic, 2005: Radar polarimetry at S, C, and X bands comparative analysis and operational implications. Preprints, *32nd Int. Conf. on Radar Meteor.*, Albuquerque, NM, Amer. Meteor. Soc., 9R.3.

Ryzhkov, A., T. J. Schuur, D. W. Burgess, P. L. Heinselman, S. E. Giangrande, and D. S. Zrnic, 2005: The Joint Polarization Experiment: Polarimetric Rainfall Measurements and Hydrometeor Classification. *Bull. Am. Meteor. Soc.*, **86**, 809-824.

Saunders, C. P. R. and S. L. Peck, 1998: Laboratory studies of the influence of the rime accretion rate on charge transfer during graupel/crystal collisions. *J. Geophys. Res.*, **103**, 13949-13956.

Sekhon, R. S. and R. C. Srivastava, 1970: Snow size spectra and radar reflectivity. *J. Atmos. Sci.*, **27**, 299-307.

Straka, J. M., D. S. Zrnic, and A. V. Ryzhkov, 2000: Bulk hydrometeor classification and quantification using polarimetric radar data: synthesis of relations. *J. App. Meteor.*, **39**, 1341-1372.

Takahashi, T., 1978: Riming electrification as a charge generation mechanism in thunderstorms. *J. Atmos. Sci.*, **35**, 1536-1548.

Tessendorf, S. A., L. J. Miller, K. C. Wiens, and S. A. Rutledge, 2005: The 29 June 2000 supercell observed during STEPS. Part I: Kinematics and microphysics. *J. Atmos. Sci.*, **62**, 4127-4150.

Testud, J., E. Le Bouar, E. Obligis, and M. Ali-Mehenni, 2000: The rain profiling algorithm applied to polarimetric weather radar. *J. Atmos. Oceanic Technol.*, **17**, 332-356.

Thomas, R., P. Krehbiel, W. Rison, J. Harlin, T. Hamlin and N. Campbell, 2003: The LMA flash algorithm. *Proc. 12th Int. Conf. on Atmos. Electricity,* Versailles, France, ICAE, 655-656.

Thomas, R., P. Krehbiel, W. Rison, S. J. Hunyady, W. P. Winn, T. Hamlin and J. Harlin, 2004: Accuracy of the Lightning Mapping Array. *J. Geophys. Res.*, **109**, doi:10.1029/2004JD004549.

Thurai, M., and V. N. Bringi, 2005: Drop axis ratios from a 2D video disdrometer. *J. Atmos. Oceanic Technol.*, **22**, 966-978.

Thurai, M., G. J. Huang, V. N. Bringi, W. L. Randeu, and M. Schönhuber, 2007: Drop shapes, model comparisons, and calculations of polarimetric radar parameters in rain. *J. Atmos. Oceanic Technol.*, **24**, 1019-1032.

Tian, L., G. M. Heymsfield, and R. C. Srivastava, 2002: Measurement of Attenuation with Airborne and Ground-Based Radar in Convective Storms over Land and Its Microphysical Implications. *J. Appl. Meteor.*,**41,** 716-733.

Ulbrich, C. W., 1978: Relationships of equivalent reflectivity factor to the vertical fluxes of mass and kinetic energy of hail. *J. Appl. Meteor.*, **17**, 1803-1808.

Ulbrich, C. W., 1983: Natural variations in the analytical form of the raindrop size distribution. *J. Climate Appl. Meteor.*, **22,** 1764–1775.

Vivekanandan, J., W. M. Adams, and V. N. Bringi, 1991: Rigorous approach to polarimetric radar modeling of hydrometeor distributions. *J. Appl. Meteor.*, **30,** 1053-1063.

Vivekanandan, J., D.S. Zrnic, S.M. Ellis, R. Oye, A. V. Ryzhkov, and J. Straka, 1999: Cloud microphysics retrieval using S-band dual-polarization radar measurements. *Bull. Am. Meteor. Soc.*, **80**, 381-388.

Wang, Y., V. Chandrasekar, and B. Dolan, 2008: Development of scan strategy for dual Doppler retrieval in a networked radar system. Preprints, IEEE Int. Geosci. Remote Sensing Symp., Boston, MA.

Weinheimer, A. J., and A. A. Few, 1987: The electric field alignment of ice particles in thunderstorms. *J. Geo. Res.*, **92**, 14,833-14,844.

Wiens, K. C., S. A. Rutledge, and S. A. Tessendorf, 2005: The 29 June 2000 Supercell observed during STEPS. Part II: Lightning and charge structure. *J. Atmos. Sci.*, **62**, 4151-4177.

Williams, E. R., 1985: Large-scale charge separation in thunderclouds. *J. Geophys. Res.*, **90**, 6013-6025.

Williams, C. M. Cooke, and K. A. Wright, 1985: Electrical discharge propagation in and around space charge clouds. *J. Geophys. Res.*, **90**, 6059-6070.

Williams, E. R., 1989: The tripole structure of thunderstorms. *J. Geophys. Res.*, **94**, 13151-13167.

Williams, E. R., M. E. Weber, and R. E. Orville, 1989: The relationship between lightning type and convective state of thunderclouds. *J. Geophys. Res.*, **94**, 13,213-13,220.

Williams, E. R., R. Zhang, and J. Rydock, 1991: Mixed-phase microphysics and cloud electrification. *J. Atmos. Sci.*, **48**, 2195-2203.

Williams, E. R., R. Zhang, and D. Boccippio, 1994: Microphysical growth state of ice particles and large-scale electrical structure of clouds. *J. Geophys. Res.*, **99**, 10787-10792.DOI:

Williams, E. R., 2001: The electrification of severe storms. *Severe Convective Storms, Meteor. Monogr.*, No. 50, Amer. Meteor. Soc., 527-561.

Willis, P. T., 1984: Functional fits to some observed drop size distributions and parameterization of rain. *J. Atmos. Sci.,* **41,** 1648–1661.

Willis, P. T. and A. J. Heymsfield, 1989: Structure of the melting layer in mesoscale convective system stratiform precipitation. *J. Atmos. Sci.,* **46**, 2008-2025.

Xu, J. L., 1983: Some hail research in China. *Bull. Am. Meteor. Soc.,* **64**, 124-129.

Zhang, G., Q. Cao, M. Xue, P. Chilson, M. Morris, R. Palmer, J. Brotzge, T. Schuur, E. Brandes, K. Iketa, A. Ryzhkov, D. Zrnic, and E. Jessup 2008: A field experiment to study rain microphysics using video disdrometers, a profiler, and polarimetric S and X-band radars. *Symposium on Recent Developments in Atmospheric Applications of Radar and Lidar*, AMS Annual Meeting, New Orleans, LA.

Zink, M, E. Lyons, D. Westbrook, D. Pepyne, B. Philips, J. Kurose, and V. Chandrasekar, 2008: Meteorological Command & Control: Architecture and performance evaluation. Preprints, IEEE Int. Geosci. Remote Sensing Symp., Boston, MA.

Zikmunda, J. and G. Vali, 1972: Fall Patterns and Fall Velocities of Rimed Ice Crystals. *J. Atmos. Sci.*, **29**, 1334-1347.

Zrnic, D. S. and A. Ryzhkov, 1996: Advantages of rain measurements using specific differential phase. *J. Atmos. Oceanic Technol.,* **13**, 454-464.

Zrnic, D. S., A. Ryzhkov, J. Straka, Y. Liu, and J. Vivekanandan, 2001: Testing a procedure for automatic classification of hydrometeor types. *J. Atmos. Oceanic Tech.*, **18**, 892-913.